LASER APPLICATIONS AND REFRACTIVE PROPERTIES OF NON-HOMOGENEOUS GAS DISTRIBUTIONS

December 20, 1995

Submitted in partial fulfilment for the PhD requirement of

Nicola Lisi

University of Natal
Department of Physics
King George V Ave.
Durban, South Africa

ACKNOWLEDGEMENTS

I am particularly grateful to Prof. Max Michaelis, my supervisor, for giving me the opportunity of joining the laser group of the Plasma Physics Research Institute at the University of Natal. It has been an interesting period of collaboration and friendship with him and the other graduate students of the group, Arnold Prause, Rodney Kuppen and Ricardo Buccellato. Many thanks to Prof. Peter Cunningham, who unfortunately left the University only one year after I joined the group, but nevertheless gave me the opportunity of a wonderful trip to Botswana, and to Gavin Hough for the interesting discussions and for teaching me how to love the country.

I am grateful to Prof. Manfred Hellberg and to the FRD for always providing the funding for my stay and research.

Many thanks to Willem De Beer who directs the physics workshop for the help and useful suggestions that he always provided. To Derek and Stanley from the mechanical workshop, John Atkinson, Terry Burham and Patrick Swanepoel from the electronic workshop for actually manufacturing all the experimental apparatuses described in this thesis and to Terry Halloway for the computer expertise.

INDEX

ABSTRACT

In this thesis the performances and the applications of several types of gas lenses are analysed. A gas lens consists of a region of space in which gas is forced into a particular spatial density distribution which can result in the focusing or defocusing of a laser beam. From basic optics theory, a refractive index gradient follows any density gradient present in a gas. This is the same effect that causes mirages when temperature and density gradients are present in the lowest layer of the earth's atmosphere. There are two possible types of mirage that one can observe on the earth's surface. A brief description on how mirages form is useful in order to introduce the working principles of gas lenses.

In the first case there is a cold layer of air close to the ground with a hotter layer above. The situation described above is commonly called 'thermal inversion' because the standard situation in which the temperature decreases with the increasing altitude is reversed. In this case the refractive index decreases with height. As a consequence the refractive index gradient bends the light rays downwards. In exceptionally still atmospheric conditions this situation can create upright images of distant objects whose direct line of sight would lie below the horizon. This phenomenon is only seen under still weather conditions and requires a highly reflecting surface, such as ice. The ground has to reflect most of the sun's radiation in order to maintain the low temperature of the lowest layer of air.

The second type of mirage is the most commonly seen at temperate and tropical latitudes and it creates inverted images of objects above the earth surface's line of sight. This is the same optical effect responsible for the 'water pools' that one might observe in summer while driving along a tar road, which in fact are inverted images of patches of sky. The air is heated in the boundary layer where it exchanges heat with the hot ground, thus its density decreases. The refractive index gradient is then directed upwards and the light rays are bent away from the ground. In this second case the mirages are always accompanied by turbulence due to the uneven effect of gravity on equal volumes of cold and hot air. This results in convective flow, and the image is never still.

A class of gas lenses, known since the 1960's as 'Thermal Gradient Gas Lenses', uses the thermal gradient created in a gas by a hot pipe in order

to establish an average radial refractive index gradient inside its cylindrical volume.

A thermal gradient gas lens is in effect a folded mirage. If the hot gas lies in the outer part of the cylinder, we have a converging lens that focuses light to a point, while if the hot gas is in the core of the cylinder, we have a diverging lens. In the latter case the pipe must be cooled with respect to room temperature.

When we consider the effect of gravity on the spatial gas density distribution of a thermal gradient gas lens, we note that a horizontal, cylindrically symmetric distribution is unstable and that convective cells are going to form a short time after the heating is switched on.

A cylindrically symmetric temperature field is achieved only when the pipe is kept vertical. The convective cells can be destroyed by flowing the gas longitudinally down the pipe, if its cross section is small, or by the vortical gas flow resulting from spinning the hot pipe about its geometrical axis. As examined in the second chapter of this thesis, where a spatially resolved temperature measurement is presented, this option can give a fairly stable and large aperture gas lens. The latter device, the Spinning Pipe Gas Lens (or SPGL), was developed in recent years at this University.

But why should one use these devices rather than just a quartz, a glass or a polymer lens?

Gas lenses are cumbersome devices and, although their optical quality is good, it cannot compete with the optical quality achievable with a well cut solid state device. The main advantage lies in the high threshold at which optical breakdown occurs.

It is well known that if a very intense beam of optical radiation propagates through a solid state material, surface or bulk radiation damage can be observed. Moreover, the damage is not simply cumulative, it can increase exponentially after the first defect has been created. In addition, the 'theoretical' radiation damage threshold can decrease dramatically in a real working environment (a dusty laboratory or a workshop).

Gas lenses do not have any surfaces to which dust or grease can adhere nor do they require AR coatings. The latter is naturally achieved by the smooth refractive index increase from unity along the optical axis. Gas lenses have an optical breakdown threshold two orders of magnitude higher and, if a breakdown occurs, there is not any permanent damage. The lens can recover after a few milliseconds.

A secondary advantage of gas lenses is the wide wavelength range over which they can be used, which depends on the dispersion relation of the particular gas utilised.

Gas lenses have an optical breakdown threshold of the order of $100 GW/cm^2$. Such a high level of optical power can be delivered as short bursts of laser radiation. When the techniques of Q-switching, or of a pulsed gas discharge are utilised, the pulse duration of the radiation burst of a typical commercial laser is in the order of 5-40 ns.

We can then ask the following question: Why do we need a steady state gas lens that works continuously, if it is going to be utilised for a few billionths of a second? In the framework of this idea we developed a pulsed gas lens, as described in the third chapter. The working principle relies on the compression of a dense central core of gas by the action of multiple converging shock waves. Various designs of Colliding Shock Lens (or CSL) were developed, all based on the gas compression operated by the central collision of multiple shock waves converging in cylindrical symmetry. Each shock wave is generated by an arc discharge between two pin electrodes facing along the arc of a circle. The CSL is a varifocal lens, whose focal length and optical aperture typically vary on the microsecond time scale. Such a pulsed lens, in combination with a pinhole can be utilised as a high power optical switch or as an optical isolator for switching speed on the 100's of ns timescale.

In the fourth chapter we present an application of both the Colliding Shock Lens and the Spinning Pipe Gas Lens, the 'all gas Q-switching' of a ruby laser. In this experiment the Q-spoiling of a ruby laser is achieved utilising almost entirely gas elements. By inserting a pulsed lens (CSL) in tandem with a converging lens (SPGL) inside the flat-flat resonator of the ruby laser, made of a 100% full reflector and of a 50% output coupler, we realise a time varying resonator geometry. Laser radiation will occur in the form of a single or double pulse as soon as the resonator becomes stable and the losses become low. For this application, a fast shock collision dynamic and a low f-number pulsed lens are important requirements.

After the description and the modelling of the Q-switching experiment, the optical quality of the CSL is examined in greater detail.

In the fifth chapter of the thesis some Mach-Zehnder interferograms of the CSL are analysed. The interferograms were recorded using a nitrogen probe laser (337nm wavelength, 1 ns pulse duration) developed and built in our laboratory. The interferograms were taken at different time delays after the central collision of the shock waves by electrically synchronising the probe laser. Each interferogram gives an instant picture of the refractive index distribution inside the lensing region and the optical quality of the CSL can then be theoretically determined at each delay. Despite some significant longitudinal aberration it was found that the optical performances of the CSL can be almost diffraction-limited when the probe laser is synchronised at some optimum delay after the central shock collision.

Up to this stage the shock waves have always been colliding with cylindrical symmetry with respect to the optical axis. However, another interesting feature of the Colliding Shock Lens geometry lies in the possibility of shaping the imploding shock front and consequently the lensing region. For example by placing the shock launching points along the arc of an ellipse rather than along the arc of a circle, we can make an elliptical lens. This is the case examined theoretically and experimentally in the sixth chapter. In an elliptical lens the refractive index level curves are ellipses rather than circles. A uniform intensity diffraction-limited laser beam is focused by a cylindrically symmetric CSL into a pattern that approximates the Airy pattern. Conversely in the case of an elliptical lens, the intensity distribution in the focal plane is something in between a line focus and a two lobed focus, as was observed experimentally.

CHAPTER 1: INTRODUCTION

1.1 THE LASER

The aim of this thesis is to demonstrate that non-uniform gas distributions can be useful in the field of laser physics. At most wavelengths, the increase of laser radiation power is actually limited by the radiation damage of the solid state components acting either as a resonator or as the active medium. Gas optics have a radiation damage threshold that is a few orders of magnitude higher than conventional solid state components and are natural candidates for high power laser applications. In the experiments described in chapters 2, 3 and 6, lasers are utilised only as a diagnostic tool. In chapter 4 we will demonstrate how a laser resonator can be made by utilising almost entirely gas elements. In the first section of the present chapter we briefly describe the principles of laser action.
Laser is an acronym which stands for Light Amplification by Stimulated Emission of Radiation. The laser mechanism is easily understood in the light of the theory of the Einstein coefficients [Einstein 1917].

1.1.1 THE EINSTEIN COEFFICIENTS

Consider an isolated cavity [Loudon 1983, Bransden 1983], in which a collection of two-level oscillators are in thermal equilibrium with radiation. A two-level oscillator can consist of any atomic or molecular system present in the cavity in two states of different excitation. The two states are separated by an energy gap and are linked by an allowed radiative transition.
The lower energy level is taken by convention to be the ground state, having zero energy. The energy difference between the two levels is ΔE, g_1 and g_2 are the degeneracies of the two levels and $\rho(\omega)$ is the radiation energy density. Then, according to the basic principles of statistical mechanics, the ratio between the level populations is:

$$\frac{N_2}{N_1} = \frac{g_2}{g_1}\exp\left(-\frac{\Delta E}{kT}\right) \qquad 1.1.1$$

In this treatment we will consider only one-photon processes. The treatment is then correct only at low and intermediate radiation densities for real atoms and molecules.
There are three possible interaction processes between oscillators and radiation: absorption, stimulated emission and spontaneous emission. Absorption is the process by which a photon is absorbed by an atom in the ground state, which then becomes excited. Spontaneous emission is the spontaneous decay of an excited atom with the creation of one photon. Stimulated emission is a process by which one photon hits an excited atom and two identical photons are emitted. Both the photons generated in this process have the same physical properties as the initial one: polarisation, phase, energy and direction. In the presence of radiation, the effects of these three interactive processes on the population variation rates are given by the following three relations:

$$\frac{\partial N_1}{\partial t} = -B_{12}\rho(\omega)N_1 \qquad 1.1.2$$

$$\frac{\partial N_2^{sp}}{\partial t} = -A_{21}N_2 \qquad 1.1.3$$

$$\frac{\partial N_2^{st}}{\partial t} = -B_{21}\rho(\omega)N_2 \qquad 1.1.4$$

Since the oscillators are at equilibrium with the radiation, as many photons are absorbed as are emitted.

$$\frac{\partial N_1}{\partial t} = -\frac{\partial N_2}{\partial t} \qquad 1.1.5$$

putting together the last four relations, we obtain

$$N_2A_{21} + N_2\rho(\omega)B_{21} = N_1\rho(\omega)B_{12}$$

By using the Boltzmann relation between levels' populations (equation 1.1.1) we obtain an expression for the radiation density in the cavity:

$$\rho(\omega) = \frac{A_{21}/B_{21}}{(g_2/g_1)\cdot(B_{12}/B_{21})\cdot \exp\left(\frac{\hbar\omega}{kT}\right) - 1} \qquad 1.1.6$$

But the cavity emits radiation with the black-body spectrum

$$\rho(\omega) = \frac{\omega^2}{\pi^2 c^3}\cdot\frac{\hbar\omega}{\exp\left(\frac{\hbar\omega}{kT}\right) - 1} \qquad 1.1.7$$

and the comparison between 1.1.6 and 1.1.7 allows one to find the following relations between the absorption and the emission coefficients:

$$\frac{A_{21}}{B_{21}} = \frac{\omega^2}{\pi^2 c^3} \quad \text{and} \quad B_{21} = \frac{g_1}{g_2} B_{12} \qquad 1.1.8$$

This derivation was performed assuming the hypothesis that the energy gap between levels, ΔE, is infinitely sharp. This is reasonable since the black body radiation spectrum is spread over a frequency range which is much wider than the transition line-width. This hypothesis ceases to be valid when we study the interaction of atoms with laser radiation.

1.1.2 THE INTERACTION OF A TWO-LEVEL SYSTEM WITH LASER LIGHT

We don't want to introduce laser beams before defining them, but we can safely say that the radiation line-width of any laser system is much sharper than the atomic transition line-width from which it originated. Consistently, when we deal with the formation and the propagation of a laser beam in the presence of a collection of atoms, we can approximate laser radiation $I(\omega)$ with a monochromatic wave whose frequency is centred about ω_s.

$$I(\omega)d\omega = \rho(\omega)\delta(\omega - \omega_s)d\omega \qquad 1.1.9$$

while the atomic transition energy exhibits a finite line-width,

$$N(\omega) = g(\omega, \omega_0) N \qquad 1.1.10$$

The function g, gives the spectral distribution of the atomic transition rate and is centred about the frequency ω_0. The finite line-width of the transition is due to many physical phenomena whose detailed treatment can be found in many laser textbooks [Loudon 1983].
The line-shape function g is normalised to unity,

$$\int_0^\infty g(\omega, \omega_0) d\omega = 1 \qquad 1.1.11$$

The equations 1.1.2, 1.1.3 and 1.1.4 can be rewritten in the following way:

$$\frac{\partial N_1}{\partial t} = -B_{12} \rho(\omega) N_1 g(\omega, \omega_0) \qquad 1.1.12$$

$$\frac{\partial N_2^{sp}}{\partial t} = -A_{21} N_2 g(\omega, \omega_0) \qquad 1.1.13$$

$$\frac{\partial N_2^{st}}{\partial t} = B_{21} \rho(\omega) N_2 g(\omega, \omega_0) \qquad 1.1.14$$

We assume that the radiation, whose frequency is centred on ω_s, is incident on a thin absorbing sample of thickness dx. Let the radiation density be high enough to neglect the spontaneous emission contribution. The number of photons is given by the balance

$$\frac{\partial N_2}{\partial t} - \frac{\partial N_1}{\partial t} = -\rho(\omega_s) B_{21} \left(\frac{g_2}{g_1} N_1 - N_2 \right) g(\omega, \omega_0) \qquad 1.1.15$$

Multiplying both sides of 1.1.15 with the photon energy hv and dividing by the volume V we get an expression for the energy density:

$$\frac{\partial}{\partial t}\left[\rho(\omega_s)d\omega\right] = -\rho(\omega_s)d\omega B_{21}\hbar\omega_s g(\omega_s,\omega_0)\left(\frac{g_2}{g_1}n_1 - n_2\right) \qquad 1.1.16$$

Equation 1.1.16 gives the rate of absorption of energy in the frequency interval $d\omega$. As the beam propagates in the material, the radiation density varies according to

$$\frac{\partial\rho(\omega_s)}{\partial x} = \frac{\hbar\omega_s}{c}\rho(\omega_s)g(\omega_s,\omega_0)B_{21}n \qquad 1.1.17$$

where we have defined the quantity n as

$$n = \left(n_2 - \frac{g_2}{g_1}n_1\right) \qquad 1.1.18$$

If we integrate with respect to x the equation 1.1.17, we find an exponential solution

$$\rho(\omega_s) = \rho_0(\omega_s)\exp\left[\hbar\omega_s g(\omega_s,\omega_0)B_{21}n\frac{x}{c}\right] \qquad 1.1.19$$

We define the absorption coefficient $\alpha(\omega_s)$

$$\alpha(\omega_s) = -ng(\omega_s,\omega_0)B_{21}\frac{\hbar\omega_s}{c} \qquad 1.1.20$$

and finally get:

$$\rho(\omega_s) = \rho_0(\omega_s)\exp\left[-\alpha(\omega_s)x\right] \qquad 1.1.21$$

Equations 1.1.18 to 1.1.21 are fundamental in order to understand how a laser works. Depending on the value of the variable **n**, the population inversion, light can be absorbed, transmitted or amplified.

1.1.3 THE POPULATION INVERSION AND THE GAIN

According to the Boltzmann distribution 1.1.1 for a collection of two-level oscillators at thermal equilibrium, the population inversion is always negative. In other words, at equilibrium there are always more atoms in the lower than in the upper energy state. Suppose now that we are able to generate a non-equilibrium situation in which

$$\frac{n_2}{g_2} > \frac{n_1}{g_1} \qquad (\text{ with } E_2 > E_1) \qquad 1.1.22$$

From equation 1.1.20 and 1.1.21 we see that the absorption coefficient has become negative and the radiation density increases exponentially as it travels in the 'inverted' medium. We define **G**, or small signal gain as:

$$\frac{\partial\rho(\omega)}{\partial x} \equiv G\rho(\omega) \qquad 1.1.23$$

When the population inversion is positive, the absorption is negative and the gain is positive. The intensity **I** which is proportional to the radiation density,

$$I(\omega) = \rho(\omega)\hbar\omega c \qquad 1.1.24$$

and increases exponentially as the wave propagates in the active medium.

$$\frac{\partial I}{\partial x} = GIx \qquad 1.1.25$$

$$I(x) = I_0 \exp(Gx)$$

The exponential solution 1.1.25 is valid only while the intensity is not too high, such as to affect the population inversion and the gain. In fact from equation 1.1.14 we learn that equation 1.1.25 must always be solved together with an analogous equation for the population inversion change rate:

$$\frac{\partial n}{\partial x} = -\left(1 + \frac{g_2}{g_1}\right) \cdot g(\omega_s, \omega_0)\rho(\omega_s)\frac{B_{21}}{c} n \qquad 1.1.26$$

The upper level population is depleted while radiation is amplified in the active medium. Then the exponential solution 1.1.25 is correct only at low intensities, and the equations 1.1.17 and 1.1.26 should always be solved together.

1.1.4 HOW TO CREATE POPULATION INVERSION

It is clear from the results of the previous paragraph that we cannot create a positive population inversion by feeding radiation into a cavity containing a collection of two level oscillators. From equation 1.1.26, as the radiation density increases, the population inversion tends to the asymptotic condition, n=0:

$$n_1 g_1 = n_2 g_2 \qquad 1.1.27$$

When condition 1.1.27 is realised, the absorption is zero $[\alpha(\omega)=0]$ and the medium is transparent.
Before examining how to create a population inversion, we will introduce the three following quantities, for any two energy levels a and b, with $E_a<E_b$: The spontaneous emission level lifetime τ_{ba}, the stimulated emission spectral cross section $\sigma_{ba}(\omega)$ and the absorption spectral cross section $\sigma_{ab}(\omega)$ [Koechner 1976]:

$$\tau_{ba} = \frac{1}{A_{ba}}$$

$$\sigma_{ba}(\omega_s) = \frac{A_{ba}\lambda_0^2}{4n_i^2} g(\omega_s,\omega_0) = \frac{\hbar\omega B_{ba}}{c} g(\omega_s,\omega_0) \qquad 1.1.28$$

$$\sigma_{ab}(\omega_s) = \frac{g_b}{g_a}\sigma_{ba}$$

Where n_i is the refractive index and λ_0 is the wavelength. The spontaneous emission lifetime coincides with the level lifetime only for two-level

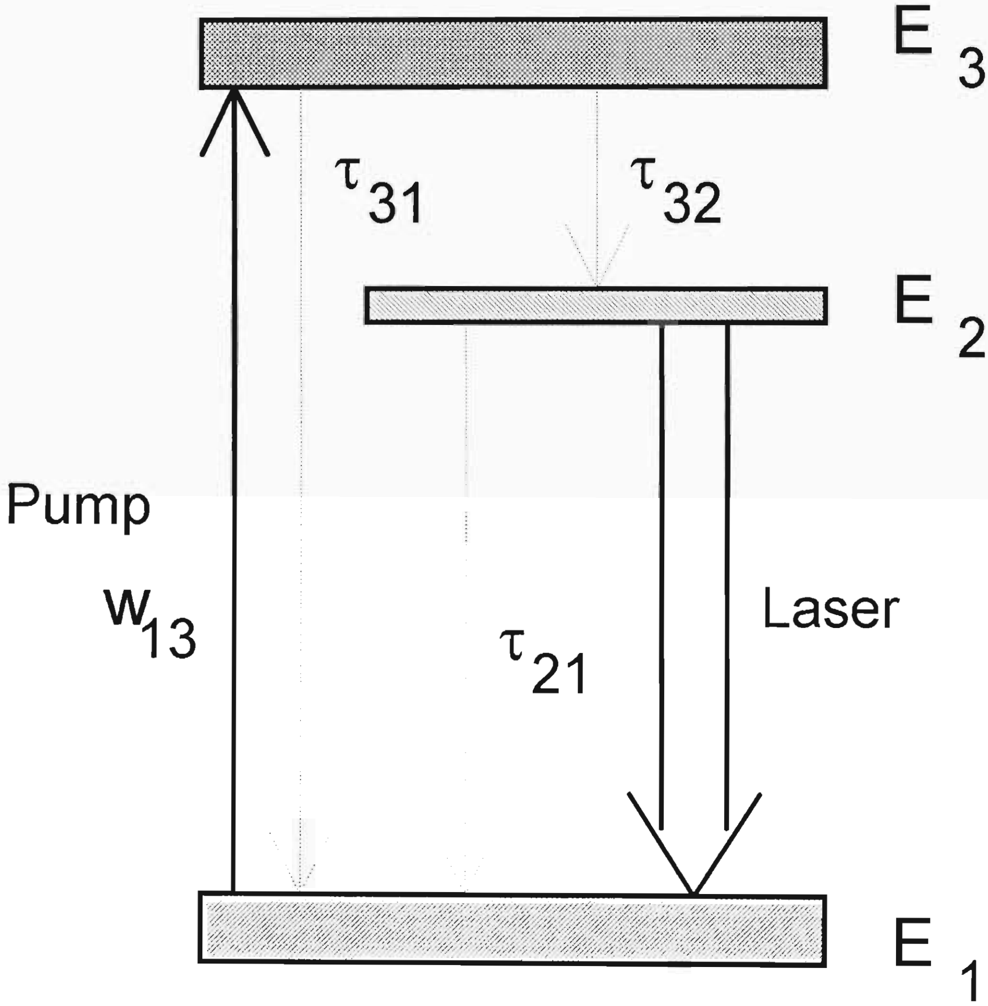

Fig.1.1.1 Transition diagram of a three-level active medium.

atoms. Other possible radiative and non-radiative decay processes result in the level lifetime being shorter than the spontaneous emission lifetime in real atoms or molecules. In order to achieve population inversion we need at least three energy levels, but most actual lasers make use of active media with four levels. The only three-level laser still in use is the Ruby laser. In one of the experiments discussed in this thesis (chapter 4) we have been using such a device.

No matter how many levels there are, the transitions between each pair of levels are still ruled by the equations 1.1.12 to 1.1.14. In figure 1.1.1 we show the transition scheme of a three-level laser system.

The idea is that some energy source, which we call the pump (W_{13}), can channel some atoms from the ground state (1) to the upper level (3). The atoms in level (3) will spontaneously decay to populate the upper laser level (2). Lasing will occur once a positive population inversion has been established between level (2) and (1). Of course the transition between level (2) and (1) must be an allowed radiative transition, while the transition between (3) and (1) must be forbidden, or $\tau_{31} >> \tau_{21}$. Two other general conditions that the system must satisfy are the following: The first is that $\tau_{31} >> \tau_{32}$, in order to establish population inversion. The second is that $\tau_{32} << \tau_{21}$, for the population inversion to be conspicuous. When these conditions are satisfied, the number of atoms in the level (3) is negligible and we can say that the atoms are either in level (1) or (2) .

$$n_1 + n_2 = n_{tot} \qquad 1.1.29$$

where n_{tot} is the total number of atoms.

In the four-level case the conditions on the transition rates are similar: $\tau_{30}, \tau_{31} >> \tau_{32}$ and $\tau_{21} >> \tau_{32}, \tau_{10}$. Though, in this second configuration, there is one important difference: the lower laser level is not the ground level of the atoms and consequently, if τ_{10} is very short, level (1) is always empty. Population inversion can then be achieved with a much lower pump power (W_{03}) and a higher efficiency than in the three-level case. When the above conditions on the transition rates are true, we can again say that

$$n_0 + n_2 = n_{tot} \qquad 1.1.30$$

where n_{tot} is the total number of atoms. The next figure shows the transition scheme of a four level system.

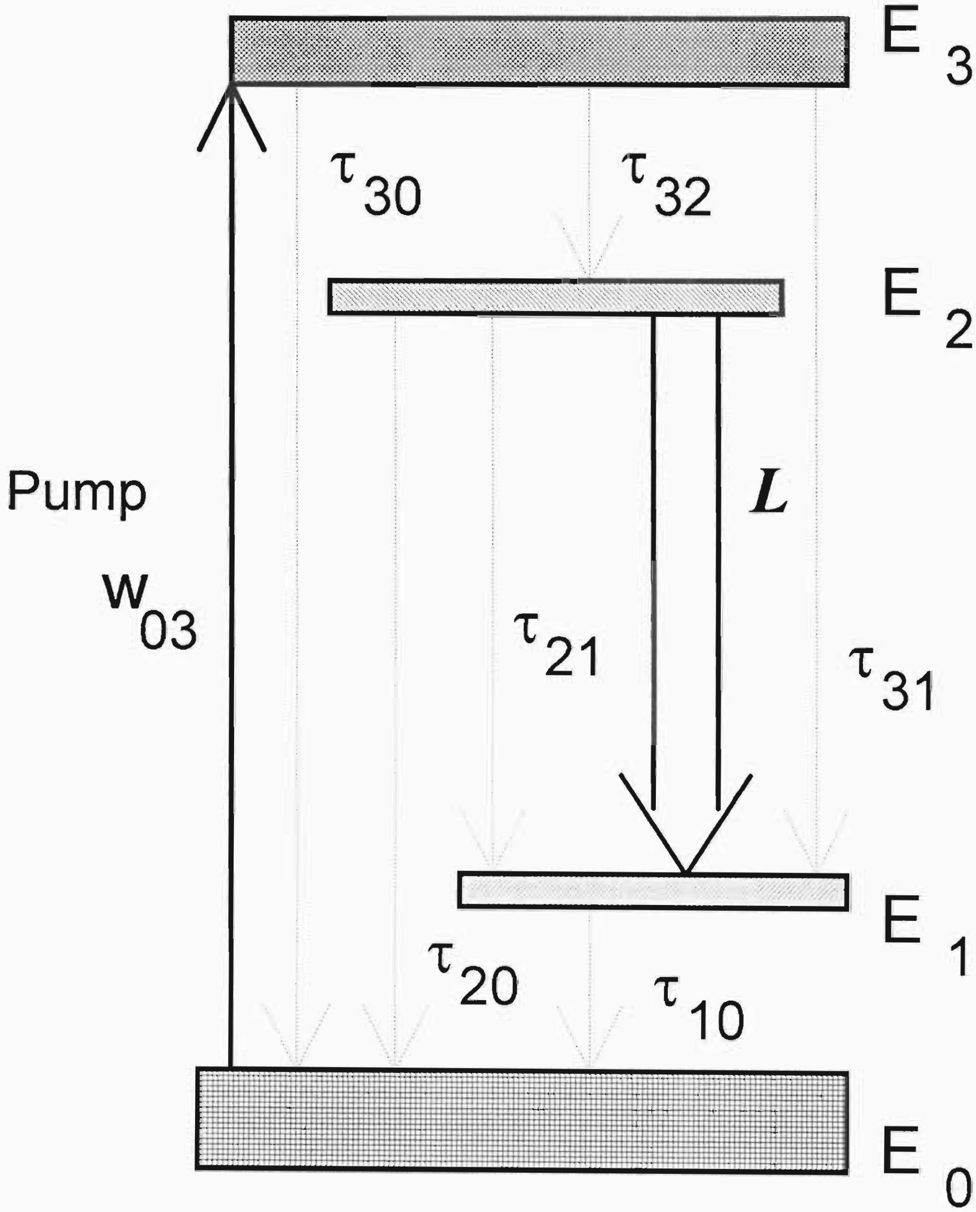

Fig.1.1.2 Transition diagram of a four-level laser medium.

1.1.4 THE LASER MECHANISM AND THE RATE EQUATIONS

When an inverted medium is placed in an optical cavity, laser radiation can be observed. When some spontaneous radiation is emitted by the active medium, it is amplified by the stimulated emission mechanism that provides a positive gain. A travelling radiation wave then starts to develop in the active medium. It propagates and it is amplified according to equations 1.1.17 and 1.1.26. A minimum active medium length is necessary for the energy to be extracted by the beam. In order to keep compact the dimensions of the system, it is possible to achieve the same effect of enhancing the active medium length by placing it inside an optical cavity (or resonator). In its commonest configuration the optical cavity consists of two spherical or plane mirrors, one of which is fully reflective (full reflector), the second beirg partially reflective (output coupler). The partial reflectivity is necessary for the beam extraction. We can describe the dynamic behaviour of a laser with a set of coupled rate equations [Koechner, 1976]. In their simplest form they consist of two coupled equations for the population inversion and for the photon density inside the cavity. The photon density ϕ can be expressed in terms of the related quantity $\rho(\omega)$ as:

$$\phi = \frac{B_{21}\rho(\omega)}{c\sigma_{21}(\omega)} \qquad 1.1.31$$

For a three-level laser system, using the 1.1.29 and 1.1.28,

$$\begin{aligned} \frac{dn_1}{dt} &= \left(n_2 - \frac{g_2}{g_1}n_1\right)c\phi\sigma + \frac{n_2}{\tau_{21}} - W_{13}n_1 \\ \frac{dn_2}{dt} &= -\frac{dn_1}{dt} \end{aligned} \qquad 1.1.32$$

Extracting the population inversion in 1.1.32 and substituting the 1.1.31 in 1.1.16, we obtain

$$\frac{dn}{dt} = -\left(1 + \frac{g_2}{g_1}\right) n\sigma\phi c - \frac{n + g_2/g_1 \cdot n_{tot}}{\tau_{21}} + W_{31}\left(n_{tot} - n\right)$$
$$\frac{d\phi}{dt} = n\sigma\phi c - \frac{\phi}{\tau_c} + S \qquad 1.1.33$$

where τ_c is the photon decay time in the resonator and S is the spontaneous emission contribution. The photon equation takes into account the photons lost from the output coupler through the loss term proportional to $1/\tau_c$.

Correspondingly in the four-level case the rate equations are:

$$\frac{\partial n}{\partial t} = -n\phi\sigma c - \frac{n}{\tau_{21}} + W_{03}\left(n_{tot} - n\right)$$
$$\frac{\partial \phi}{\partial t} = n\phi\sigma c - \frac{\phi}{\tau_c} + S \qquad 1.1.34$$

1.1.5 SOME CONSIDERATIONS ABOUT LASERS

The laser rate equations give a very general description of a typical laser system. Depending on the values of the physical parameters of the system, lasers exhibit a wide range of different behaviours. What is common to all laser systems is their nature of coherent "Amplifiers of Quantum Noise". The most interesting properties of lasers lie in the thermodynamic and coherence properties. Let us consider a flash-lamp pumped laser. From a pump source which is a source of chaotic radiation, having poor spatial and temporal coherence, we can generate a beam with the two following features:

a) Temporal Coherence;

b) Spatial Coherence;

The temporal coherence implies that the radiation is emitted into a narrow spectral line, while the spatial coherence implies a high beam brightness. It is due to these two features that laser light found so many applications. In the pumping process, an appreciable fraction of the pump energy can be transferred to a highly collimated radiation beam. If such a beam is focused onto a target, it can create a plasma with a temperature of several kV, much hotter than the pump itself. The generation and the handling of such energetic beams of light is a big technological problem and involves many branches of applied physics and engineering.

1.2 THE PROPAGATION OF LIGHT

In this section we will introduce Maxwell's equations for the propagation of an electromagnetic field in a medium which has a linear response. In the next section we will deal with a particular approximation of Maxwell's equations known as Geometrical Optics. The latter will allow us to solve numerically the problem of the propagation of a laser beam inside a gas lens.

1.2.1 THE MAXWELL EQUATIONS AND THE WAVE EQUATION

Let us consider the electromagnetic field in an isotropic material with linear response characteristics. In a linear medium we can define the polarisation **P** as.

$$\vec{P} = \chi\vec{E} \qquad 1.2.1$$

and the dielectric induction vector **D**,

$$\vec{D} = \varepsilon_0\varepsilon_r\vec{E} = (1 + \chi)\vec{E} \qquad 1.2.2$$

for an external electric field **E** of finite amplitude.
Analogously we define the magnetic permittivity μ and the magnetic vector **H** to express the linear response to a finite amplitude magnetic induction field **B.**

$$\vec{B} = \mu_0\mu_r\vec{H} \qquad 1.2.3$$

$\varepsilon_0 = 8.854 \cdot 10^{-12}$ F/m and $\mu_0 = 4\pi \cdot 10^{-7}$ H/m are the electric permittivity and the magnetic permeability of free space. ε_r and μ_r equal unity in free space and never differ much from a few times unity in most materials (at least in non-ferromagnetic materials). The values of ε_r and μ_r must be calculated with the help of a microscopic theory for each medium and can depend on some characteristics of the external field such as its frequency. Since they are defined as linear responses, they do not depend on the field amplitude. In such linear and isotropic media, the laws that govern the evolution of the electric and magnetic field are the Maxwell equations [Born and Wolf 1993]:

$$
\begin{aligned}
&\vec{\nabla} \wedge \vec{H} - \frac{1}{c}\vec{D}'' = \frac{4\pi}{c}\vec{J} \\
&\vec{\nabla} \wedge \vec{E} + \frac{1}{c}\vec{B}'' = 0 \\
&\vec{\nabla} \cdot \vec{D} = 4\pi\rho \\
&\vec{\nabla} \cdot \vec{B} = 0
\end{aligned}
\qquad 1.2.4
$$

We must add to Maxwell's equations the material equations 1.2.2 and 1.2.3, and

$$\vec{J} = \sigma \vec{E} \qquad 1.2.5$$

to define the response of the medium. Here σ is the specific conductivity of the medium and equation 1.2.5 describes the motion of the free charged particles under the effect of the field.

After some manipulation we can separate the electric and magnetic field in the 1.2.4 to get two propagation equations for the electric and magnetic field:

$$\nabla^2\vec{E} - \frac{\varepsilon\mu}{c^2}\vec{E}'' + \left(\vec{\nabla}\log\mu\right) \wedge \left(\vec{\nabla} \wedge \vec{E}\right) - \vec{\nabla}\left(\vec{E} \cdot \vec{\nabla}\log\varepsilon\right) = 0 \qquad 1.2.6$$

$$\nabla^2\vec{H} - \frac{\varepsilon\mu}{c^2}\vec{H}'' + \left(\vec{\nabla}\log\varepsilon\right) \wedge \left(\vec{\nabla} \wedge \vec{H}\right) - \vec{\nabla}\left(\vec{H} \cdot \vec{\nabla}\log\mu\right) = 0 \qquad 1.2.7$$

Where the medium is homogeneous, the gradient of the dielectric constant and of the magnetic permeability are zero, and 1.2.6 and 1.2.7 reduce to:

$$\nabla^2\vec{H} - \frac{\varepsilon\mu}{c^2}\vec{H}'' = 0$$
$$\nabla^2\vec{E} - \frac{\varepsilon\mu}{c^2}\vec{E}'' = 0 \qquad 1.2.8$$

These are the standard wave equations. Their solutions are electromagnetic waves propagating with the velocity:

$$v \equiv |\vec{v}| = \frac{c}{\sqrt{\varepsilon\mu}} \qquad 1.2.9$$

The constant c is the velocity of the EM waves in vacuum. Its value is c=299792.458 Km/s and it is a universal constant.
The ratio between the electromagnetic wave velocity in vacuum and in the medium, is known as the refractive index of the medium n,

$$n \equiv \frac{c}{v} \qquad 1.2.10$$

n can be measured or it can be calculated with the help of a microscopic theory of the medium.

1.3 GEOMETRICAL OPTICS

The wave equations 1.2.6 and 1.2.7 cannot be solved in their general form. We will look for some approximations that make them easier to handle. The typical wavelength of a laser radiation ranges between 200nm to a few tens of microns, that is from near ultraviolet to far infrared. Suppose now that the dielectric constant and the magnetic permeability relative variations are small on the spatial scale of one wavelength. Under these conditions light propagation obeys much simpler rules than in the general case.
Alternatively, we can imagine dealing with electromagnetic fields whose wavelengths tend to 0. The light propagation properties in this approximation $(\lambda \to 0)$ constitute a branch of optics known as Geometric

Optics. The limitations of applicability of the geometric optics become evident when light is propagated through spatial structures whose typical dimension is comparable to the radiation wavelength, such as diffraction gratings, pinholes and edges of sharp objects.

At the moment we are interested in a set of equations that describe the way light propagates through non-homogeneous media, where the spatial scale of the in-homogeneities is much larger than the wavelength. In particular we will investigate the propagation of light into non-uniform gas density distributions.

1.3.1 THE EIKONAL EQUATION

We will now derive the propagation equations of light in the geometric optics approximation. Consider the generic time harmonic field, or quasi-monochromatic wave:

$$\begin{aligned} \vec{E}(\bar{r},t) &= \vec{E}_0(\bar{r})\exp(-i\omega t) \\ \vec{H}(\bar{r},t) &= \vec{H}_0(\bar{r})\exp(-i\omega t) \end{aligned} \qquad 1.3.1$$

We can decouple the spatial variation of the field into a fast plane wave dependence and a slow variation.

$$\begin{aligned} \vec{E}_0(\bar{r}) &= \vec{e}(\bar{r})\exp\left[ik_0\sigma(\bar{r})\right] \\ \vec{H}_0(\bar{r}) &= \vec{h}(\bar{r})\exp\left[ik_0\sigma(\bar{r})\right] \\ k_0 &= \frac{\omega_0}{c} = \frac{2\pi}{\lambda_0} \end{aligned} \qquad 1.3.2$$

The second factor on the right hand side of 1.3.2 varies over the spatial scale of one wavelength, while the first varies over the spatial scale of several times the wavelength. $\sigma(\mathbf{r})$ is a scalar function of the position and it is known as the Optical Path.

Equation 1.3.2 is our trial solution to be substituted into the wave equations 1.2.6 and 1.2.7.

By using well known vector identities and grouping the members according to the power of λ_0 (or $1/k_0$) we obtain the following equation:

$$K(\vec{e},\sigma,n) + \frac{1}{ik_0} L(\vec{e},\sigma,n,\mu) + \frac{1}{ik_0^2} M(\vec{e},\varepsilon,\mu) = 0$$

with

$$K(\vec{e},\sigma,n) = \left[n^2 - \left(\vec{\nabla}\sigma\right)^2\right]\vec{e} \qquad 1.3.3$$

$$L(\vec{e},\sigma,n,\mu) = \left[\vec{\nabla}\sigma \cdot \vec{\nabla}\log\mu - \nabla^2\mu\right]\vec{e} - 2\left[\vec{e}\cdot\vec{\nabla}\log n\right]\nabla\sigma - 2\left(\vec{\nabla}\sigma\cdot\vec{\nabla}\right)\vec{e}$$

$$M(\vec{e},\varepsilon,\mu) = \left(\vec{\nabla}\wedge\vec{e}\right)\wedge\vec{\nabla}\log\mu - \nabla^2\vec{e} - \vec{\nabla}\left(\vec{e}\cdot\vec{\nabla}\log\varepsilon\right)$$

while the equation for the magnetic field, taking into account the symmetry of the wave equation, is the following:

$$K\left(\vec{h},\sigma,n\right) + \frac{1}{ik_0} L\left(\vec{h},\sigma,n,\varepsilon\right) + \frac{1}{ik_0^2} M\left(\vec{h},\mu,\varepsilon\right) = 0 \qquad 1.3.4$$

with K.L.M defined as in 1.3.3 where μ and ε have been swapped. In the hypothesis that the wavelength of the electromagnetic field tends to zero, $\lambda_0 \to 0$, $k_0 \to \infty$. and we can neglect the second and third terms of equations 1.3.3 and 1.3.4. The resulting equation is known as the eikonal equation:

$$\nabla^2\sigma = n^2$$

$$\left(\frac{\partial\sigma}{\partial x}\right)^2 + \left(\frac{\partial\sigma}{\partial y}\right)^2 + \left(\frac{\partial\sigma}{\partial z}\right)^2 = n^2(x,y,z) \qquad 1.3.5$$

The eikonal equation is the basic equation of geometric optics. The surfaces $\sigma(\mathbf{r})=$*constant* defines the geometrical wave-front of the propagating wave in the refractive index field.

1.3.2 THE LIGHT RAYS AND THE RAY EQUATION

The eikonal equation 1.3.5 defines the geometrical wave-front, that is the surfaces on which the electromagnetic field has a constant phase. Consider the expressions of the electric and magnetic energy density and the Poynting vector:

$$\langle w_e \rangle = \frac{\varepsilon}{16\pi}\vec{e}\cdot\vec{e}^* \quad \langle w_h \rangle = \frac{\mu}{16\pi}\vec{h}\cdot\vec{h}^* \qquad 1.3.6$$
$$\langle S \rangle = \frac{c}{8\pi}\mathrm{Re}\left(\vec{e}\wedge\vec{h}^*\right)$$

If we use the second of the Maxwell equations 1.2.4 in the limit of geometric optics ($\vec{\nabla}\sigma\wedge\vec{e}-\mu\vec{h}=0$), the Poynting vector can be expressed in terms of the electric and magnetic energy density:

$$\langle S \rangle = \frac{2}{n^2}\left(\langle w_e \rangle + \langle w_h \rangle\right)\vec{\nabla}\sigma \qquad 1.3.7$$

The Poynting vector can be expressed in terms of s, the unitary vector perpendicular to the wave-front

$$\vec{s} = \frac{\vec{\nabla}\sigma}{n} \qquad 1.3.8$$

$$\langle S \rangle = \frac{c}{n}\langle w \rangle\vec{s} = v\langle w \rangle\vec{s} \qquad 1.3.9$$
$$\text{with} \quad \langle w \rangle = \langle w_e \rangle + \langle w_h \rangle$$

The cycle averaged Poynting vector lies in the direction normal to the geometrical wave-front. Consequently the average energy density propagates perpendicularly to the wave-front, with velocity v=c/n.

We define now the light rays as the orthogonal trajectories to the geometric wave-front (defined as σ=constant). The solution of the eikonal equation involves the determination of the surfaces σ=constant and it is equivalent to the determination of the rays' trajectories.

Let **r** be the position vector of the ray,

$$\frac{d\bar{r}}{ds} = \bar{s} \qquad 1.3.10$$

and,

$$n\frac{d\bar{r}}{ds} = \vec{\nabla}\sigma \qquad 1.3.11$$

The intensity I is defined as the absolute value of the cycle averaged Poynting vector. then, from equation 1.3.9

$$I = |\langle S\rangle| = v\langle w\rangle \qquad 1.3.12$$

The energy conservation assumes the following expression:

$$\mathrm{div}(I\bar{s}) = 0 \qquad 1.3.13$$

In figure 1.3.1 we show a simple and intuitive geometrical interpretation of 1.3.13 as a conservation law.
The calculation of the rays' trajectories. together with the 1.3.13 allows one to calculate the value of the cycle averaged electric field at any point in space.

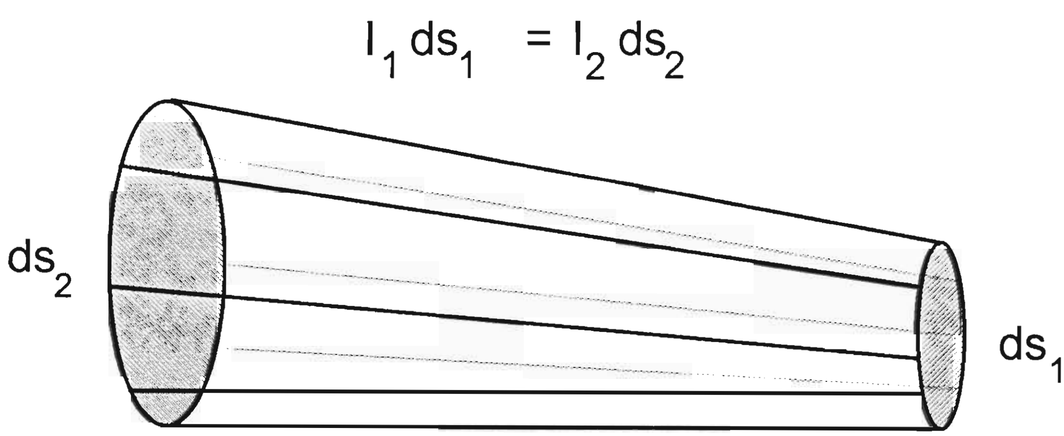

Fig 1.3.1 Geometrical interpretation of the intensity conservation law: the intensity flux is constant

1.3.2 DIFFERENTIAL EQUATIONS FOR THE LIGHT RAYS

The direct solution of the eikonal equation, that is the determination of the surfaces of constant phase, is a much harder problem than the computation of the rays' trajectories. We start from equation 1.3.11 and we differentiate again with respect to s:

$$\frac{d}{ds}\left(n\frac{d\vec{r}}{ds}\right) = \frac{d}{ds}\left(\vec{\nabla}\sigma\right)$$

$$\frac{d}{ds}\left(n\frac{d\vec{r}}{ds}\right) = \frac{1}{n^2}\left(\vec{\nabla}n^2\right) \qquad 1.3.14$$

$$\frac{d}{ds}\left(n\frac{d\vec{r}}{ds}\right) = \vec{\nabla}n$$

Each of the equations 1.3.14 consists of a system of ordinary second order differential equations and allows one to solve the ray trajectories once the refractive index spatial profile is known. Given the ray trajectories and the conservation equation 1.3.13 it is possible to calculate the intensity at any point in space. The only assumption being that the geometric optics approximation is justified.

1.3.4 THE PARAXIAL RAYS' APPROXIMATION

A further approximation that simplifies the solution of 1.3.14, can be performed when the wave-front propagates mainly in one direction and the refractive index gradients perpendicular to the propagation direction are weak. As an example, consider a narrow beam of light, such as a laser beam, propagating along the z direction and finding along its trajectory only small refractive index gradients: the deflection angle will also be small. If it is so small that $ds \cong dz$, equation 1.3.14 can be written as

$$\frac{d}{dz}\left(n\frac{d\vec{r}}{dz}\right) = \vec{\nabla}n \qquad 1.3.15$$

and two independent differential equations for the two transverse directions x and y can be written:

$$\frac{d}{dz}\left(n\frac{dx}{dz}\right)=\frac{\partial n}{dx}$$
$$\frac{d}{dz}\left(n\frac{dy}{dz}\right)=\frac{\partial n}{dy} \qquad 1.3.16$$

Moreover, if the refractive index is close to unity, such as in a gaseous medium at nearly atmospheric pressure ($n\approx 1$), the rays' equations take a particularly simple form:

$$\frac{d^2x}{dz^2}=\frac{1}{n}\frac{\partial n}{dx}$$
$$\frac{d^2y}{dz^2}=\frac{1}{n}\frac{\partial n}{dy} \qquad 1.3.17$$

or

$$\frac{d^2x}{dz^2}=\frac{\partial n}{dx}$$
$$\frac{d^2y}{dz^2}=\frac{\partial n}{dy} \qquad 1.3.17a$$

Depending on the characteristics of the medium and on the initial wave-front geometry, it is possible to utilise the ray equations 1.3.14, 1.3.16, 1.3.17 or 1.3.17a.

1.4 THE REFRACTIVE INDEX AND THE DISPERSION RELATION

1.4.1 THE MATERIAL RELATIONS: MICROSCOPIC THEORY

During our derivation of the eikonal equation and the refraction law we assumed the material relations 1.2.2 and 1.2.3. In non-conducting materials which are transparent to the visible wavelengths, say between the near UV and the near IR, the magnetic permeability μ is close to unity. The relations 1.2.13 and 1.2.14 define the refractive index as:

$$n = \sqrt{\varepsilon\mu} \qquad 1.4.1$$

but the only contribution that renders the refractive index significantly different from unity comes from the dielectric constant ε. Then from now on, we will say that

$$n \cong \sqrt{\varepsilon} = \sqrt{1+\chi} \qquad 1.4.2$$

The quantity χ is known as the dielectric susceptibility of the material and is due to the polarisation of the atoms as the light propagates in the material. When the radiation frequency is such as to excite an atomic transition the refractive index varies sharply with the wavelength and absorption appears. A bit further away from the transition frequency, the dielectric constant still depends on the wave frequency, but we can neglect absorption. In the following treatment we will consider radiation whose frequency is far enough from any transition of the material, for the absorption to be negligible. In the following paragraph we start from a very simple classical model (The Lorentz-Lorentz model) of the atom radiation interaction to get an expression for the dispersion relation of gases.

1.4.2 ATOMIC POLARISABILITY AND REFRACTIVE INDEX

Following [Born and Wolf 1993], let us consider a non-conducting medium. It is possible to demonstrate that the microscopic electric field **E'** experienced by the atoms (or molecules) is related to the macroscopic field **E** and to the polarisation **P** by

$$\vec{E}' = \vec{E} + \frac{4\pi}{3}\vec{P} \qquad 1.4.3$$

The polarisability α is the linear response per atom to the microscopic electric field

$$\vec{P} = N\alpha\vec{E}' \qquad 1.4.4$$

where N is the number of atoms per unit volume. Equation 1.2.1 together with 1.4.3 and 1.4.4 gives

$$\varepsilon = \frac{1 + \frac{8\pi}{3} N\alpha}{1 - \frac{4\pi}{3} N\alpha} \qquad 1.4.5$$

and its inverse:

$$\alpha = \frac{3}{4\pi N} \cdot \frac{\varepsilon - 1}{\varepsilon + 2} = \frac{3}{4\pi N} \cdot \frac{n^2 - 1}{n^2 + 2} \qquad 1.4.6$$

In a gas, the refractive index n is close to unity and equation 1.4.6 can be simplified,

$$\alpha \approx \frac{n^2 - 1}{4\pi N} \approx \frac{2(n - 1)}{4\pi N} \qquad 1.4.7$$

Combining the 1.4.7 with the equation of state for a perfect gas $P = NRT$ and with the density relation $\rho = NM$, where M is the average molecular weight,

$$n = 1 + 2\pi\alpha \frac{\rho}{M} = 1 + 2\pi\alpha \frac{P}{RT} \qquad 1.4.8$$

Equation 1.4.8 expresses the relation between the refractive index of the gas and its density. The relationship in which the density is replaced by the pressure is valid where the medium behaves as a perfect gas. Equation 1.4.8 is rather important for gas optics, since it governs the performance of a class of gas lenses known as Thermal Gradient Gas Lenses. In a gas at constant pressure, the hotter the gas the lower its refractive index.

1.4.3 THE DISPERSION RELATION

In the previous paragraph we have seen how to relate the refractive index to the polarisability of the medium. This relation is important since it constitutes a bridge in between microscopic physics and a macroscopic and measurable quantity such as the refractive index. The polarisability α is the linear response of the atoms (or molecules) to the rapidly oscillating microscopic electric field, and, as we anticipated, is a function of the field pulsation ω. The relation $n(\omega)$ is known as the dispersion relation.
In most materials transparent at visible wavelength, $n(\omega)$ is an increasing function of ω. A very simple classical model of the interaction between the external field and atoms can explain several qualitative features of the dispersion relation and to a quantitative semi-empirical formula for the latter.
Let the electron charge e be distributed on a hard shell of mass m around the nucleus and let the hard shell be bound to the nucleus by an elastic force [Ashcroft 1976].

$$\vec{Q} = -q\vec{r} \qquad 1.4.9$$

Where **r** is the displacement of the hard shell due to the external field. The equation of motion for the electron shell is,

$$m\vec{r}'' + q\vec{r} = e\vec{E}' \qquad 1.4.10$$

Using the trial time solution,

$$\vec{r} = \vec{r}_0 \exp(-i\omega t)$$

we get the following condition:

$$\vec{r} = \frac{e\vec{E}'}{m\left(q/m - \omega^2\right)} \equiv \frac{e\vec{E}'}{m\left(\omega_0^2 - \omega^2\right)} \qquad 1.4.11$$

The polarisability α then is:

$$\alpha(\omega) = \frac{e\vec{r}}{\vec{E}'} = \frac{e^2}{m} \cdot \frac{1}{\omega_0^2 - \omega^2} \qquad 1.4.12$$

Substitution in 1.4.7 immediately gives an expression for the refractive index.

$$n(\omega) = 1 + 2\pi N\alpha(\omega) = 1 + \frac{2\pi Ne^2}{m} \cdot \frac{1}{\omega_0^2 - \omega^2} \qquad 1.4.13$$

In most materials transparent to the visible wavelength there are strong absorption bands in the UV side of the spectrum due to electronic transitions and weak absorption bands in the IR side due to photon-phonon interaction in solids and excitation of vibrational or rotational transitions in molecular gases. This explains why the refractive index normally increases with the field frequency ω. At pulsations closer to ω_0 a damping term can be introduced in equation 1.4.13, in order to account for absorption.

In the case of several electron shells tied to the nucleus , each by its own elastic force, we have several resonance frequencies. Equation 1.4.13 can be rewritten as:

$$n(\lambda)^2 = 1 + \sum_k \frac{\rho_k}{c^2} \cdot \frac{\lambda^2 \lambda_k^2}{\lambda^2 - \lambda_k^2} \ , \qquad \text{with} \qquad \rho_k = N \frac{e^2}{\pi m} f_k \qquad 1.4.14$$

In this equation the external field ($E_0 e^{i\omega t}$) displaces each electronic shell independently and the interaction between the displaced shell's fields is not taken into account. The model is thus valid only for low density materials such as gases [Ashcroft 1976]. In the case of solids or liquids an equation similar to 1.4.14 can be derived by using the relation 1.4.6 rather than 1.4.7.

The classical formulation of the atom-radiation interaction, which lead us to equation 1.4.14, does not allow us to calculate the refractive index of real gases to any degree of accuracy.

Anyhow when the calculations are performed on the basis of quantum mechanics, an equation formally identical to 1.4.14 is found [Landenburg 1921, Landenburg 1928], where the coefficients f_k are replaced by their quantum counterpart.

In the classical formula the numbers f_k represent the density of hard electronic shells that exhibit resonance at $\nu_k = 2\pi\omega_k$. In the quantum

mechanical formulation they do represent the transition probabilities to each virtual state. Although the virtual states (and then the numbers f_k) are infinite in number, it is found [Mitchell 1971] that only few of them give an appreciable contribution to the refractive index.
Equation 1.4.14 can be rewritten as

$$n(\lambda)^2 = 1 + a + \sum_k \frac{b_k}{\lambda^2 - \lambda_k^2} \qquad 1.4.15$$

with:

$$a = \frac{1}{c^2} \sum_k \rho_k \lambda^2{}_k$$
$$b_k = \frac{1}{c^2} \rho_k \lambda^4{}_k \qquad 1.4.16$$

From the above discussion it is clear that 1.4.15 is a good starting point for a semi-empirical formula to represent the dispersion relation of gases in the visible to near UV range. In a range that does not contain resonance frequencies, equation 1.4.15 can be developed in power series of ν (or $1/\lambda$). Taking into account only the strong (due to electronic transitions) absorption bands in the UV side of the spectrum and retaining only terms proportional to $1/\lambda^2$ we obtain Cauchy's formula. In the case of a gas at about atmospheric pressure, the refractive index is close to unity and $n^2 - 1 = 2 \cdot (n - 1)$.

$$n(\lambda) = 1 + A_1 \left(1 + \frac{B_1}{\lambda^2} \right) \qquad 1.4.17$$

The coefficients A_1 and B_1 can be either calculated from first principle performing a quantum mechanical calculation or obtained from a dispersion measurement as empirical parameters.
In table 1.4.1 the measured values of the constants A_1 and B_1, when λ is expressed in cm, are reported for various gases.
The Cauchy formula is an excellent empirical formula for gases at about atmospheric pressure in the wavelength range between 300nm and 800nm. The condition for the validity of Cauchy's formula for each gas is that the

GAS	$A_1 \cdot 10^5$	$B_1 \cdot 10^{11}\ cm^{-2}$
Argon	27.92	5.6
Nitrogen	29.19	7.7
Helium	3.48	2.3
Hydrogen	13.6	7.7
Oxygen	26.63	5.07
Air	28.79	5.67
Ethane	73.65	9.04
Methane	42.4	14.41

Table 1.4.1 constants of the Cauchy's dispersion formula for different gases at standard conditions

λ(nm)	$10^8(n-1)$
200	32408
210	31746
250	30146
300	29155
340	28698
400	28275
500	27896
600	27697
700	27579
760	27530
1000	27416
1500	27330
2000	27300

Table 1.4.2 Refractive index of air at standard conditions

wavelength λ is longer than the electronic absorption band wavelength, which generally falls in the UV.
Cauchy's formula is good for our purposes, since in the experiments treated in this thesis we have been using ruby lasers (763nm) and nitrogen lasers (337nm) whose wavelength falls well within its validity range.
Finally in table 1.4.2 we report the values of the index of refraction of air at standard conditions as a function of the wavelength [CRC Handbook 1995, Edlen 1966].

1.5 GAS LENSES

In this section, after a simple and intuitive description of the thin spherical glass lens, we describe in detail the graded index lens and other gas lenses.

1.5.1 THE THIN GLASS LENS

The laws for reflection and refraction at the interface between two dielectric materials, having refractive indices n_1 and n_2, are well known. In a refraction process, the transmitted rays will emerge at angles according to the refraction law. If θ_r and θ_i are the angles about the normal to the surface:

$$\frac{\sin(\theta_i)}{\sin(\theta_r)} = \frac{n_1}{n_2}$$

While in the case of reflection: $\theta_r = \theta_i$. Let us consider a thin slab of dielectric material in air. The two interfaces being described by the surfaces obtained from rotating the curves $f_1(r)$ and $f_2(r)$ about a common axis, the optical axis.
The refractive index of air can be approximated to equal unity and the dielectric refractive index is n>1. We will consider only homocentric paraxial rays, that is rays starting from a common point on the optical axis and having small angles θ about the axis, such that:

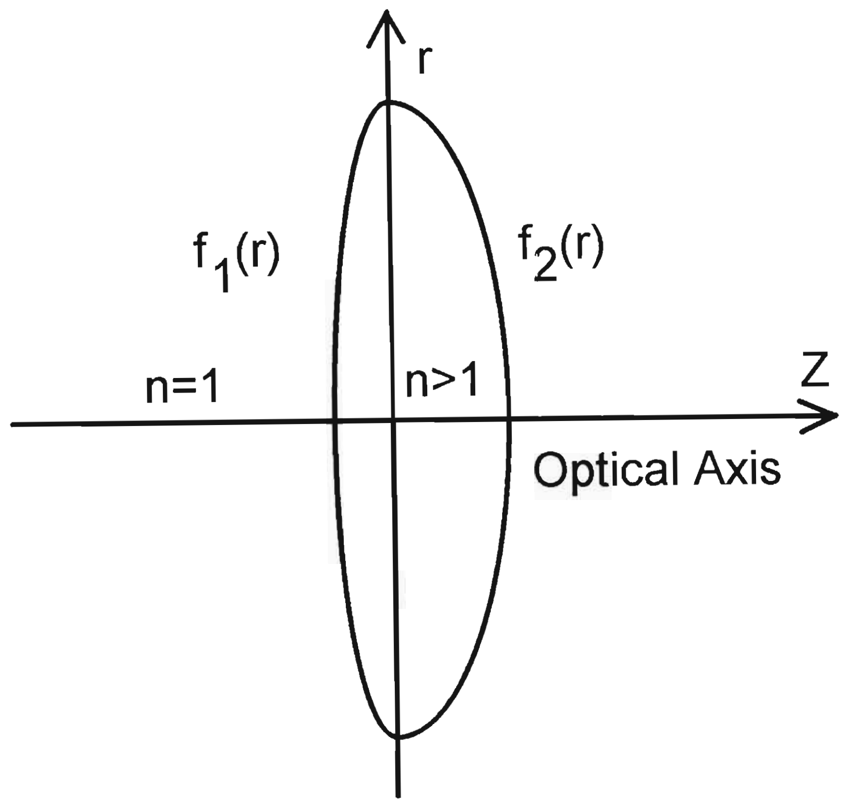

Fig 1.5.1 Geometry of a Glass Lens

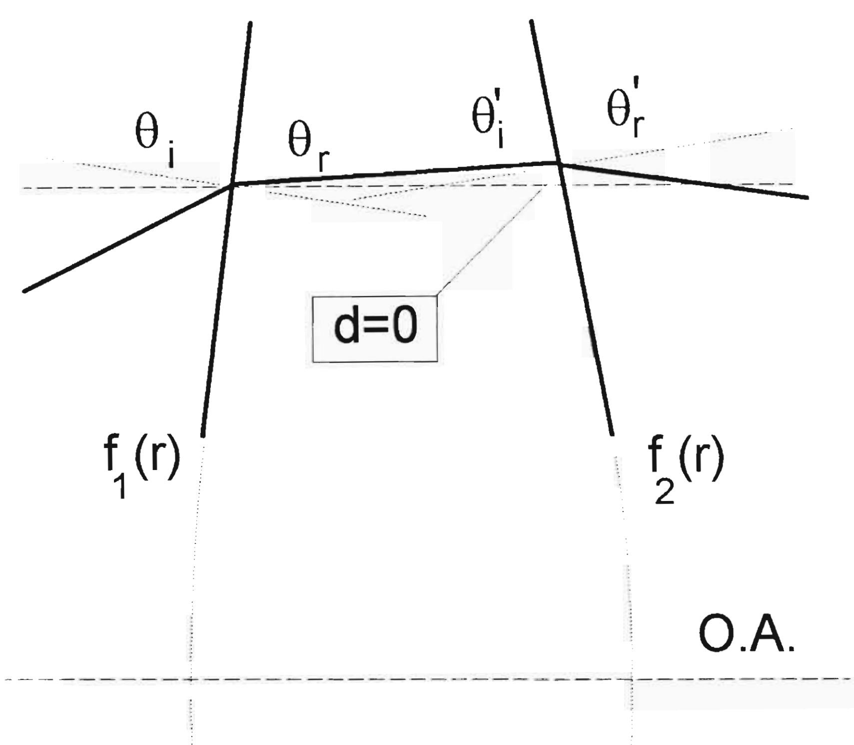

Fig 1.5.2 Refraction from a thin lens

$$\sin(\theta) \cong \tan(\theta) \cong \theta$$

Given the beam characteristics of most lasers. it is in general a very good approximation to model a laser beam with paraxial homocentric rays. The same approximation is not necessarily valid when we study the formation of images from wide angle objects.
A ray incident in **r** with the angle θ_1 about the optical axis is refracted according to Snells law

$$\theta_r = \frac{1}{n}\theta_i \qquad 1.5.1$$

$$\theta_i(r) = -\theta_1 + \arctan\left(\frac{df_1}{dr}\right) \cong -\theta_1 + \frac{df_1}{dr} \qquad 1.5.2$$

In the thin lens hypothesis rays will not be displaced inside the lens and the exit point r' will coincide with the entrance point r.

$$\theta'_r = n\theta'_i \qquad 1.5.3$$

$$\theta'_i(r) = \frac{df_2}{dr} + \frac{df_1}{dr} - \theta_r \qquad 1.5.4$$

The refraction scheme is depicted in figure 1.5.2. The deflection angle after the two interfaces is given by the 1.5.3 together with the 1.5.4, 1.5.1 and 1.5.2.

$$\theta'_r = n\left(\frac{df_1}{dr} + \frac{df_2}{dr}\right) + \theta_1 - \frac{df_1}{dr}$$
$$\theta_{rr} = (n-1)\cdot\left(\frac{df_1}{dr} + \frac{df_2}{dr}\right) + \theta_1 \qquad 1.5.5$$

Let for simplicity the two curves coincide. $f(r)_1 = f_2(r) = f(r)$. For paraxial rays we can approximate the curve f(r) with a parabola

$$f(r) = a - br^2 \qquad 1.5.6$$

Substitution in equation 1.5.5 gives immediately:

$$\theta_{rr} = -2b(n-1)r + \theta_1 \equiv \theta_1 - \alpha r \qquad 1.5.7$$

Equation 1.5.7 means that the larger the distance of the rays from the optical axis the more they are deflected. A collection of parallel rays incident on the thin lens with a profile such as the 1.5.6, will all meet at one point, the focus (fig.1.5.3).

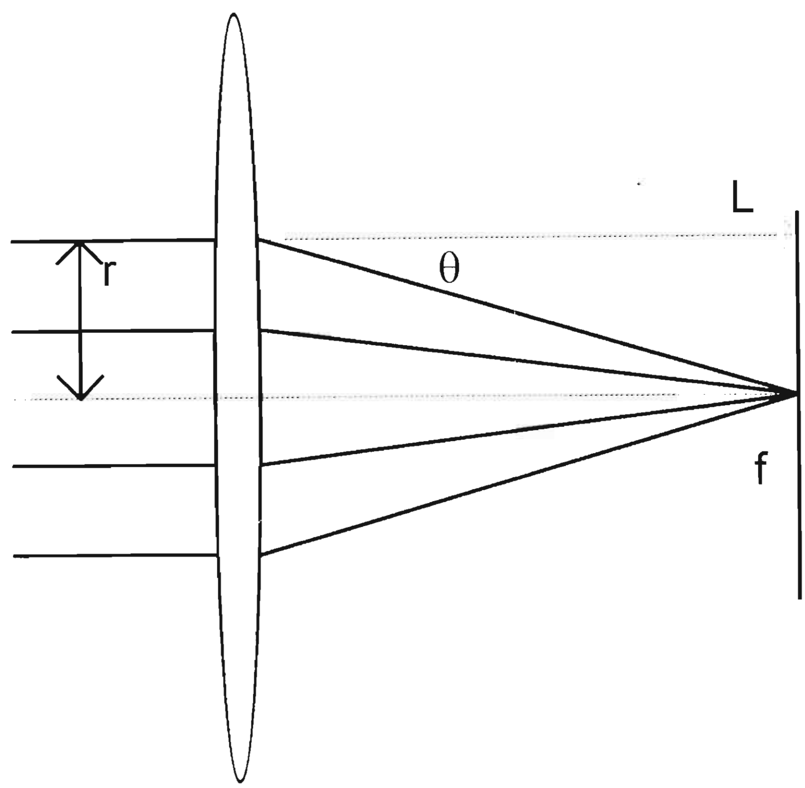

Fig 1.5.3 Parallel rays incident on a thin lens are focused to a sharp point.

In general the distance L at which the rays will cross the optical axis of the system is a function of the distance from the axis r. In this case we speak of longitudinal aberration. But for a profile such as 1.5.6 with the thin lens hypothesis, we have:

$$L = r/\tan[\theta(r)] \cong r/\theta(r) = \frac{1}{\alpha} \equiv f \qquad 1.5.8$$

which is independent of r. This analysis was performed with the hypothesis of paraxial rays, homocentric rays and of a thin lens. These three hypotheses remove aberrations from our discussion. Longitudinal aberrations are defined as non-ideal properties of a lens that prevent its focal length f from being constant, but rather a function of the distance from the optical axis and of the wavelength. From the previous discussion it is clear that a spherical glass lens suffers from longitudinal aberrations for two reasons: first, as soon as the incoming rays cease being paraxial the curvature cannot be approximate as a parabola, and second, the higher the angle θ (and the thicker the lens), the higher is the ray displacement inside the lens.

Moreover the focal distance f as defined in equation 1.5.8 is inversely proportional to the difference between the refractive index and unity. Since this quantity depends on the wavelength through the dispersion relation, the focal length depends on colour. This effect is called chromatic aberration and it is in general negligible for lasers because of their narrow spectral emission.

Other classes of aberrations arise when we consider homocentric skew rays. In this case, and especially at large angles, we cannot define a focal plane but rather a curved focal surface. Moreover the latter configuration introduces astigmatism, because the lens is not seen by the homocentric beam as rotationally symmetric. Astigmatism rises even in the case of homocentric meridional rays, if the surface of the lens is not rotationally symmetric, such as for the elliptical CSL described in chapter 6.

Detailed discussion of aberration theory is beyond the scope of this thesis. The design and realisation of aberration-free lenses is an applied optics and an engineering problem and aberration-free lenses are realised in practice [Welford 1974, Slyusarev 1984].

The previous analysis is a geometrical optics approach and diffraction is not included. Including diffractive effects makes the rays of an aberration-free lens not all arrive at a point, but within a finite region of space. An ideal lens can hope to be diffraction-limited. A diffraction-limited lens focuses light into the smallest possible region of space according to the basic principles of wave mechanics. A lens that suffers any aberration whose effect is negligible when compared to diffraction, is an ideal lens. The importance of realising a diffraction-limited optical system is evident when we consider either classical applications of lenses such as microscopy, telescopy and photography, or the focusing of high power laser beams to achieve very high intensities.

1.5.2 GRADED INDEX LENSES

In a gas, the refractive index is proportional to the density. The case of spatial gas refractive index distributions having cylindrical symmetry is interesting [Marchand 1978]. In general, by controlling the local temperature and/or the density within a gas volume, figure 1.5.4, we can control the propagation of light within its boundaries, performing many kinds of operations on the transmitted wave-front [Marcuse 1972]. In this section we will assume that the ray optics approximation is valid and we will neglect diffractive effects due to the finiteness of the transverse wave-front dimension.

Most often, in a gas, sharp discontinuities in the refractive index are not present. Let us consider a shock. A shock is a discontinuity in the local thermodynamic properties of a gas, such as pressure and density. In theory a shock wave can be as thin as the mean free path of the gas molecules, roughly 10^{-7}m [Zel'dovich, 1966], but in practice, due to energy dissipation on the shock-front (the gas viscosity), a shock wave is seldom narrower than several tens of μm's. A shock produced by a spark in air was measured to be as thin as 10^{-4}m [Hamamoto 1981]. Such discontinuity is seen as a smooth refractive index variation for visible light whose wavelength is less than 10^{-6}m, thus the ray optics is an adequate description.

If we make a lens out of gas, we cannot use refractive index discontinuities to deflect rays as in the case of the glass lens. In order to obtain two relations such as 1.5.7 and 1.5.8 with a gas device we must use smooth gradients. Devices that utilise smooth refractive index gradients to achieve focusing or imaging are called graded index or "GRIN" lenses.

GRIN lenses can be realised either by doping glasses with ions that locally modify the refractive index or by staking together slabs of glass with different refractive indices. The human eye is a GRIN lens that achieves diffraction-limited performances in the fovea.

The general problem of a radial and axial refractive index gradient does not have an analytical solution. In the case of a purely radial gradient the rays' equations can be solved explicitly only in a few special cases [Marchand 1972]. In the case of a cylindrical rod having a radial profile:

$$n(r) = n_0 \operatorname{sech}(\alpha r)$$

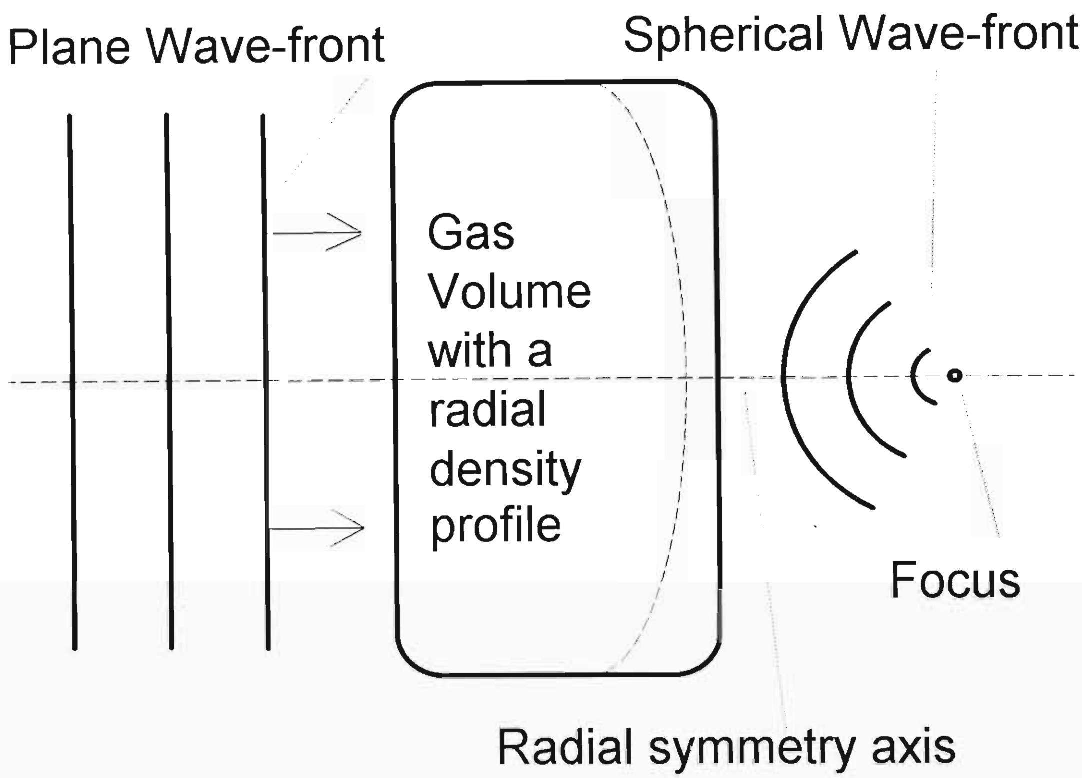

Fig 1.5.4 Possible effect of a non-uniform gas density distribution on the propagation of a plane wave-front

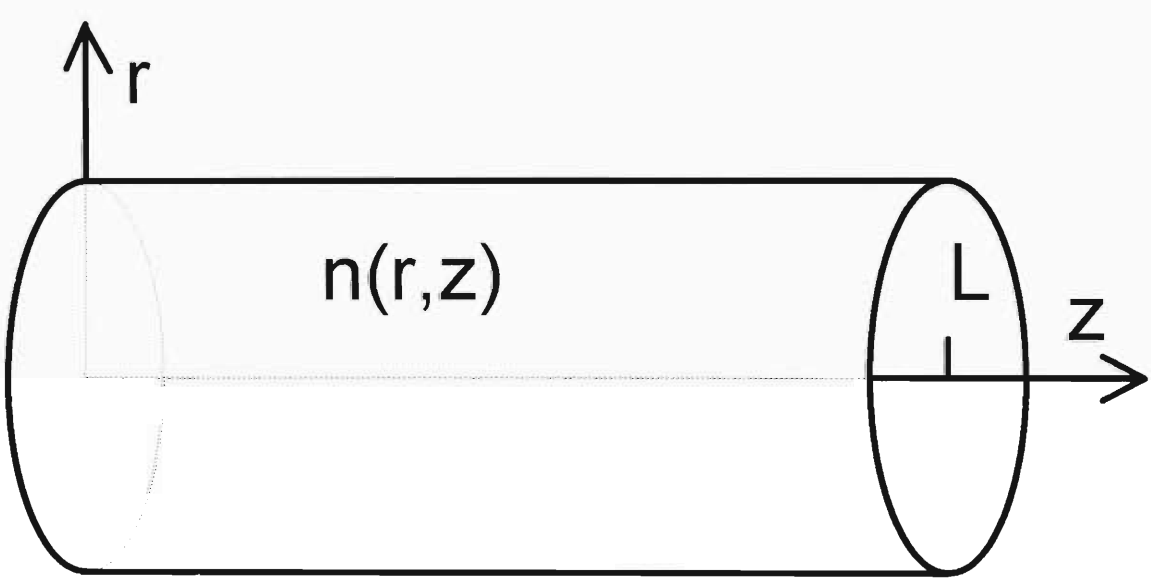

fig 1.5.5 Cylindrical geometry of a gas lens

Every fan of meridional rays is periodically sharply imaged within the rod. Such a profile does not image skew rays sharply since they travel inside the rod along helical trajectories.
Another interesting case is when the refractive index profile is:

$$n(r) = \sqrt{n_0^2 - br^2}$$

where the rays' trajectories have a particularly simple form. The rays just oscillate about the optical axis. (The problem is separable in x and y).

1.5.3 GAS LENSES

Let us consider a cylinder of length L filled with gas whose refractive index is a function of the radial distance r and of the position along the optical axis Z. We will look for a solution of the rays' trajectory only in the case of the paraxial rays approximation (paragraph 1.3.3). Only the radial gradients contribute to the rays deflection.

$$\frac{\partial n}{\partial r} \equiv G(r,z) \qquad 1.5.9$$

If the function G(r.z) is known, we can easily calculate the rays' trajectories inside the gas cylinder and the lens performances. Conversely, now we want to compute the refractive index gradient profile G that gives a point focus for an input beam of parallel rays. Again we use the paraxial ray approximation. Writing equations 1.3.17 in cylindrical coordinates, and taking into account that at densities reasonably close to atmospheric the refractive index differs very little from unity, the rays propagate inside the gas cylinder according to:

$$\frac{d^2r}{dz^2} = \frac{1}{n}\frac{dn}{dr} \cong \frac{dn}{dr} \qquad 1.5.10$$

Equation 1.5.10 must be integrated in z. Since the ray position r changes as the beam travels along the optical axis z, the equation 1.5.10 does not have a general analytical solution r(z). Though, under one hypothesis similar to the 'thin lens', we can get one. Let the refractive index gradient be small, such as that

$$\frac{\partial n}{\partial r} L << 1$$

the dependence r(z) is then very weak. In other words, the ray position r does not vary appreciably along the trajectory within the refractive index gradient region. This implies that the device's focal length is much larger than L. With this hypothesis we find an analytical expression for the ray deflection:

$$\frac{dr}{dz} = \int_0^L \frac{dn}{dr} dz = L\frac{dn}{dr} \qquad 1.5.11$$

In order to get a point focus (paragraph 1.5.1),

$$\frac{dr}{dz} = \frac{dn}{dr} \propto -r \qquad 1.5.12$$

The latter equation can be solved in n, its solution being:

$$n(r) = n_0 - \beta r^2 \qquad 1.5.13$$

In the hypothesis that the ray position r does not change as light travels inside the gas lens, a parabolic density profile produces a sharp focus. By direct substitution in equation 1.5.10 we discover that the profile that we just found gives a point focus even without the hypothesis that **r** is constant along the ray trajectory. The solution of 1.5.10 is:

$$\frac{d^2r}{dz^2} = -2\beta r$$

$$r = r_0 \cos\left(\sqrt{2\beta}z\right) + \frac{\theta_0}{\sqrt{2\beta}} \sin\left(\sqrt{2\beta}z\right) \qquad 1.5.14$$

$$\frac{dr}{dz} = -r_0\sqrt{2\beta}\sin\left(\sqrt{2\beta}z\right) + \theta_0 \cos\left(\sqrt{2\beta}z\right)$$

If we let the initial angle of the ray θ_0 be zero, both the final angle and position of the ray are directly proportional to the initial radial distance from the optical axis and at any position **z** we have:

$$\left.\frac{dr}{dz}\right|_L = -r_0\sqrt{2\beta}\sin\left(\sqrt{2\beta}L\right) \propto -r_0$$
$$\left.r\right|_z = r_0\sin\left(\sqrt{2\beta}L\right) \propto r_0 \qquad 1.5.15$$

Since the focal length is proportional to the ratio between the first and the second of the 1.5.15, the refractive index profile in 1.5.13 gives a point focus.

We have reduced the problem of making a gas lens to the problem of creating a gas density profile close to parabolic. Optical fibre with parabolic refractive index profiles, or self-focusing wave-guides, are widely used in long-distance communications. The beam is refractively confined in the centre of the fibre and there is zero reflective loss.

1.5.4 STEADY STATE AND PULSED GAS LENSES

A gas density distribution such as 1.5.13 is not in dynamic equilibrium. More generally, most non-uniform gas distributions are not in equilibrium. This is a simple consequence of the gas-dynamic equations, where a gas flow follows any pressure gradient [Bejan 1984]. The presence of a density gradient and consequently of a gas pressure gradient causes a gas flow in its direction, to establish equilibrium and uniformity again. We have two options in order to realise in practice a profile like 1.5.13. The first is to build a device that forces the gas to achieve a steady state condition in which a parabolic density profile is maintained. The second consists in creating a transient non-uniform gas distribution and in using it as a lens only for the time that its refractive index profile is convenient for focusing.

A steady state gas lens is ideal for use with CW laser sources, while a pulsed lens can be coupled with a pulsed laser. The typical duration of a q-switched laser pulse is $\Delta t_l=10ns$ while a density perturbation propagates at the typical speed (in air) of $v=330m/s$ (the speed of sound), thus

moving a few μm's during the laser pulse duration and then maintaining almost unchanged its focusing properties.
Both the options of continuous and pulsed lenses have been investigated in this thesis. We will first talk about the optical quality of a steady state gas lens known as 'Spinning Pipe Gas Lens' or SPGL [Notcutt 1988] in Chapter 2, then in Chapter 3 we will describe a pulsed gas lens that works on the principle of multiple shock collision in air, the 'Colliding Shock Lens', or CSL.

1.5.5 OPTICAL BREAKDOWN AND DAMAGE IN GASES AND SOLIDS

There is a twofold convenience in preferring a gas to a solid state optical component for high power laser applications. First, the breakdown threshold is about three orders of magnitude higher. Second, the optical damage eventually following the breakdown is permanent only for the solid state component.
Optical damage occurs when high power radiation is unduly absorbed by the component. Optical damage can then occur either internally or on the surface of the optical material. Internal damage can be due to: multi-photon absorption, presence of internal inclusions, defects or self focusing of the laser beam. The latter case occur when a CW or long pulse laser beam locally heats the optical material thus creating a GRIN lens. Surface damage risk is dramatically increased by the presence of scratches, dust or dirt on the component's surface. High power lasers are thus incompatible with many real environments, especially where the wavelength (IR and UV) requires expensive and soft optical materials (e.g. ZnSe for CO_2 lasers).
When the laser pulse duration is in the 10's of ns range, typically the best coatings achieve a fluence damage threshold of $10 J/cm^2$ while the best raw polished surfaces reach the breakdown threshold of $20 J/cm^2$ [Melles Griot Catalogue 1992]. We must stress the cumulative and diverging nature of the optical damage that can cause the complete destruction of the component only a few shots after the first appearance of the damage.
It is experimentally found [Gower 1981, Raizer 1990] that the breakdown threshold of air is $10^{11} W/cm^2$ for the KrF wavelength of 248nm and a pulse duration of 18ns.
In the case of helium the breakdown irradiance value rises to $10^{13} W/cm^2$.

It is then clear that a laser whose components are entirely made out of gas can produce radiation fluences about three orders of magnitude higher before optical breakdown intervenes.

1.6 BRIEF NOTES ON INTERFERENCE AND DIFFRACTION OF LIGHT

We will give here a very simple description to two important phenomena such as interference and diffraction of EM waves. Interference provides us with a sensitive and useful tool to measure local refractive index in-homogeneities. In chapter 3 we will utilise a Mach-Zehnder interferometer to measure the refractive index radial distribution inside a small pulsed gas lens. Then, in chapter 5, by using the results of this measurement we will determine the optical quality of the device. Diffraction theory determines the ultimate physical limit for the "concentration" of EM energy into a small volume of space. It defines the limiting performance of any lens given its focal length and diameter, and the quality of our gas lenses will be determined by the comparison with the diffraction limit.

1.6.1 TWO BEAM INTERFERENCE

As seen in section 1.3, the intensity I is the amount of energy that crosses the unit area perpendicular to the propagation direction of the field. Let us consider a quasi-monochromatic beam of light. In the geometrical optics approximation, using 1.3.12, 1.3.6 and 1.3.7, we get the following expression for the intensity,

$$I = v\langle w\rangle = \frac{2c}{n}\langle w_e\rangle = \frac{c}{4\pi}\sqrt{\frac{\varepsilon}{\mu}}\langle E^2\rangle \qquad 1.6.1$$

where the electric vector **E** can be expressed as the real part of a complex amplitude:

$$\vec{E} = \mathrm{Re}\left[\vec{A}(r)\exp(-i\omega t)\right] \qquad 1.6.2$$

We want to calculate the intensity I in a region of space where two beams of equal frequency ω overlap. Let the two electric fields be linearly polarised along the same direction.
At any point of space where the two quasi-monochromatic waves are superimposed, the total field is:

$$E = E_1 + E_2$$
$$I = \langle E_1^2 \rangle + \langle E_2^2 \rangle + 2\langle \vec{E}_1 \cdot \vec{E}_2 \rangle = I_1 + I_2 + I_{12} \qquad 1.6.3$$

The Intensity equals the sum of the intensities of the single beams plus an "Interference" term. From equation 1.6.3 it follows that,

$$I_{12} = 2\langle \vec{E}_1 \cdot \vec{E}_2 \rangle = \frac{1}{2}\left(\vec{A}_1 \cdot \vec{A}_2^* + \vec{A}_1^* \cdot \vec{A}_2\right) \qquad 1.6.4$$

the functions A contain the spatial variation of the field, which, for plane waves, is:

$$\vec{A} = \vec{a}\exp\left[i\left(\vec{k} \cdot \vec{r} - \phi\right)\right] \qquad 1.6.5$$

For simplicity we let the field be directed along the X axis, Z being the propagation direction. With these hypothesis we rewrite equation 1.6.4 as:

$$I_1 = \frac{1}{2}a_1^2, \quad I_2 = \frac{1}{2}a_2^2, \quad I_{12} = a_1 a_2 \cos(\delta) = 2\sqrt{I_1 I_2}\cos(\delta) \qquad 1.6.6$$

with

$$\delta = \vec{k} \cdot (r_2 - r_1) + \phi_2 - \phi_1 \equiv \frac{2\pi}{\lambda}\Delta S \qquad 1.6.7$$

δ is the phase difference, while ΔS is known as the optical path difference between the two beams. Substituting the 1.6.6 into 1.6.3, we see that if the phase or the optical path difference are varied, the intensity oscillates between a maximum and a minimum value. As an example we can observe the interference of two plane waves incident at an angle on a flat screen.

The phase difference will be a function of the screen coordinate x.

$$\delta(x) = \frac{2\pi}{\lambda}\sin(\theta)x \qquad 1.6.8$$

and the spatial periodicity of the intensity pattern on the screen is Δx

$$\Delta x = \frac{\lambda}{\sin(\theta)} \qquad 1.6.9$$

Interference is a very common phenomenon when we deal with quasi-monochromatic light sources such as lasers. In order to observe interference between two waves, they must maintain a constant phase difference during the recording or observation time. This sets a few stringent conditions on the interfering waves.

a) They must be quasi-monochromatic, because for each wavelength we would get a different intensity pattern periodicity (equation 1.6.9)).

b) It is almost impossible to compel two independent sources to interfere. Consider atomic vapour lamps, which emit light on a narrow atomic line. Phase jumps occur in the emitted radiation on the time-scale of the average time between two atomic collisions [Loudon 1983]; the coherence time is then much smaller than the typical observation interval. The two light sources maintain a precise phase relation only over the time τ_c which is called the coherence time, in other words, the quantity τ_c is the time over which the field remains correlated with itself.

If one overlaps two independent beams in order to observe interference, the intensity pattern will change over a time-scale equal to the shorter of the two coherence times.

c) The two beams must be spatially coherent. In the example shown in figure 1.6.1, we would observe straight fringes only if the two beams are spatially coherent. Spatial incoherence would first bend the fringes and then make them disappear when coherence is lost over the spatial scale of a few pixel elements of the detector.

A straightforward way of creating two temporally coherent beams is to split any quasi-monochromatic beam by means of the partial reflection of a dielectric surface (beamsplitter).

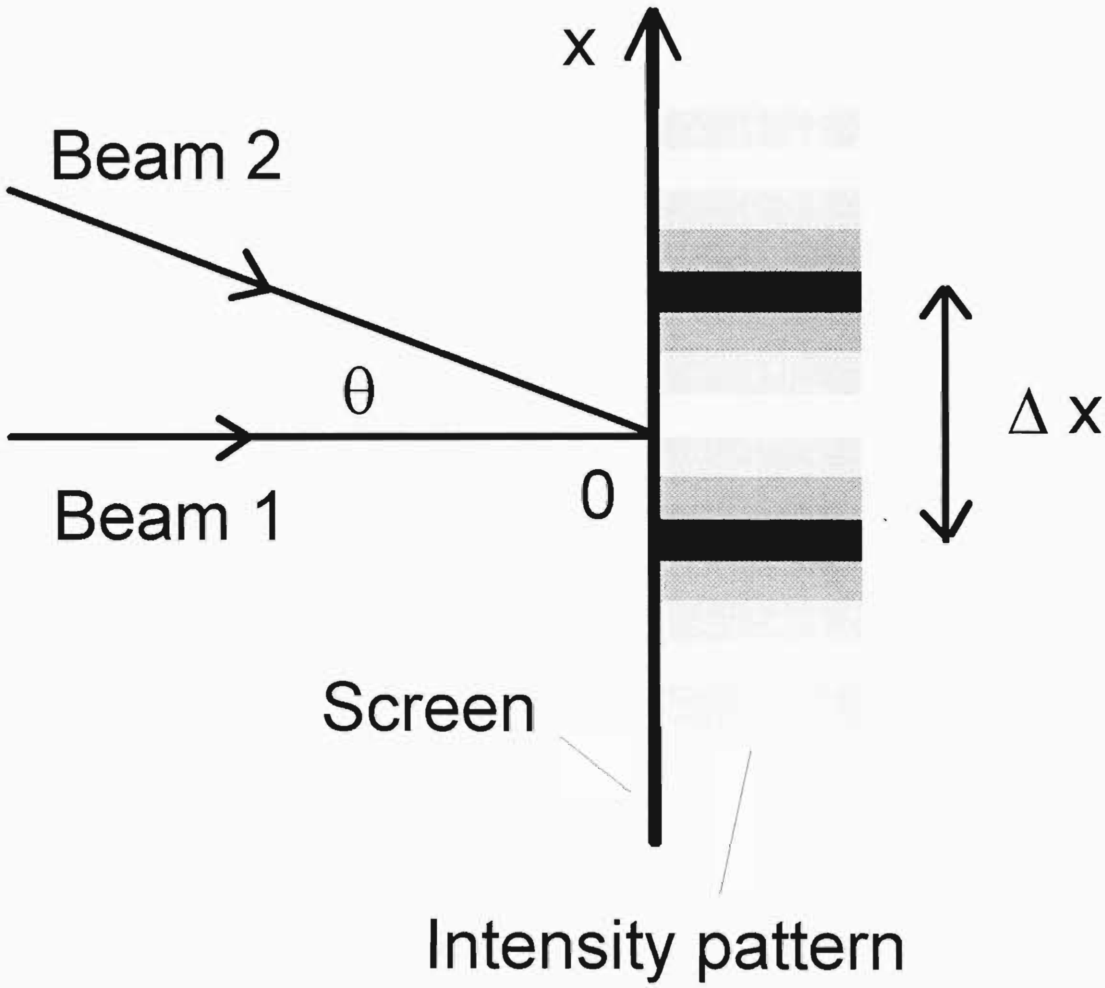

Fig 1.6.1 Interference of two plane waves on a flat screen.

1.6.2 THE MACH-ZEHNDER INTERFEROMETER

The interferometer is an optical instrument that allows the observer to measure the fringe pattern of two interfering beams. An interferometer allows one to measure the local variation of phase along the beam cross-section as one of the two beams propagates through a phase object. A phase object is a refractive index spatial distribution. There are many possible interferometer configurations. Let us study in detail the Mach-Zehnder interferometer, as shown in Fig.1.6.2.
The mirrors M1 and M4 are partially reflective dielectric mirrors, while the mirrors M2 and M3 are totally reflective mirrors. M1 initially splits the beam in two. Part of the beam travels along path 1 and reaches the screen. The other half travels along path 2, passes through the Phase Object and interferes with the other part on a screen. The screen can be a detector such as a T.V. camera face plate or a photographic film. It is vital in this configuration that beam 2 is not deflected inside the phase object, which is not always the case when there are refractive index gradients perpendicular to its propagation direction. If there is deflection, a fringe pattern due to refraction overlaps with the interference fringes, and one must use a positive lens to image the phase object plane onto the detector. The latter procedure is then correct only for thin refractive objects. A simple test to avoid this problem is to check the absence of any fringe on the screen while the beam 1 is blocked. When the interferometer is optimally aligned the two beams interfere on the screen either constructively or destructively, giving rise to a constant intensity profile.
According to Fig.1.6.3, the phase delay that the beam 2 experiences as it passes through the Phase Object is:

$$\delta(x,y) = \frac{2\pi}{\lambda}\int_0^L n(x,y,z)d\bar{s} \cong \frac{2\pi}{\lambda}\int_0^L n(x,y,z)dz \qquad 1.6.10$$

and a succession of dark and bright fringes will be seen on the screen. We can relate the local fringe intensity to the phase delay experienced by the beam 2.
On the peak intensity of a bright fringe there is constructive interference:

$$\delta(x,y) = 2n\pi \quad n = 0,1,2,... \qquad 1.6.10a$$

While at the minimum of a dark fringe the interference is destructive:

$$\delta(x,y) = 2(n+1)\pi \quad n = 0,1,2,... \qquad 1.6.10b$$

From the maxima and minima positions on the screen we get in a straightforward way the value of the refractive index integrated along the optical path of the ray:

$$\tilde{n}(x,y) = \int_0^L n(x,y,z)dz \qquad 1.6.11$$

The problem of this "optimally aligned" configuration is that we cannot measure phase variations larger than 2π.

If we misalign the Mach-Zehnder Interferometer, by tilting any of the four mirrors, we can make the two beams overlap at an angle, and create on the screen a regular pattern of straight fringes The fringes are straight when there is no phase object in the interferometer and are bent when a local phase delay is introduced. We follow each fringe in the x,y plane of the screen and by measuring its deflection from the straight pattern, we find the phase change due to the object.

While the measured phase change is determined only within 2π in a perfectly aligned Mach-Zehnder interferogram, on the contrary when we measure the deflection of straight fringes, we lose information only when there is a phase change of more than 2π within a fringe period.

1.6.3 REFRACTIVE FRINGES

We have seen how partial reflections from dielectric surfaces can cause interference. In general, any beam deflection causes interference as soon as two or more mutually coherent regions of the beam are overlapped. Let a spatially coherent beam arrive on a screen after being deflected (such as in fig.1.6.3). At each point x,y we will have to add together the contributions from the electric fields (of all the rays falling in x,y) taking into account the relative phase due to the different optical paths.

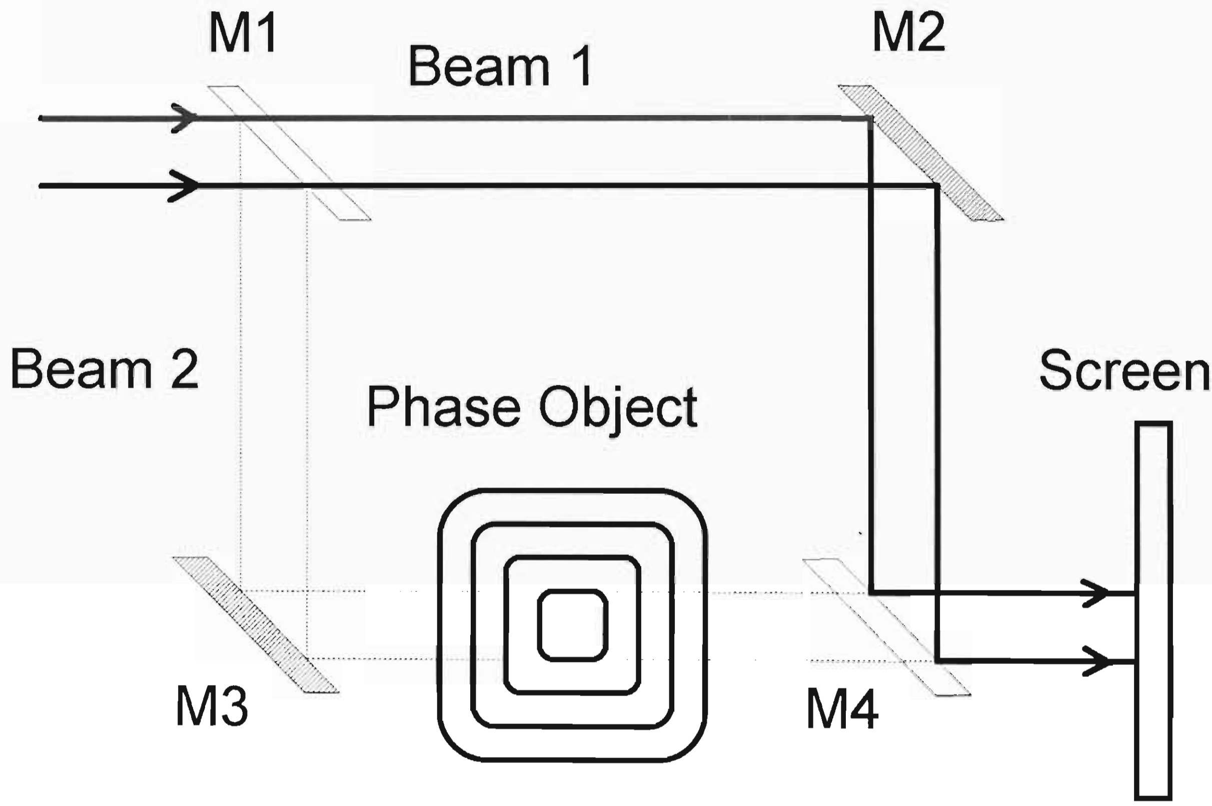

Fig.1.6.2 The Mach-Zehnder interferometer scheme.

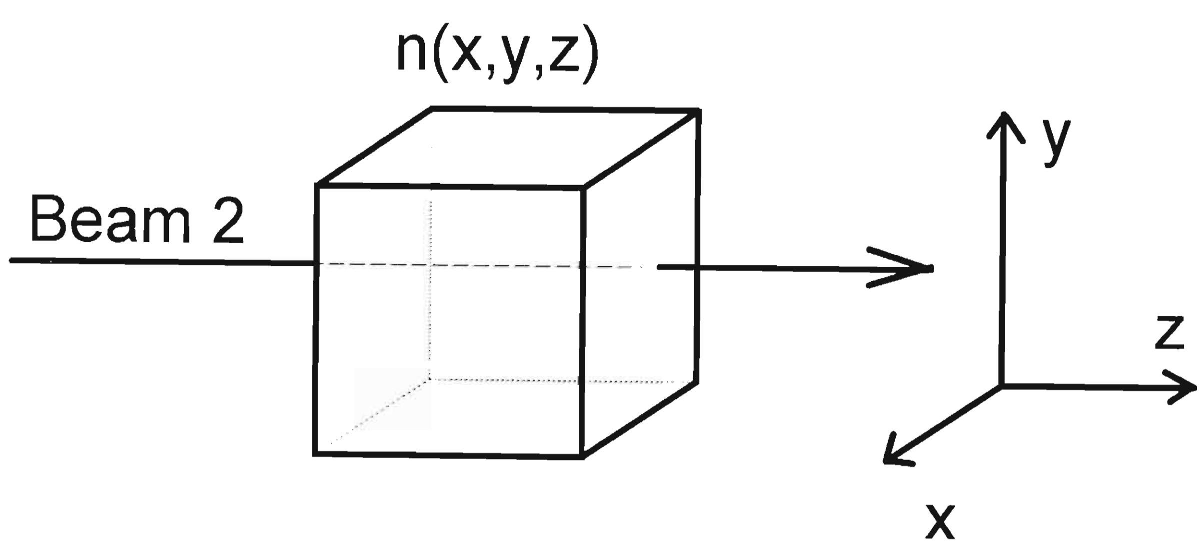

Fig.1.6.3 Propagation inside a phase object.

It is possible to get some information about the refractive index spatial distribution from the refractive fringes [Michaelis B 1991], although the information is more convoluted than in an interferogram were it can be extracted in the straightforward way described in the previous paragraph.

1.6.4 DEPARTURE FROM GEOMETRICAL OPTICS

Light always propagates straight in vacuum. This is true only in the approximation of geometric optics. Examples were light does not propagate straight are well known: light passing close to an obstacle or through a slot is deflected. In general diffraction is a consequence of the uncertainty relation of Heisenberg applied to single photons. On the other hand, and more intuitively, it is a consequence of the wave-like nature of light. Interference and diffraction are closely linked together. When a coherent beam is diffracted, fringes appear as the deflected light interferes with the non-deflected part of the beam. A conceptually simple theory of diffraction is the Huygens-Fresnel construction. It postulates that any point of the propagating wave-front acts as a source of secondary spherical wave-fronts which mutually interfere. A more exact theory was formulated by Kirchhoff: let the spherical wave-front

$$f(r) = \frac{A\exp(ikr)}{r} \qquad 1.6.12$$

hit a wall with an aperture B. If the radius of the wave-front is much larger than the linear dimension of the aperture, the Fresnel-Kirchhoff diffraction formula states that the perturbance at the point **P** is,

$$U(P) = -\frac{iA}{2\lambda}\iint_B \frac{\exp[ik(r+s)]}{rs}[\cos(\mathbf{n},r) - \cos(n,s)]dS \qquad 1.6.13$$

Particularly relevant for laser physics is the Fraunhofer diffraction formula which is an approximation of the Kirchhoff diffraction formula in some operating conditions. The typical laser beam characteristics make the Fraunhofer diffraction formula a very good approximation. We will consider the diffraction pattern from an aperture on a plane screen. The

approximation consists in letting both **r** and **s** be much larger than the linear dimension of the aperture, so that they can be replaced by **r'** and **s'**, as shown in figure 1.6.5. Moreover the cosine term will remain constant as we integrate on the screen aperture, that is $\cos(n,r) - \cos(n,s) \cong 2\cos\delta$.
The diffraction formula becomes:

$$U(P) \approx -\frac{Ai}{\lambda}\frac{\cos(\delta)}{r's'}\iint_B \exp[ik(r+s)]dS \qquad 1.6.14$$

Let **q** be a generic point in the aperture and u,v its coordinates. In the hypothesis that $r'\lambda >> d$ and $s'\lambda >> d$, (where d is the maximum transverse dimension of the aperture) equation 1.6.14 can be further simplified. After some manipulation we get

$$U(P) = C\iint_B \exp[ik(pu+qv)]dS$$

$$p = \frac{x}{s'} + \frac{x_0}{r'}, \qquad q = \frac{y}{s'} + \frac{y_0}{r'} \qquad 1.6.15$$

A collimated beam produces a Fraunhofer diffraction pattern at infinity, or equivalently in the focus of a well corrected lens. The diffraction pattern given by 1.6.15 can be analytically calculated only in few special cases, such as the rectangular aperture and the circular aperture. The last one is of particular interest for laser physics.

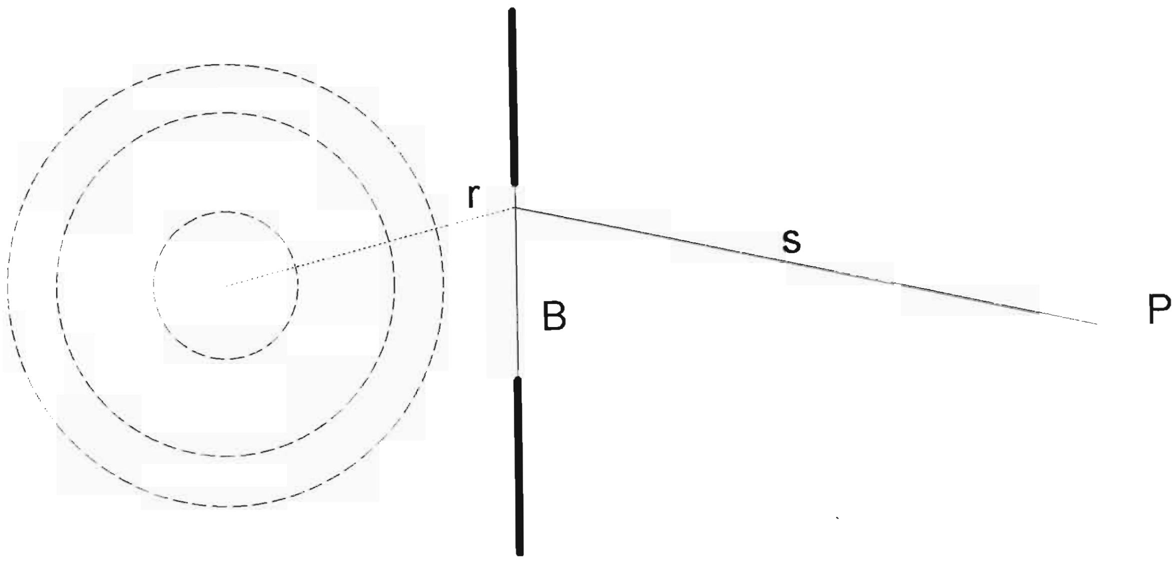

Fig.1.6.4 Geometry of Kirchhoff diffraction.

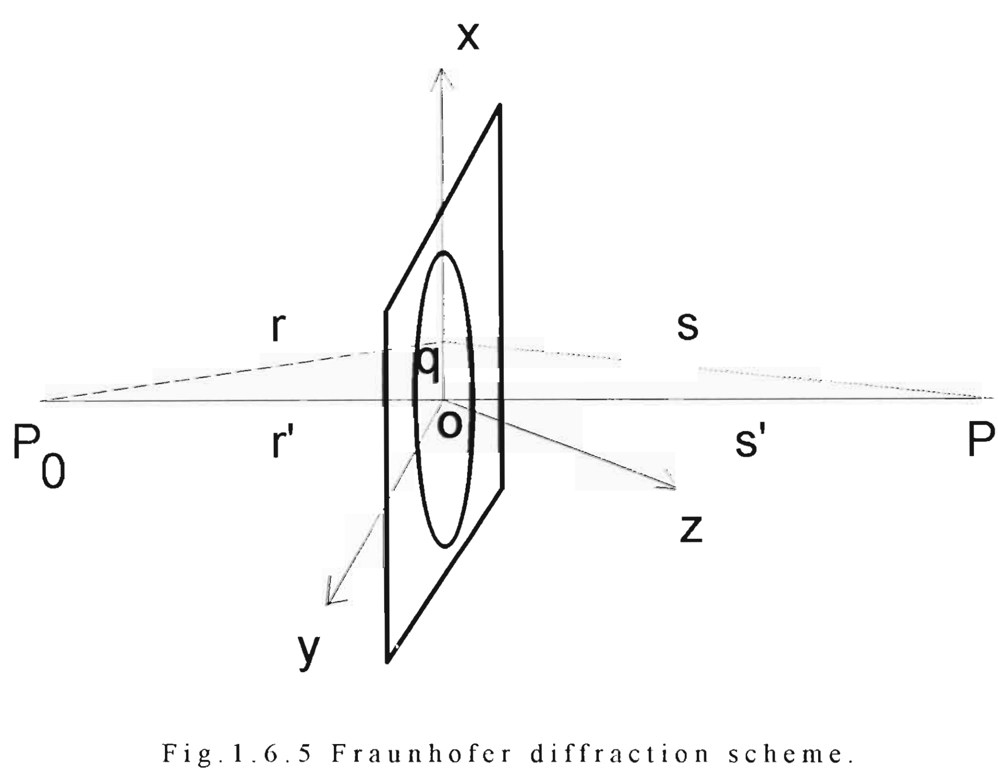

Fig.1.6.5 Fraunhofer diffraction scheme.

1.6.5 DIFFRACTION-LIMITED LASER BEAMS AND DIFFRACTION-LIMITED FOCUSING OPTICS

The deflection of light produced by diffraction sets the ultimate limit on the collimation that we can expect from a laser beam. In particular let us consider a circular laser beam. The Fraunhofer diffraction pattern of a circular aperture is given by

$$I(r) = I_0 \cdot \left(\frac{2J_1\left(\frac{2\pi ra}{\lambda L}\right)}{\frac{2\pi ra}{\lambda L}} \right)^2 \qquad 1.6.16$$

Where a is the radius of the circular aperture, J_1 is the well known Bessel function [Guenther 1990] and L is the focal length of the "well corrected lens" that we are using to focus the beam.
The radial profile of the Bessel function J_1 will tell us the minimum spot size we can focus a laser beam. It is found that almost 85% of the beam energy falls within its first minimum. The first dark ring occurs at:

$$r_m = 1.22 \frac{\lambda L}{2a} \qquad 1.6.17$$

The radius of the first minimum, given in 1.6.17, coincides with the intensity FWHM spot diameter.
Conversely, starting with a laser beam which is diffraction-limited, we can define a diffraction-limited lens as a device able to focus 85% of the beam energy into a spot similar in size to 1.6.17. Thus the quantity given in 1.6.17 defines absolute physical units to measure the optical quality both of lenses and laser beams.

CHAPTER 2: THE SPINNING PIPE GAS LENS

2.1 EXPERIMENTAL SYSTEM

In this section we describe in detail the spinning pipe gas lens and the experimental system on which we performed a temperature profile measurement [Lisi 1994]. A spatially resolved temperature measurement in a device of aperture 2.25 cm and of length 1 m is presented.

2.1.1 THE SPGL

The spinning pipe gas lens investigated in this chapter was developed at the University of Natal in recent years. Thermal gradient gas lenses are typically long focal length, small aperture devices. In the early versions, the thermal gradient gas lenses consisted of a small cross section metal pipe in which a gas was fluxed along the optical axis [Marcuse 1965, Xie 1985]. Heat exchange processes heated the gas close to the pipe, giving rise to a radial temperature gradient. The obvious difficulty that is encountered in scaling up the aperture while keeping the focal length short is the consequent increase of the temperature radial gradients. These larger gradients give rise to convection currents which impair or even destroy the action of the lens [Gloge 1967]. Some improvement could be obtained by spinning the lens [Notcutt 1988], in order to eliminate the convection cells. In this case the gas flow stops being laminar and directed only along one direction. No analytical theory is available to describe the gas flow. A sketch of the SPGL is shown in figure 2.1.1.

The gas lens consists of a pipe spun at the typical speed of some 10 Hz by a variable speed AC motor. The pipe is heated by a resistor, powered by a variable voltage power supply. It is possible to vary independently both rotation speed and pipe temperature in order to optimise the performances. There are a few strict requirements on the pipe characteristics.

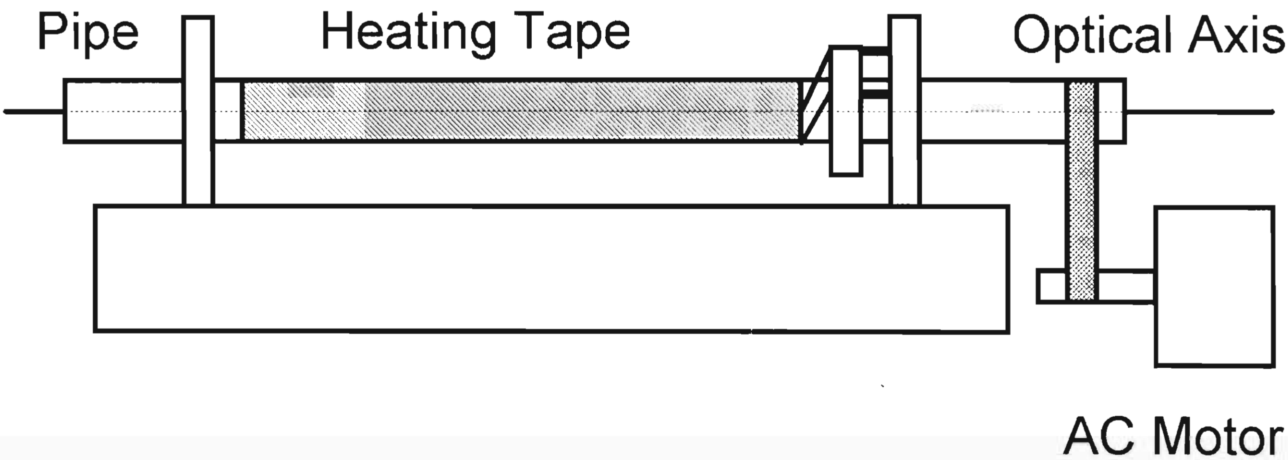

Fig 2.1.1 The Spinning Pipe Gas Lens. It consists of a spinning heated pipe.

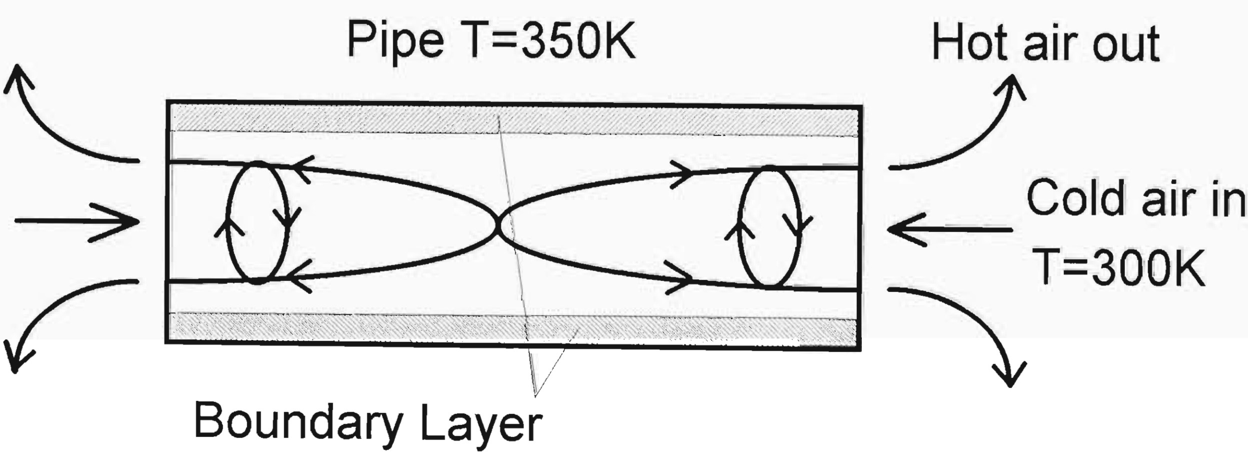

Fig 2.1.2 Simple scheme of the air flow inside a spinning pipe.

1) It must be straight within a good degree of accuracy in order not to vibrate when spun.

2) The thermal expansion coefficient of the material must be as low as possible to avoid deformations. Deformations have to be avoided since they introduce vibrations as the pipe is spun.

Any vibration can destroy the steadiness of the gas flow and of the temperature profile, impairing the optical quality. The SPGL we have utilised in our experiment has the following specifications: Length L=1m, Diameter d=2.25cm, Pipe Temperature<100C, Revolution Rate<50Hz.

The gas flow inside the pipe is complex and no analytical theory is available, but an heuristic description of the gas flow can be as follows:

As the pipe is spun, cold air flows in from the edges of the pipe towards the centre. Meanwhile it is accelerated in the angular direction by friction with the air in the boundary layer, co-rotating with the pipe. As the gas spins faster and faster in the centre of the pipe, it is centrifuged out, flowing along the pipe boundaries. Correspondingly the cold air is sucked in along the pipe axis. The pipe being hot, the air that flows out close to its boundaries is hotter than the air sucked in along its spinning axis. The density distribution resulting from this flow was found to give a good, but high f-number lens.

In a perfect gas, the temperature and the refractive index are related by a simple thermodynamic relationship. The refractive index difference from unity is proportional to the gas density, and the density at constant pressure, is inversely proportional to the temperature. As seen in section 1.4, relation 1.4.19 tells us that:

$$n \approx 1 + 2\pi\alpha \frac{P}{RT}$$

If we define n_0 as the refractive index at standard atmospheric conditions (T=273.3K, P=1Atm) then:

$$n(T) = 1 + (n_0 - 1)\frac{T_0}{T} \qquad 2.1.1$$

The value of the refractive index at standard atmospheric conditions is a well known experimental quantity (table 1.4.2). It weakly depends on the radiation wavelength as given by the Cauchy formula 1.4.18 and in table

1.4.2. At visible wavelengths its value is:

$$n_0 - 1 = 2.93 \cdot 10^{-4} \qquad n_0 = 1.000293 \qquad T_0 = 273.3K.$$

Once the temperature profile inside the pipe is known, so is the refractive index and we can then determine the optical properties of the lens.

2.1.2 THE TEMPERATURE MEASUREMENT

In an early device [Steier 1965] the temperature profile was measured for a fluxed small diameter gas lens and the results showed good agreement with the theory. We have measured the temperature profile of our spinning pipe gas lens both along the optical axis and along the vertical section. We preferred the vertical direction to the horizontal in order to check for eventual gravitational effects on the temperature distribution of the gas.
Our aim was to measure the gas temperature inside the heated spinning pipe with a spatial resolution of 1.0mm along the radius of the lens and 1.0cm along its optical axis. A temperature gauge for such measurement must have the following characteristics:

1) Small dimensions. Since we want a radial resolution of 1.0mm, the probe dimensions must not exceed at least 0.5mm. (<0.5mm). Moreover, the smaller the probe, the less it affects the gas circulation.

2) The temperature difference between ambient atmosphere and pipe surface temperature is about 100K. The temperature difference between air at the edge and air at the centre will be rather smaller (about 50K) because of the fast flow rapidly replacing the hot gas in the boundary layer. We expect the temperature profile to be roughly parabolic along the radial direction of the pipe. This gives a temperature difference over the first radial 1.0mm of about 1K. The temperature resolution must then be at least $\Delta T < 0.5K$.

3) The thermal capacity of the detector must be small, in order to reach thermal equilibrium fast enough as we change the probe position. The measurement must then be as fast as possible in order to avoid fluctuations in the system.

4) The detector must exchange heat only with the gas, for this to be possible it has to be thermally insulated from its support. Moreover the electrical connections of the thermocouple must be performed with thin

wire for heat not to be lost through them.
Given the previous four points our choice was for a Ni-Cr thermocouple. We made it by welding two Ni and Ni-Cr 200μm diameter wires. (This is as small as feasible in our workshop). The Thermocouple was secured via a thermally insulated material (epoxy glue) on a thin steel wire (d=400μm) which was suspended between two XYZ mounts. The mounts were held on a long optical bench. The experimental set-up, shown in figure 2.1.3 allows us to move the probe inside the lens with the required precision. The alignment is performed by checking the wire position both at the entrance and at the exit of the pipe with micropositioners.
The probe thermocouple is referenced to a second Ni-Cr thermocouple, submerged in a mixture of ice and water at 273.3K. The output voltage is read on a Keithley 199 Voltmeter and the measured voltage values are then normalised according to the polynomial for type k (Ni-Cr) thermocouples [Practical Temp. Meas.]. The circuit is shown in figure 2.1.4.
The presence of a reference thermocouple is necessary to eliminate the effect of the two thermocouples introduced by the copper (Cu) contacts of the Voltmeter with two different metal wires (Ni and Cr). The output voltage is then normalised to the type k thermocouple reference polynomial (8th order) and this will give the probe temperature difference from 273.3K. In figure 2.1.5 we show the measured temperature profile and in the following figure, 2.1.6, the refractive index profile computed with the help of equation 2.1.1.
The temperature distribution is flat in the middle region of the pipe (50cm on the optical axis) where the co-rotating vortexes [Michaelis B 1991] meet and there is almost no longitudinal gas flow (figure 2.1.2) while two regions of strong transverse thermal gradients are present near the edges of the pipe. The asymmetry between these two regions is due to the asymmetry in the heating of the pipe. It was found empirically that the lens works better under such conditions.
During the experiment we kept the rotation speed of the lens at 30Hz and the temperature of the pipe at 400K, which gave a focal length of 2m. Figures 2.1.7 and 2.1.8 show the vertical asymmetry eventually caused by gravity in greater detail. In these two figures we show the contour lines of the surfaces shown in the figures 2.1.5 and 2.1.6.

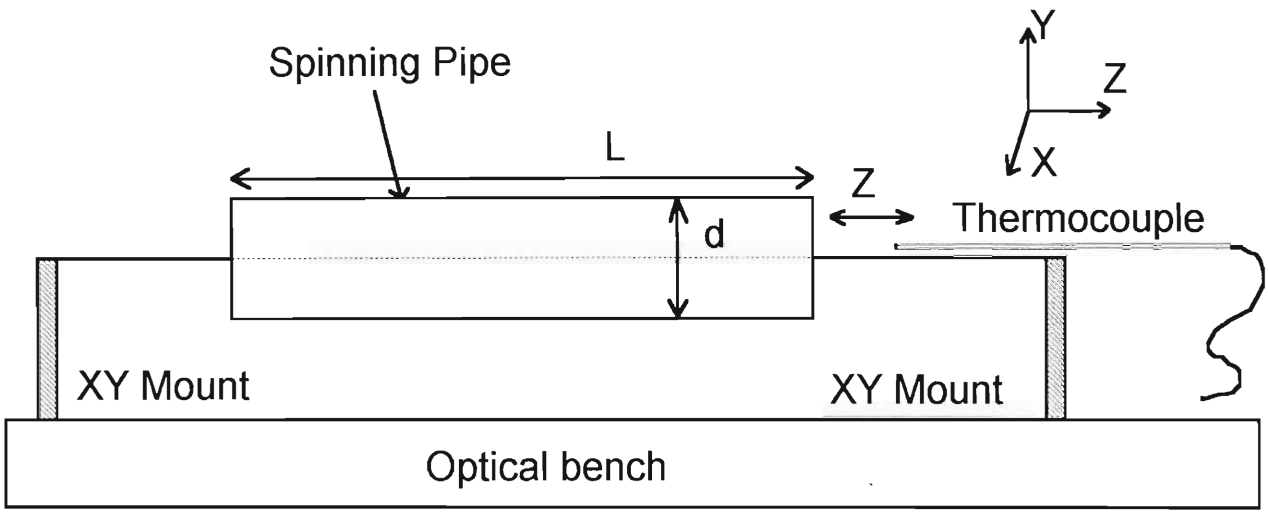

Fig.2.1.3: Experimental set-up for the temperature measurement. D=2.25 cm, L=100 cm.

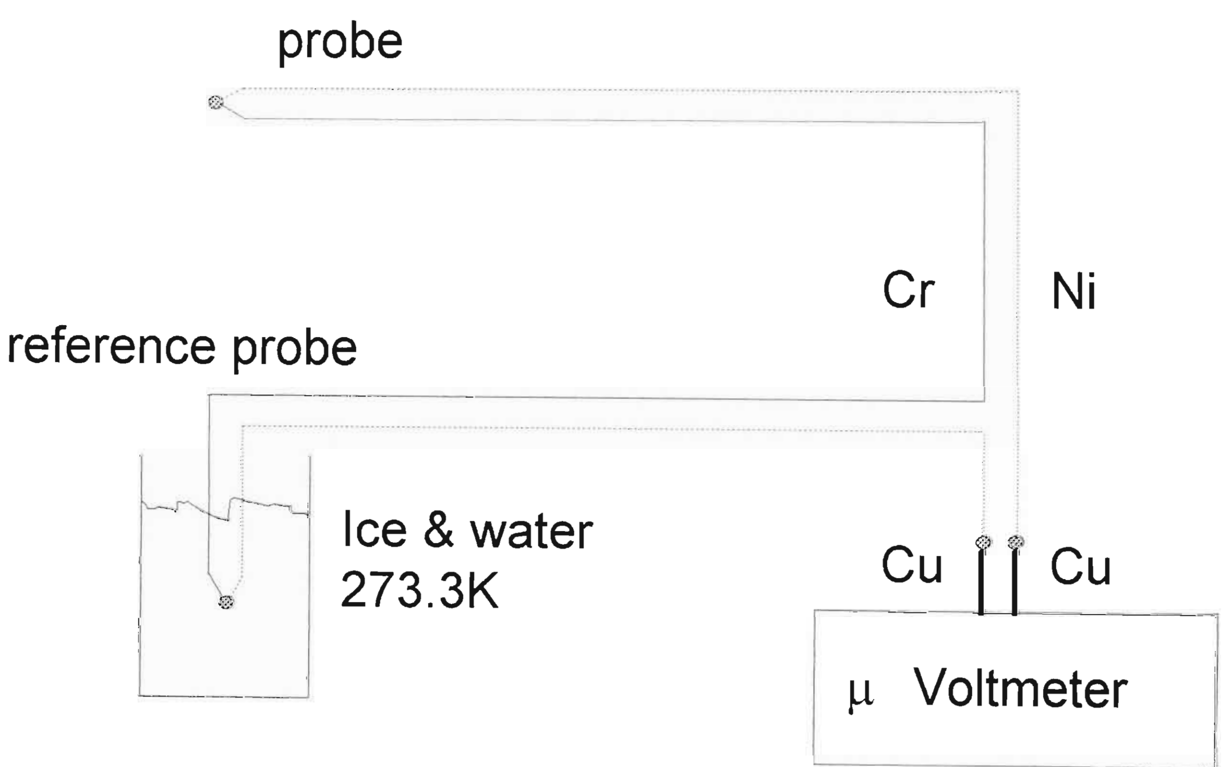

Fig.2.1.4 Electric circuit for the temperature measurement.

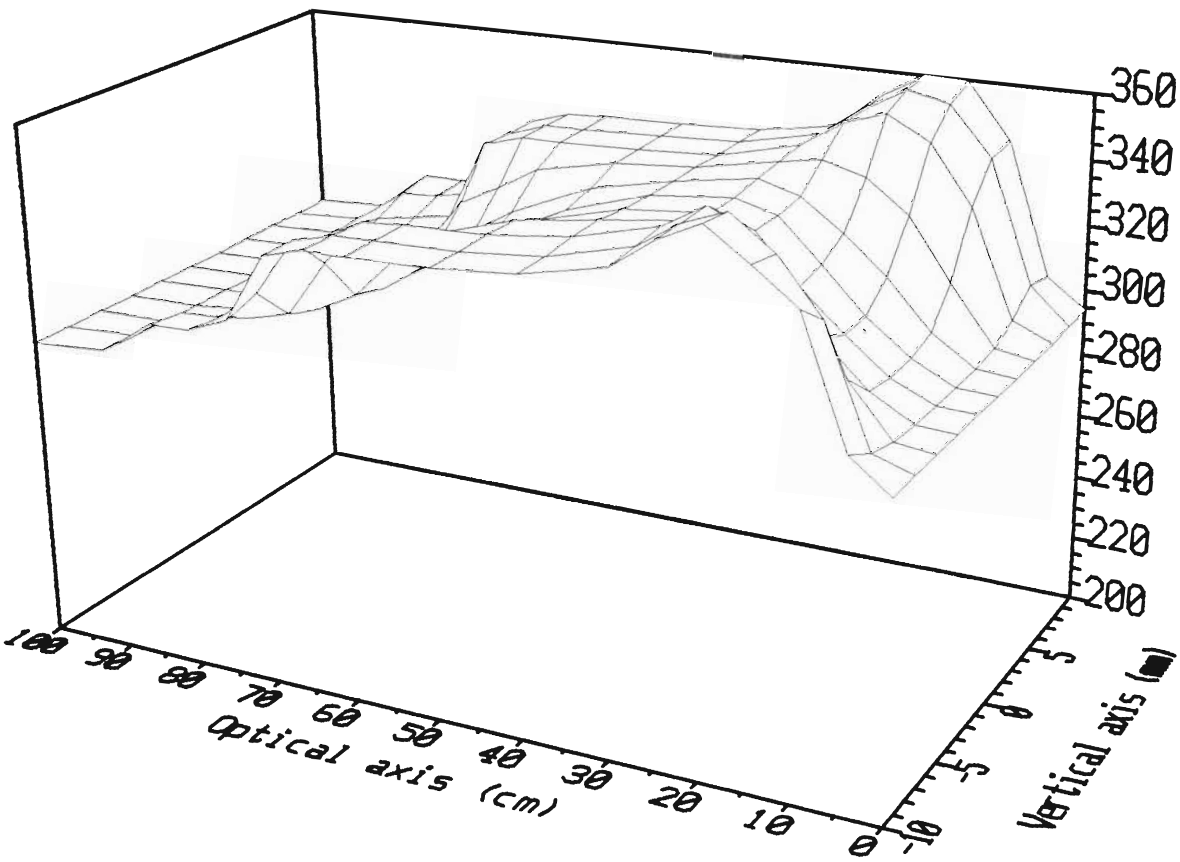

Fig 2.1.5 Measured temperature profile inside the Spinning Pipe Gas Lens.

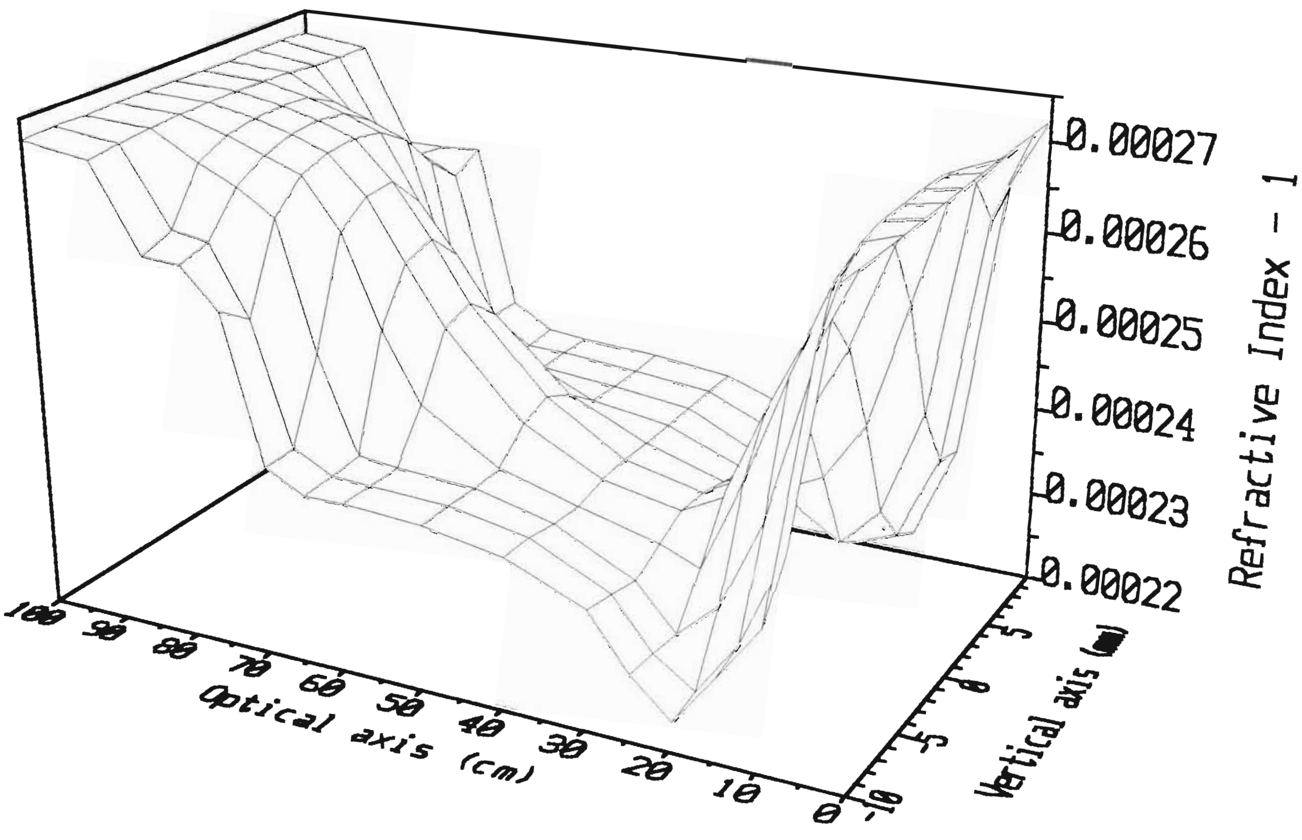

Fig.2.1.6 Refractive index profile calculated from the temperature profile shown in figure 2.1.5.

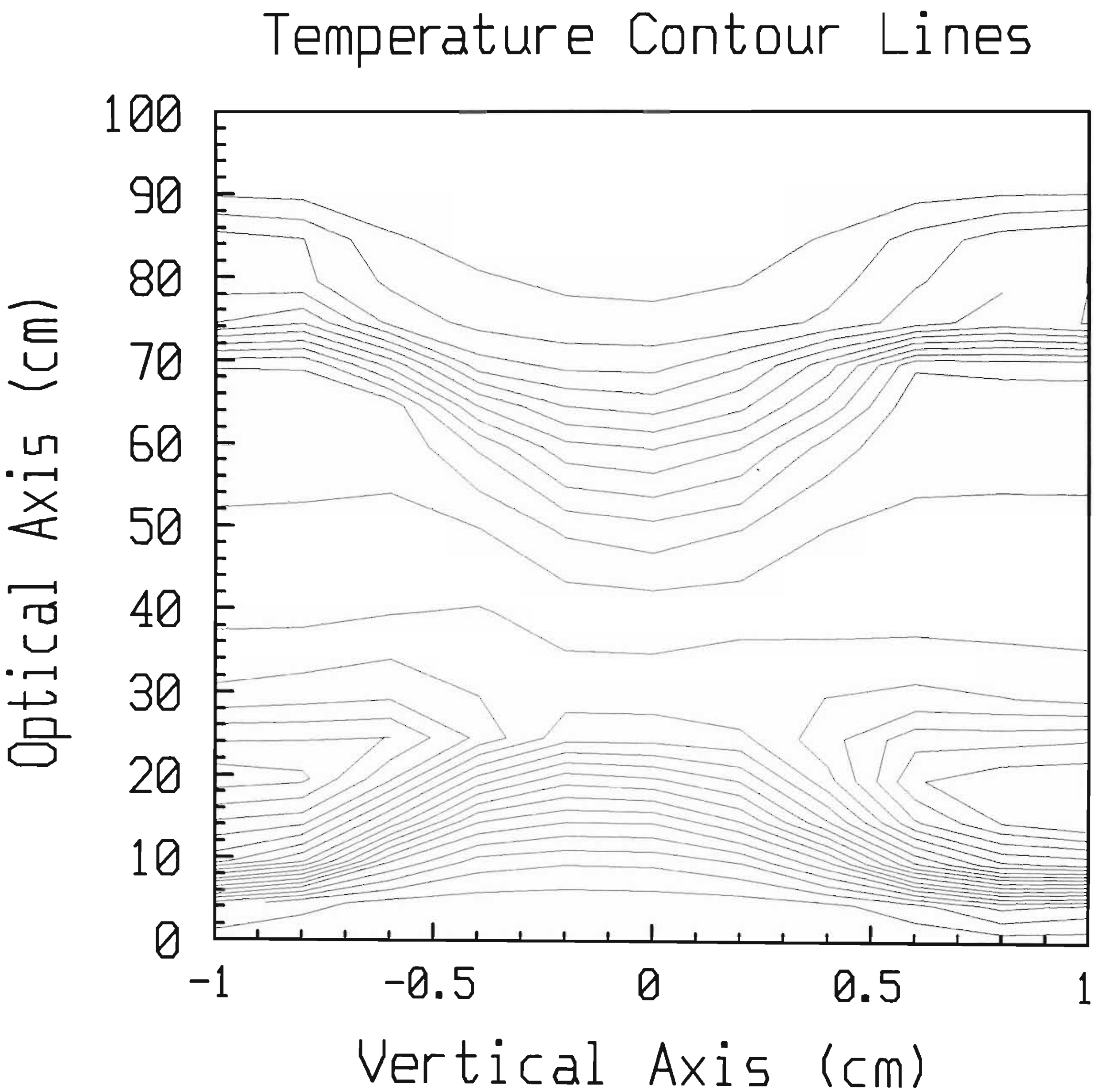

Fig.2.1.7 Isothermal lines from fig.2.1.5.

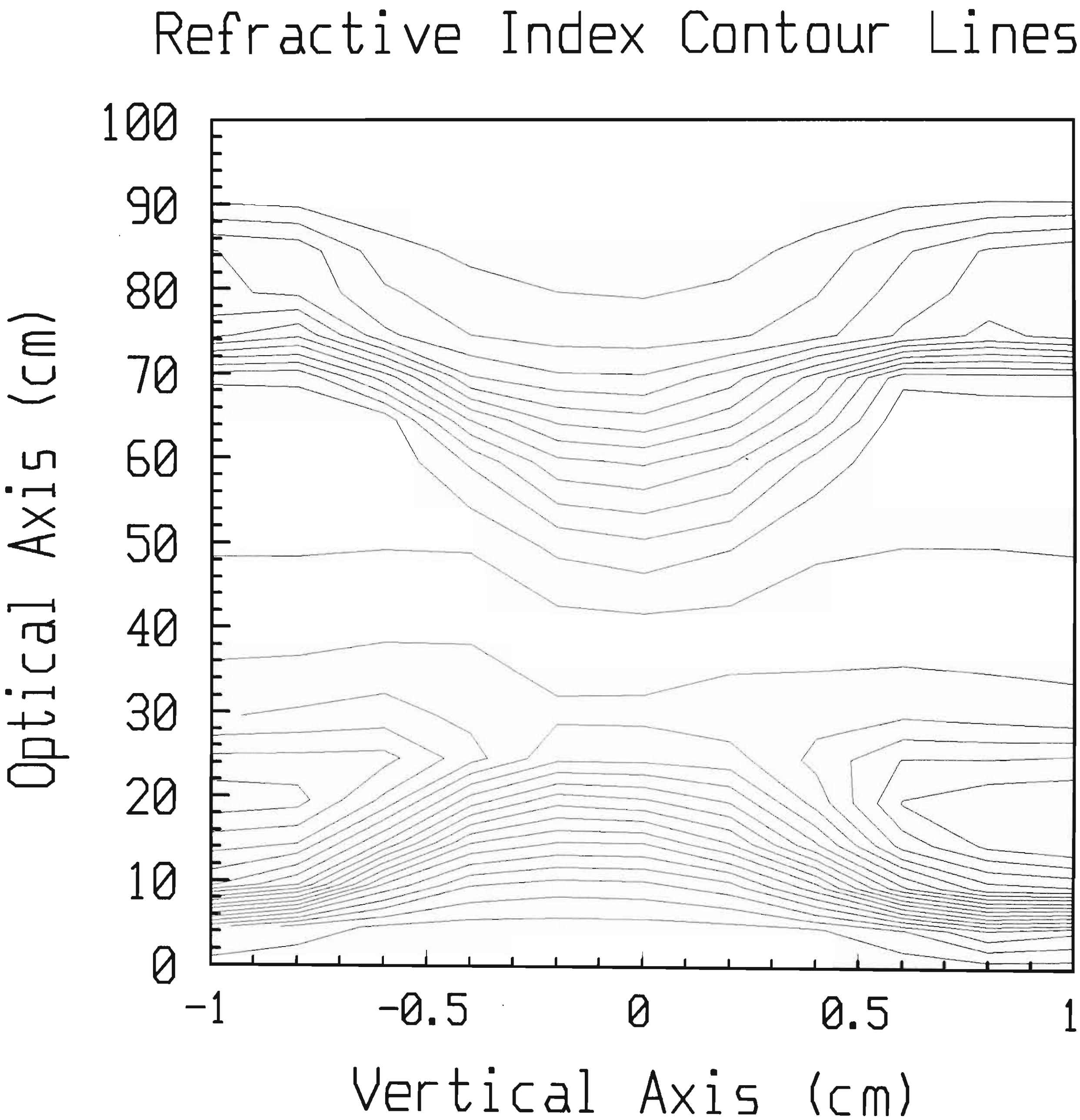

Fig.2.1.8 Refractive index contour lines from fig.2.1.6.

2.1.2 SOME OBSERVATIONS ABOUT THE EXPERIMENT

After changing the measurement position our probe typically requires a few seconds to reach a steady asymptotic value. While taking the measurement, we noted that the gas flow inside the spinning pipe is very sensitive to the flow conditions surrounding the lens, such as draughts in the laboratory. Big fluctuation in local temperature are sometimes observed corresponding to small external perturbations. To obtain reproducible results, as with all continuous gas lens experiments, a still environment is essential. We also verified that there was no horizontal (X) axis asymmetry. The finite size of the probe could possibly have an effect on the gas flow. We assumed, justified by the reproducibility of the results with different geometries, the effect to be negligible.

2.2 TRACING RAYS INTO THE MEASURED REFRACTIVE INDEX PROFILE

In this section we will perform some ray tracing through the measured refractive index profile. We show that by reducing the optical aperture of the lens (to 1 cm), an angular resolution of twice the diffraction limited is obtainable.

2.2.1 THE SOLUTION OF THE RAY EQUATION

The ray equation in the paraxial ray approximation is, with the help of equation 2.1.1:

$$\begin{aligned}
\frac{d^2x}{dz^2} &= \frac{1}{n}\frac{dn}{dx} \cong \frac{dn}{dx} = \frac{(n_0 - 1)T_0}{T^2}\frac{dT}{dx} \\
\frac{d^2y}{dz^2} &= \frac{1}{n}\frac{dn}{dy} \cong \frac{dn}{dy} = \frac{(n_0 - 1)T_0}{T^2}\frac{dT}{dy} \qquad 2.2.1 \\
T &= T(x,y,z)
\end{aligned}$$

Equations 2.2.1 are a system of second order non homogeneous differential equations. In the right hand side we can use either the temperature profile shown in figure 2.1.5 or the refractive index profile shown in figure 2.1.6. The solutions have the form:

$$r(z) = \begin{cases} x(z) \\ y(z) \end{cases} \qquad 2.2.2$$

and are the rays' trajectories inside the SPGL. They are completely determined when we know the temperature or refractive index field inside the pipe (figures 2.1.5 and 2.1.6). We numerically solved the ray equation 2.1.2 in the three dimensional refractive index profile obtained by interpolating the experimental points. To reduce computational time, our interpolation is with splines along the vertical direction (Y), linear along the optical axis (Z) and with a combination of sine and cosine terms to get the refractive index value off the Y axis. A fully 3D smooth interpolation is time consuming and the paraxial ray equations 2.2.2 require smooth gradients only in the direction transverse to the ray propagation. The program (listed in Appendix A) can give a histogram representation of the light intensity from an input object at any image plane. As is shown in figure 2.2.1, we start from a uniform distribution of rays arriving from the point source on the entrance plane of the SPGL. Each of these rays is represented by its positions x and y on the entrance plane and by its initial angles Θ_x and Θ_y. Their trajectory in the non uniform temperature region enclosed in the spinning pipe is obtained by the numerical solutions of the ray equations 2.2.1. We opted for a Runge-Kutta fourth order integration with a constant step size. On the exit plane we save the values of the ray positions and angles. After the exit plane the light will propagate straight again so that the rays' path is determined geometrically in terms of the four quantities $x1, y1, \Theta_{x1}$ and Θ_{y1}. The distribution of these four numbers onto the exit plane will define the radiation intensity at any plane after the exit plane.

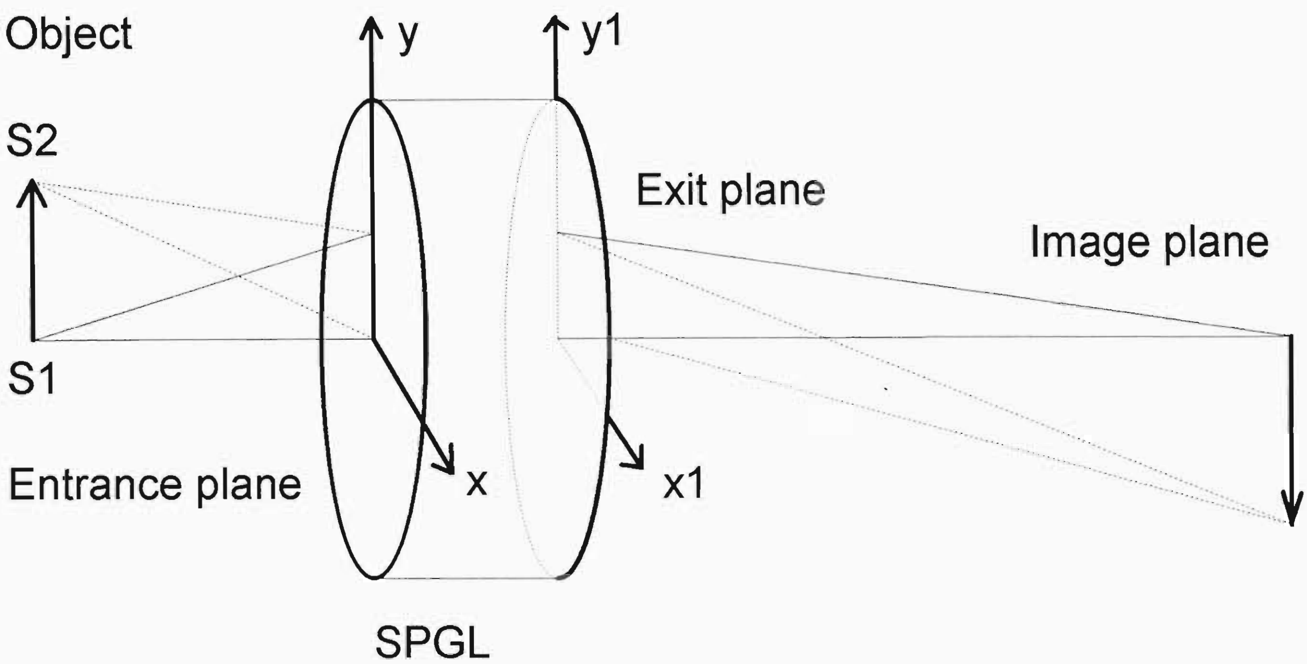

Fig.2.2.1 Imaging scheme with the SPGL.

Remembering what we said about geometrical optics in paragraph 1.3.2 (in equation 1.3.6) we can interpret the rays as the field line of the intensity field, which has zero divergence. The radiation intensity that crosses the unit surface area at some point after the SPGL is then proportional to the local density of rays. A histogram representation of the rays' intersections with any image plane is then proportional to the intensity field onto the image plane. The proportionality factor is easily found from the normalisation condition. Ray tracing was performed also using a non-paraxial rays algorithm [Sharma 1982], but we could not note any difference in the outputs.

2.2.2 DETERMINATION OF THE SPGL LIMIT RESOLUTION

The procedure described at the end of the previous section consists of a computational imaging of an incoherent source of light. We choose to image two distant point sources and to decrease their angular separation until they became unresolvable onto the image plane. Since we are imaging distant sources, the image plane coincides with the focal plane. We tried to apply Rayleigh criteria of resolution, which is nontrivial when the focus resembles more a ring (figure 2.1.8) than a Bessel function. Some images were recently taken with the same gas lens [Michaelis C 1991]. The best results were obtained limiting the aperture to 1 cm, and features close to the diffraction limit were observed. For the full aperture device (2.0 cm) the limit resolution obtainable is certainly worse than 0.2 mrad (see figures 2.2.2 and 2.2.3) which is very poor if compared to the diffraction limit. Moreover most of the energy hitting the lens is focused well outside the central area.

The focal length, in the following figures, is defined as the distance between the exit plane and the image plane, when the source is at infinity. By limiting the useful aperture to 1cm it is possible to obtain a resolution of 0.2mrad (figures 2.2.4 and 2.2.5) which is only about twice the diffraction limit. It can be easily seen that the outer rays are too weakly refracted to arrive in the same focus as the inner rays. Possibly the worst feature of the SPGL is that part of the light is spread out on a large ring around the point focus due to the central region of the lens.

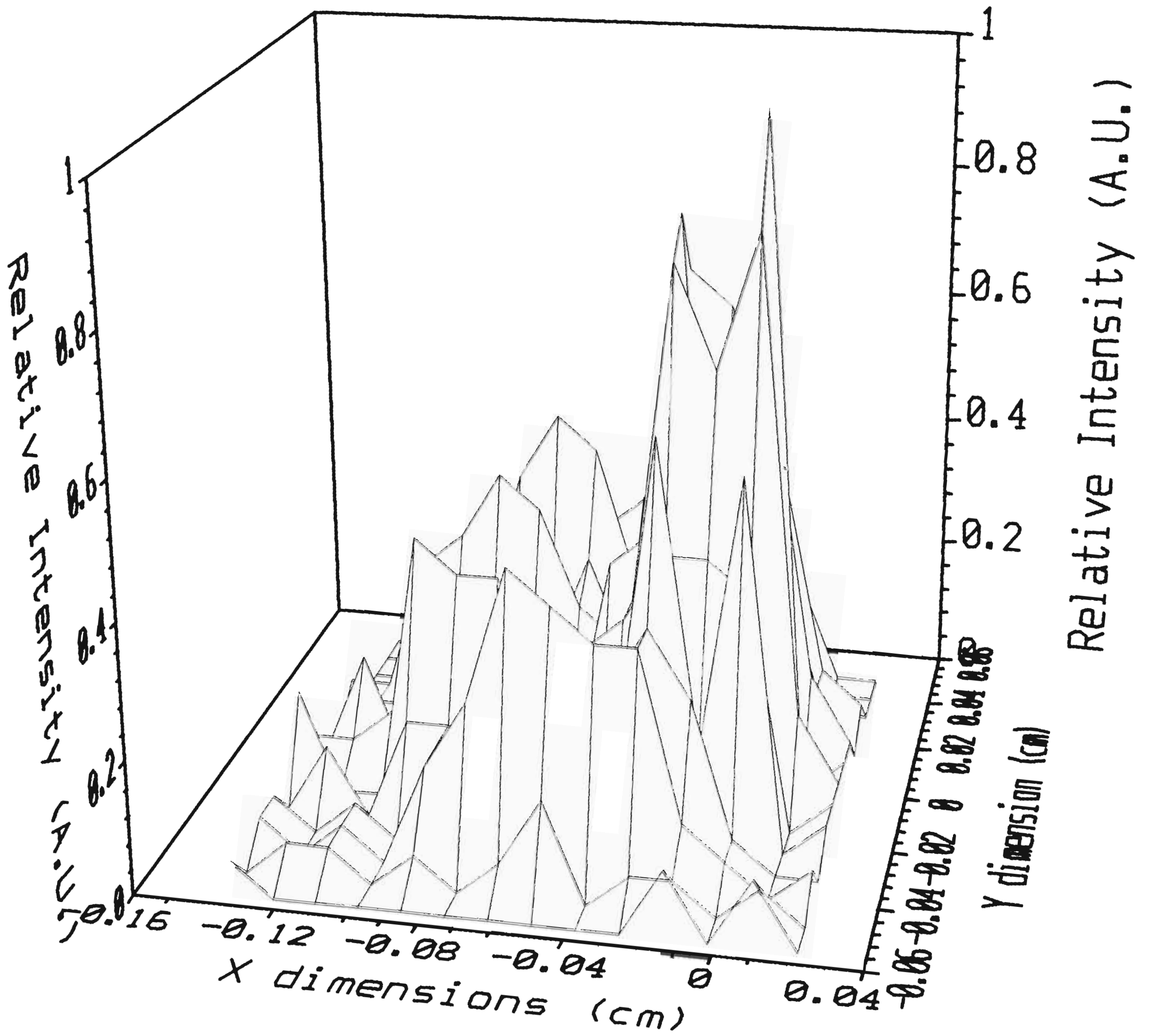

Fig.2.2.2 Intensity histogram on the focal plane for two distant point sources at 0.2mrad. Optical aperture=2cm. Focal length =1.6m.

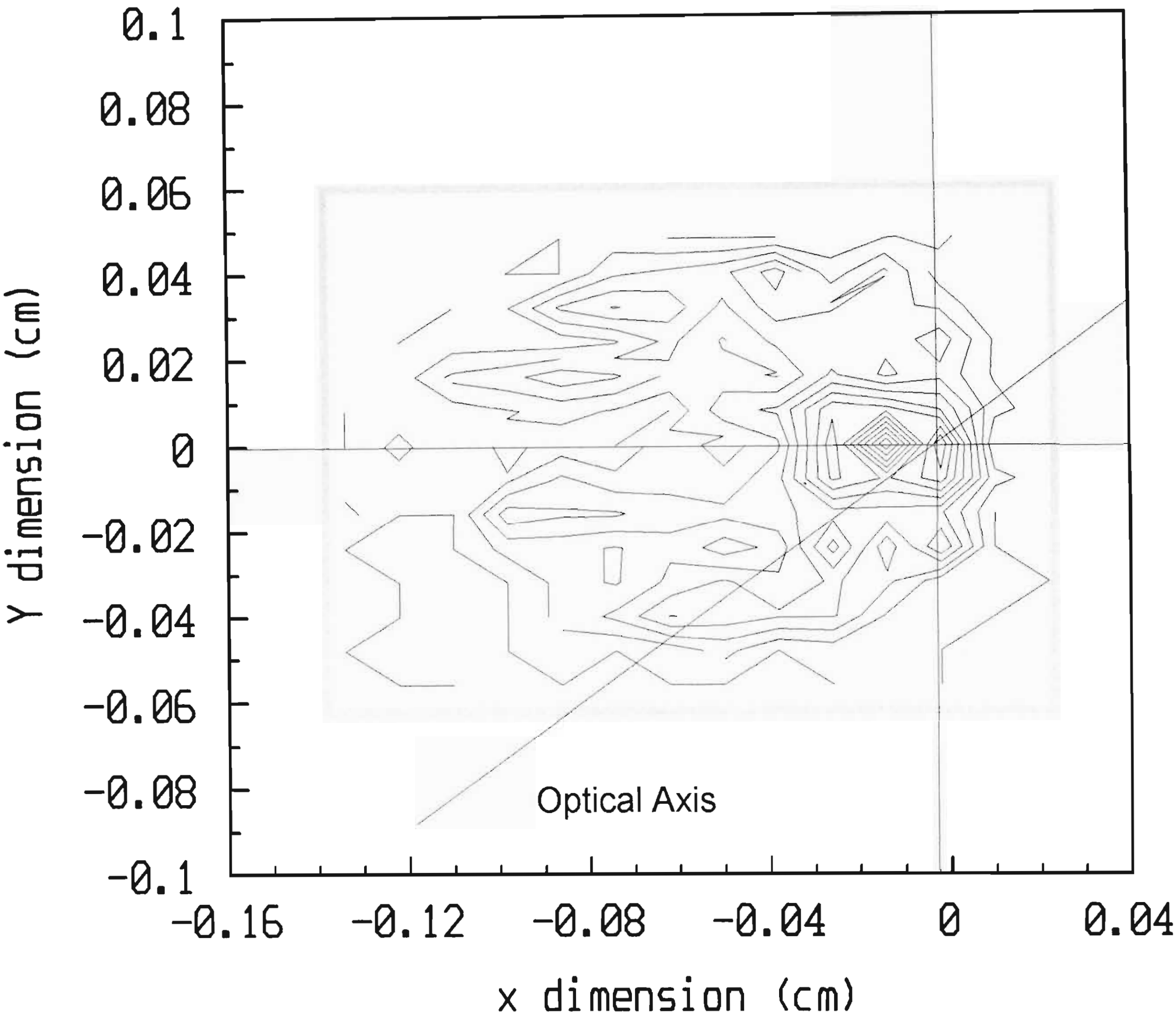

Fig.2.2.3 Intensity contour plot for the profile shown in fig.2.2.2. In the grey box is 30.5% of the total energy. The rest of the energy is spread over a large ring around the central region. This is caused by the longitudinal aberration of the lens.

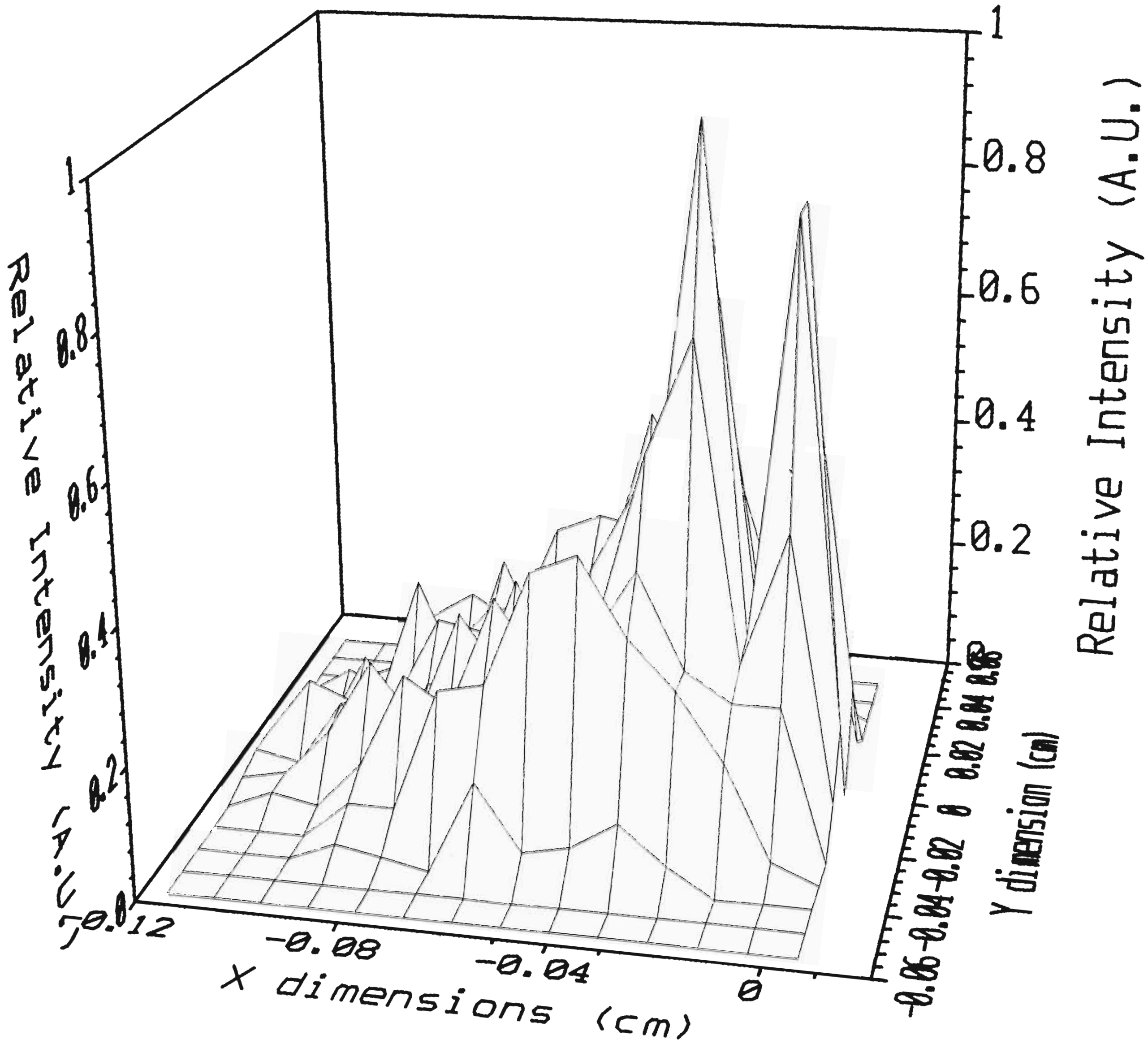

Fig.2.2.4 Intensity histogram in the focal plane for two point source at 0.2mrad. Optical aperture = 1.0cm, Focal length=1.6m.

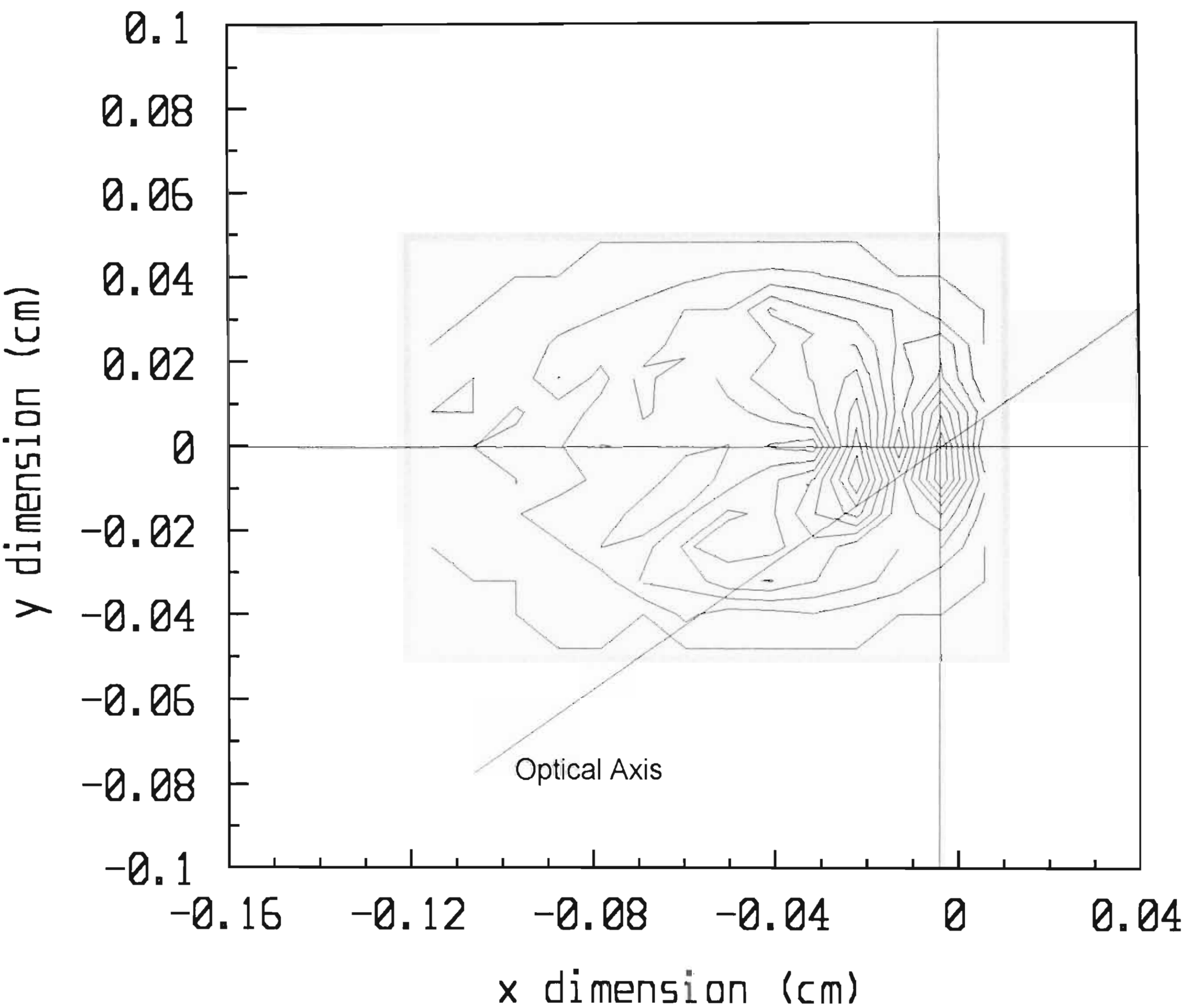

Fig 2.2.5 Intensity contour plot of fig.2.2.4. Inside the grey box is 100% of the total energy.

In figure 2.2.6 we show how the focal length varies as a function of the distance from the optical axis along the vertical direction. This is a quantitative measurement of the longitudinal aberrations of the lens. It explains too the reason why it is necessary to limit the gas lens diameter in order to achieve decent performances. The focal length is measured from the exit plane of the pipe.

The sharp increase in focal length close to optical axis is rather a feature of the simple method utilised to calculate the focal length than a real physical feature of the lens. Given the quantities θ_y and y, the generic angle and position on the exit plane (figure 2.2.1), the focal length L is determined geometrically as

$$L = \frac{y}{\tan(\theta_y)} \qquad 2.2.3$$

since θ_y tends to zero as y goes to zero. the focal length is not determined close to the optical axis, since a small experimental uncertainty on θ leeds to big fluctuation of L. We remember that θ_y is determined by ray-tracing into the measured refractive index profile.

In other words rays close to the optical axis might never cross it, giving an infinite focal length according to 2.2.3, but then they end up a few μm away from the optical axis at the image plane, thus contributing to the intensity in the focus. The focal length of this gas lens is more or less constant for diameters up to 1cm and increases rather sharply at larger diameters. Lastly in figure 2.2.7 we show the focal length against the angle about the axis of the input beam lying on the horizontal plane. At a small angle the focal plane is really a plane and not a curved surface. At each horizontal angle about the optical axis a curve similar to the one shown in figure 2.2.6 was determined. The average focal length within a 1cm aperture was then determined. The values coincide within 1% at small angles. At larger angles the beam is cut by the edges of the pipe.

Another feature, visible in figures 2.2.3. 2.2.5 and 2.2.6 (where the "vertical axis" has been shifted by 0.3mm), is that the focus is displaced along the vertical direction, below the optical axis, due probably to the effect of gravity on the temperature distribution (figure 2.1.6).

Ray tracing through the measured refractive index profile of a spinning pipe gas lens, satisfactorily explains two important features: decrease in optical quality as the optical aperture approaches that of the pipe, and lowering of the image centre due to gravity.

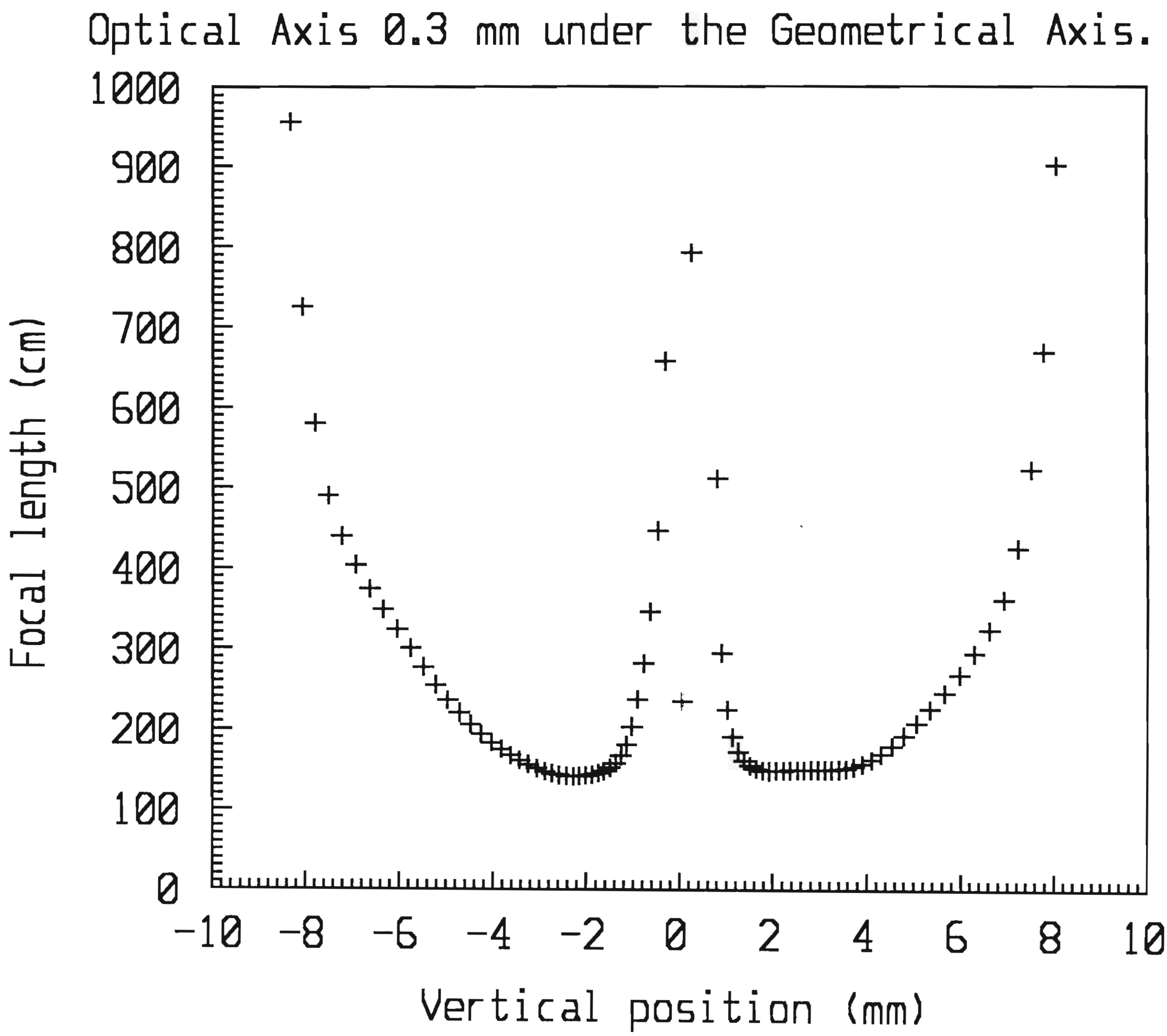

Fig.2.2.6 Computed focal length vs position of the Spinning Pipe Gas Lens.

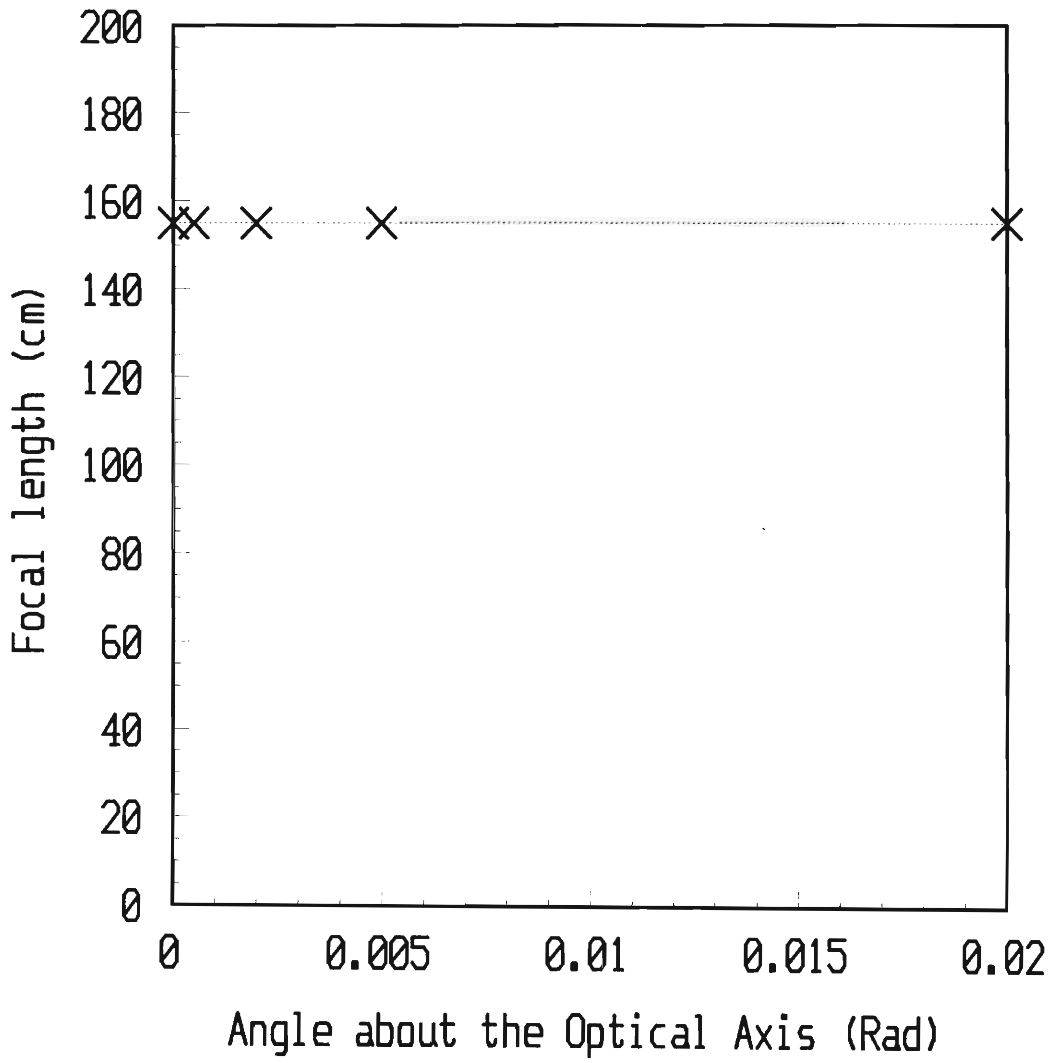

Fig 2.2.7 Focal length vs angle about the axis. The focal surface is a plane.

2.3 THE SPGL AS AN INTRACAVITY PASSIVE OPTICAL ELEMENT

The SPGL optical quality is found to be good, though not excellent. Its advantages are: Very high optical breakdown threshold, good optical quality at low aperture, absence of reflective surfaces. Its disadvantages are the high f-number and the longitudinal aberration. The latter effect increases with the increasing aperture and is clearly visible in figure 2.1.6.

Moreover the Spinning Pipe Gas Lens performances can be unstable, being sensitive to draught and requiring still laboratory conditions. Last the spinning pipe can introduce vibrations.

As seen in the previous paragraph its optical quality is good for apertures up to 1 cm, which is the typical transverse dimension of a commercial laser beam. The absence of reflective surfaces and its long focal length suggests use as a laser intracavity optical element. When employed so, It is important to decouple the vibrations introduced by the spinning pipe from the laser resonator optics, though this is a relatively easy problem to solve. Inside a laser cavity, the absence of reflective surfaces renders the radiation losses equal to zero. In an early experiment performed at the Bell Laboratories a gas lens waveguide as long as 70 m was inserted inside a He-Ne cavity, and did not prevent it from lasing [Beck 1967]. As we will see in a following chapter the performances of a SPGL as an intracavity element can be very good, even superior to an equivalent glass lens.

CHAPTER 3:
THE COLLIDING SHOCK LENS

In reference [Buccellato A 1993] a macroscopic pulsed gas lens is described that could be used as a final focusing element in a laser driven thermonuclear fusion experiment. Here we describe a novel type of pulsed gas lens which would be suitable for operation in conjunction with a small pulsed laser, the colliding shock lens (CSL) [Buccellato B 1993, Buccellato 1994]. In the first section of this chapter we describe in very general and heuristic terms, the working principle of the colliding shock lens. In section 3.2 we will experimentally characterise the focusing performance of the very early version of the device, a small, 8 pin, 1 cm electrical diameter CSL. In section 3.3 we will present a measurement of the refractive index profile of a larger version of the same device, an 8 pin, 3 cm electrical diameter lens. The measurement was performed using a Mach-Zehnder interferometer. The refractive index profiles will be analysed in detail in a later chapter to determine the optical quality of the CSL. In section 3.4 we will characterise its use as a high power electro-optical switch and discuss some other potential applications.

3.1 THE WORKING PRINCIPLE

The colliding shock lens working principle relies on the interaction of multiple shocks in air in order to create a non-uniform density distribution in a gas. The transient density perturbation deflects and focuses light. We can divide the study of the CSL into two main subjects: Gas Dynamics and Optics. We will give here only an heuristic description of the gas dynamics and we will concentrate our efforts on the study of its optical properties in a later chapter. The gas dynamics of colliding shocks are discussed in detail in [Buccellato 1994].

3.1.1 SHOCK WAVES

There are several possible approaches to a description of shock waves in a gas. It depends first on the picture that one has in one's mind of the gas

itself and secondly on the level of precision that one wants the description to achieve. From the thermodynamic point of view, a shock is a surface discontinuity of the values of the thermodynamic quantities such as temperature, pressure, entropy and mean molecular velocity (t,p,s and u). The strength of a shock can then be defined in terms of the quantity $\mathbf{M}_0$, the Mach number. The Mach number is the ratio of the discontinuity propagation speed to the sound speed of the medium. If one wants then to solve the discontinuity into a continuous spatial profile, as experimentally observed, the thermodynamic description must be replaced by a gas-dynamic description. Since one of the basic hypotheses in order to write down the gas-dynamic equations is the continuity of the medium, the discontinuity is replaced by a sharp but continuous variation of the physical properties across the shock-front. The gas-dynamic equations are partial differential equations and can be solved by many numerical methods. Dealing with a shock, though, is complex and the reason is the spatial scale of the phenomenon. All the numerical methods concerned are based on dividing the space into a grid of cells and substituting the derivative with "finite differences". Since the shock width can be orders of magnitude smaller than the dimensions of the system and the cell dimension must be much smaller than the shock-width, a very high number of cells is necessary to model a realistic shock. Often beyond the performances of big computers for realistic three-dimensional situations.
Moreover the continuity hypothesis becomes invalid when sharp density gradients are on a spatial scale comparable to the average molecular distance. In the latter case the gas-dynamic equations cease to be valid and a statistical model becomes necessary.
The situation is further complicated by energy dissipation on the shock-front which has to be taken into account when the local temperature is such as to excite electronic transitions of the gas molecules (or vibrational transitions, at a much lower temperature). The situation is already complex enough for a plane shock but becomes much harder when we deal with the interaction of many shocks and/or with shock-fronts of non-planar geometry.
Shock theory and modelling has become a science in itself, as often happens when physics investigates a system away from its equilibrium. For the purpose of this thesis, we see a shock wave as a gas compression wave which travels faster than sound does. The speed of the "Shock" depends on the peak density at the shock front of its profile. It is in general easier to

measure the density profile and its velocity, for example with interferometric techniques, than to try to compute it.

3.1.2 SPHERICAL SHOCKS

Let us consider a point explosion in air. During an explosion in a gaseous medium, energy is transferred to the gas molecules and part of it goes into their kinetic energy. The increase in particle velocity, that is, in pressure and temperature, creates a low density region close to the explosion centre. In a simple picture, the gas which was contained in a sphere of volume **V** is distributed after the explosion in a thin spherical layer around an empty volume **V**. The gas compression generates a spherically symmetric expanding compression wave. The intensity of the perturbation decreases as the shock expands for two reasons. The first is the increase (with the square of the radius) of the volume concerned by the perturbation as it moves away from the explosion centre with the sound speed. The second is the energy dissipation at the shock-front. The shock "intensity", or its Mach number $\mathbf{M_0}$, typically decreases with a power law with the distance from the explosion centre. The problem of shock wave motion in cylindrical and spherical symmetry was first formulated and solved by Guderley [Guderley 1943] and Taylor [Taylor 1946]. Guderley first developed a method for the solution of the gas-dynamic equations in spherical symmetry. It is found that a weak spherical shock propagates radially with a constant velocity. the sound speed of the medium. This is the case when the flow is isentropic, that is there is not entropy change across the shockfront. In other words the gas does not increase its entropy as the shock wave passes through.

Conversely it was found [Taylor 1946] that the radius of a strong spherical shock (or a blast wave) does not increase linearly with time, but obeys to a power law with exponent less than one:

$$R(t) = \Xi t^{2/5} \qquad 3.1.1$$

Where Ξ is a constant of the medium. It is intuitive that during propagation, as the velocity of the shock decreases the shock becomes weaker and weaker. The flow becomes isentropic and the shock velocity equals the sound speed.

When two spherical shocks in air collide, the interaction depends on their strength [Courant 1948]. At Mach numbers close to unity the waves simply pass unmodified through one another. At intermediate $\mathbf{M}_0$ they pass but are somewhat delayed. At higher $\mathbf{M}_0$, there is a period of stagnation during which the fronts merge into a high density plane slab, and at very high $\mathbf{M}_0$ the collision generates turbulence. When several shocks are launched from explosion points placed on the arc of a circle, one might expect behaviour similar to that of the double shock interaction. Moreover, since many shocks now collide at one point, non-linearities in the shock interaction are expected to occur at lower $\mathbf{M}_0$ than for two colliding shocks. The regime of interest here, is at an intermediate $\mathbf{M}_0$ when the fronts interact in a non-linear but orderly manner [Courant 1948].

3.1.3 THE COLLIDING SHOCK LENS

When several spherical shocks, produced by arc discharges, expand from points equi-spaced on a circumference, a cylindrically symmetric converging shock-front is formed. In the actual device, the shock waves are produced by arc discharges between opposing pin electrodes. In the configurations described in this thesis there are eight pairs of electrodes, but we tried geometries with 16, 32 and 36 arcs. When the expanding spherical shock-waves, launched from points equi-spaced on the arc of a circle, collide at the centre, a cylindrically symmetric cigar shaped density distribution results at the centre, as shown in figure 3.1.1. The cylindrical symmetry is obtained starting from a polygonal shaped shock-front, due to the non-linear interaction between shock-waves, such as Mach reflections. In figure 3.1.1 and 3.1.2, for simplicity we display only four of the shocks.

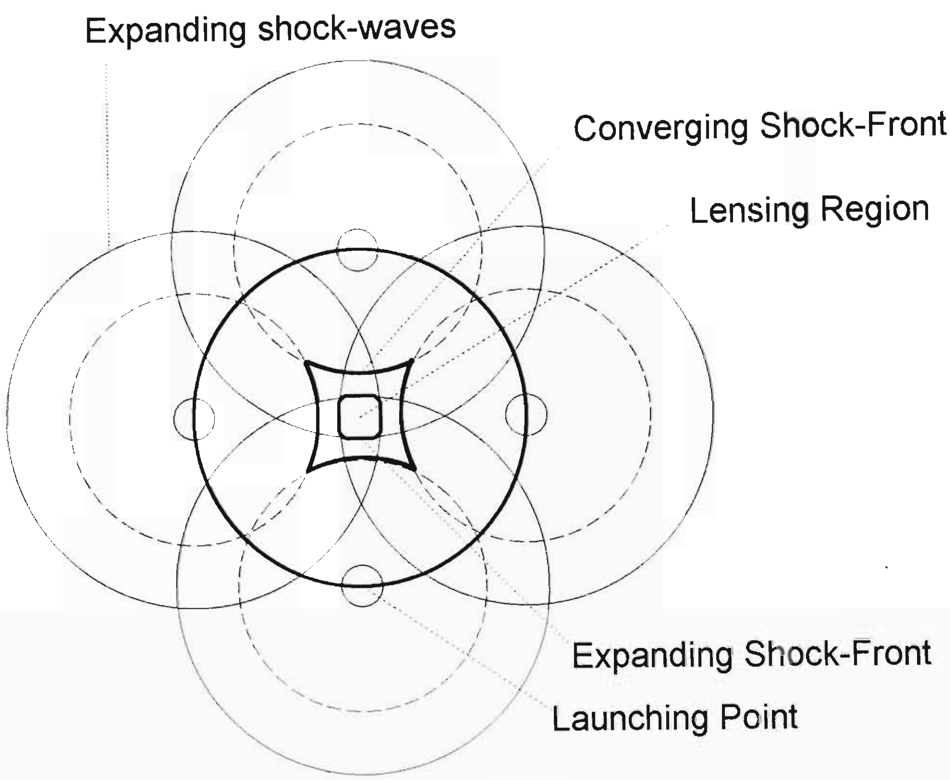

Figure 3.1.1. Geometry of the Colliding Shock Lens, front view.

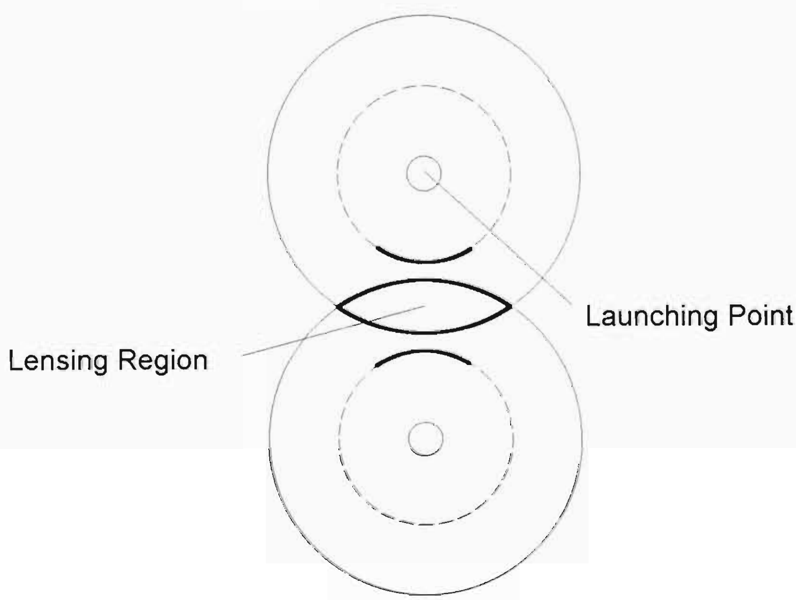

Figure 3.1.2. Geometry of the Colliding Shock Lens, Side view. These geometrical constructions do not consider the interactions between the overlapping shock-waves that smear out the collision angle, making the converging shock-front cylindrically symmetric before and after collision.

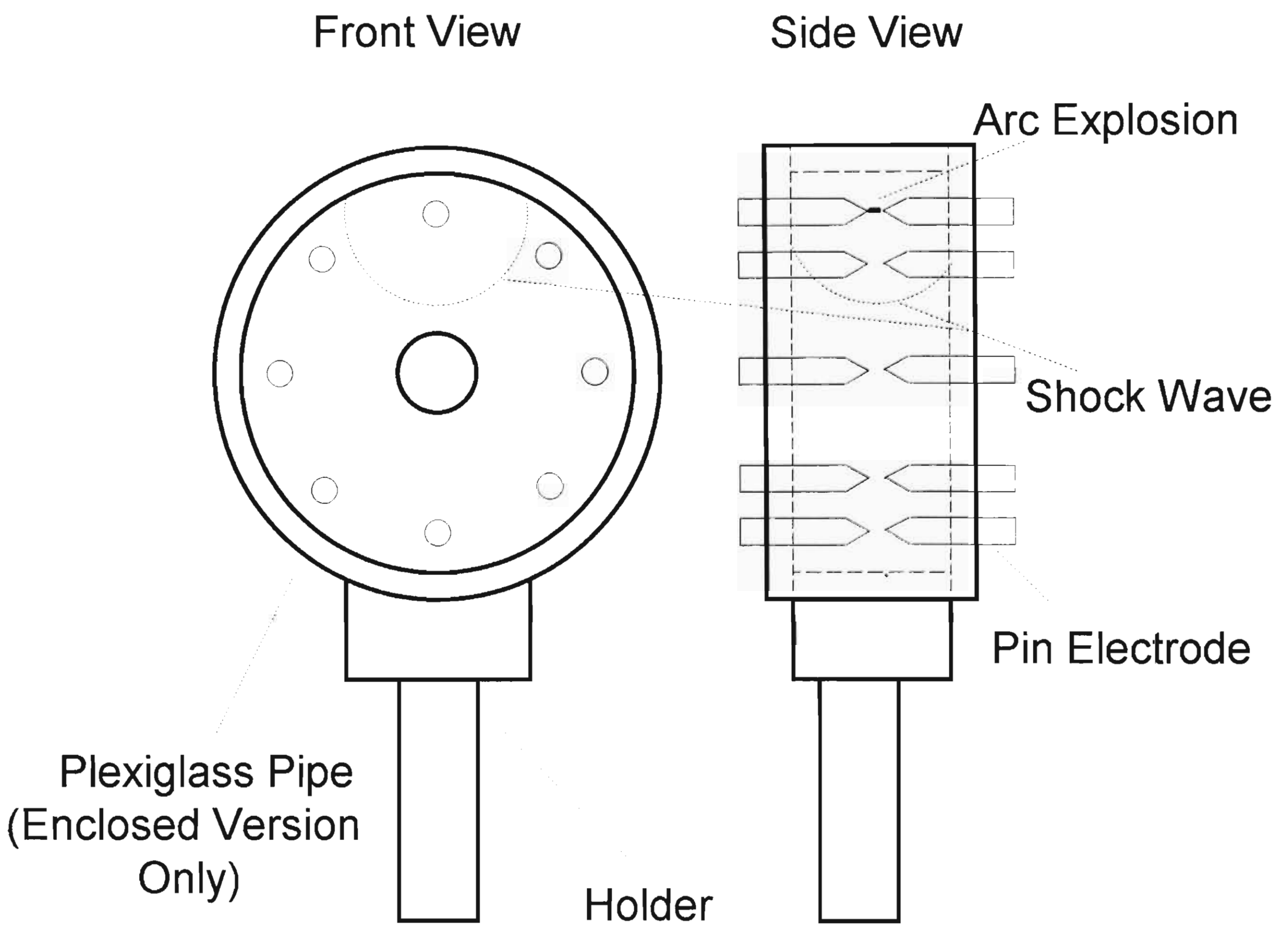

Figure 3.1.3 The Colliding Shock Lens. The arc discharges between opposing pins can be enclosed inside a Plexiglas pipe.

In [Schwendeman 1987] it was noted that converging cylindrical shocks with regular polygonal shaped cross-sections are stable and tend towards a circular cross-section. Converging cylindrically symmetric shock waves produce a condition of high pressure, temperature and density in the region of implosion. After the spherical shock converges to a point, a regular and stable [Matsuo 1981] axi-symmetric cigar shaped expanding density distribution results. It is in this region that we expect the density distribution to act as a graded-index lens. Figure 3.1.3 is a schematic diagram of an 8 arc CSL.

3.2 FOCUSING EXPERIMENT

The first diagnostic utilised in conjunction with the CSL consisted of a single probe laser beam directed along its optical axis. The laser beam intensity profile was then recorded on the face plate of a T.V. camera. This simple set-up detects refractive fringes as well as focusing due to the passage through the gas lens.

3.2.1 EXPERIMENTAL SET-UP

The spherical shocks were created at points equi-spaced on a circumference (diameter=11mm) by eight pairs of opposing electrodes. We utilised needles of diameter 850μm and an arc gap spacing of 1mm. The electrodes are mounted on two opposing Plexiglas plates with a circular hole in the centre (diameter=7.5mm) allowing the probe laser beam to be directed along the axis of the CSL. The gaps were connected in series in order to breakdown simultaneously. The breakdown occurs in nanoseconds and appears to be instantaneous on the microseconds time-scale of the lens. In figure 3.2.1 the geometry of the colliding shock lens is represented.

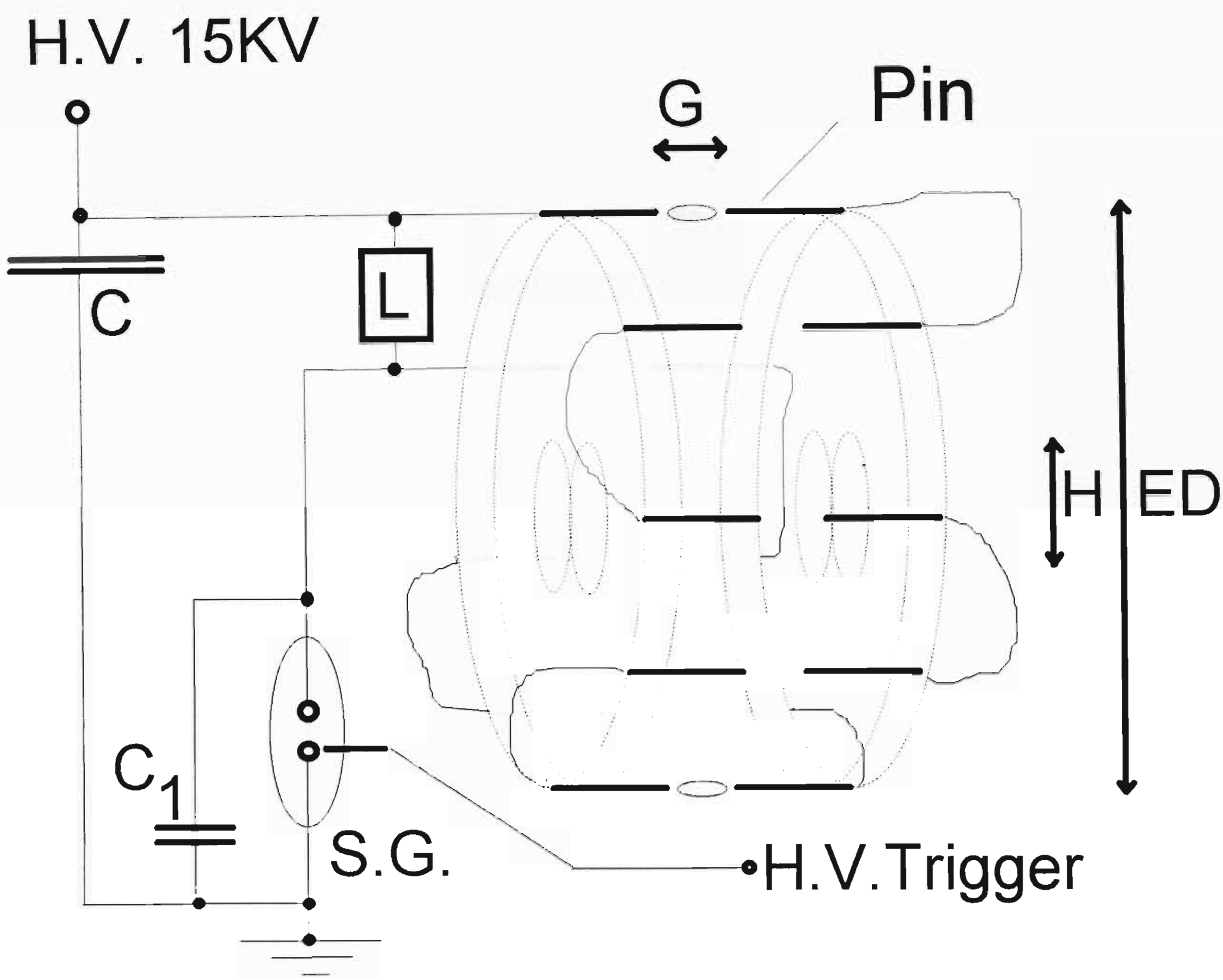

Fig.3.2.1 Eight pin Colliding Shock Lens geometry and driving circuit in the focusing experiment: Storage capacitor C=5nf, Breaking Capacitor C_1=1nf, Charging Inductance L=0.1H, Hole for the laser beam H=8mm, Electrical Diameter ED=11mm, Electrode Gap G=1mm. S.G: Spark Gap.

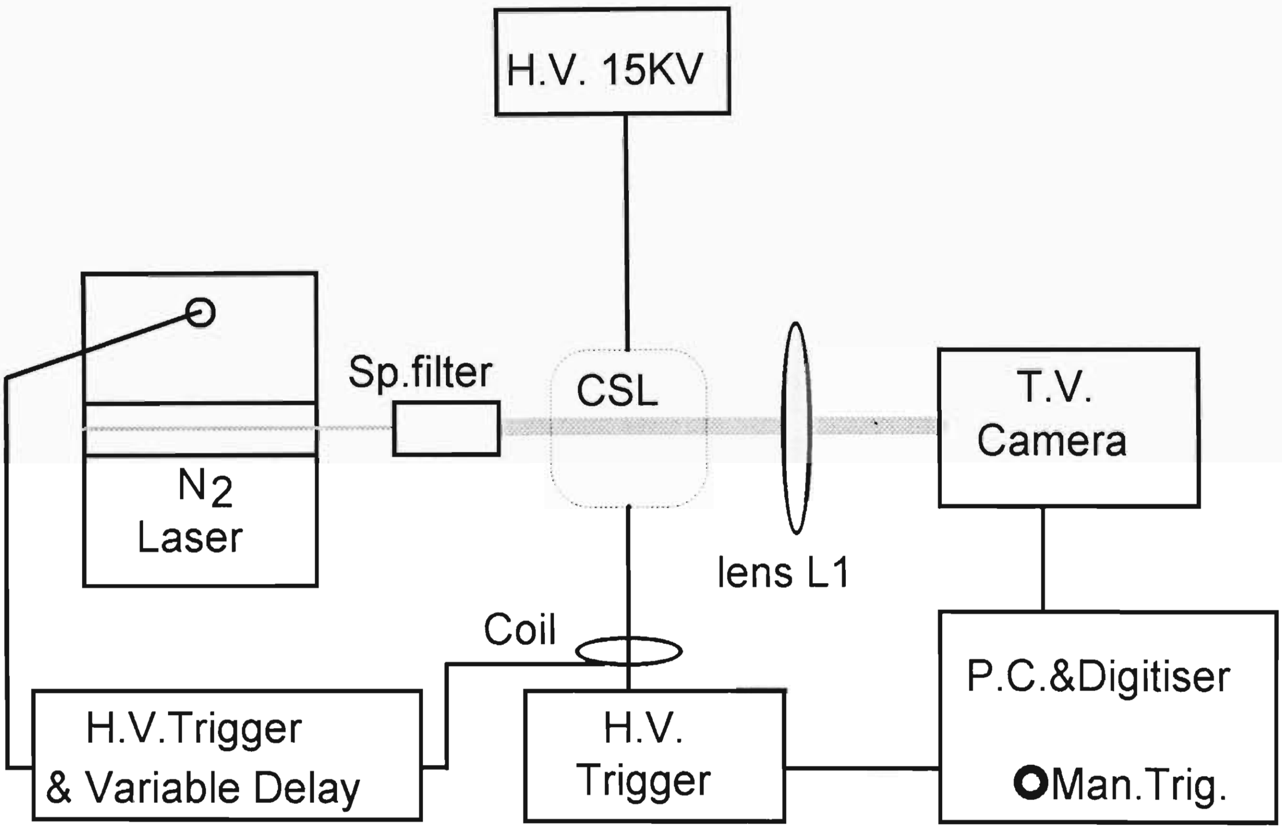

Fig.3.2.2 Experimental set-up for the focusing experiment.

A spatially filtered and expanded nitrogen laser beam (FWHM=1ns, λ=337nm) was directed through the collision region onto a T.V. camera face plate through an imaging lens and a nitrogen interference filter (330nm, Band-width=10nm). A PC synchronised the triggering of the CSL with the image digitiser. The signal from a Rogowsky coil in the CSL high voltage circuitry, triggered the nitrogen laser via a variable delay box. The value of the capacitor C determines the energy provided to the colliding shocks and a 5nF capacitor was chosen. A schematic representation of the experimental set-up is shown in figure 3.2.2.

3.2.2 EXPERIMENTAL RESULTS

The CSL properties were investigated by recording images at different distances from the CSL and at different delays. Parasitic fringes were due to the interference filter. A time sequence for the colliding shocks is given in figure 3.3.3 ($\mathbf{M}_0$=1.5). From left to right and from the top down we can follow the collision sequence. The first frames (1-5) show the non-linear interaction between the shock waves resulting in non-cylindrically symmetric illumination patterns. As the shock-front implodes, the angles between colliding shocks tend to be smeared out and the front tends towards cylindrical symmetry. The interesting point is that after the shocks have collided at the centre (frames 6,7) there is a cylindrically symmetric core. "The shocks have forgotten where they originated". A high density expanding region is created (frame 8-16). A sharp focus is observed in frames 8 and 9. Frames 10 to 16 show the typical diffraction pattern when focusing is achieved further away from the CSL.
The detailed illumination pattern (i.e. dark and bright rings, coarse and fine fringes) in figure 3.2.3 is best understood by referring to articles on refractive fringe diagnostics of spherical shocks in air [Cunningham 1986, Waltham 1987, Michaelis A 1991, Michaelis D 1991]. The next figure 3.2.4 shows in details the focusing obtained with the eight arc CSL (C=5nF) at a distance of 39cm. In the central region of high intensity the camera is heavily saturated.

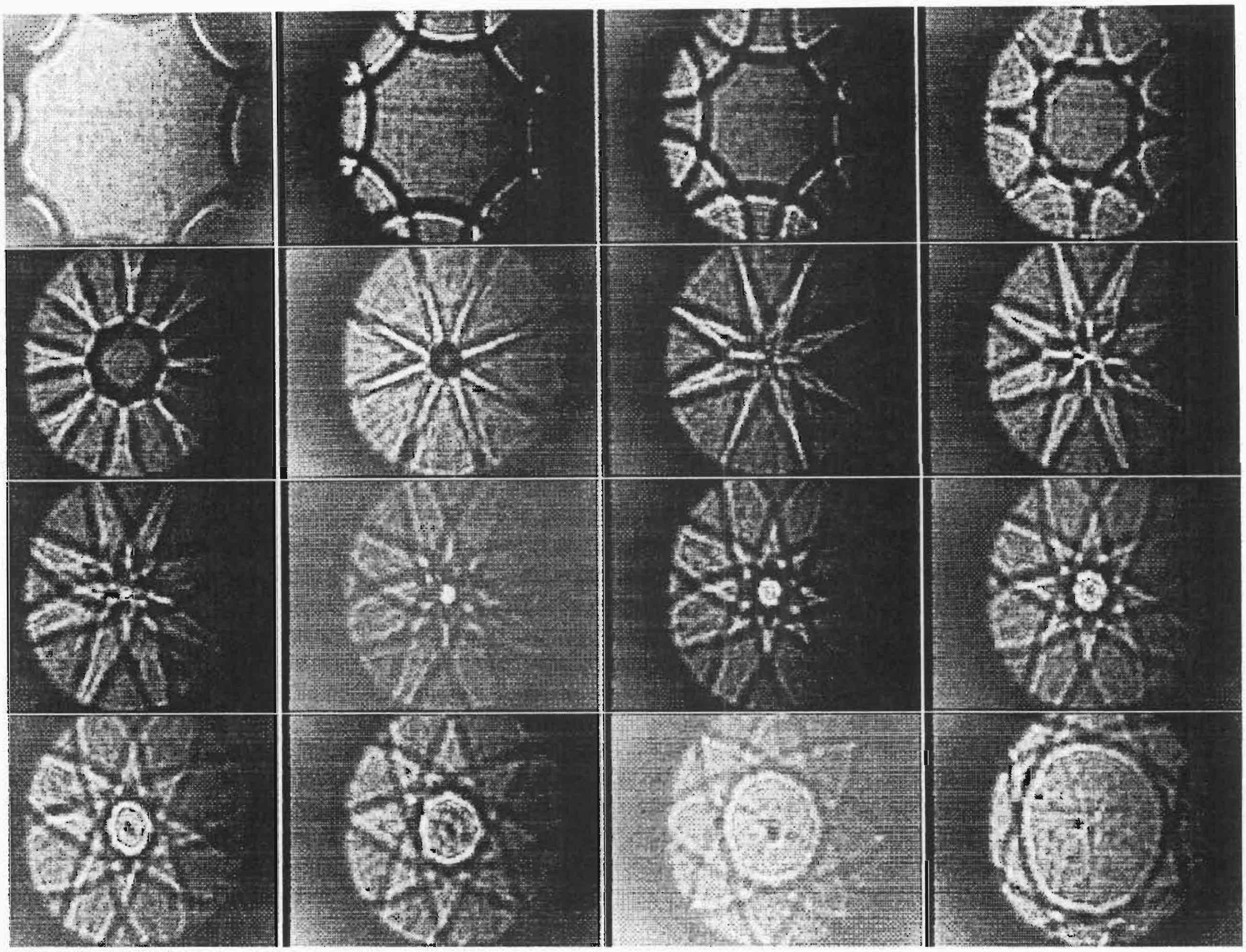

Fig. 3.2.3. From the top left, time sequence of an eight arc CSL imaged 48.7cm from the CSL at (1) 3.2μs, (2) 5μs, (3) 6μs, (4) 6.9μs, (5) 8μs, (6) 10μs, (7) 10.4μs, (8) 10.9μs, (9) 11.3μs, (10) 11.6μs, (11) 11.8μs, (12) 12.2μs, (13) 12.4μs, (14) 13.1μs, (15) 14μs, (16) 15.6μs.

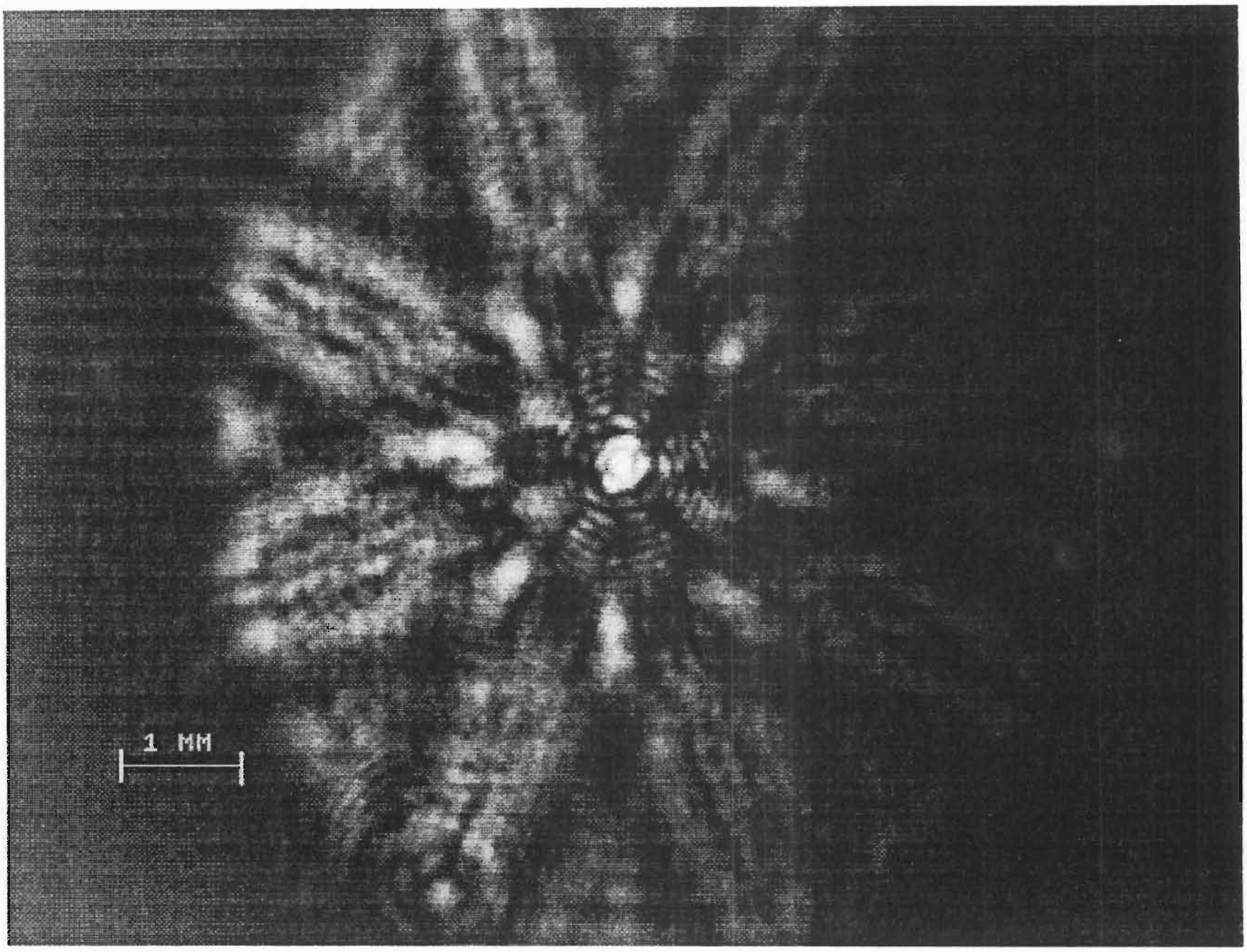

Fig.3.2.4 Eight arc CSL focal spot (focal length=39cm, delay=11.8μs).

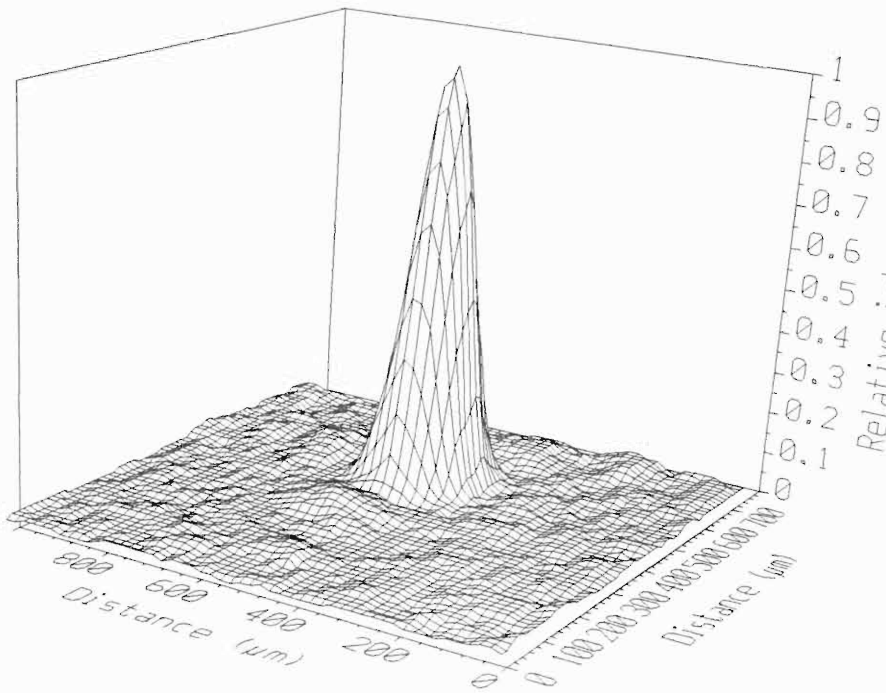

Fig.3.2.5 Intensity plot of the CSL focal spot.

If the same image as the 3.2.4 is recorded with an additional filter in order to avoid the saturation of the camera, a FWHM focal spot diameter of 100μm is obtained [Buccellato B 1993].

Here we do not show the unsaturated image, but figure 3.2.5 shows a three-dimensional intensity plot taken from its central region.

The CSL is a varifocal lens in which the focal length and the lens diameter vary with time according to the curves shown in figure 3.2.6 and figure 3.2.7.

The effective lens diameter was obtained by imaging with the lens **L1** on the shock collision plane. Due to the expansion of the shock-front after the collision, the effective lens diameter increases with time: figure 3.2.3. As the CSL diameter varies, the relative diffraction limited spot size changes.

This time dependence is in agreement with the measured evolution of the focus spot size reported in figure 3.2.8. In this figure the diffraction limited spot size is calculated according to equation 1.6.7. The values of lens diameter are obtained by linearly interpolating figure 3.2.7 at each time experimnetal images of the focal spot size were available (at a known focal length).

Even the position of the rings surrounding the central spot (as seen in figure 3.2.4) is in reasonable agreement with the theoretical Airy rings radii (see figure 3.2.9). A detailed study of the CSL optical quality taking diffraction into account is reported in chapter 5.

The CSL was utilised to focus a ruby laser beam (FWHM =30ns, E=500mJ) onto photographic paper in order to obtain a burn pattern at the distance of 39cm. The Q-switched ruby beam was synchronised in order to fire at the corresponding time delay. First the diffraction-limited ruby beam was directed through the lensing region and a burn-pattern was obtained. Then a glass convex lens of equal focal length was apertured to 1.3mm, which is the effective aperture of the CSL at the focal length of 39cm, and a comparison burn pattern was obtained. The central burn regions for both lenses were approximately 200μm in diameter [Buccellato B 1993].

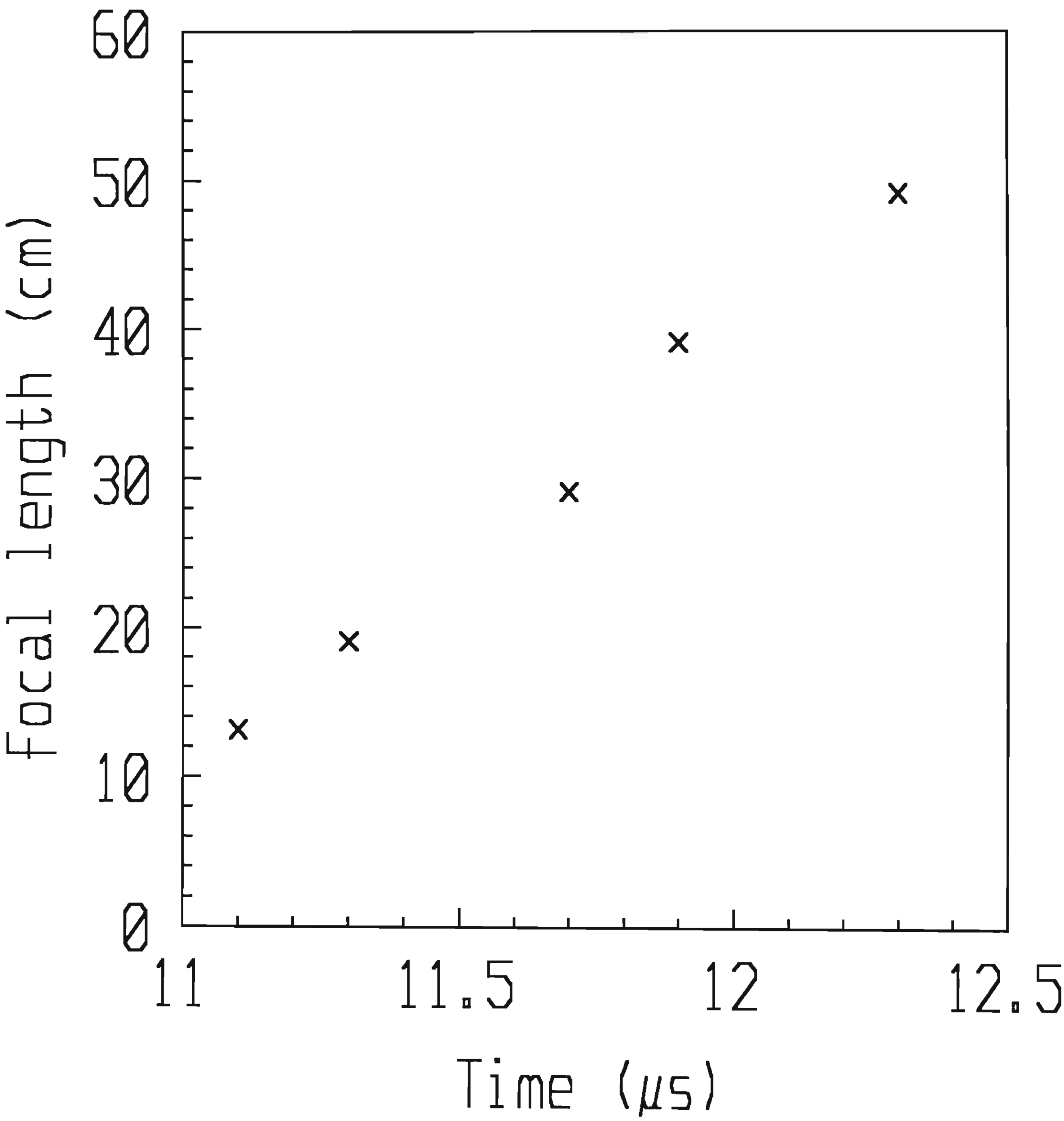

Fig.3.2.6 CSL focal length vs Time after arc explosions.

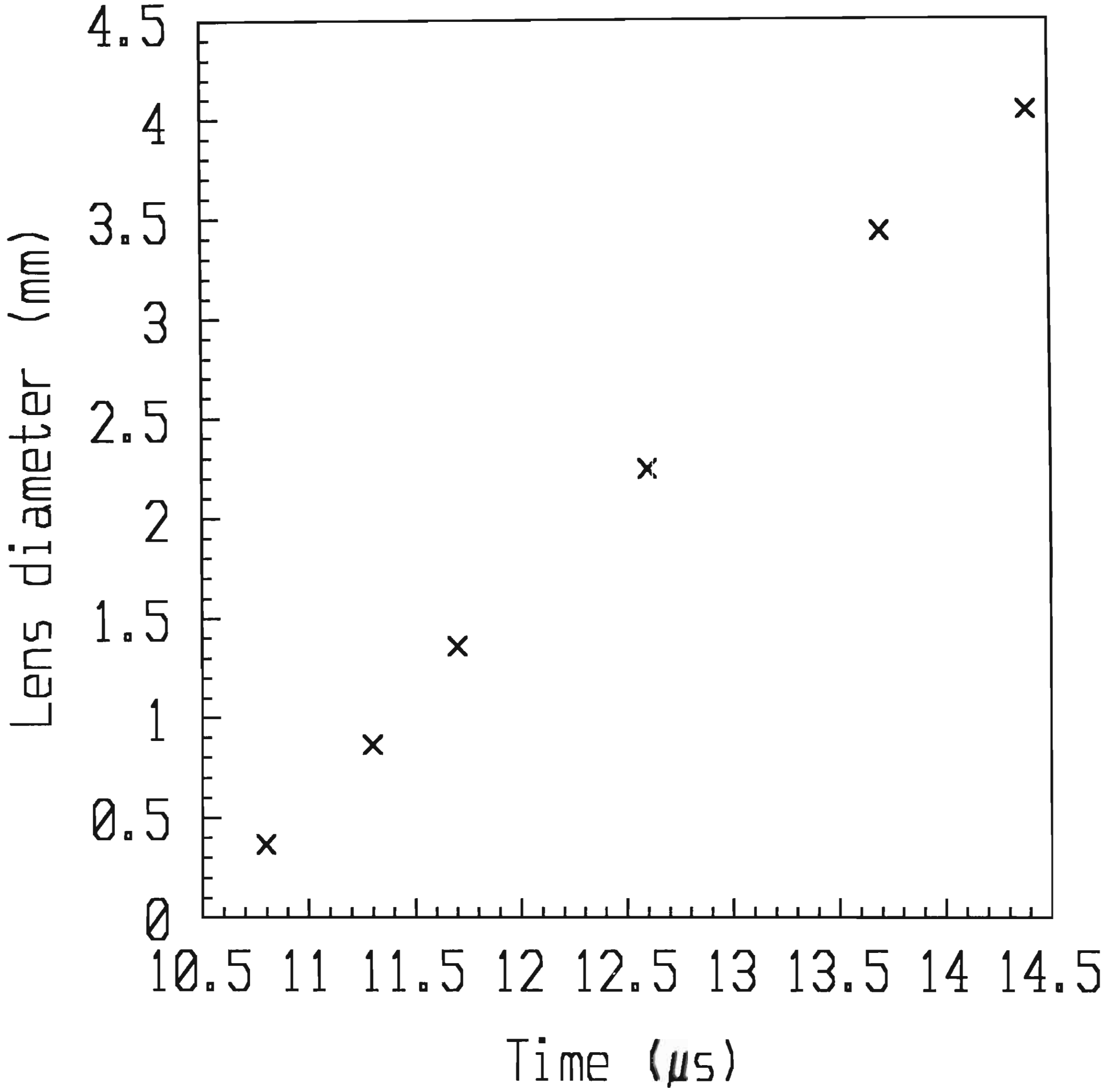

Fig.3.2.7 CSL Diameter vs Time after arc explosions

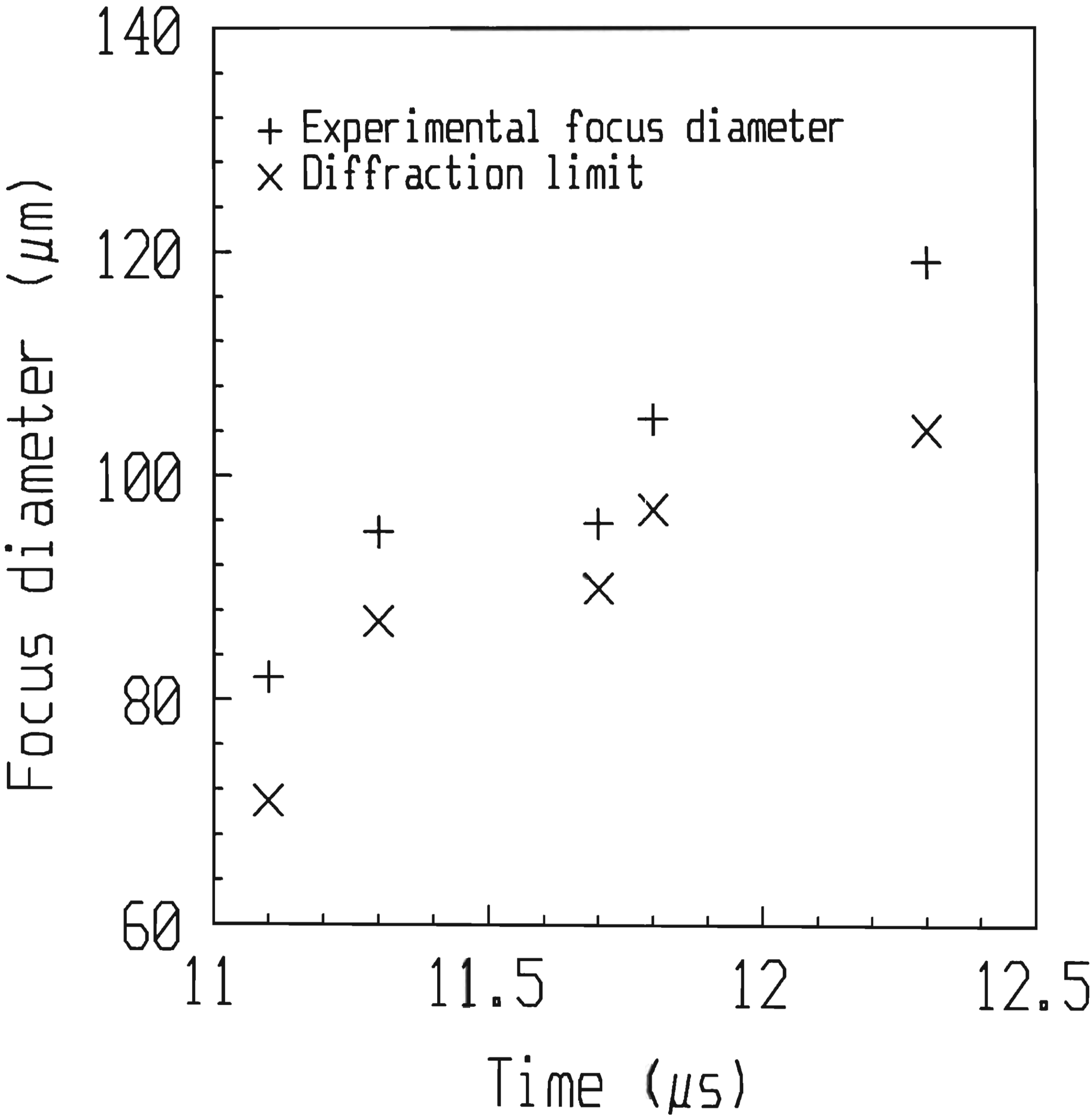

Fig.3.2.8 Measured focal spot and diffraction limited focal spot vs Time

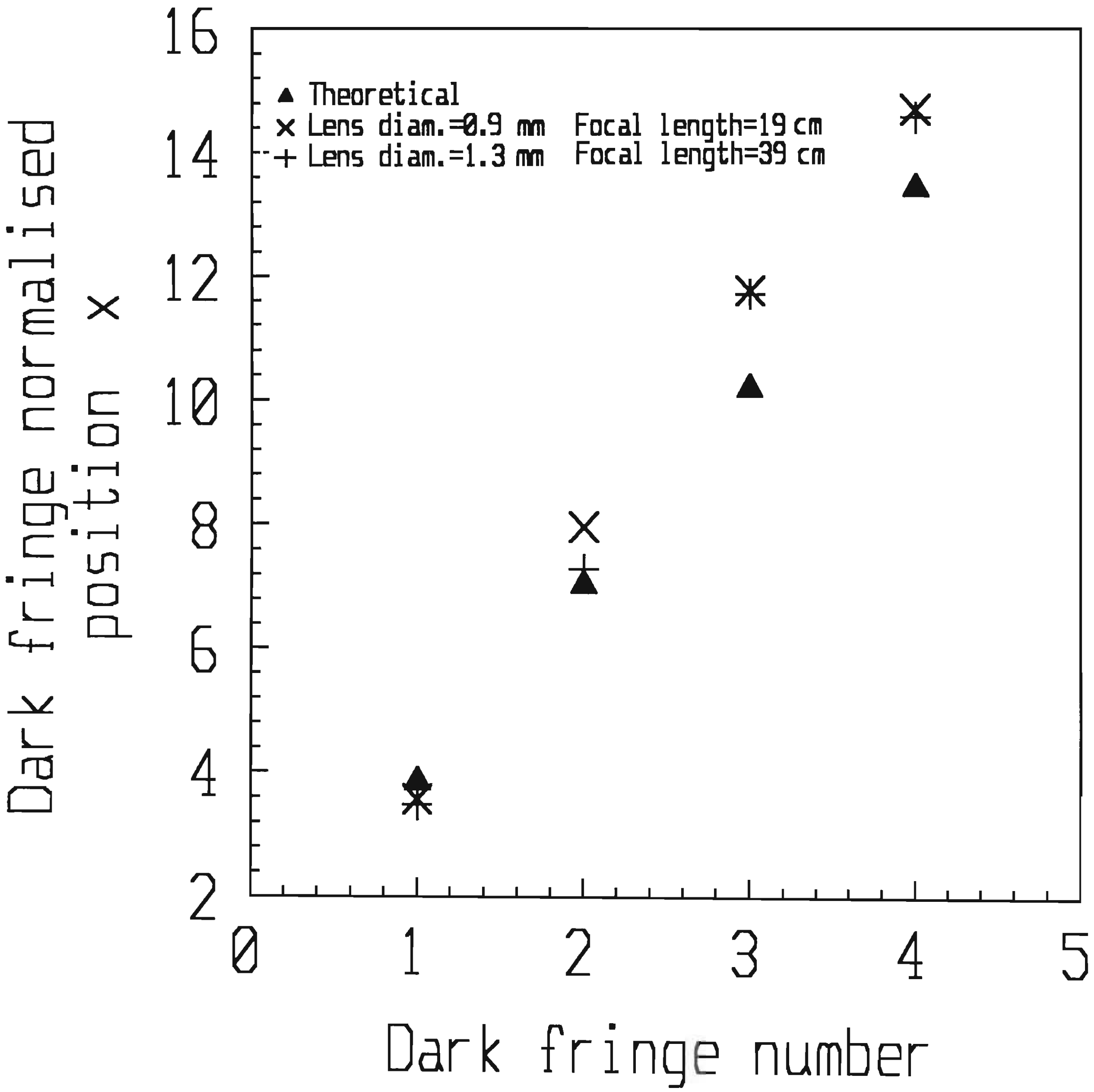

Fig.3.2.9 Comparison with Airy theory. Dark fringe number versus dark fringe normalised position $x = (\pi D d_f)/\lambda f$; d_f = dark fringe position; D,f = Lens diameter, focal length.

3.3 REFRACTIVE INDEX PROFILE MEASUREMENT

After the promising results obtained with a 10mm electrical diameter colliding shock lens presented in the previcus section, a larger version of the CSL was developed. The new version differs from the one shown in figure 3.2.1 in two ways. The first difference is in the dimensions which are larger. The second important feature of the new device is that the arc discharge region is confined inside an enclosed region. In particular we utilised a Plexiglas pipe. The energy is delivered by the arc discharges into shock waves which are now confined inside the pipe. This new CSL design is shown in figure 3.3.1.

As shown in figure 3.3.1 the arc gap is 1.5mm and the Electrical Diameter is 3cm. Due to the larger dimension of the device we were forced to use higher values of the discharge capacitor, between C=20nF and C=100nF. In order to withstand more energy, the new electrodes were made with 2mm steel screws filed down to a conical tip. This new version of the colliding shock lens has been characterised with the experimental set-up described in the previous section. In figure 3.3.2 we present the main results, the time evolution of the focal length and the time evolution of the lens diameter for the capacitor value C=100nF.

In figure 3.3.2 we note that the CSL works up to diameters of 5mm. This diameter starts to be an interesting value for some applications. Given the good performance of this upgraded version of the CSL we decided to measure the refractive index profile to quantify its optical performance and quality. In this experiment we used a Mach-Zehnder interferometer (Paragraph 1.6, figure 1.6.1) and an experimental set-up very similar to the one shown in figure 3.2.2.

The data shown in figure 3.3.2 were obtained with the same experimental set-up as that described in the previous section. consisting of a probe nitrogen laser beam, some imaging optics and a recording camera.

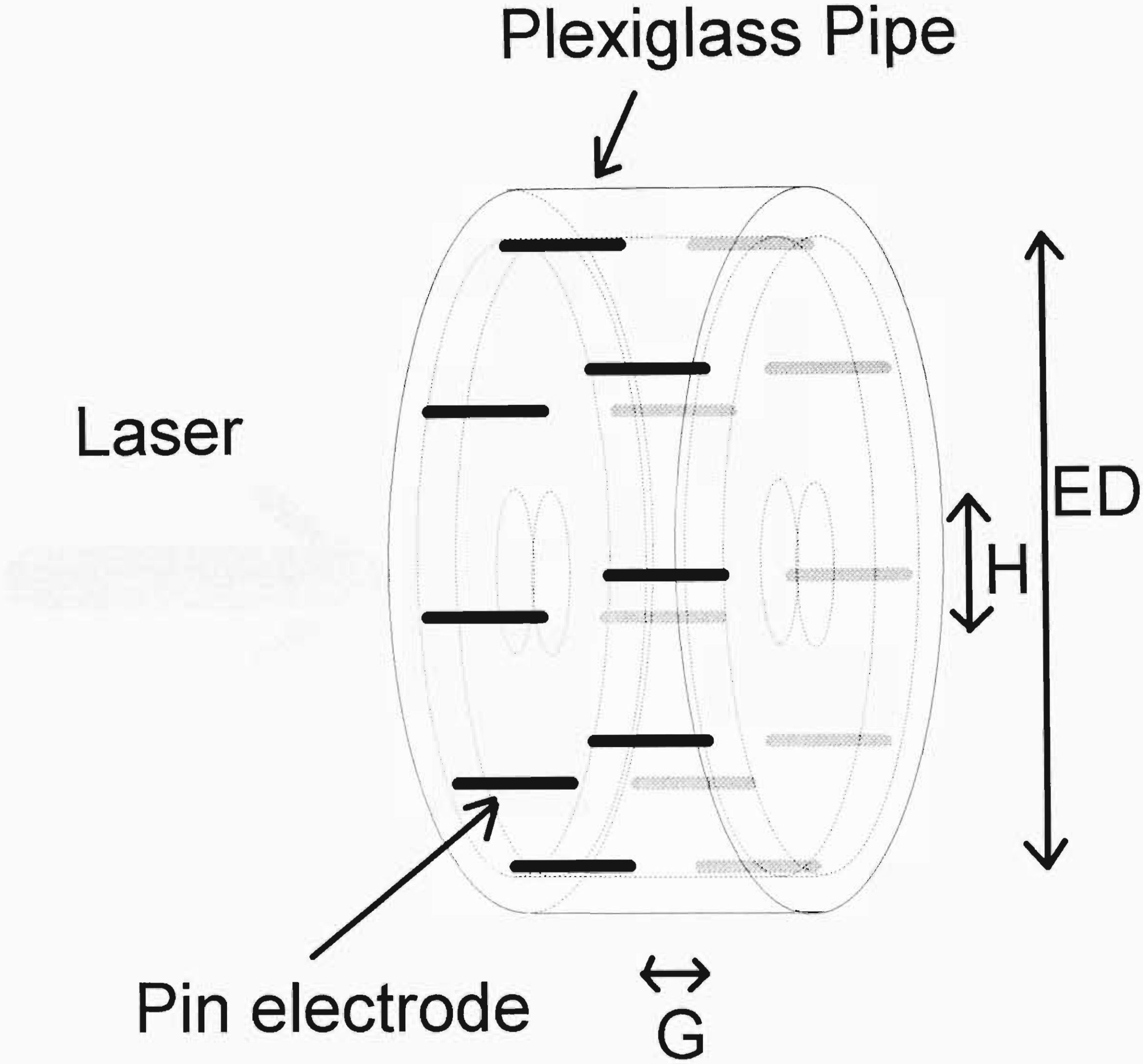

Fig.3.3.1 Enclosed version of the Colliding Shock lens. The arcing circuit is the same as for figure 3.2.1. The component values are: Storage Capacitor C=20-100nF, Pin electrode gap G=1.5mm, Electrical diameter ED=3cm. Hole for the laser beam H=1cm.

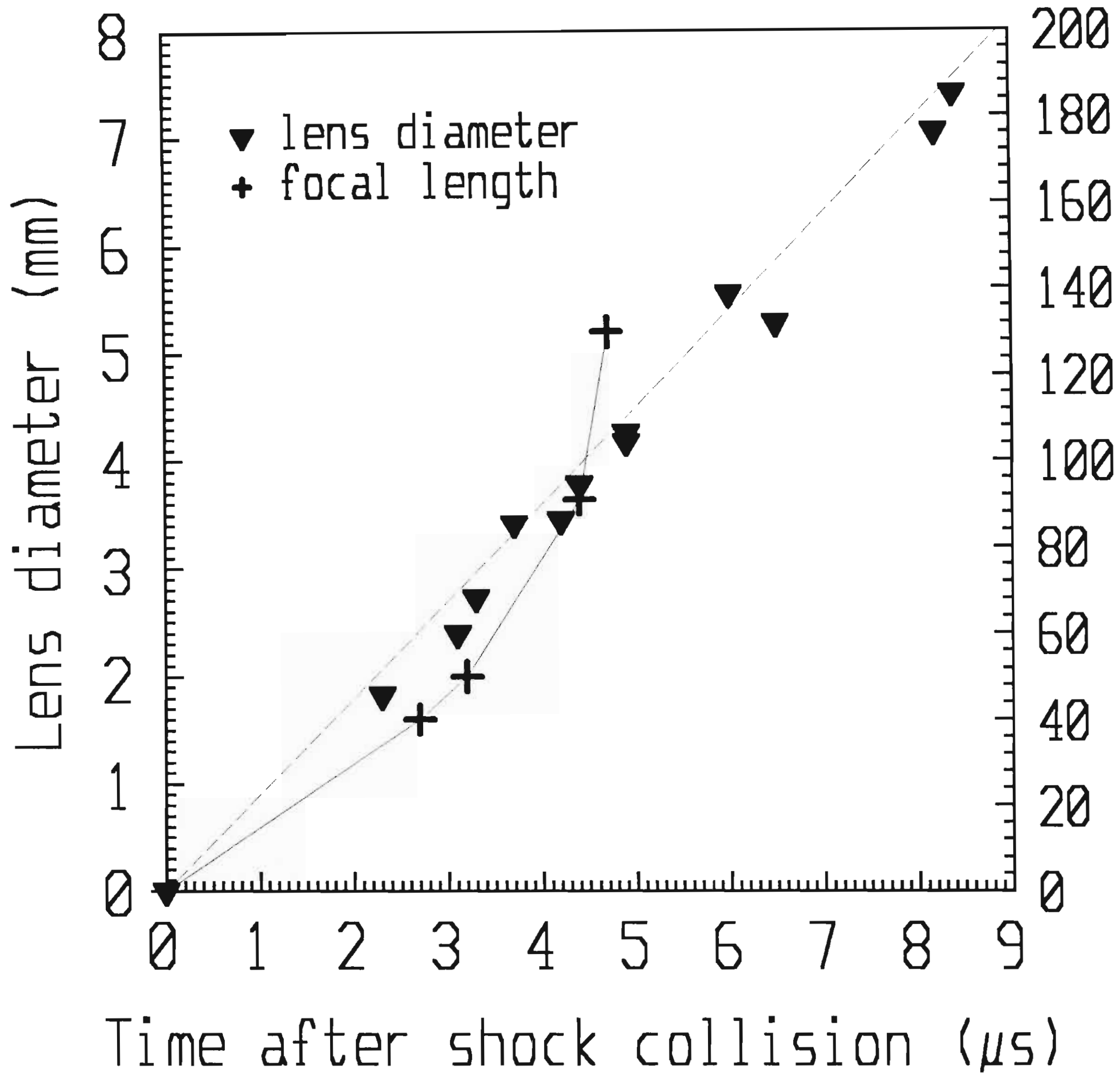

Fig.3.3.2 Enclosed CSL Focal length and diameter vs time after shock collision. C=100nF. The shock collision is 30μs after the arc explosion.

3.3.1 EXPERIMENTAL SET-UP

The Mach-Zehnder interferometer has been described in section 1.6. The CSL was placed in one of its arms, as shown in the next figure 3.3.3.

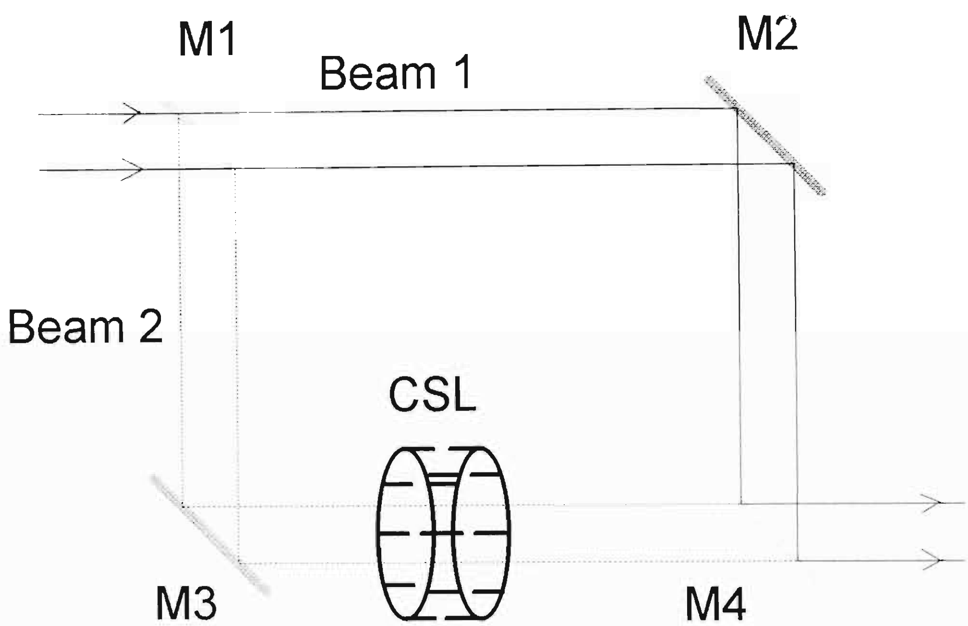

Fig.3.3.3 The Mach-Zehnder interferometer and the CSL.

A schematic diagram of the complete experimental set-up is given in figure 3.3.4. The Nitrogen probe laser is synchronised with the arc explosion of the CSL and the interferograms were recorded on the face plate of a T.V. Camera. The lens L1 allows one to image the shock collision plane. While recording the interferogram, it is necessary to image the collision plane in order to cancel the refractive contribution to the fringes.

The experimental set-up is almost exactly the same as for the experiment discussed in the previous section.

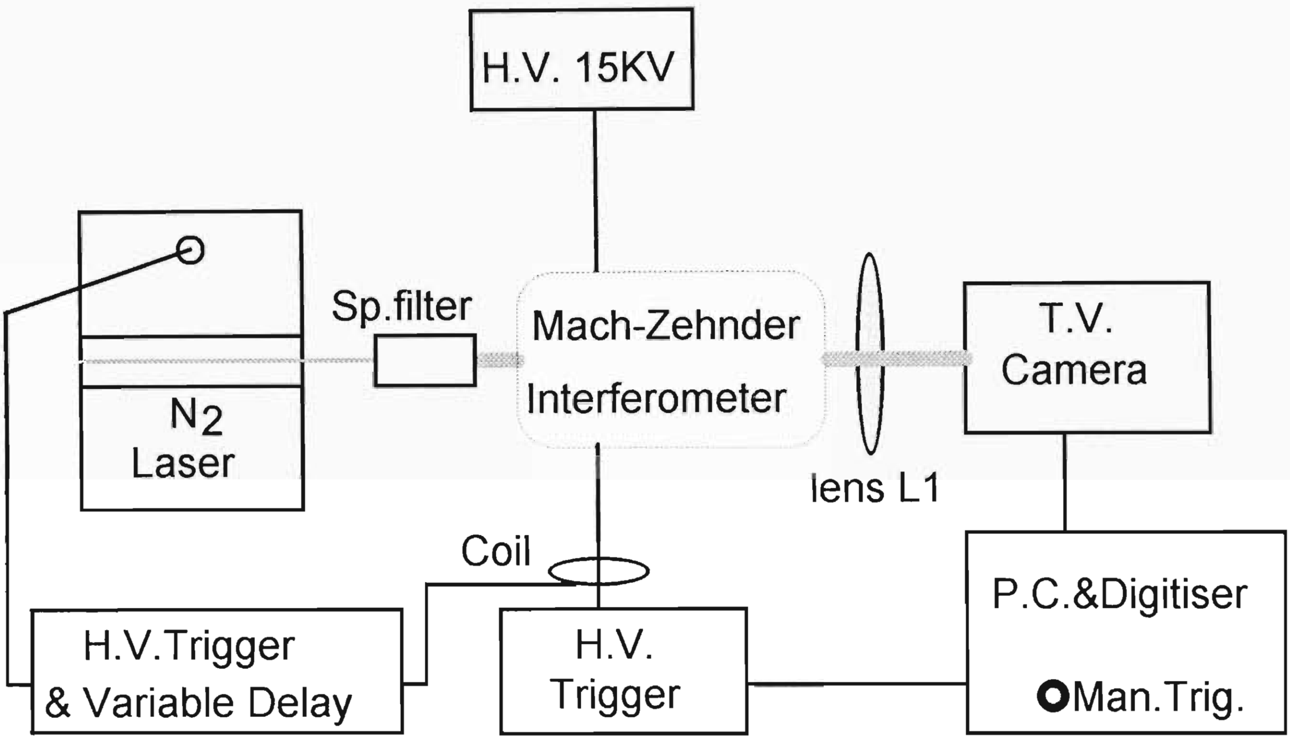

Fig.3.3.4 Experimental set-up for the refractive index profile measurement.

3.3.2 EXPERIMENTAL RESULTS

As described in section 1.6 there are mainly two ways of recording and analysing interferograms. Let us briefly summarise the two procedures.

1) The interferometer is well aligned. When no phase object is present (in our case the CSL is not fired) no fringes are visible over the whole imaged field. When we insert the phase object (we fire the CSL), it introduces a phase shift and creates a pattern of bright and dark fringes on the screen. Each dark-bright period corresponds to a relative phase change of 2π. This technique allows the experimenter to measure the exact value of the phase unless it exceeds 2π. There is no way of deciding if the "next" dark-bright period is due to a phase increase or a phase decrease.

2) The interferometer is "misaligned" in order to create a regular pattern of straight fringes over the imaged field. In this case the relative phase of the two beams increases linearly in the direction perpendicular to the fringes. The presence of the phase object will bend each fringe by an amount proportional to the phase change. This technique gives a better measurement of the value of the phase. Since we follow the shifts of the fringe maxima or minima, the spatial resolution is typically of the order of half the separation between unperturbed fringes.

In our experiment we utilised the second technique. In figure 3.3.6 we show a reference shot. The unperturbed fringe pattern is visible in this picture where the shocks have not yet arrived. In the next four images 3.3.7-3.3.10 we can follow the eight shocks during their collisions.

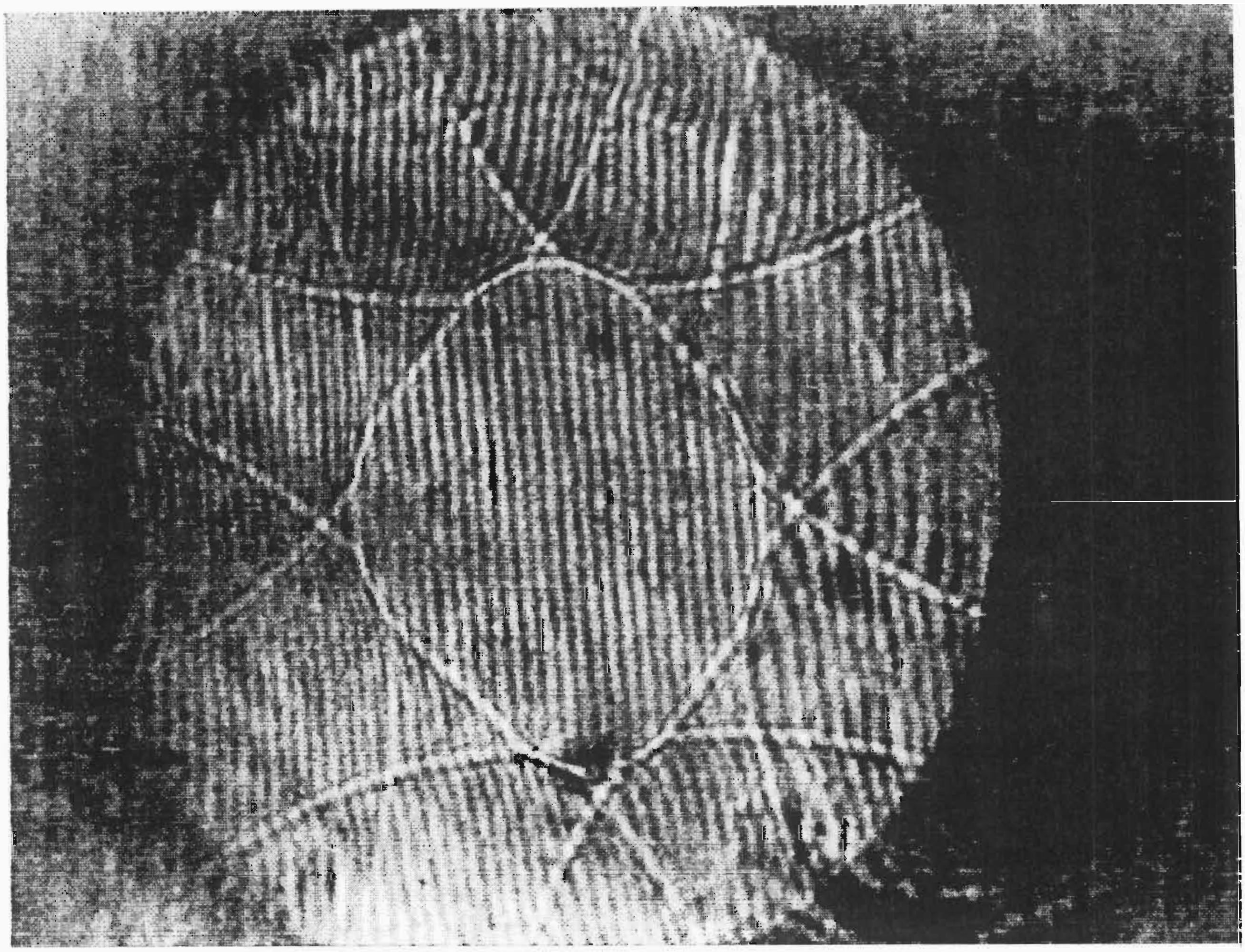

Fig.3.3.6 Reference shot, before shock collision. Delay=28.8μs after arc explosions.

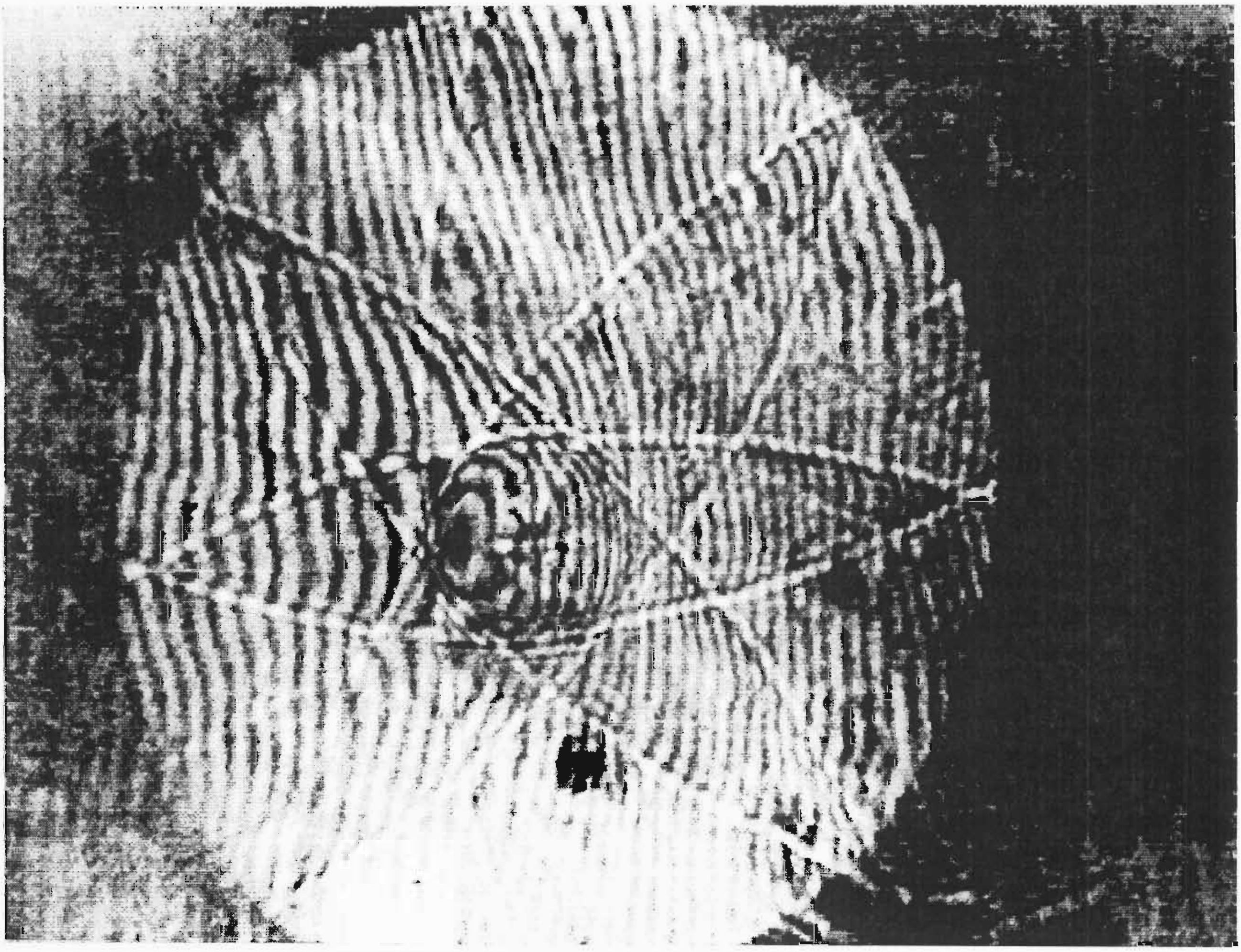

Fig.3.3.7 CSL interferogram. Delay=36.1μs.

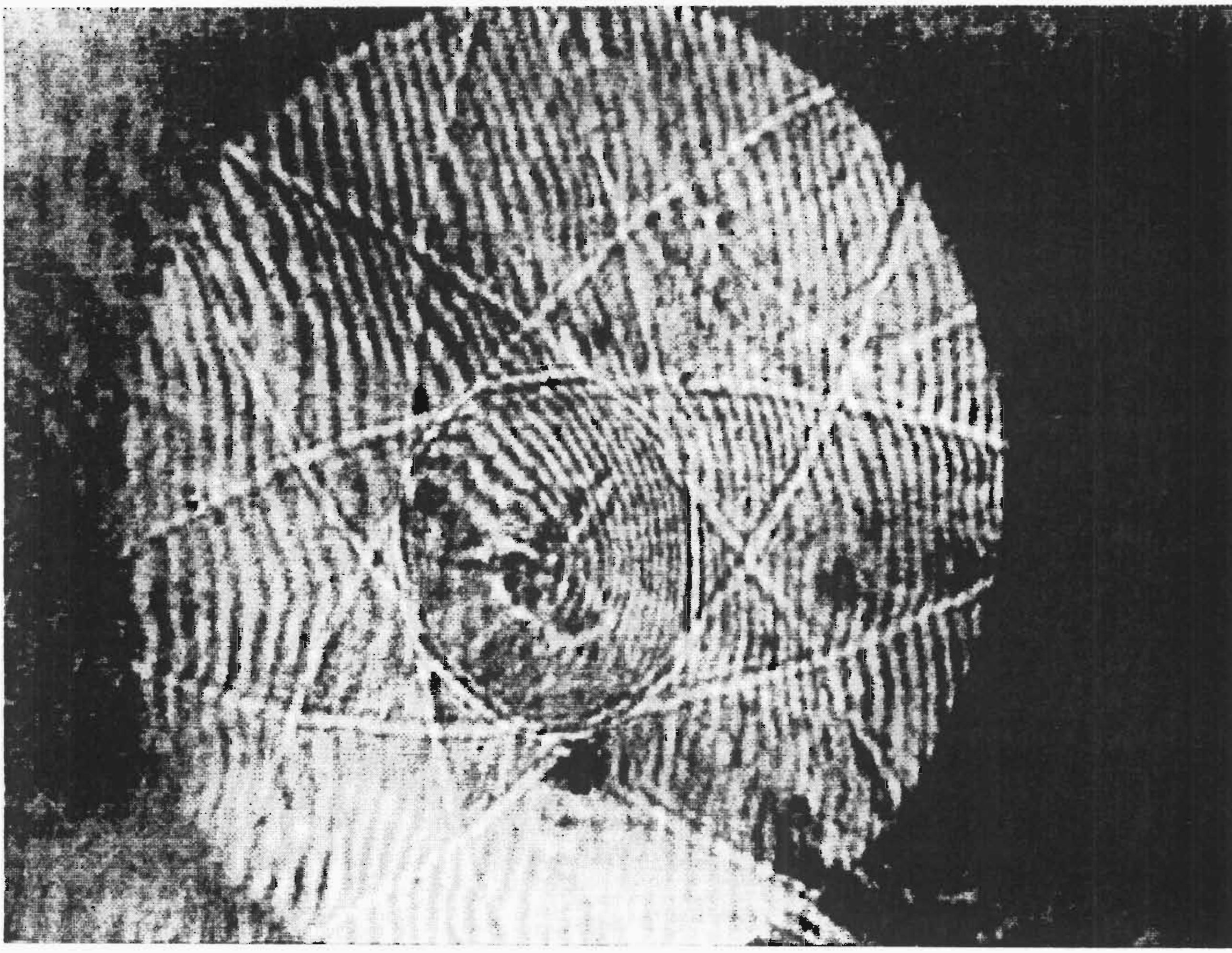

Fig.3.3.8 CSL interferogram. Delay=36.7 μs

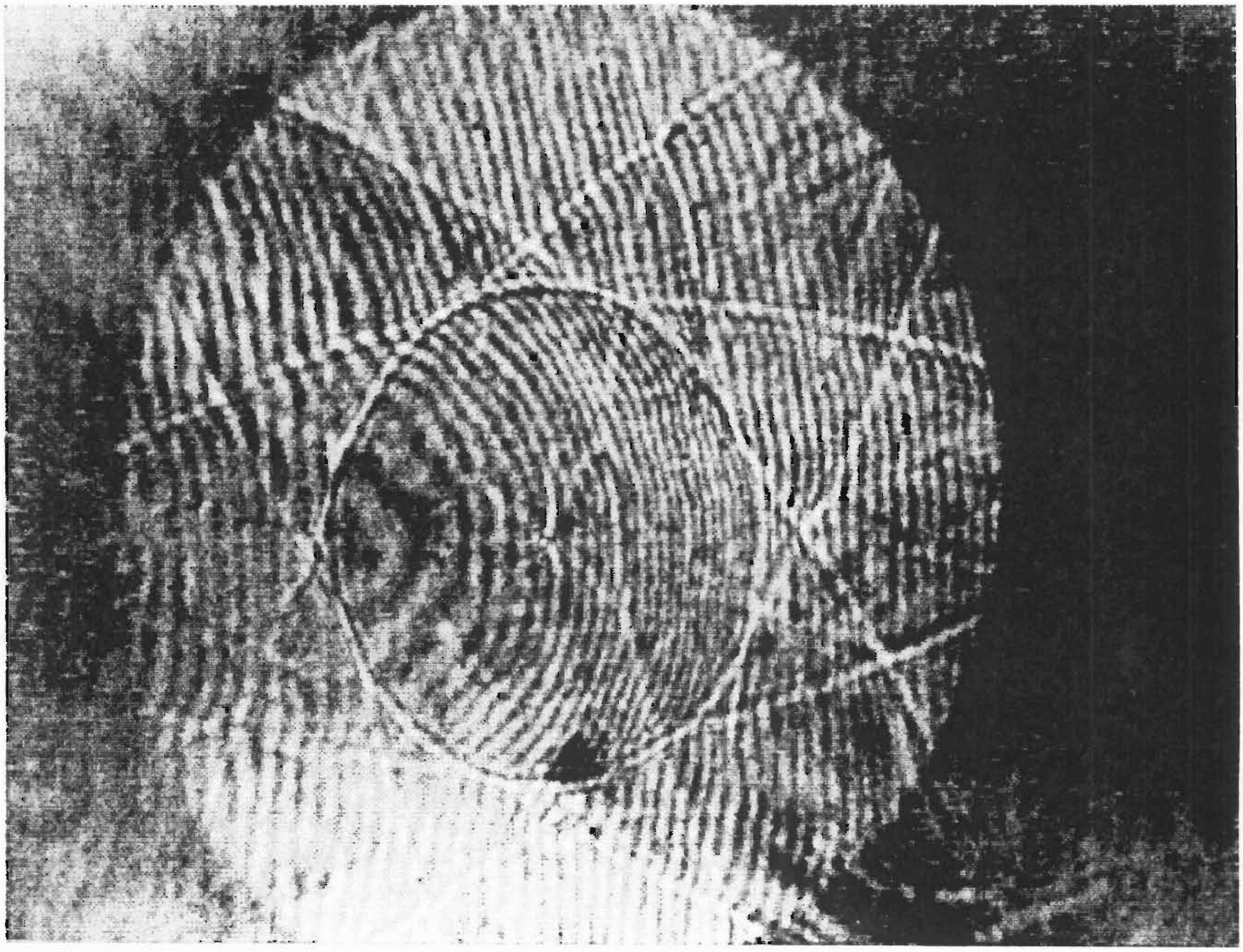

Fig.3.3.9 CSL interferogram. Delay=38.2μs.

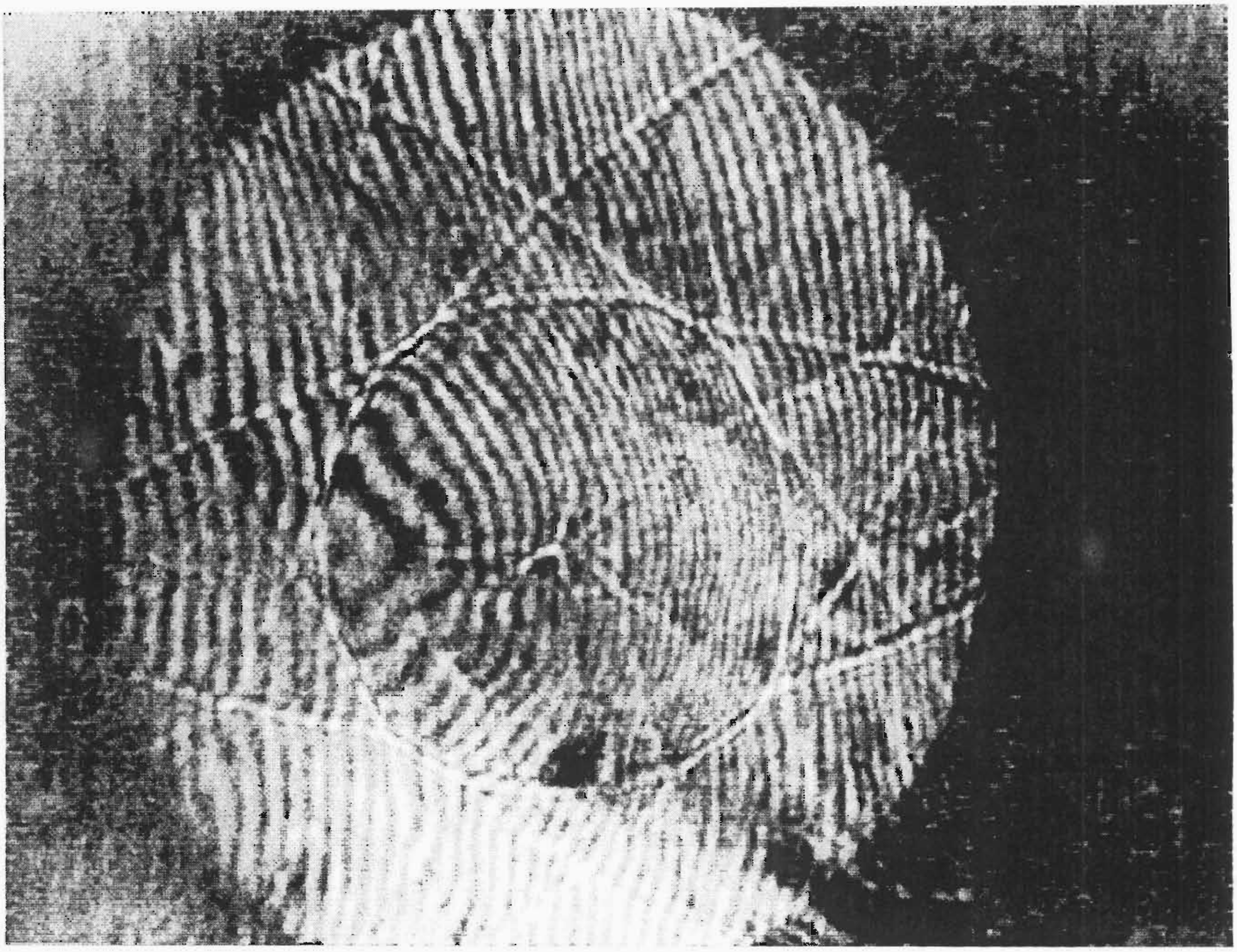

Fig.3.3.10 CSL interferogram. Delay=39.0μs.

To be exact we cannot extract from the interferogram the three-dimensional refractive index profile without any hypothesis about its spatial symmetry [Bockasten 1960].
Since in the shock collision region we expect a rather complex spatial density distribution, we cannot determine the complete three-dimensional refractive index profile. However, for the optical analysis of the device, the interesting quantity to measure is the two dimensional (planar) distribution of the 'optical path length' on the shock collision plane. Once this quantity is known we can quantify the optical quality of the CSL and no further information on the density profile is required.
Let us explain this point with the help of graphs and formulas. The radial density profile of a single expanding spherical shock wave has been measured by several authors [Waltham 1985, Michaelis A 1991]. We can briefly summarise their results in the profile shown in figure 3.3.11.
The typical linear scale of the shock-front is around 100μm, depending on the mach number M_0 and on the type of gas.
If the shocks were passing unperturbed through each other, we would expect the geometry shown in figure 3.3.12. Despite the non-linear interactions, the geometry will be rather similar as it can be seen in the interferograms in figures 3.3.6-3.3.10.
We image the shock collision plane with the lens L1 onto the face plate of the camera where we introduce the coordinate system (x1,y1). The interferogram appears as an almost periodic pattern of dark and bright fringes. We analyse them in the following way. Given a point of the image plane where the fringes are bent, we move along the locus of points having the same intensity until we get to the region where the fringes are straight. In other words we follow the fringe until we get to the unperturbed region. At each point, the distance of our trajectory from the straight fringe (and perpendicular to it), divided by the width of the unperturbed fringe, gives the phase difference in 2π's.

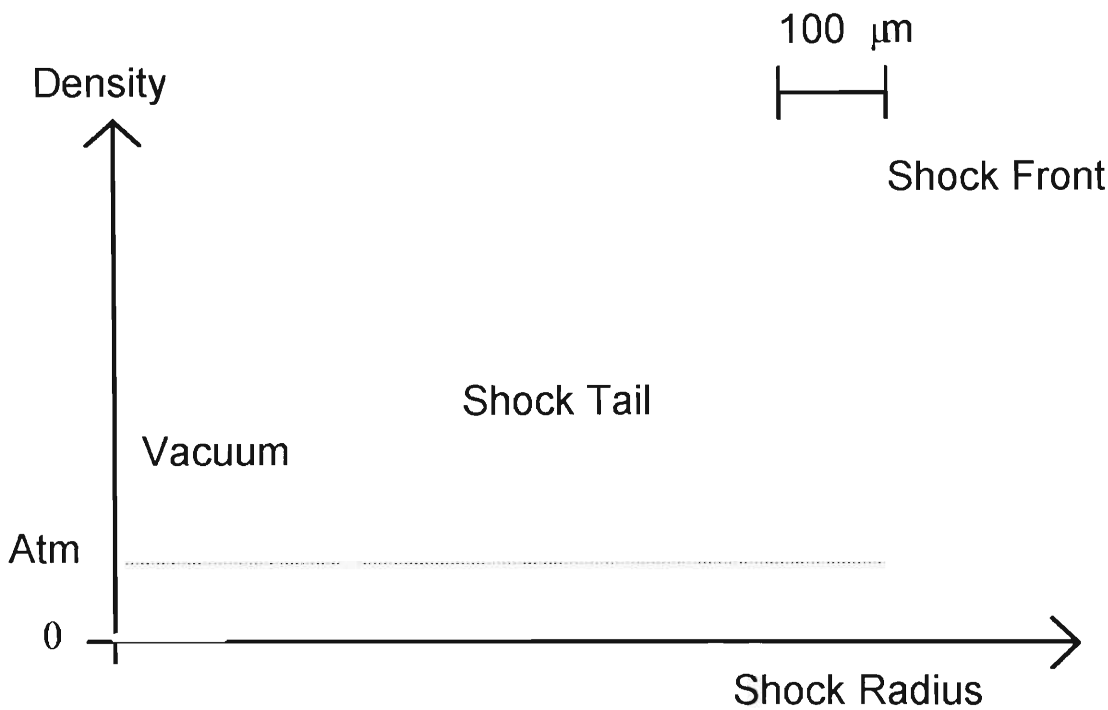

Fig.3.3.11 Geometry of an expanding shock wave. The typical spatial scale of sharp density gradients is in the range of 0.1mm.

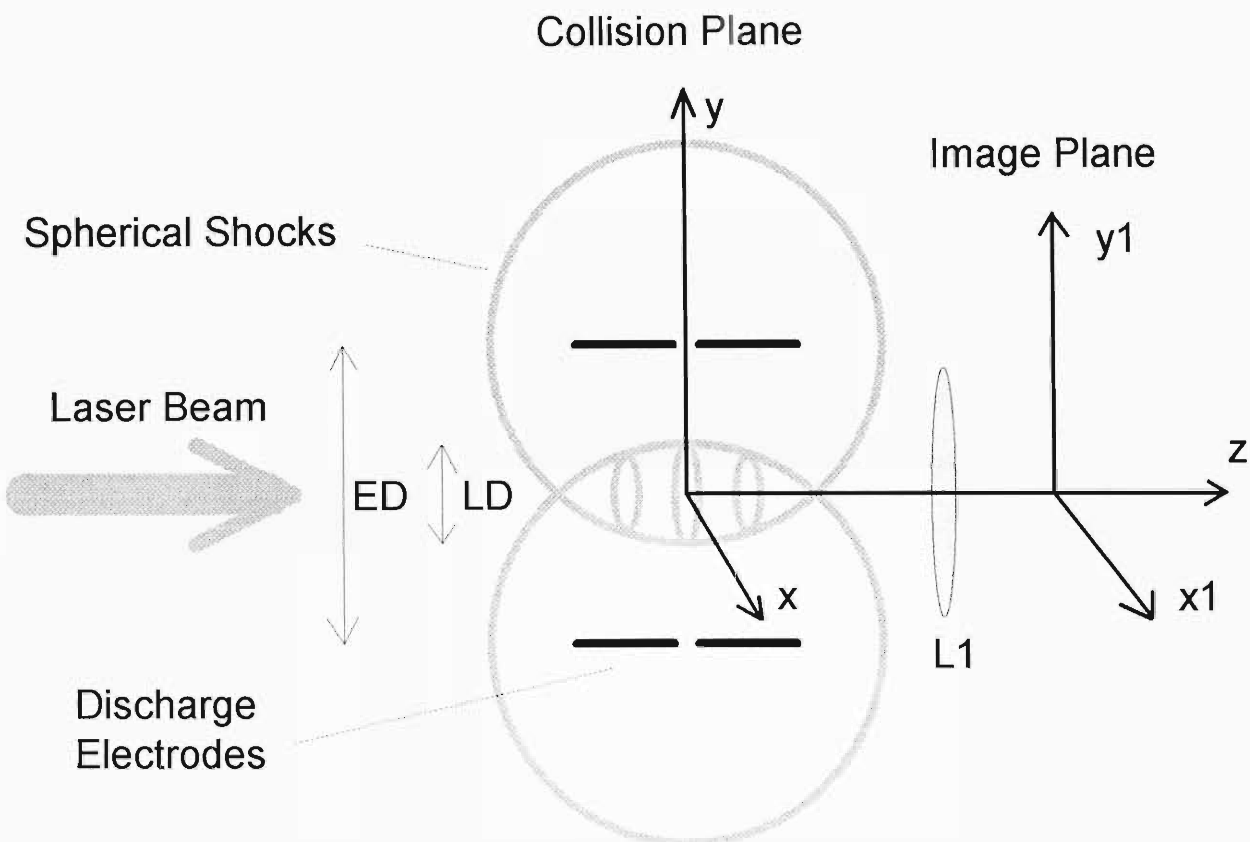

Fig 3.3.12 The Colliding Shock Lens geometry. Electrical diameter ED=3cm; Lens Diameter LD=0-5mm.

In practice we can follow the fringe without errors only where it is darkest or brightest, and this limits the spatial resolution of the measurement to half of the fringe spacing. As a result, at each point **x,y** we measure the following quantity:

$$\tilde{n}(x,y) = \int_0^{L(x,y)} n(x,y,z)\,dz \qquad 3.3.1$$

Where **z** is the optical axis (and the laser beam) direction and **L(x,y)** is the distance travelled at **x,y** inside the colliding shock region. Since after the central collision the shock front is cylindrically symmetric with respect to the optical axis.

$$\tilde{n}(r) = \int_0^{L(r)} n(r,z)\,dz \qquad 3.3.2$$

According to geometrical optics and under the paraxial ray approximation, the deflection angle for a light ray travelling at X,Y will be:

$$\vartheta(r) = \int_0^{L(r,z)} \frac{\partial n(r,z)}{\partial r}\,dz \qquad 3.3.3$$

We use now the very reasonable hypothesis that rays do not change their position **r** while they travel inside the CSL, which is fully justified given the lens diameter and focal length which are in play (figure 3.3.2). Since r does not change along the trajectory, which is the integration path, we can say that:

$$\vartheta(r) = \frac{\partial}{\partial r}\int_0^{L(r)} n(r,z)\,dz = \frac{\partial}{\partial r}\tilde{n}(r) \qquad 3.3.4$$

In conclusion, under these rather general conditions, the Optical Path Length ($\tilde{n}(r)$) can be directly measured from the interferograms and then linked to the optical quality of the device.

3.3.3 ANALYSIS OF THE EXPERIMENTAL RESULTS

In this paragraph we will briefly analyse the four interferograms shown in figures 3.3.7, 3.3.8, 3.3.9 and 3.3.10. The fringe analysis is performed as described in paragraph 3.3.2 and the optical path lenght radial profile and lens optical diameter are determined.

Then the optical prformances of the colliding shock lens can be computed from the OPL radial profiles. Chapter 5 will be completely dedicated to this further analysis. In this paragraph we will determine only the OPL radial profiles.

The reader can refer now to figures 5.1.5 to 5.1.8 for the focal lenght radial profile.

The four 'Optical Path Length' (OPL or $\tilde{n}(r)$) profiles are shown below in figures 3.3.13 to 3.3.16 together with the relative polynomial fits. One problem of the measurement is that the fringes can undergo a big shift as they cross the shock-front which expands after the collision. If the phase jump is more than 2π on the spatial scale of a few pixels we see a discontinuity. In this case we can determine only the relative value of the OPL inside the region enclosed by the expanding shock-front. Though, as seen in equation 3.3.4, the interesting quantity to use to define the optical quality of the CSL is the radial gradient of the OPL, which is insensitive to such uncertainty.

In table 3.3.1 we report the values of the polynomial coefficients for the fits of the OPL profiles. In table 3.3.2 the radial dimension of the CSL is reported at the corresponding times. Due to the radial symmetry, only the even terms are different from zero.

Time	a_0	a_2	a_4	a_6	a_8
2.1μs	2.33e-6	1.07	-6.23e6	9.88e12	-5.61e18
2.7μs	3.33e-6	-1.23	1.72e5		
4.1μs	3.67e-6	-0.47	1.21e4		
5μs	3.44e-6	-0.21	-7.41e3		

Table 3.3.1 Polynomial fit coefficients of the OPL profiles at the various interferograms recording times after the shock collision.

Time	Radius
2.1μs	0.81mm
2.7μs	1.4mm
4.1μs	2.1mm
5μs	2.4mm

Table 3.3.2 CSL radius vs Time.

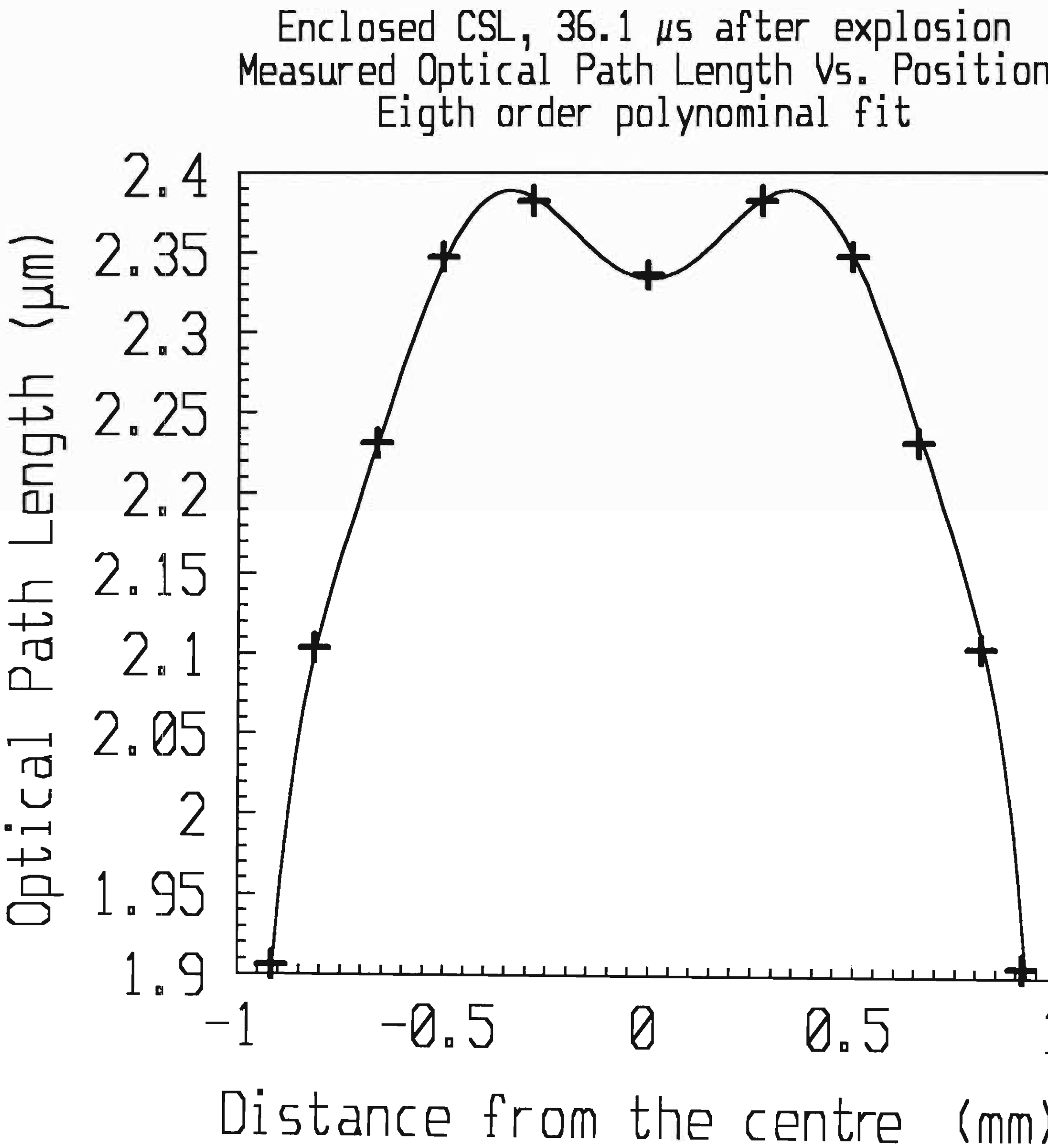

Fig.3.3.13 OPL radial profile just after collision. From the interferogram shown in fig.3.3.7.

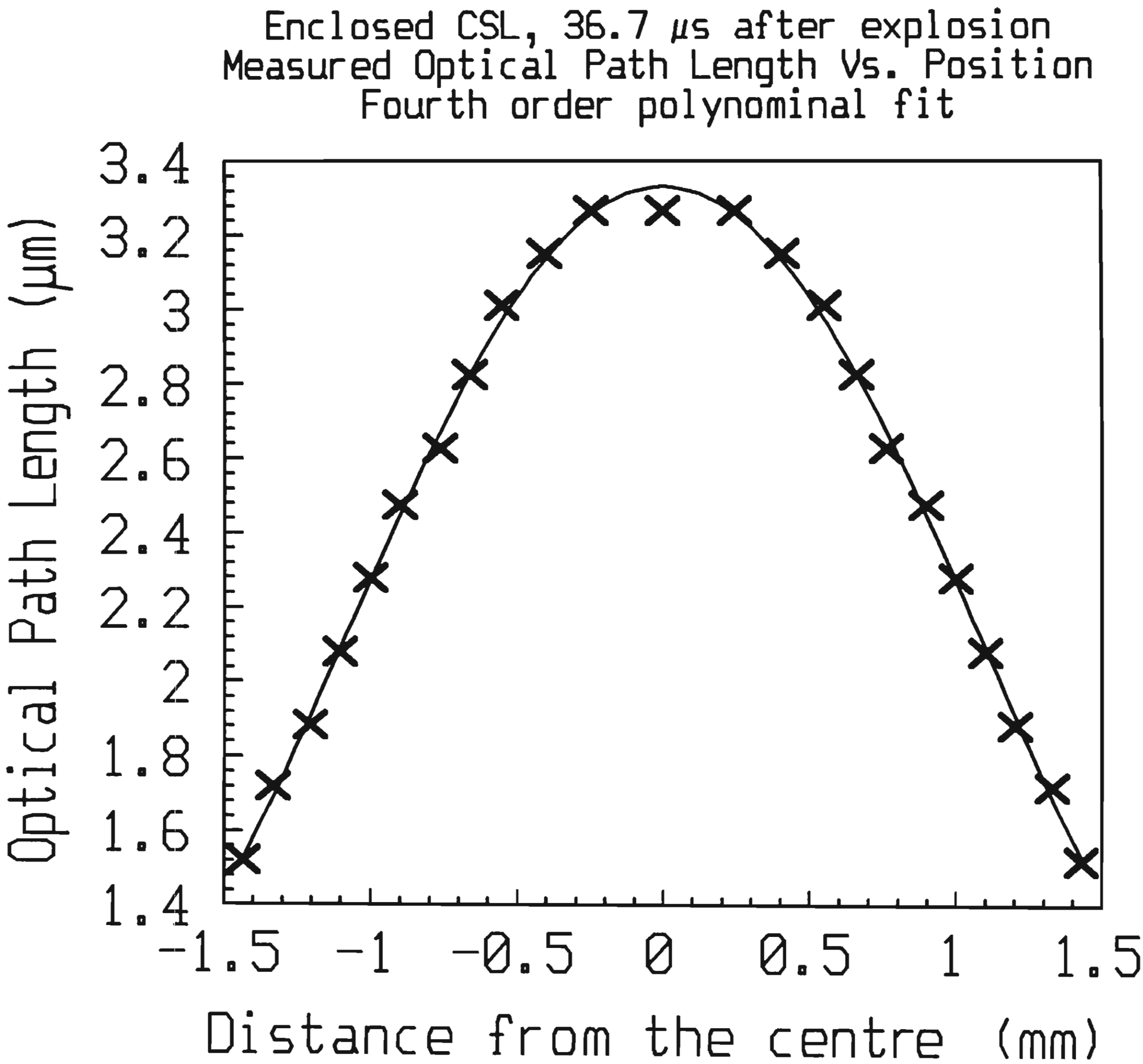

Fig.3.3.14 OPL profile from the interferogram in fig.3.3.8

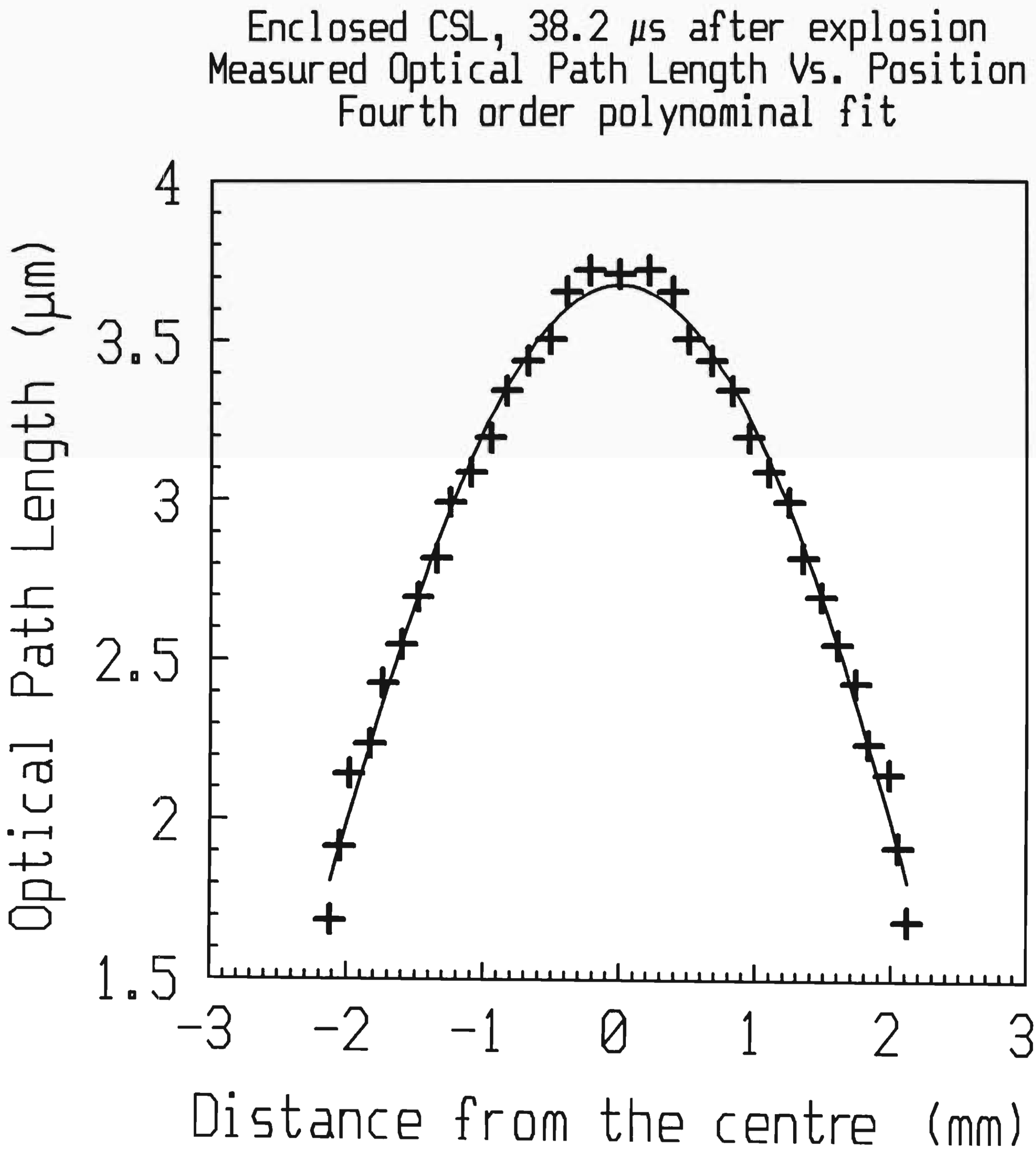

Fig 3.3.15 OPL profile from the interferogram in fig.3.3.9.

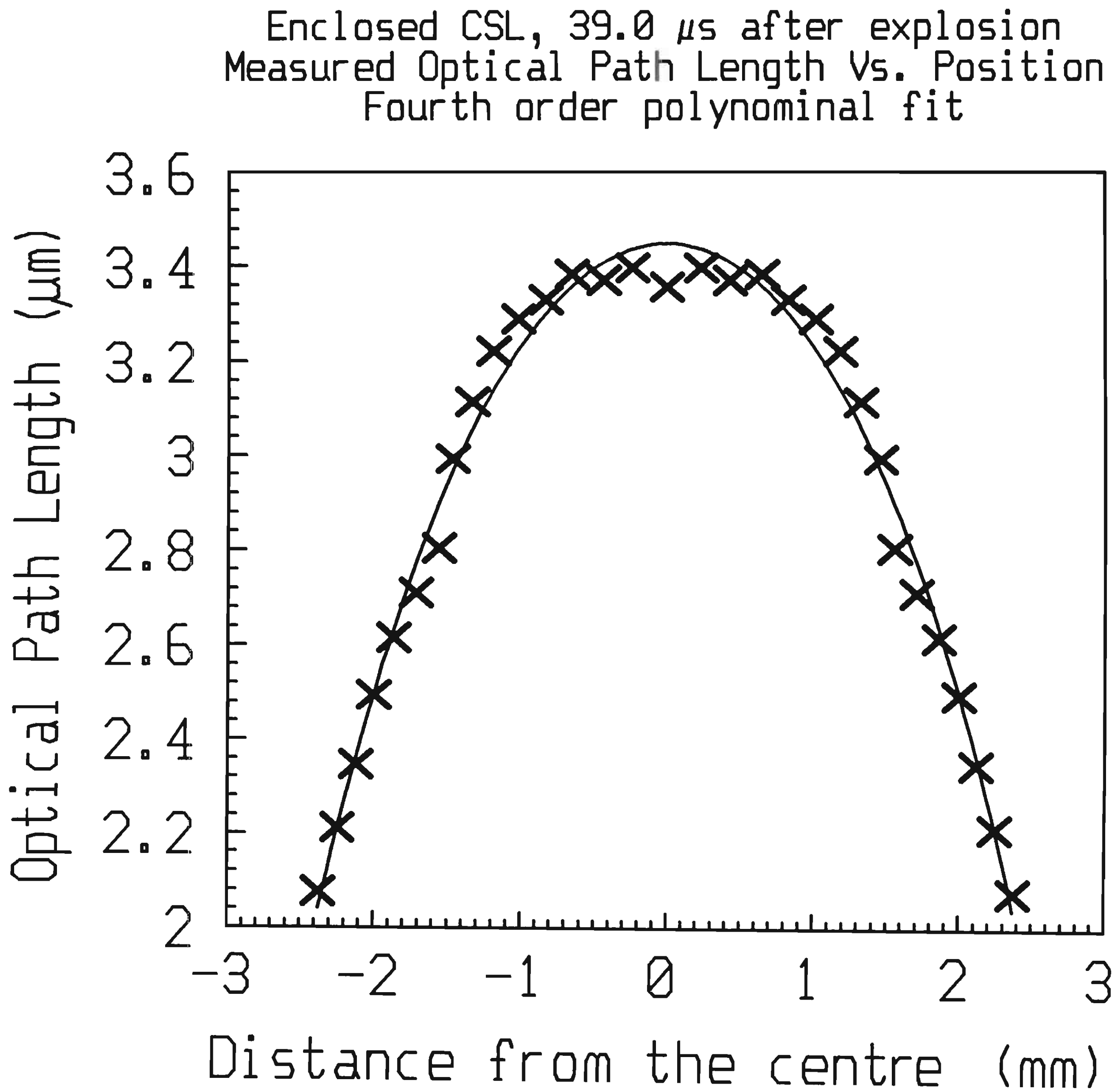

Fig 3.3.16 OPL profile from the interferogram in fig.3.3.10.

3.4 APPLICATIONS OF THE COLLIDING SHOCK LENS

In the last section of this chapter we propose and discuss some of the possible applications of the CSL [Michaelis 1994]. The operation of the CSL as an optical switch will be treated in detail. The time evolution, scaleability and repetition rate operation are investigated. This section is divided into two parts: a characterisation of the CSL as an electro-optical switch and a list of potential applications suitable for the CSL.
As previously stated, it is important to distinguish between the electrical diameter ED being that of the circle of arcs and the optical aperture (the lens diameter LD), being that of the effective lens (figure 3.3.12). The optical aperture turns out to be an order of magnitude smaller than the electrical diameter. It is not yet clear whether the optical aperture will scale with the system geometry or with the typical shock width dimensions. The former would mean that the f-number could remain more or less constant with increasing optical aperture; the latter, that it does not scale at all. A first attempt at scaling up the first 1.1cm electrical aperture device to 3cm, (figure 3.3.2) indicates that the truth lies somewhere in between.

3.4.1 THE COLLIDING SHOCK LENS AS A SWITCH

We have measured the CSL switching ability. Our experimental apparatus (depicted in figure 3.4.1) is very simple and consists of a 10 mW HeNe laser followed by the small CSL (figure 3.2.1) and a receiving photodiode at a distance L with a pinhole of diameter Φ immediately in front of it. The HeNe laser beam was spatially filtered and expanded.
We vary the distance L, the diameter Φ and also the energy delivered to the shocks by changing the discharge capacitor (C in figure 3.2.1). On a digital oscilloscope we read the trace of the photodiode signal. Figure 3.4.2 shows a typical switching time curve. The pinhole diameter is here $\Phi=300\mu m$, $L=40cm$ and $C=5nF$.
The voltage output of the oscilloscope has been normalised to a comparable but arbitrary constant signal. We chose the voltage signal read when focusing the HeNe laser beam with a 3mm aperture, 50cm focal length, plano-convex glass lens on the same photodiode and a pinhole $\Phi=250\mu m$.

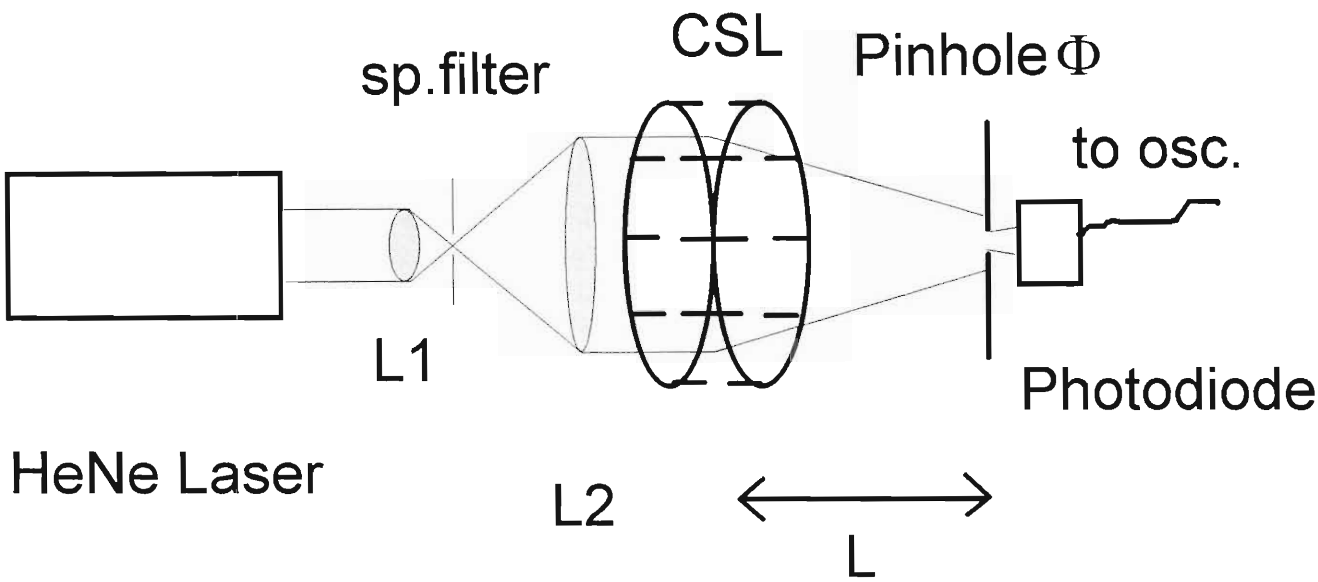

Fig 3.4.1 Experimental set-up. Measuring the CSL switching performances. L1=3cm, L2=15cm.

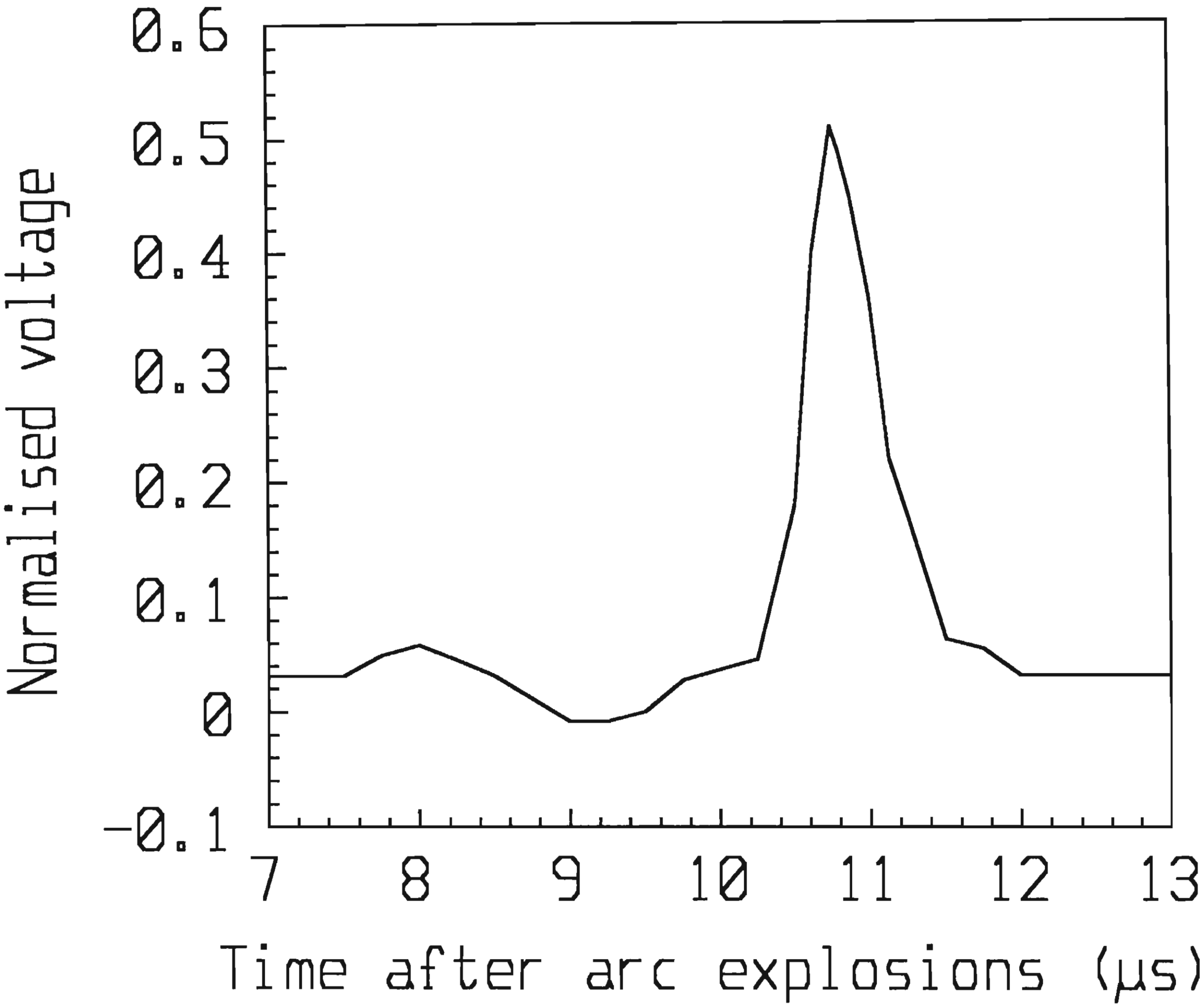

Fig.3.4.2 Normalised photodiode voltage during switching. C=5nF, F=300mm, L=40cm. (typical trace)

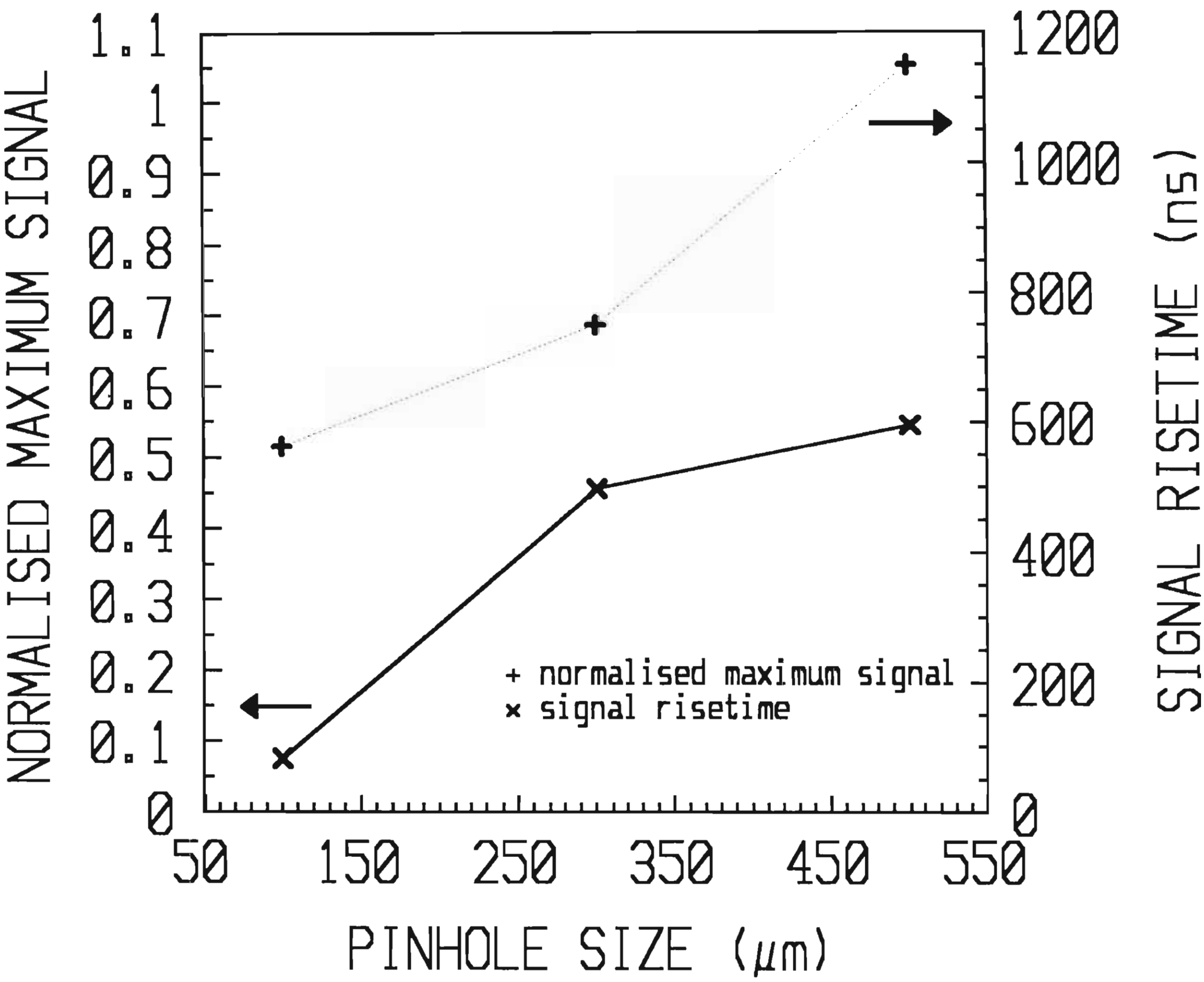

Fig.3.4.3 Small CSL C=1nF. Switching vs Pinhole size.

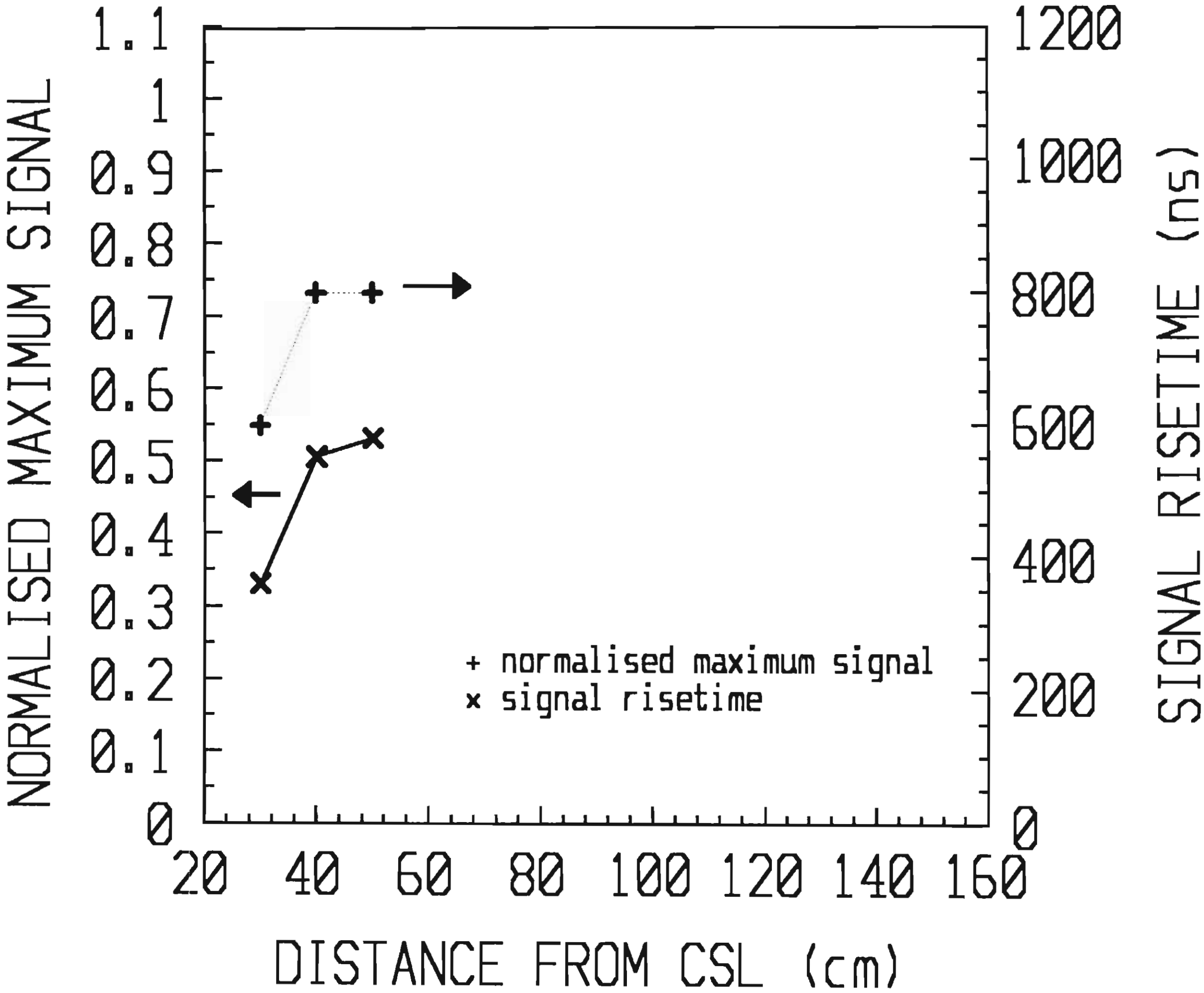

Fig.3.4.4 Small CSL, C=1nF. Switching vs Distance L.

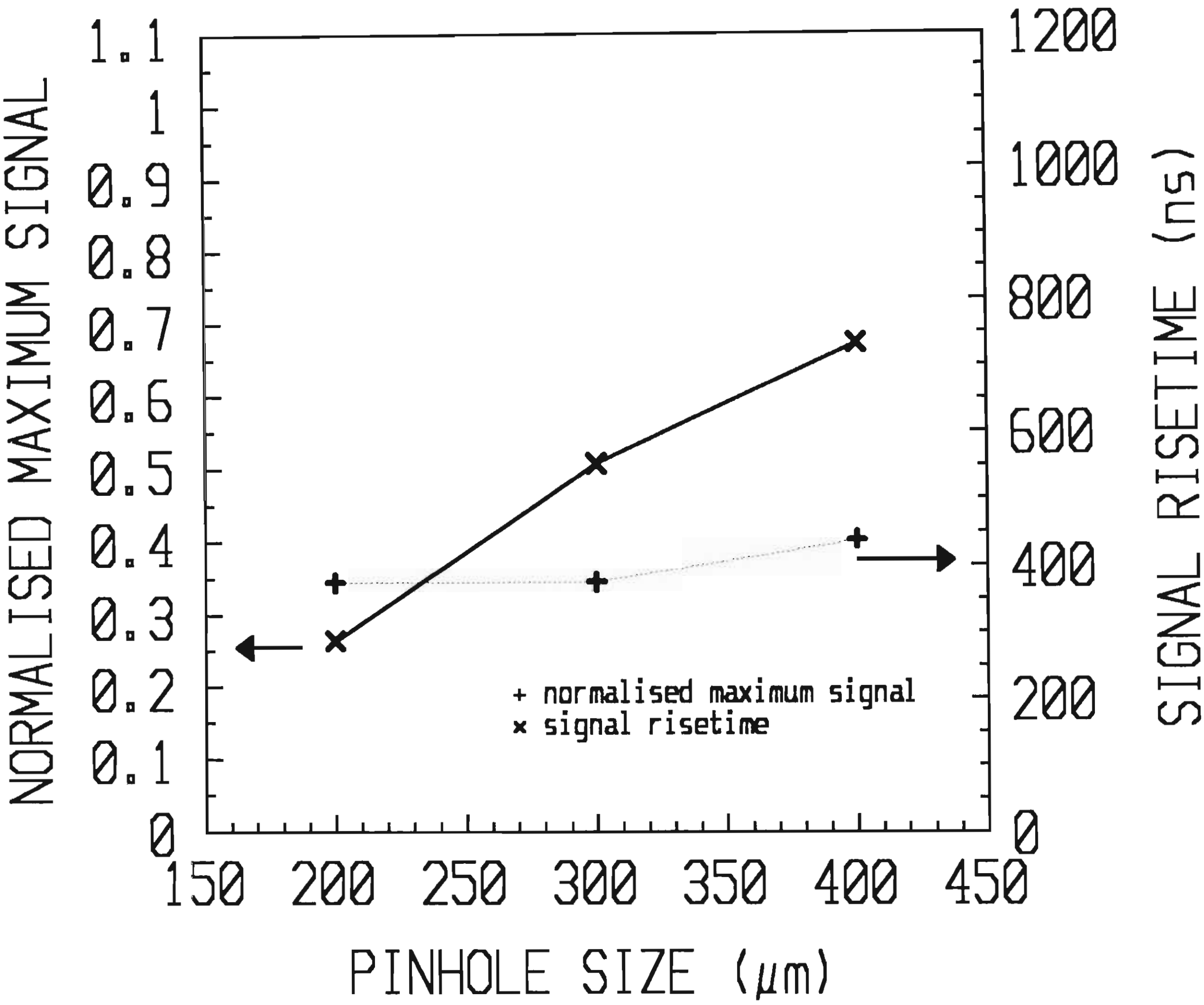

Fig.3.4.5 Small CSL, C=5nF. Switching vs Pinhole size.

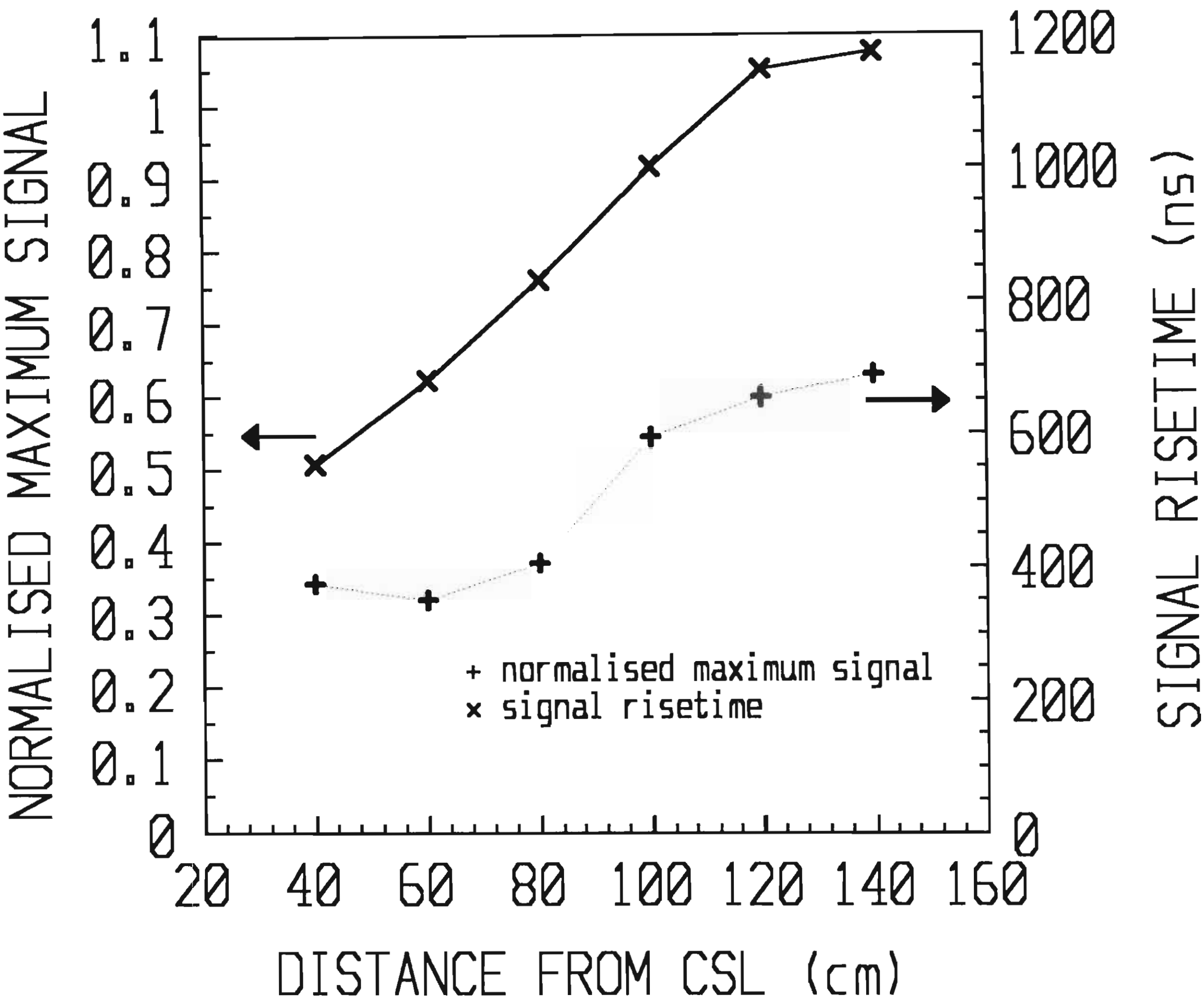

Fig.3.4.6 Small CSL, C=5nF. Switching vs Distance L.

Starting with a capacitor value of 1nF. In figure 3.4.3 we show how the switching risetime and the maximum signal vary with the pinhole size Φ at a fixed distance L. In figure 3.4.4, how the same quantities vary with the focal length L at a fixed Φ.
In figure 3.4.5 and 3.4.6 we repeat the last measurements with a discharge capacitor of 5nF.
As can be seen from switching curves like figure 3.4.2, the fall-time of the signal is always comparable with the rise-time (to within say 50%), the latter being a less critical quantity for an efficient quality switching of a laser cavities (Q-switching). As we expected, by increasing the shock energy we can make the switching faster. Though if one compares figures 3.4.4 and 3.4.6 we see that the increase in shock energy impairs the optical quality of the CSL at short focal length and small optical diameter.

3.4.2 POTENTIAL APPLICATIONS

a. Drilling, cutting and welding.
A good reason why lasers have not penetrated every industrial workshop is that their output windows and lenses are expensive and sensitive devices. It has already been shown that CO_2 lasers coupled to gas lenses are capable of drilling through thick steel sheets [Michaelis E 1991]. However, the lenses that were used were unwieldy CW devices with very long focal lengths (of order 1m). The "dream" gas lens for this purpose would be a short focal length device (10cm), capable of being "rep-rated" (100Hz.), with an optical aperture of at least one centimetre and a minimal power consumption and a minimal weight.
b. Q-switching and laser intracavity operation.
The combination of a pulsed lens (CSL) and a CW lens, (such as a conventional glass or gas lens) in a laser resonator could in principle perform simultaneously the Q-switching and the mode selection of the laser oscillation [Lisi 1994]. In the previous paragraph we characterised the CSL as a switch and opening times of about 0.5μs were obtained. Q-switching requires that the cavity losses decrease on the time-scale of 10's or 100's of ns [Siegman 1986]. Such switching performances can be achieved with the colliding shock lenses. In the next chapter we will demonstrate the feasibility of the CSL Q-switching.

For engineering applications (point a), the focal length should not vary too quickly, whereas for Q-switching and beam handling (e.g. optical isolator) functions, fast switching is essential.

c. Ultra high power and "all gas" lasers.

It is well known that even under clean room conditions lenses operating for pulse lengths of tens of nanoseconds start to fail at intensities in the GW/cm^2 range. Also multi-photon processes at ultra-high intensities render conventionally transmitting materials opaque or absorbing. We have previously pointed out that gas lenses could help alleviate these problems. We foresee, without having the means to observe it, that very high intensities will ionise the gas in the shock front region. This laser shock interaction might create a plasma that destroys the optical quality of the CSL, though those damages do not cumulate such as on the surface of a solid state lens. But for intermediate powers, the CSL could fill the present gap. The final application we envisage is that of an "all gas" (or nearly all gas) system. Conventional pulsed gas laser systems are designed with beam diameters corresponding to the breakdown thresholds of solid optical components. A combination of aerodynamic windows, diverging and converging gas intracavity elements could give gas laser design a new degree of freedom.

3.4.3 SUMMARY OF CSL PERFORMANCES

All the applications listed above pose the following questions:

a. How good is the focus? Is it near diffraction-limited?

b. How short is the focal length?

c. How large is the aperture and is any light lost?

d. Can they be "rep-rated"? How much power do they consume?

a. From the very first experiments, we realised that this was somewhat surprisingly, given the limited number of arcs, an excellent lens. In figure 3.2.5 we showed the relative intensity plot of a typical focus of the small CSL. In figure 3.2.6 and following, the optical performance of the same device is analysed.

b. The shortest focal length for an eight arc device is about 20cm. This is too long for many applications.

c. Possibly the worst feature of CSL's is the large electro-optic aspect ratio. The largest aperture obtained so far was only about 5mm. In the future we plan to test a 10cm electrical diameter lens in the hope of obtaining a 10 mm. optical aperture.

d. The question of "rep-rating" the lens has only been partially answered experimentally for want of a suitable high voltage power supply. 10Hz operation confirmed our expectations that the lens could run at moderate frequencies without degradation of the focus. At this repetition rate a typical switching curve such as that in figure 3.4.2 remains virtually unaltered. Based on dimension and speed of sound arguments, we would expect the limiting period to be of order:

$$\frac{\text{Electrical Aperture}}{\text{Sound Speed}} \approx 1\text{ms}$$

The corresponding "rep-rate" would be 1kHz, a useful frequency for industrial applications. The final question is that of power consumption. At a rep. rate of f=1kHz, our present small eight pin lens (figure 3.2.1) would consume:

$$W = f \cdot \frac{1}{2} CV^2 = 1\text{kW}. \quad (C = 5\text{nF}, V = 20\text{kV})$$

This is a considerable amount of pulsed power, especially if we increase the electrical diameter of the CSL and consequently the capacitor value. In order to reduce the power in the larger devices we made the enclosed CSL which confines the shocks in its interior (figure 3.3.3), and a considerable reduction in energy consumption and noise occurred.

CHAPTER 4:
THE COLLIDING SHOCK LENS AS AN INTRACAVITY Q-SWITCHING ELEMENT

4.1 INTRODUCTION

Quality factor or "Q-switching" of lasers is an important method of enhancing the power of pulsed lasers [Koechner 1984, Siegman 1986]. Mechanical Q-switches and dye cell switches have generally been discarded in favour of triggerable opto-electronic devices based on the Kerr or Pockels effect.

In this chapter we show how a varifocal pulsed gas lens, the Colliding Shock Lens, can be utilised as an intracavity element to Q-switch a ruby laser [Lisi B 1994]. By placing the shock lens in tandem with a second lens a giant pulse is obtained. The second lens may be a conventional glass lens or a continuous wave gas lens.

4.1.1 OPERATION PRINCIPLE

The principle of colliding shock Q-switching (CS-QS), relies on the insertion of a steady state converging lens and of the rapidly varying CSL in a laser cavity. The CSL focal length and lens diameter increase with time over a few microseconds (see figure 3.3.2). When the CSL is switched off, the steady state lens renders the cavity unstable. Only when the CSL is switched on and while the focal regions of the two lenses overlap, does the laser cavity become stable and the losses low. If this condition is achieved when the population inversion is at its peak in the active medium, lasing occurs in the form of a giant pulse. As soon as the two focal lengths overlap we have a telescopic resonator. Telescopic laser resonators have been used in ref. [Hanna 1981, Routledge 1986] in order to achieve large volume Q-Switched diffraction limited TEM00 beams whilst keeping the laser cavity short. Q-Switched pulse rise-time is roughly proportional to the cavity transit time. As a secondary advantage of this configuration one can utilise the telescope to compensate for the thermal expansion of the laser rod in high rep. rate operations. The main disadvantage of the configuration is the possibility of optical damage on the intracavity optical components which are in the de-magnified side of the laser beam.

Potential advantages of CS-QS over other electro-optic switches are economy, simplicity and robustness. The economy lies in the absence of solid state optical components (e.g. pile of plates polariser and Pockels cell). The simplicity and robustness stem from the absence of polarisers and the need to adjust the polarisation. One obvious disadvantage is the possibility of laser breakdown in the confocal region, though the risk of this happening may be mitigated by gas lens aberrations.

4.2 EXPERIMENT

In order to test this new Q-Switching operation scheme we designed a separate experiment. We utilised a commercial ruby laser and the enclosed CSL described in section 3.3.

4.2.1 EXPERIMENTAL SET-UP

In the experiment designed to test the CS-QS concept, a commercial ruby laser was modified to incorporate the additional Q-Switching components. Figure 4.2.1 is a schematic of the experiment. The laser consists of a ruby head, a full reflector R2 and an output mirror R1. The Q-Switching components are the Colliding Shock Lens L2 with the relative arc discharge electronics, a continuous lens L1 and a fluorescence-sensing photodiode PD1. The value of the discharge capacitor of the CSL was set to C=100nF. The distance from the output coupler R1 and the lens L1 is d1. The distance between the two lenses is d and finally the distance between the CSL and the full reflector is d2. We already described the CSL in detail in the previous chapter. Very briefly the CSL consists of eight arc discharges, struck simultaneously between pairs of opposing points located on the arc of a circle (figure 3.3.1). Each point explosion produces an expanding spherical shock wave. After the eight shock waves collide at the centre of the circle, a cigar shaped, high density, axially symmetric core expands outwards. Lensing is due to the radially symmetric density gradients within the expanding region.

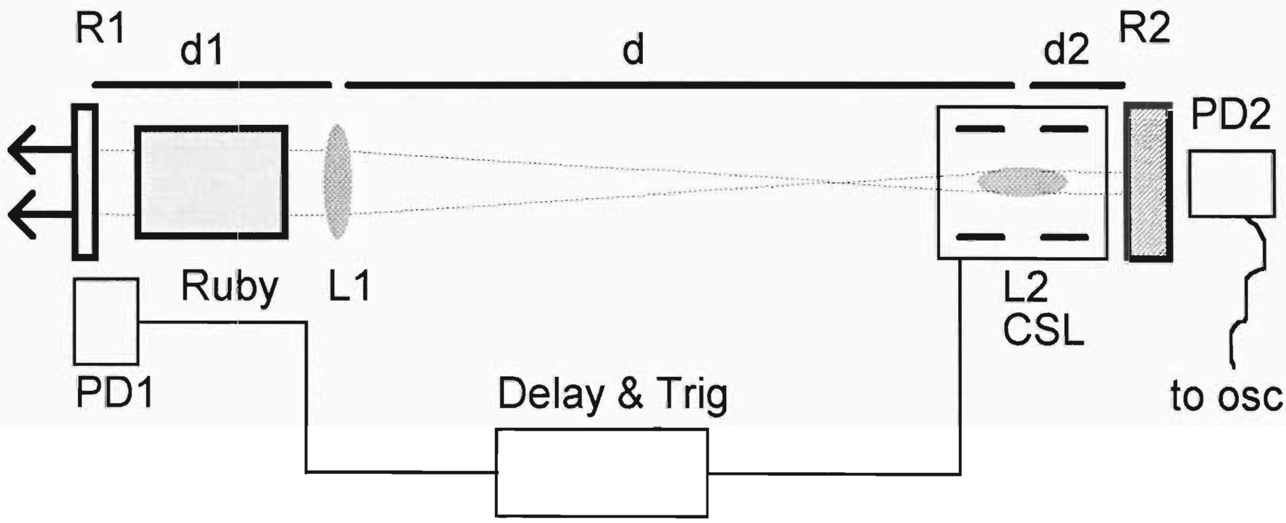

Fig 4.2.1 Experimental set-up of the Colliding Shock Lens Q-Switching (CSL-QS).

As the lens diameter increases, the density diminishes and the focal length increases as depicted in figure 3.3.2. The CSL used for these experiments, was specially chosen for its fast switching and acceptable optical aperture. It consists of a 5cm diameter cylinder closed at both ends. The gaps are set to 1.5mm and the diameter of the circle of pins is 3cm. The central windows are 1cm in diameter. A 100 nF capacitor, charged to 15KV, is connected to the eight gaps in series via a triggerable spark gap. This series connection ensures simultaneous arcing.

4.2.2 THE LENS L1

The lens L1 can be either a conventional solid state device or a continuous wave gas lens. The Spinning Pipe Gas Lens, which we described in detail in chapter 2, was used in some experiments. The device consists of a 1m long, 2cm diameter heated tube, spun at 30 Hz. The rotation centrifuges warm air out of the two ends and causes cold air to be aspired along the axis. The resulting density and refractive index gradient produces a long focal length lens, the quality of which fluctuates. The focal length can be varied from 1.5m to several meters (as measured from the centre of the pipe) by changing the pipe temperature and rotation speed. The laser head is a commercial ruby laser [Korad K1], the two flat end mirrors are a Full Reflector (measured reflectivity R1=96%), and an Output Coupler (measured reflectivity R2=45%).

4.2.3 OPERATION PROCEDURE

The operation sequence for all CS-QS experiments is the following. First the ruby flashlamp is fired and the PD1 photodiode detects the fluorescence signal from the active medium. This signal is electronically delayed and used as a trigger for the CSL master spark gap circuit (figure 3.2.1). The signal from the photodiode PD2, placed behind the full reflector R1, is read by a storage oscilloscope and gives the laser pulse waveform. The laser beam energy is measured with an energy meter on the main output beam. A burn pattern of the attenuated beam at the focus of a lens is used to measure the divergence.

4.2.4 MODES OF OPERATION

Depending on the choice of the lens L1 and on the intracavity distances d1, d and d2 we can operate the cavity in many different conditions. We decided to operate the cavity in only three different modes described below.

Mode a, maximises the output energy and beam diameter.

Mode b, minimises the Q-switched laser pulse-duration.

Mode c, explores the feasibility of a cavity with intracavity beam expansion optics consisting entirely of gas.

As we will see in much greater detail in the second and theoretical part of the chapter, the stability of the laser resonator can be determined in terms of the complex parameter **m**. In the formalism of ray matrix optics **m** is half the trace of the round trip resonator matrix [Siegman 1986, Kogelnik 1974]. For an unstable resonator, the absolute value of m is greater than one (abs(**m**)>1). For this case we can introduce the magnification M as:

$$M = \begin{cases} m + \left(m^2 - 1\right)^{1/2} & \text{if } m > 1 \quad \text{(positive branch)} \\ m - \left(m^2 - 1\right)^{1/2} & \text{if } m < -1 \quad \text{(negative branch)} \end{cases} \qquad 4.2.1$$

where **M** is the amplification of the beam cross section per round trip and can be related to the cavity losses. When abs(**m**)<1 the cavity is stable. Abs(**m**)=1 for a plane parallel configuration which corresponds to the confocal situation of our intracavity "telescope". The cavity losses can be directly related to the cavity geometry, that is to the parameter **m** (or M). Generally speaking we can state that the cavity losses are high when the resonator is unstable and the value of M is high, becoming progressively lower as the value of M is decreased. In the present simple scheme we can say that the losses become zero when the cavity configuration is plane parallel or stable. After the shock collision, as the CSL focal length increases, the cavity geometry will go through stable and unstable phases. In the light of this simple analysis let us examine the three operating modes in detail.

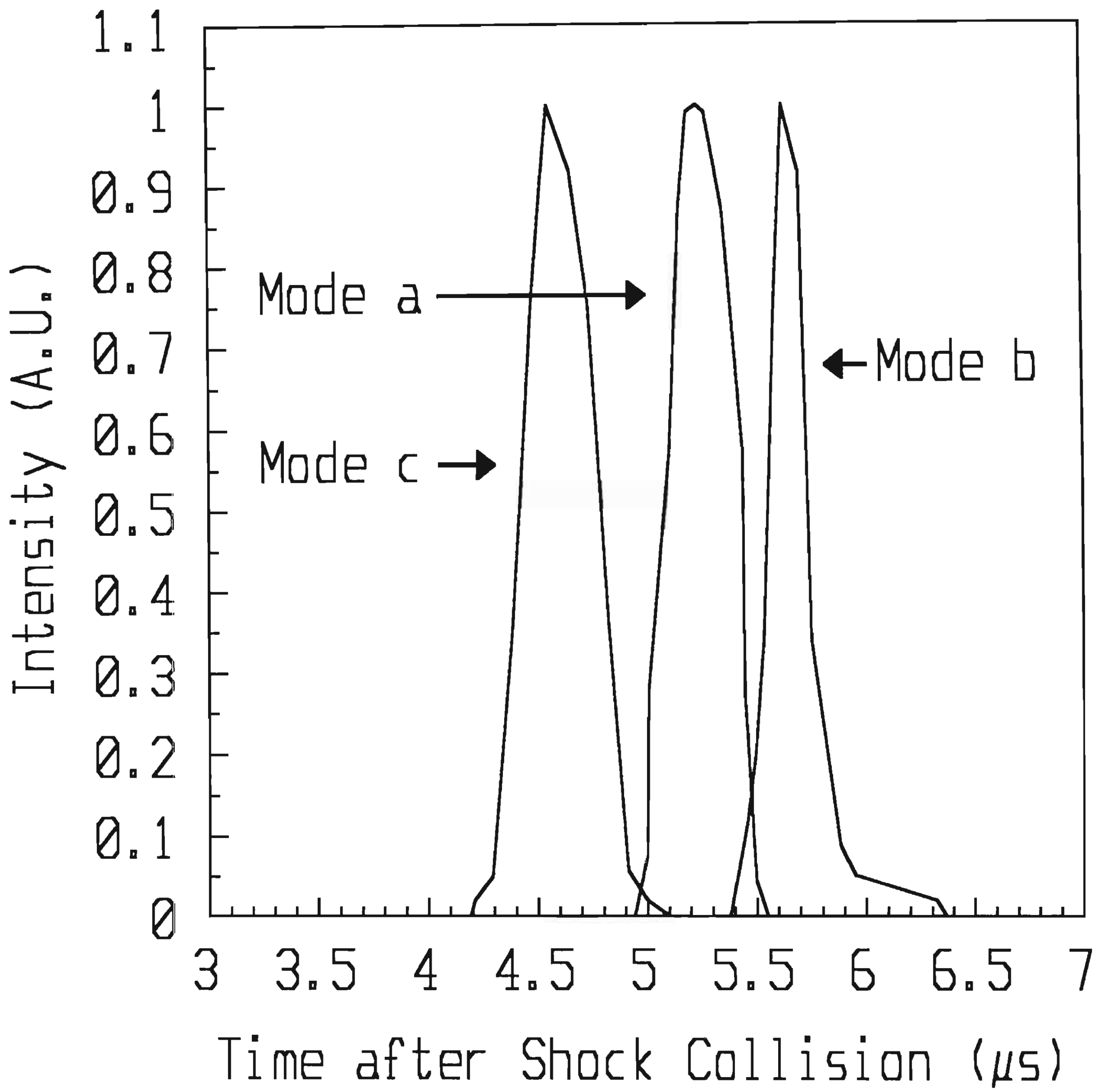

Fig.4.2.2 Measured intensity profiles of the Q-Switched laser pulse.

Mode a. L1 is a 200cm focal length glass lens. The lens separation d is 250cm. The condition abs(**m**)=1 is achieved when f_{CSL}=50cm. The CSL lens aperture is d_{CSL}=3.0mm (see figure 3.3.2) and the beam fills the ruby rod (10mm). At slightly later times, the resonator becomes stable and we expect lasing to occur. A drawback of this operating condition is that the cavity is long (3m) as is consequently the rise-time of the laser pulse. In this case the initial magnification of the resonator (before the CSL is operated) is low: M=2.8. We must therefore operate the flashlamp below 4.3kV to avoid free running lasing. A 2J laser pulse of duration 360ns (FWHM) is observed 5μs after the shock collision. Figure 4.2.2 shows the pulse waveform.

Mode b. L1 is a 50 cm focal length glass lens (d=100cm). Again m=1 is achieved when f_{CSL}=50cm, d_{CSL}=3.0mm and the beam diameter on the output coupler is expected to be 3.0mm. The initial magnification is now M=4.4 and free running is inhibited at any flashlamp voltage. We operated at 4.5 kV. In this case we expect shorter pulses and a very narrow beam together with lower energy. A 100mJ pulse, of duration 175ns (FWHM) is observed 5.5μs after the shock collision (see figure 4.2.2). On a few occasions when the CSL alignment appeared to be optimised, a pulse length of about 50ns was observed.

Mode c. L1 is a spinning pipe gas lens operated at 200cm focal length. For this "all gas" Q-switch we expected similar performance to mode a. Figure 4.2.2 shows a 375ns (FWHM) pulse 4.5μs after shock collision. However, the energy for this mode is slightly higher (3 J). The absence of reflective losses in the cavity appears to outweigh the effect of the spinning pipe gas lens aberrations. The scheme of the "all gas Q-switch is in figure 4.2.3.
In Table 1 we summarise the results of the experiment: laser energy, pulse length, beam diameter and beam divergence for all three operating modes. The energy values reported in this paper are the maximum values obtained over a large number of experiments.

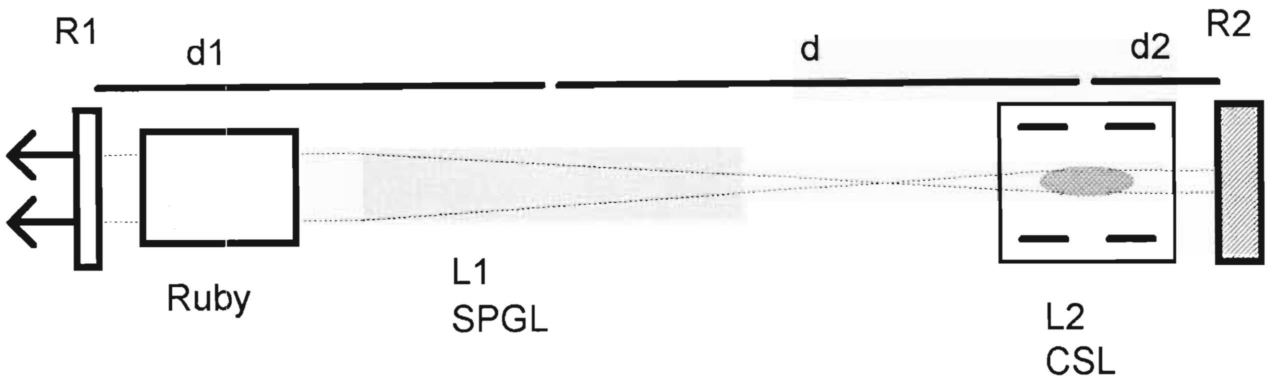

Fig.4.2.3 Laser resonator scheme for the "all gas" Q-Switching experiment

	E_{max}/J	Δt/ns	Φ/mm	Div (mrad)
Mode a	2.0	360	8.0	1.0
Mode b	0.1	175	2.0	3.3
Mode c	3.0	375	8.0	1.4

Table.4.3.1. Summary of the results of the Colliding Shock Q-Switching experiment. Emax is the maximum recorded value of the output energy in the three different resonator geometries. Δt is the typical pulse duration (FWHM). Φ is the laser spot diameter and Div is the divergence.

Although the fluctuations are large, especially for mode c, due in this case to the unstable behaviour of the SPGL [LisiA 1994], we noted that the operations do not critically depend on the cavity alignment and gas lens aberrations. After tilting mirror R2 by 3mrad, enough to completely inhibit the free running laser output, the Q-switched pulse decreases by only 50% (1.5J). Furthermore we must note that the aberrations of the spinning pipe lens and its focusing instabilities seemed to affect the output energy much less than expected. Laser radiation occurs as soon as the CSL focal length sweeps through the right value that allows light to resonate with low losses. In a stable cavity the above condition is satisfied for a broader range of modes than for the plane parallel cavity of the free running laser.

4.3 THEORY AND MODELS

This third section contains a detailed description of a computer model that was proposed in order to compute the temporal evolution of the radiation density and the population inversion of the ruby laser system during CSL Q-Switching operations. The listing of the programmes is in Appendix B.

4.3.1 THE RATE EQUATIONS

It is well known that it is possible to model the behaviour of a laser system using the rate equations [Koechner 1984]. The rate equations consist of a system of coupled non-linear first order differential equations. In the most general and exact form they relate the time evolution of the upper level's population at each point of the laser medium, to the local radiation density. The temporal evolution of the population of each level is then determined by the initial population values, by the radiation density and by the transition probabilities. The pump contribution, for a flash lamp pumped laser, is included into the radiation density term. The population values of the three (or four) levels at any location in the active medium are coupled to the population values at different positions via the mode structure of the radiation. The coupling coefficients are proportional to the absorption and stimulated emission cross sections. The mode structure depends on the resonator geometry and on the spatial structure of the gain in the active medium [Statz 1965], which is determined by the population difference between upper and lower laser level. The upper laser level population by itself has the important effect of triggering the laser amplification, via the radiation initially emitted by spontaneous decay. A complete solution of the three-dimensional case is computationally hard, especially when the number of radiation modes in the cavity becomes high. Nor does it help to reduce the dimensions to two as, for example, with cylindrical symmetry. Under some general conditions it is possible to model a laser system with a set of zero-dimensional equations which are simple to solve numerically. The conditions are:

1) Spatial uniformity of the gain.

2) Spatial uniformity of the radiation intensity along the cross section of the beam.

3) Laser pulse duration longer than the round trip time.

The conditions 1) and 2) are never completely true, but in many cases of practical interest they represent a very good approximation.

4.3.2 THE ZERO-DIMENSIONAL RATE EQUATIONS

In the zero-dimensional case we can describe the evolution of the photon density in the cavity with only one equation. A ruby laser is a three-level system. The zero-dimensional rate equations, after an initial population inversion has been established, can be written in the following form:

$$\frac{\partial\phi}{\partial t} = \phi\left(nc\sigma_{st}\frac{l_A}{l_C} + \frac{\ln(1-\varepsilon(t))}{\tau_R} \right) \qquad 4.3.1$$

$$\frac{\partial n}{\partial t} = -\phi\gamma\, nc\sigma_{st} \qquad 4.3.2$$

Where l_C is the cavity length and l_A is the active medium length, n is the population inversion, ϕ the photon density, c the speed of light, σ_{st} the stimulated emission cross section, γ is the degeneracy of the upper laser level and τ_R is the round trip time.

Normal Q-Switching operations can be investigated by splitting the loss term ε in three parts.

$$\varepsilon(t) = 1.0 - \left\{R_1 \cdot \left[1 - los_1\right] \cdot \left[1 - los_2(t)\right]\right\} \qquad 4.3.3$$

The first two are constant, they take into account the transmission of the output coupler the first and the scattering by defects, reflections from glass lenses and diffraction losses the second. The third term is set artificially high at the beginning (for example by means of crossed polarisers) in order to establish a high population inversion without allowing lasing to occur. As the gain reaches its peak, the losses are suddenly lowered to a value that allows amplification to occur in the cavity. Amplification occurs now at a rate much higher than if the losses had remained low. In the latter case, a ruby laser releases its energy in a train of low intensity pulses, or free running. Conversely the result of the Q-Switching operation is a giant pulse in which all the energy stored in the upper level of the active medium is released in a very short time. According to an approximate theory [Koechner 1984], the laser pulse rise time is inversely proportional to the cavity round trip time $\tau_{\mathbf{R}}$.

4.3.3 RATE EQUATIONS FOR OUR SYSTEM

We want to write down the zero-dimensional rate equations to model the system described at the beginning of this chapter and shown in figure 4.3.1. We will utilise the equations 4.3.1 and 4.3.2. The most important issue to solve in order to set a correct model is to find a suitable expression for the loss term ε. The constant term Los1 is easily calculated (or guessed) to be about 30%. The variable second term requires more attention. We have to take into account that in our Q-Switching configuration the resonator geometry, and not only the quality factor Q, is changed during the operations.

4.3.5 THE CAVITY GEOMETRY

A laser resonator is a periodic focusing system. This can be treated in the formalism of ABCD matrix optics [Siegman 1986] in the paraxial ray approximation. The paraxial ray approximation is fully justified in our system since, given the maximum beam diameter (1cm) and the cavity length (3m), the maximum angle about the optical axis that radiation can exhibit is <3.5mrad. The resonator scheme is shown in figure 4.2.1. d1 is the distance between output coupler and lens L1, d is the distance between the two lenses and d2 is the distance between the CSL (L2) and the full reflector. We can divide a round trip inside this resonator into nine successive steps (figure 4.3.1). Each step consists in a propagation in vacuum or a focusing by positive lenses.

According to the ABCD matrix theory, each step can be represented by a two-by-two matrix. The matrix acts on a two component vector (or ray), the first component is the radial distance from the optical axis and the second one is the angle.

The product of all these matrices will give the round trip resonator matrix. We call it M_{tot}:

$$M_{Tot} = ABCDEFGHI \qquad 4.3.4$$

I and A represent propagation through d1, H and B the focusing due to L1, C and G the propagation through d, F and D represent the focusing due to the CSL (L2) and finally E is a propagation through 2d2. The matrices F and D depend explicitly on time.

$$A = I = \begin{pmatrix} 1 & d1 \\ 0 & 1 \end{pmatrix} \qquad B = H = \begin{pmatrix} 1 & 0 \\ \dfrac{-1}{f1} & 1 \end{pmatrix}$$

$$C = G = \begin{pmatrix} 1 & d \\ 0 & 1 \end{pmatrix} \qquad D = F = \begin{pmatrix} 1 & 0 \\ \dfrac{-1}{f2(t)} & 1 \end{pmatrix} \qquad 4.3.5$$

$$E = \begin{pmatrix} 1 & 2d2 \\ 0 & 1 \end{pmatrix}$$

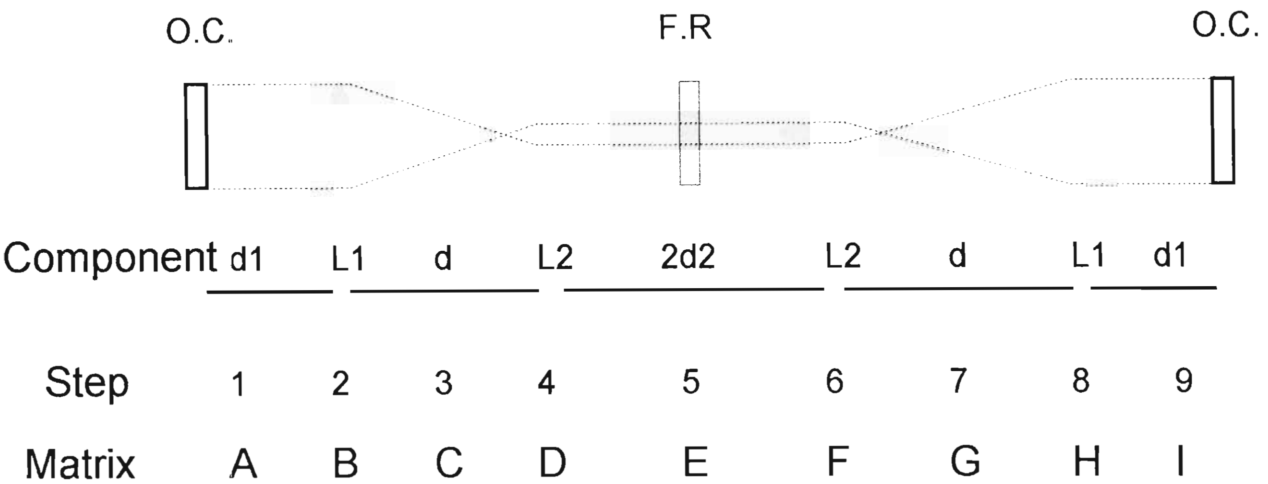

Fig 4.3.1. Resonator scheme. The path of each ray can be subdivided in nine steps per round trip. O.C.: output Coupler, F.R.: Full Reflector, L2: Colliding Shock Lens, L1: Cavity Lens.

We now set on to the rays the condition that they must resonate. This is done by imposing on the rays a matching condition at the edges of the resonator after one or more round trips. This gives us an eigenvector equation:

$$M_{Tot}\vec{X} = \lambda\vec{X} \qquad 4.3.6$$

Where **X** is a ray. As previously mentioned, X(1) is the distance from the optical axis and X(2) is the angle. The two eigenvalues λ_1 and λ_2 can be determined as the solutions of the following equation:

$$\lambda^2 - 2\lambda \cdot \mathrm{tr}(M_{Tot}) + \det(M_{Tot}) = 0 \qquad 4.3.7$$

We introduce now the parameter **m** as half the trace of the resonator matrix M_{tot}. Taking into account that the ABCD matrices are always unitary, equation 4.3.7 becomes:

$$\lambda^2 - 2m\lambda + 1 = 0 \qquad 4.3.8$$

If abs(**m**)>1 the eigenvalues are real while if abs(**m**)<1 they are imaginary. When abs(**m**)=1 the eigenvalues equal unity.

$$\left.\begin{array}{l}\lambda_1 = 1\\ \lambda_2 = 1\end{array}\right\} \text{ if } \mathrm{abs}(m) = 1 \qquad 4.3.9a$$

$$\left.\begin{array}{l}\lambda_1 = m + \sqrt{m^2 - 1}\\ \lambda_2 = m - \sqrt{m^2 - 1}\end{array}\right\} \text{ if } \mathrm{abs}(m) > 1 \qquad 4.3.9b$$

$$\left.\begin{array}{l}\lambda_1 = \exp[i \cdot \mathrm{arcos}(m)]\\ \lambda_2 = \exp[-i \cdot \mathrm{arcos}(m)]\end{array}\right\} \text{ if } \mathrm{abs}(m) < 1 \qquad 4.3.9c$$

In the first case we have an unstable resonator [Anan'ev 1972], in the second one a plane parallel cavity and in the third case a stable resonator. Soon we will see how we can relate the losses to the eigenvalues, but before we will discuss in some detail the unstable resonator case. The two eigenvalues assume the form:

$$\left.\begin{aligned}\lambda_1 &= M\\ \lambda_2 &= 1/M\end{aligned}\right\} \quad \text{if } \ \mathrm{abs}(m) > 1 \qquad 4.3.10$$

where we have defined M as the cavity magnification. The physical interpretation is rather simple. If we start with an arbitrary beam, we can decompose it into the two eigenstates corresponding to λ_1 and λ_2. After several round trips, if **m**>1 then only the eigenstate corresponding to λ_1 will survive while if **m**<-1 only the eigenstate corresponding to λ_2. We talk in this cases of Positive Branch (**m**>1) or Negative Branch (**m**<-1) unstable resonators.

4.3.5 CAVITY LOSSES

We consider now a beam carrying an intensity I_0 on the active medium surface S. After one round trip, its cross section will be linearly amplified by **M**. The intensity I_0 will then be spread over the surface $\mathbf{SM^2}$. The intensity will consequently decrease by $\mathbf{1/M^2}$. When the cavity is unstable, the variable loss term in our cavity is then:

$$los_2 = 1 - \frac{1}{M^2} \quad \text{if } \mathrm{abs}(m) > 1 \qquad 4.3.11$$

Let us now examine the stable cavity case. Without going into too much detail, we can simply say that the value of the position and angle of a ray at the active medium position oscillates about the zero value after one or more round trips. Then a beam of intensity $\mathbf{I_0}$ over several round trips will lose no intensity. We can say that:

$$los_2 = 0 \quad \text{if } \mathrm{abs}(m) \le 1 \qquad 4.3.12$$

We have found so far an expression for the intensity losses both for the unstable and the stable cavity cases. los_2 is an explicit function of time as seen from equations 4.3.11, 4.3.9 and 4.3.5. We can now put the loss expression 4.3.11, 4.3.12 into the Zero-Dimensional rate equations. We expect the losses to become low when the configuration of the resonator is

approximately plane parallel. Two such configurations exist for two different values of the CSL focal length; their ray diagrams are depicted in figure 4.3.2. In case a) the CSL is in its weak condition but is just strong enough to render the diverging rays parallel. In case b) the CSL is strong and focuses the diverging rays to a point onto the mirror. We note that configuration b) occurs in time before configuration a), but the CSL optical diameter in configuration b) is much smaller than in configuration a). This is a dangerous situation if lasing occurs because the mirror can be damaged. To avoid this damage it is necessary to make the distance d1 (between CSL and Full Reflector) as small as possible.
In figures 4.3.3, 4.3.4 and 4.3.5 we show the computed evolution of: Stability parameter m, Cavity losses and magnification and laser pulse intensity for Mode a: d1=25cm, d2=10cm, d=250cm, L1=200cm. In figures 4.3.6 to 4.3.9 the same quantities are reported for Mode b: d1=25cm, d2=10cm, d=100cm, L1=50cm. Again in figures 4.3.9 to 4.3.11 for Mode c: d1=75cm, d2=10cm, d=250cm, L1=200cm (SPGL).
It can be seen that in all three configurations, the losses exhibit two minima, which corresponds to the plane parallel ray diagrams shown in figure 4.3.2. The first minimum does not last long enough for laser radiation to develop.

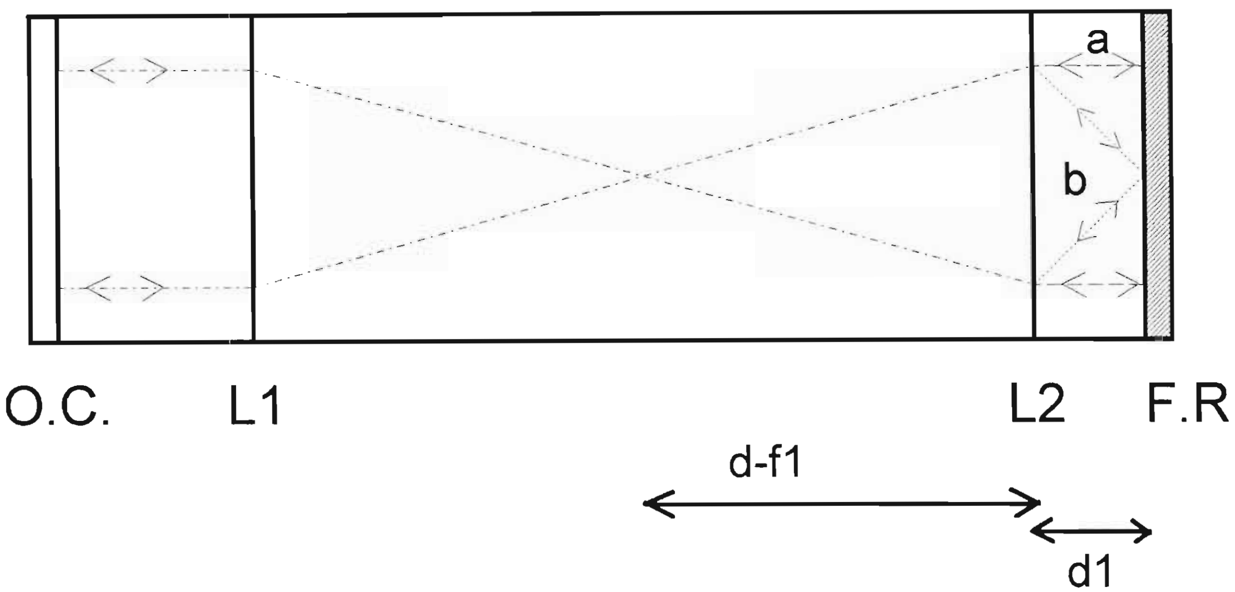

Fig.4.3.2 Plane parallel configurations of the resonator. A plane-wave incoming from the output coupler is transformed by the resonator in an equivalent plane-wave after one round trip. f1:focal lenght of the L1 lens.

a) The focal lenght of the CSL is such that 1/(d-f1)=1/fcsl.

b) The focal lenght of the CSL is such that 1/(d-f1)+1/d1=1/fcsl.

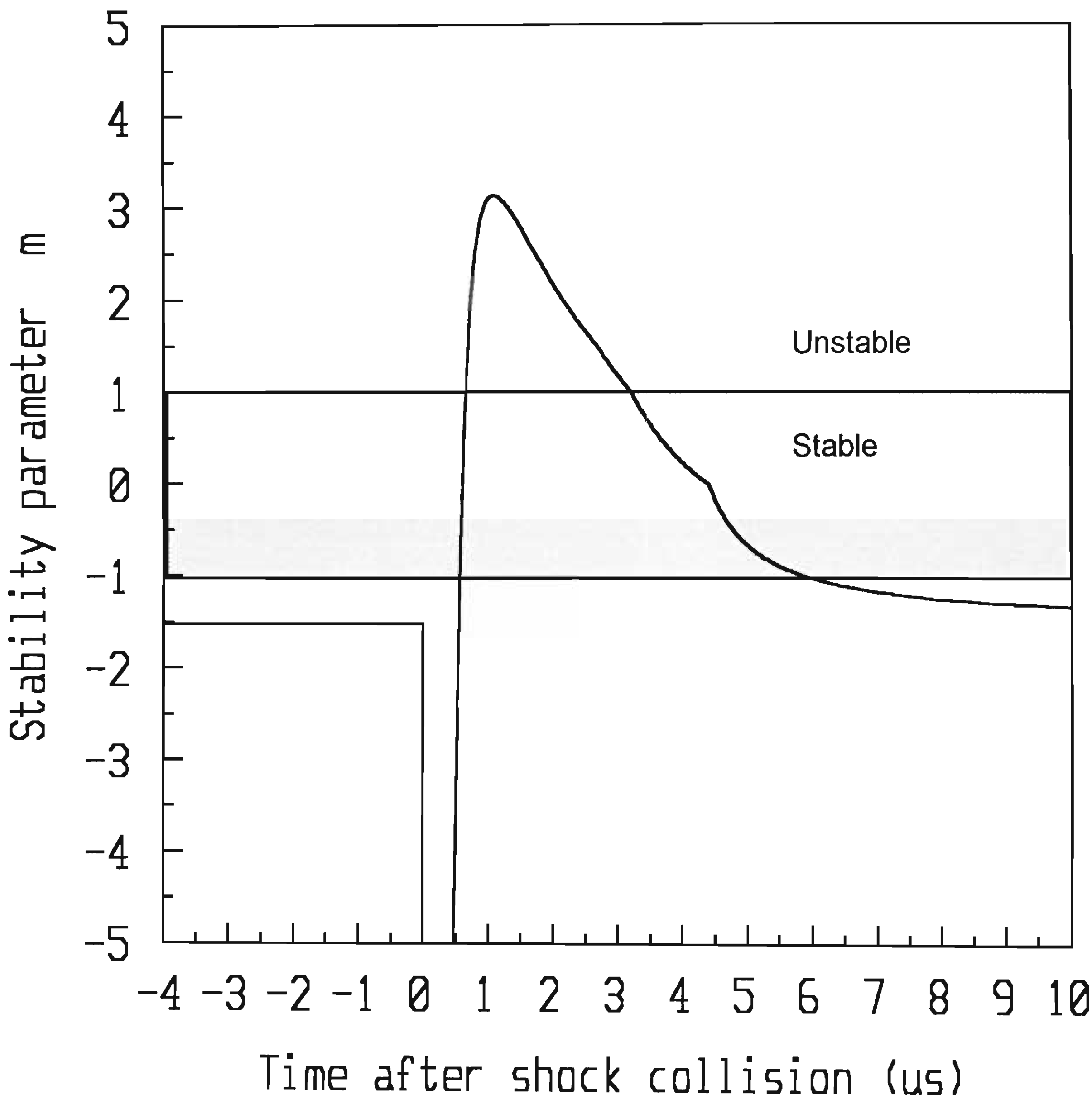

Fig.4.3.3 Stability parameter **m** for Mode a.

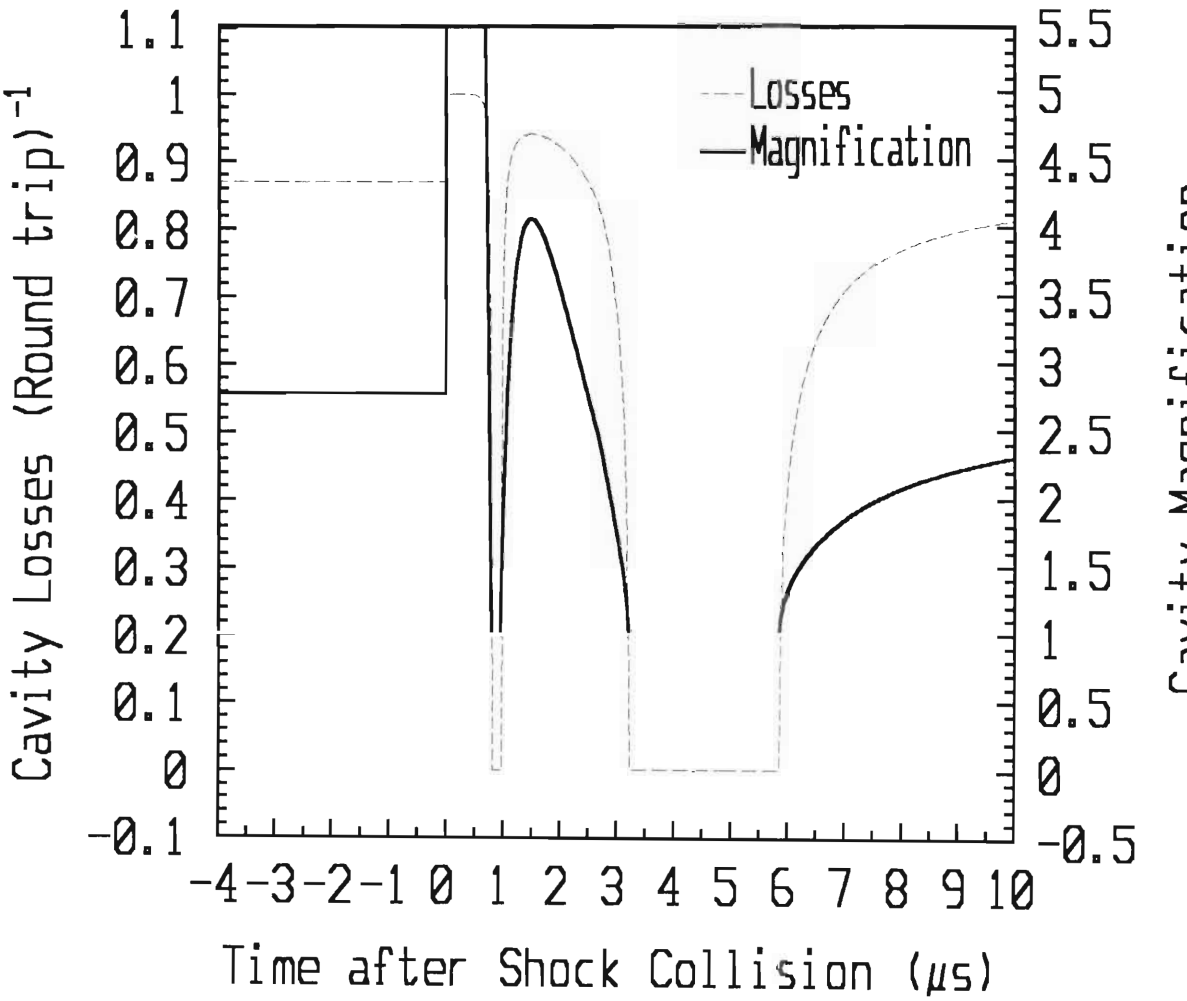

Fig.4.3.4 Losses and Magnification for Mode a.

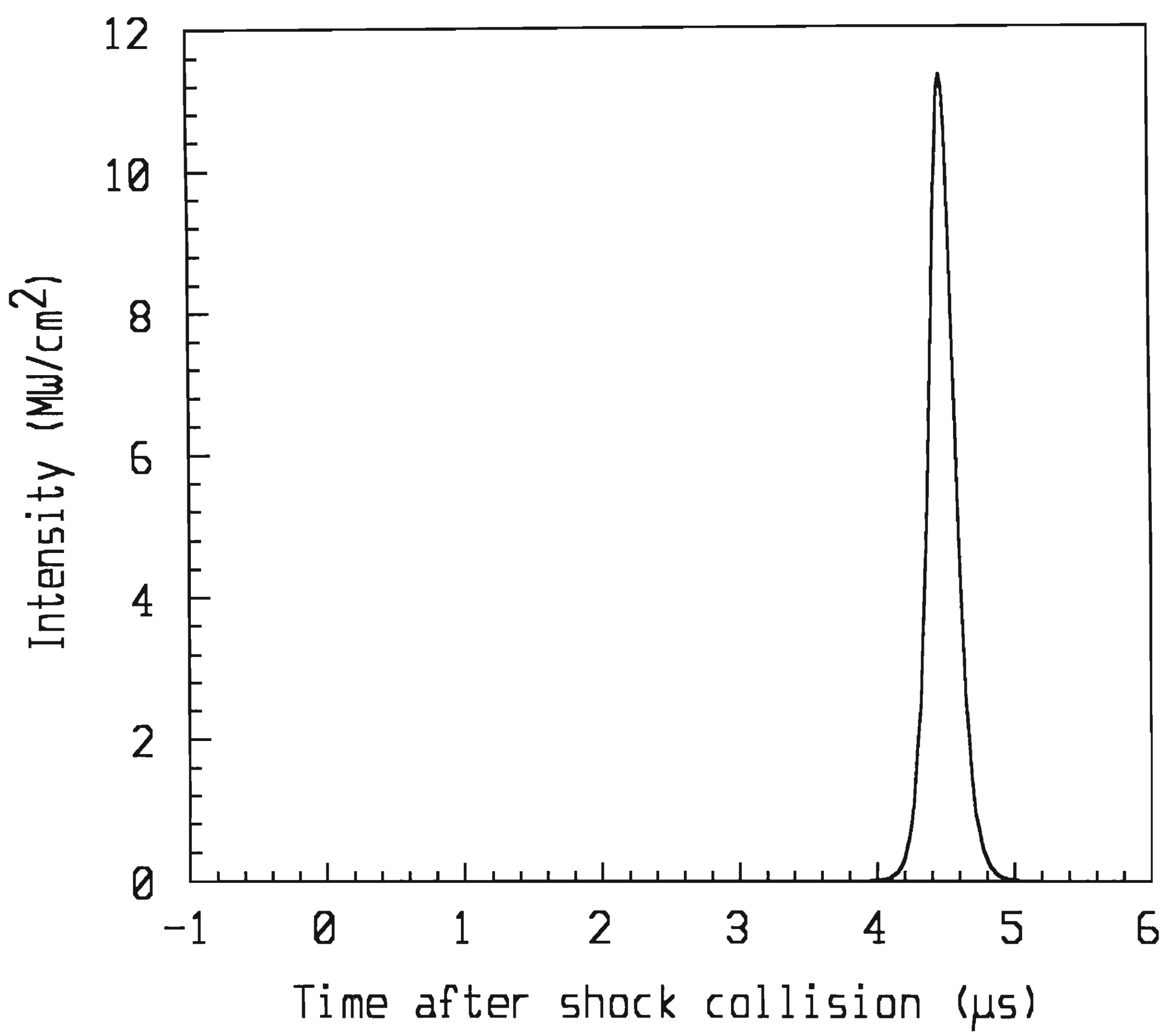

Fig 4.3.5 Intensity of the q-switched laser pulse for Mode a.

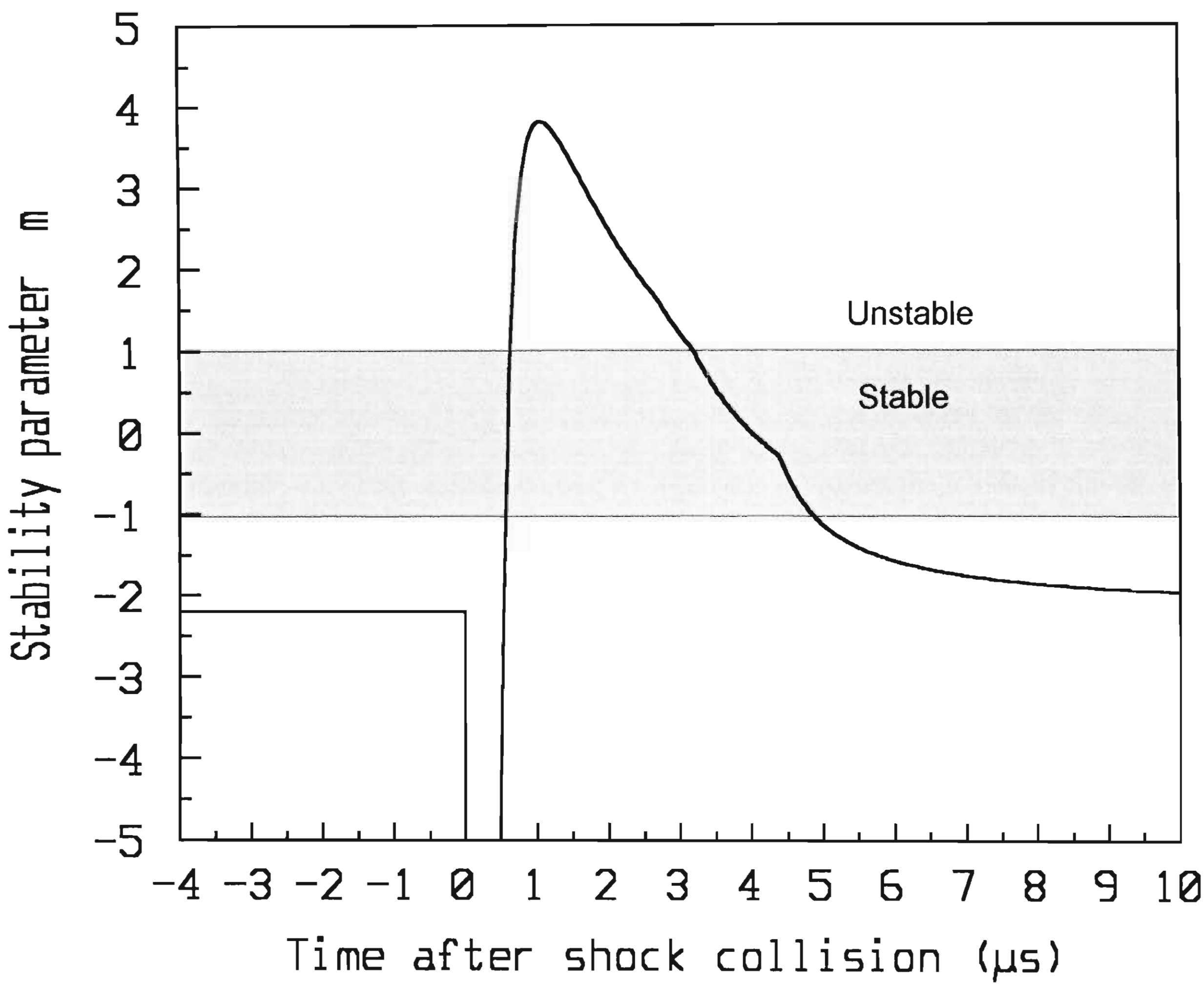

Fig.4.3.6 Stability parameter **m** for mode b.

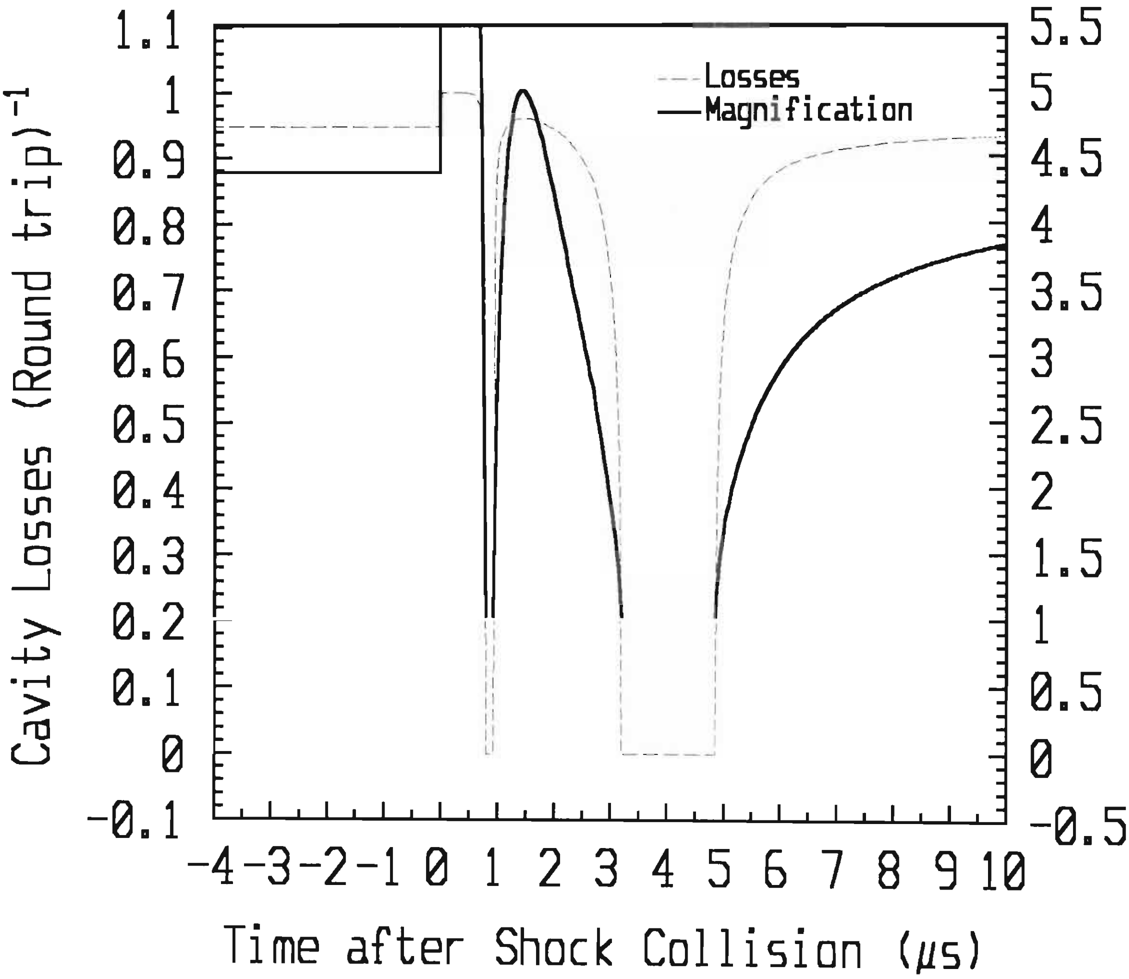

Fig.4.3.7 Losses and Magnification for Mode b

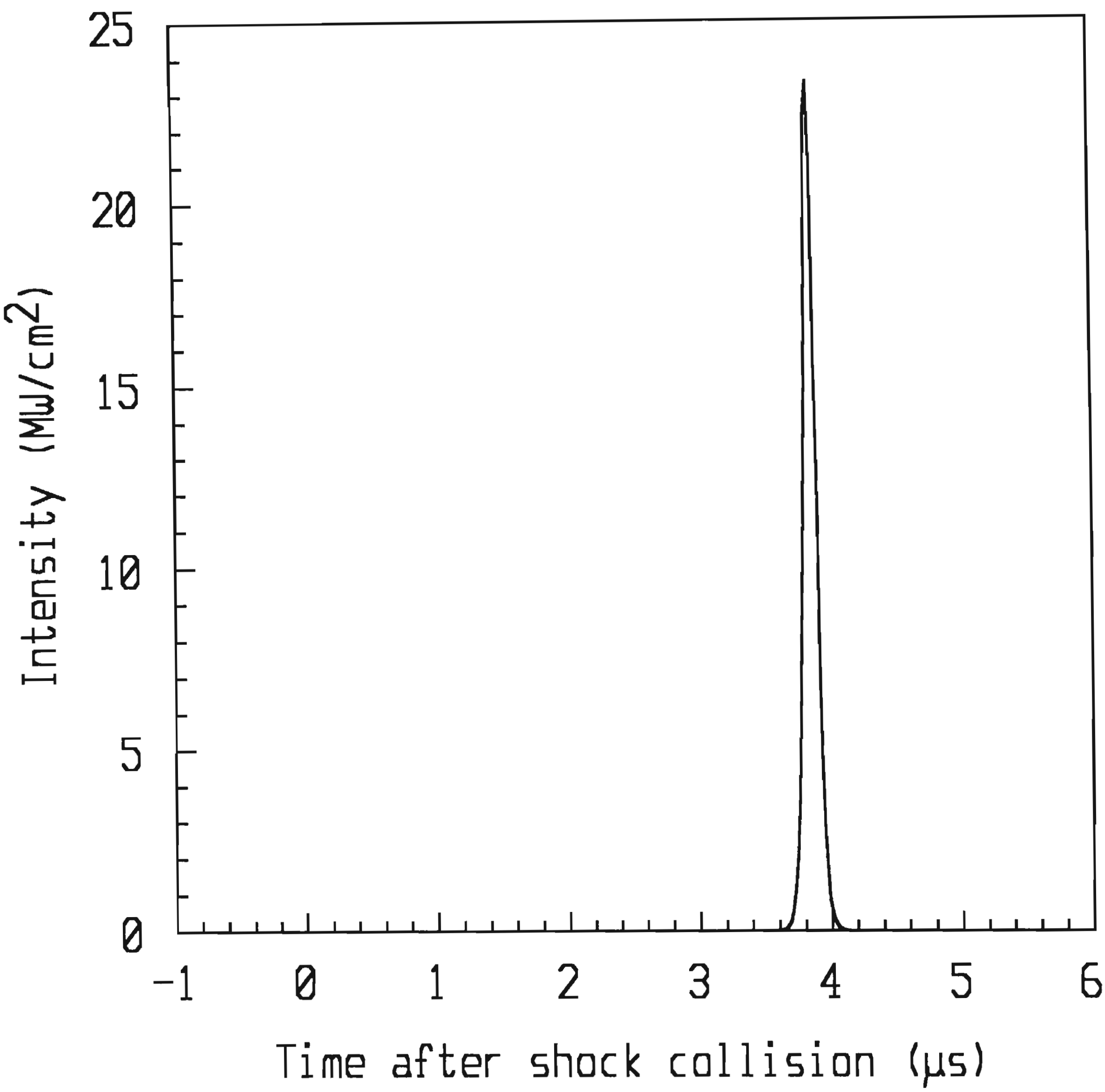

Fig.4.3.8 Laser pulse intensity for Mode b.

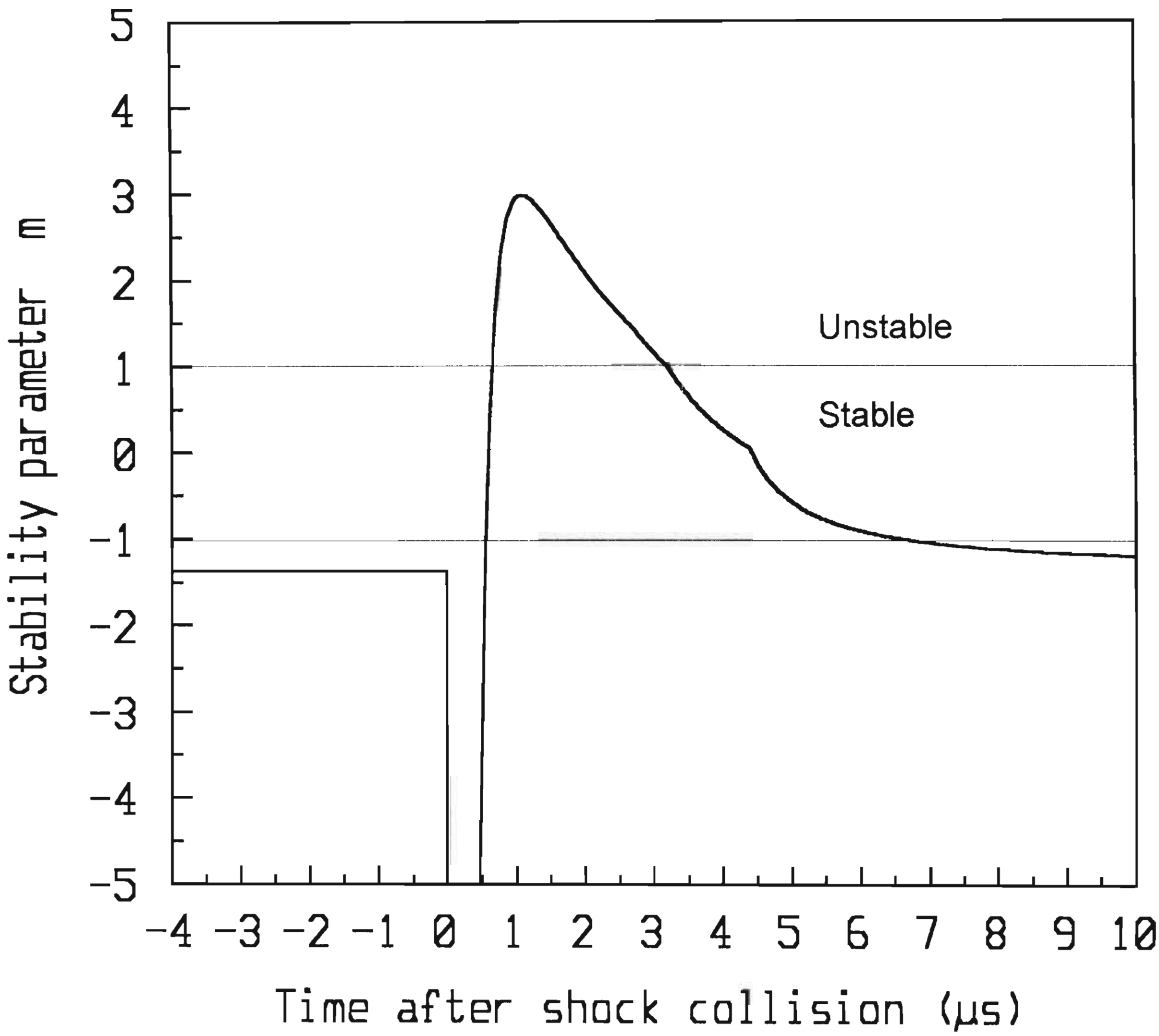

Fig.4.3.9 Stability parameter **m** for Mode c.

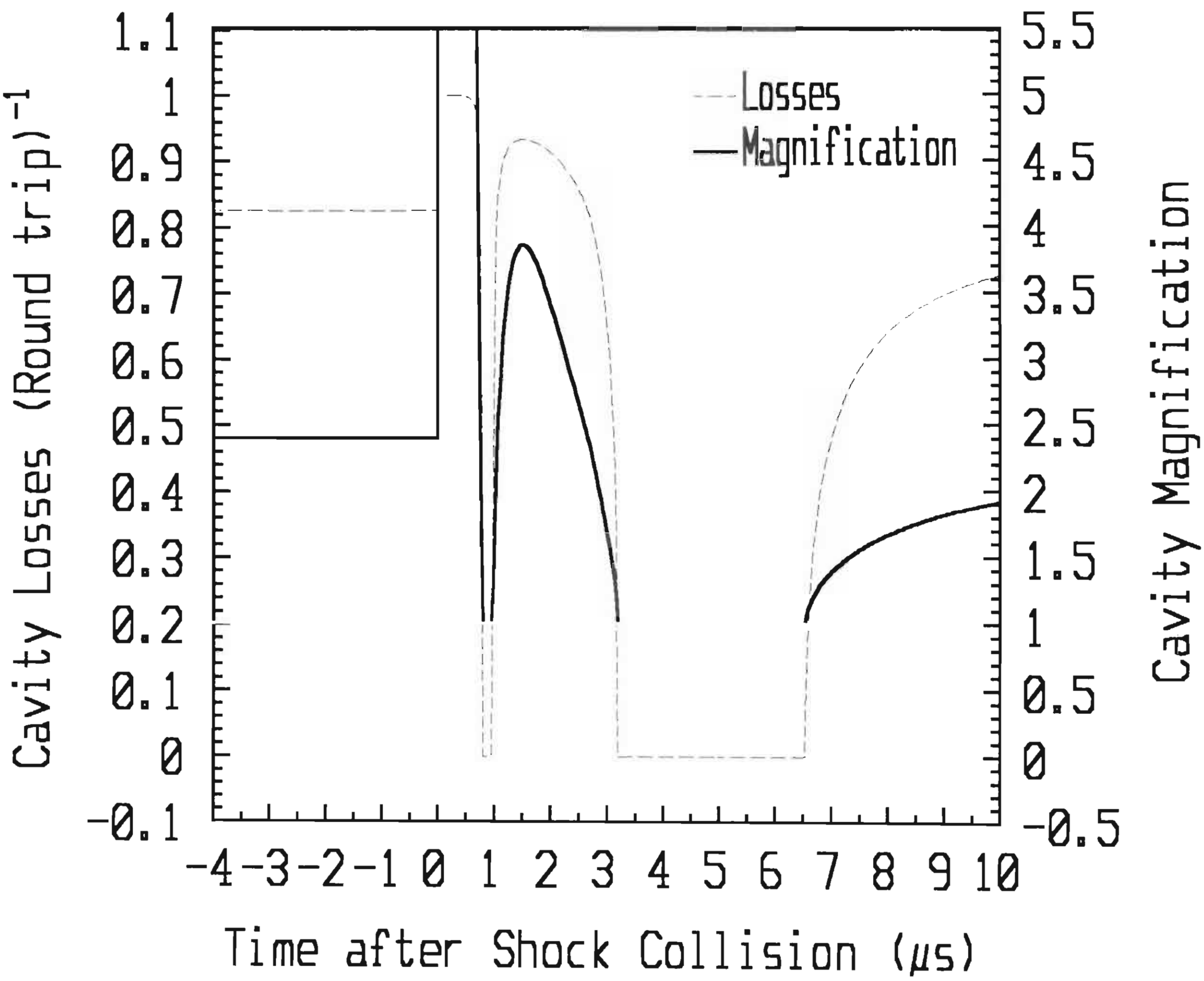

Fig.4.3.10 Losses and Magnification for Mode c.

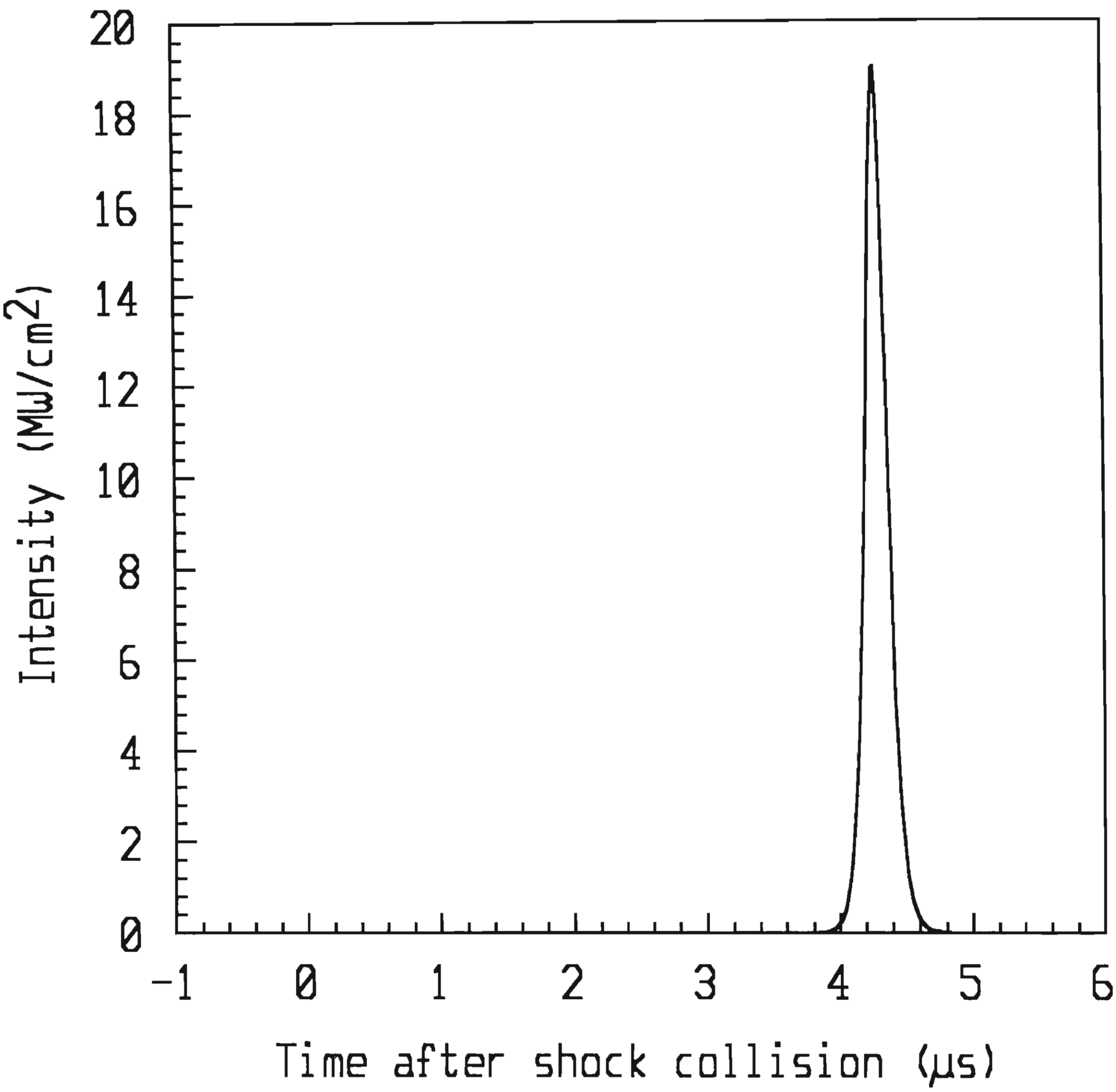

Fig 4.3.11 Laser pulse intensity for Mode c

4.3.6 LIMITS OF THE ZERO-DIMENSIONAL MODEL

In our system, the fundamental limitation of a zero-dimensional solution of the rate equations is that the loss calculation does not take into account the presence of apertures in the cavity. We must remember that, as shown in figure 3.3.2, the CSL diameter increases with time on a scale of microseconds and its value is in the millimetre range. We expect this to have a large effect on the beam diameter of the Q-Switched laser and consequently on the output energy. Only the laser radiation that travels close to the optical axis will not see any aperture and the expression for the losses will be given by equations 4.3.12, 4.3.13. But some of the intensity of the radiation that travels further away from the axis is lost, due to the finite aperture of the CSL. The latter acts as a pinhole.

4.3.7 ONE-DIMENSIONAL MODEL. RADIAL PROFILES

The calculation of the fractional intensity lost per round trip is accomplished in the following way. We divide the variable loss term Los2 into three contributions.

$$\mathrm{los}_2(R,t) = 1 - \mathrm{trans}_1 \cdot \mathrm{trans}_2 \cdot \mathrm{trans}_3 \qquad 4.3.13$$

The loss ε, as defined in equation 4.3.3, is now a function of beam radius and time. A collimated "input" light beam of radius R enters the cavity from the output coupler. R is taken to be less than or equal to the ruby rod radius. As the initial ray (R,0), propagates in the cavity, its components expand and contract according to the matrix algebra as previously introduced. When the beam "arrives" at the CSL location in the cavity we determine its diameter. From the ratio of the square of the beam diameter and the square of the CSL diameter we can determine the fractional intensity loss. A new beam is then propagated from the CSL position, having the same diameter as the CSL. The procedure is then repeated as the beam comes back to the CSL after a reflection from the back mirror and again as it reaches the ruby active medium. After one round trip we have calculated three intensity transmission coefficient. From the product of the three of them we calculate the fractional intensity loss per round trip according to equation 4.3.13. It is easily seen that the loss term coincides with the one calculated from equations 4.2.11, 4.3.12 for input beams of small cross section. But the losses become much higher as the input beam diameter increases. The loss term ε, as defined in equation 4.3.3), is now a function of beam radius and time.

$$\varepsilon = \varepsilon(R,t) \qquad 4.3.14$$

Once this function is known, a one dimensional generalisation of the laser rate equation can be set as follows. We divide the laser beam into a collection of $\mathbf{N_{shell}}$ annular beams. The $\mathbf{j^{th}}$ annulus having radius $\mathbf{R_j}$. We set the losses of an annular beam of radius $\mathbf{R_j}$ equal to the losses of an "input" beam of the same radius $\mathbf{R_j}$. In each annulus we solve independently the zero-dimensional laser rate equation.

$$\frac{\partial \phi_j}{\partial t} = \phi_j \left(n_j c \sigma_{st} \frac{l_A}{l_C} + \frac{\ln(1-\varepsilon(R_j,t))}{\tau_R} \right) \qquad 4.3.15$$

$$\frac{\partial n_j}{\partial t} = -\phi_j \gamma n_j c \sigma_{st} \qquad 4.3.16$$

$$j = 1 \ldots . N_{shell}$$

The output intensity of the laser beam now exhibits a radial profile. The two approximations in this treatment are the following:

1) In the computation of the losses, the radial intensity profile of the "input" beam is taken to be uniform during its propagation in the cavity.

2) The laser beam is perfectly collimated and, as a consequence, there is absence of energy exchange between different annuli.

We expect the effect of these two approximations to be small and in the spirit of a simplified model of the system. In figure 4.3.12 we show the computed radial energy density profiles for the three different operating modes. The energy density is the time integral of the laser pulse intensity waveform as shown in figures 4.3.5, 4.3.8 and 4.3.11.

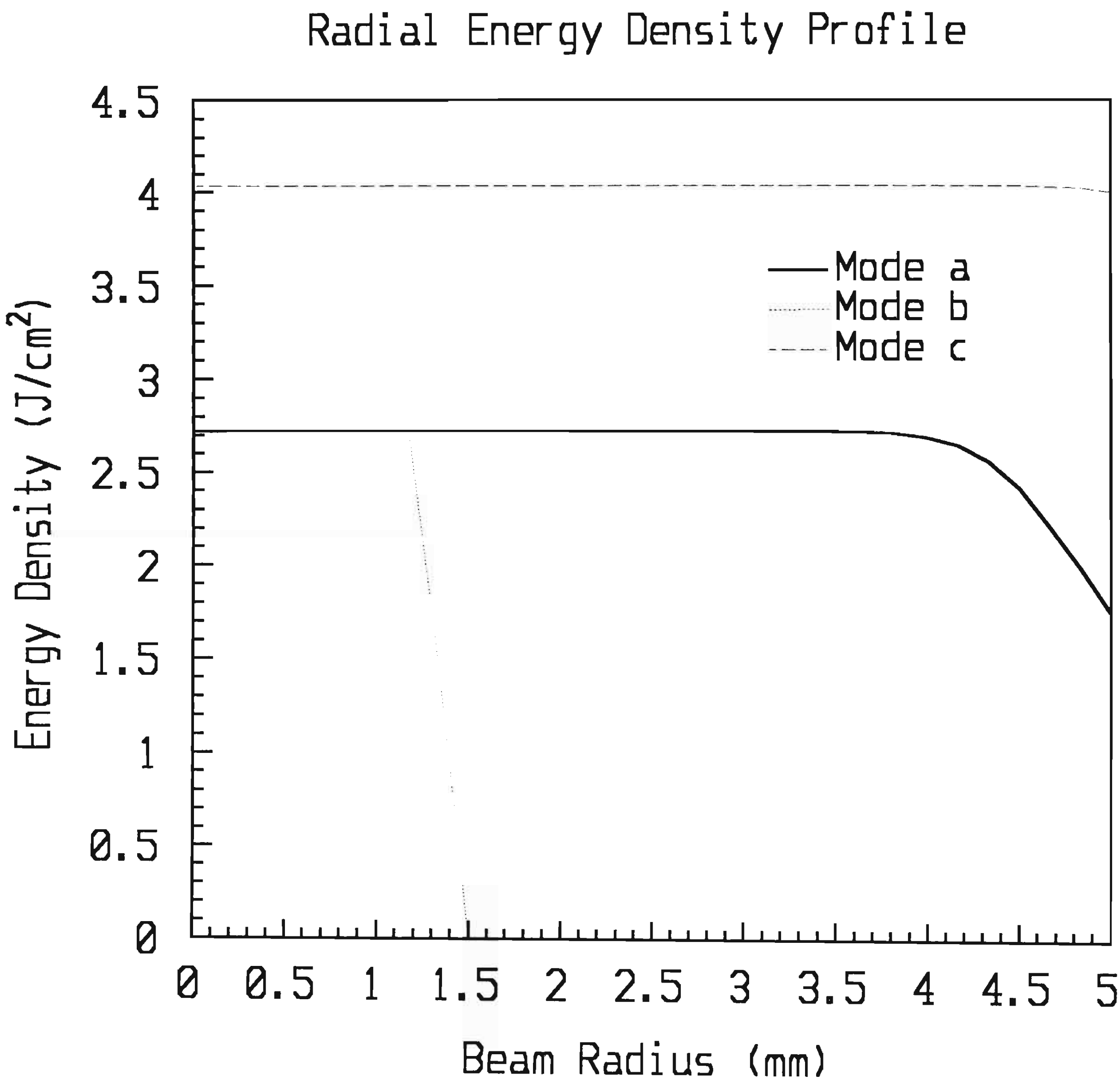

Fig.4.3.12 Radial intensity profiles for mode a,b and c

4.3.8 BEAM DIVERGENCE CALCULATION

The previous model can be regarded as a first order approximation to solve the radial profile of the laser beam. As stated at the end of the last paragraph, this approximation holds in the case that the laser radiation is perfectly collimated within the cavity. Again in the spirit of greater simplification we want to solve the angular profile of the laser beam using a different approach. We generate a uniform planar distribution of rays at the active medium position. We follow then the path of each of them for several round trips, recording the values of their position and angle on the output coupler. A histogram representation of the angular values will give us the angular distribution of the laser beam. In our system the cavity geometry varies with time, as does the laser divergence. This calculation is then performed for the cavity geometry that occurs when lasing is at its peak. The time at which the radiation intensity is maximum is calculated by the computer program described in the previous section. In figure 4.3.6 we show the computed angular profile of the beam for the three operating modes.

As we could expect, the short resonator configuration gives a narrow laser beam with a rather large divergence. The other two configurations give results comparable with the measurements. According to [Statz 1964] the output of our laser is multimode.

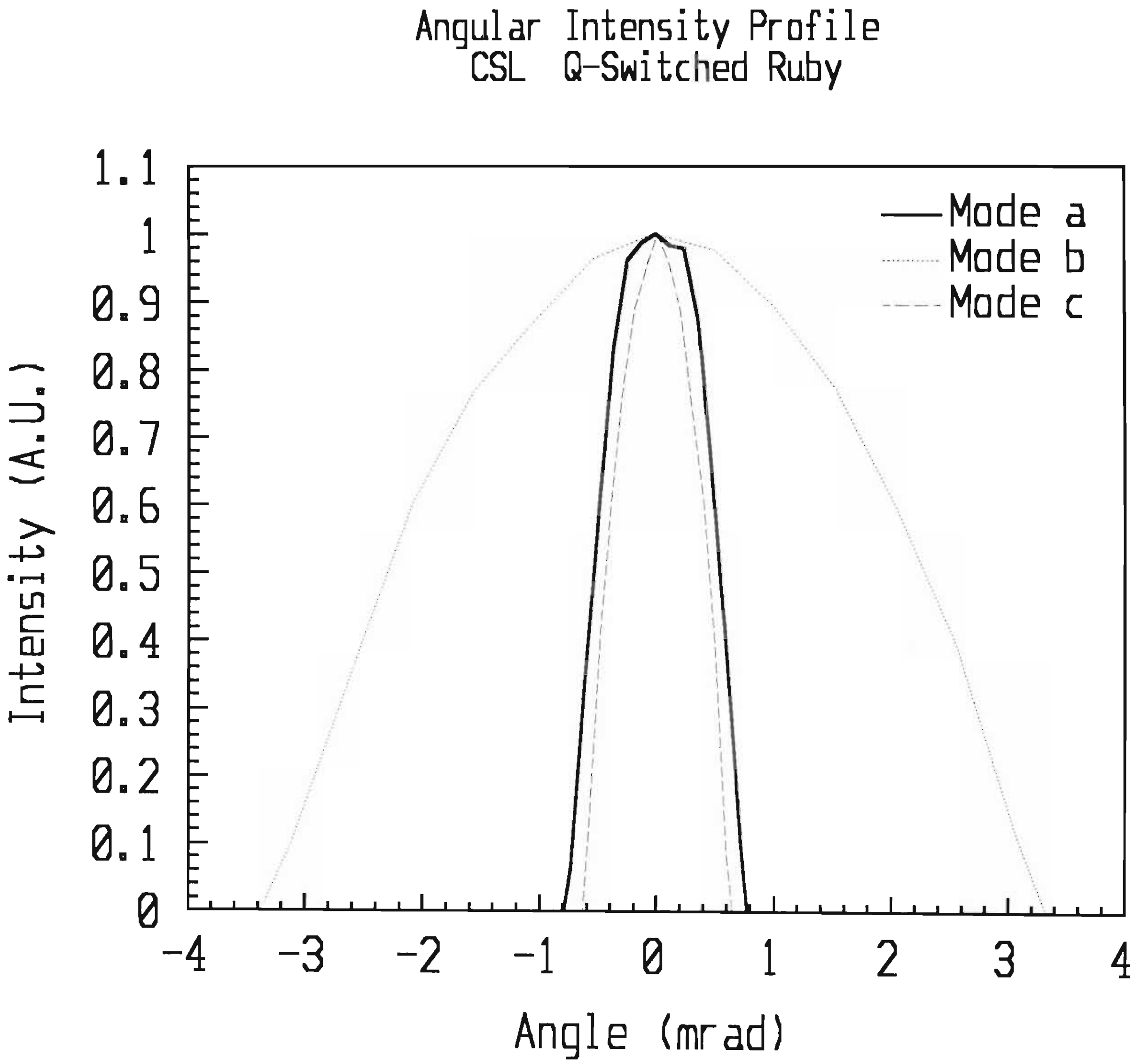

Fig.4.3.13 Angular Intensity profile of the lascr beam for mode a,b and c

4.3.10 DOUBLE PULSE

In some early results we observed the formation of a double laser pulse. The system was then operated in Mode a, but the distance between the CSL and the full reflector (R1) was d2=40cm. In figures 4.3.14 and 4.3.15 we show the evolution of the stability parameter, cavity magnification and losses for this specific configuration.

d=250cm, d1=25cm, d2=40cm, L1=200cm.

The double pulsing is easily explained referring to figure 4.3.2. The plane parallel configuration is first achieved when F_{CSL}=25cm, soon after the losses are high again. Later, as the F_{CSL}=40cm the losses are low again. The losses are low twice at a time distance of few μs which is the delay between the two pulses as experimentally measured.

Double pulsing must be avoided. As can be seen in figure 4.3.2 the radiation density on the full reflector during the first pulse can be very high and we observed surface damages on the full reflector coating. In figure 4.3.16 we have shown the intensity waveform of the double pulse.

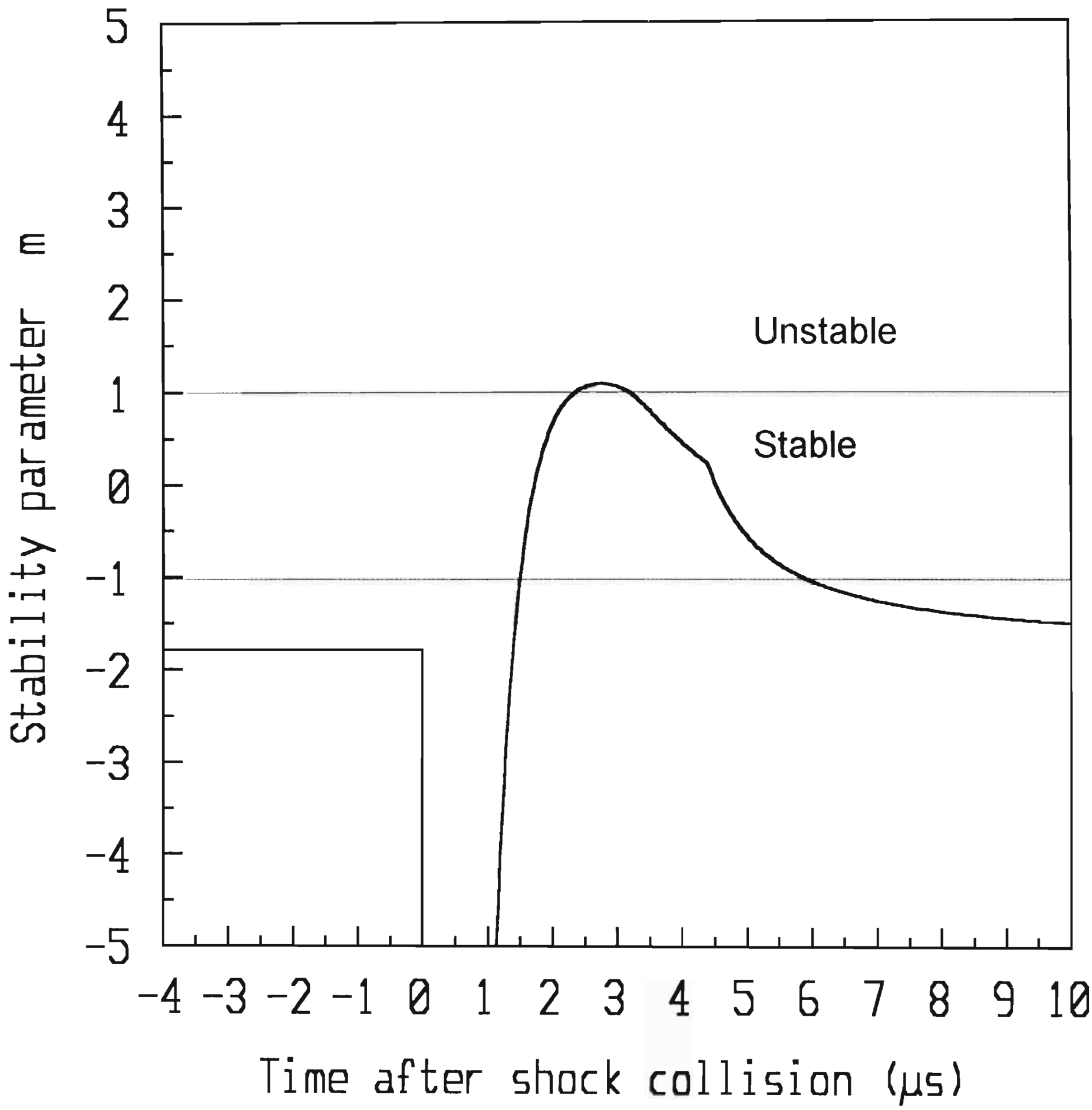

Fig.4.3.14 Stability parameter **m** for the double pulse configuration.

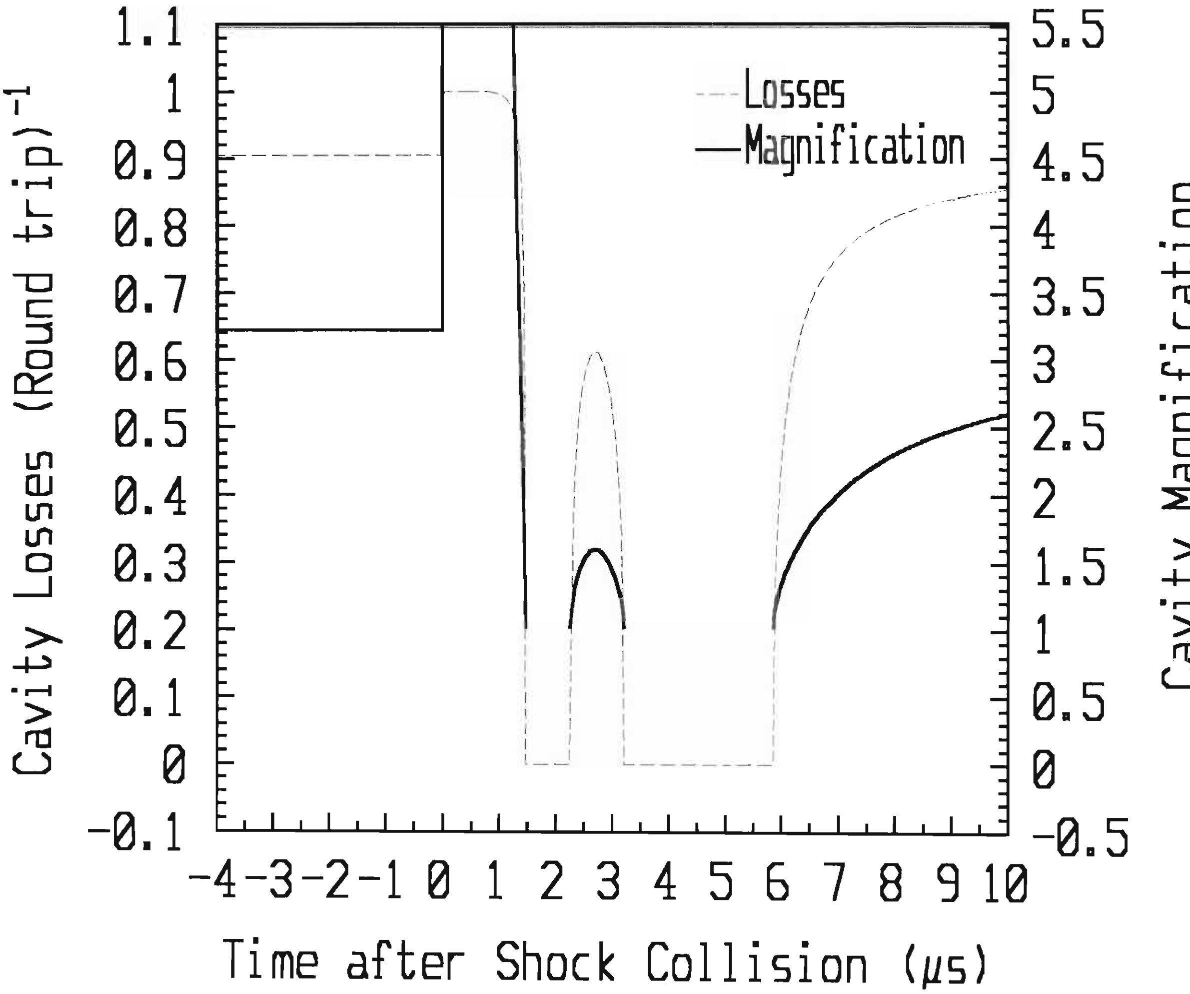

Fig.4.3.15 Magnifications and losses in the conditions in which double pulsing is observed.

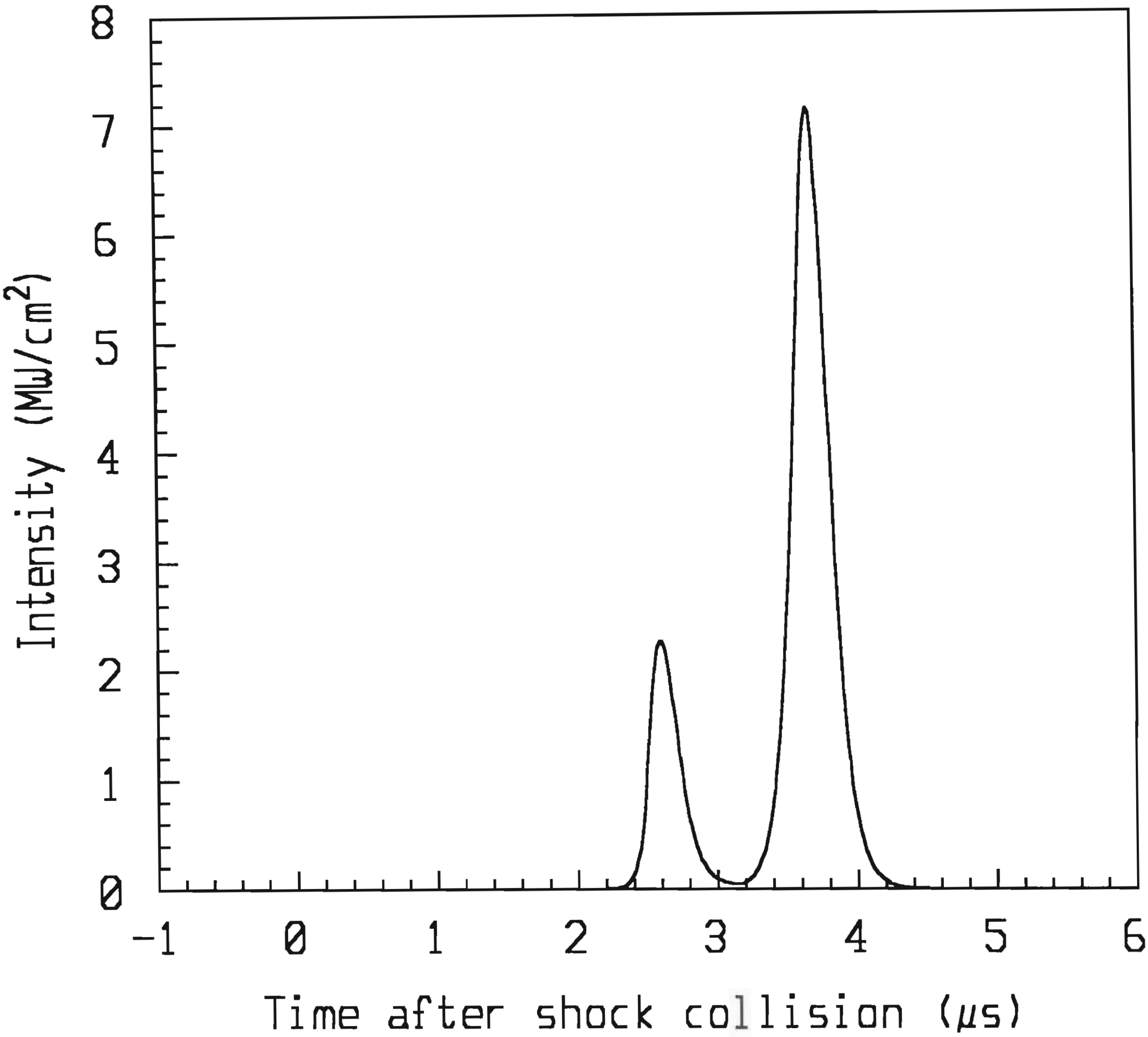

Fig.4.3.16 Modelled laser double pulse.

	E_{max}/J	$\Delta t/ns$	Φ/mm	Div (mrad)
Mode a	2.0	225	10	1
Mode b	0.13	105	2.8	4
Mode c	3.0	200	10	0.9

Table.4.3.2. Summary of the computational results of the Colliding Shock Q-Switching. E is the energy, Δt is the FWHM pulse-duration, Φ is the laser beam diameter and div is the divergence.

4.4 CONCLUSIONS

Finally in Table 4.3.2 we report the computed values of the laser energy, pulse-length, beam diameter and divergence to be compared with the experimental values of Table 4.3.1. Reasonable agreement is obtained between experimental and measured values bearing the approximations of the one dimensional model in mind.

In conclusion we have demonstrated a novel Q-Switching configuration that can use only gas optics. The advantages of the method are: no laser damage threshold, both for high peak power and average power; absence of polarisation and polariser. A major disadvantage is the necessity of having a long cavity which results in a long laser pulse. Improvements in the colliding shock lens design and performance may correct this problem by scaling down the CSL f-number.

CHAPTER 5:
OPTICAL QUALITY OF THE COLLIDING SHOCK LENS

In chapter 3 we recorded some interferograms of the colliding shock lens (CSL) at various delays, by using an electrically synchronised probe nitrogen laser. In that chapter we interpreted the interferograms and determined the optical path length (OPL) radial profiles (shown in figures 3.3.13 to 3.3.16 and in table 3.3.1) and the optical aperture of the device (reported in table 3.3.2) of the enclosed version of CSL.

The present chapter is completely dedicated to the determination of the optical quality of the CSL through the analysis of these OPL profiles.

In section 5.1 we will compute the CSL's focal length by using simple ray optics. Then we determine the refractive index radial profile, with the working hypothesis that the refractive index is constant along any line parallel to the optical axis. In the following section 5.2 we will define a focal plane for the CSL and we will compute the intensity profile for a uniform input laser beam. The two cases of diffraction limited and divergence limited laser beams are examined.

5.1 THE ANALYSIS OF THE INTERFEROGRAMS

We are going to analyse the radial profile of the OPL inside the colliding shock lens. The experimental profiles, together with a polynomial fit, have already been shown in figures 3.3.11 to 3.3.14 and in table 3.3.1. For clarity and easier reference of the later results we will show again in figures 5.1.1, 5.1.2, 5.1.3 and 5.1.4 the polynomial fit of the OPL radial profiles.

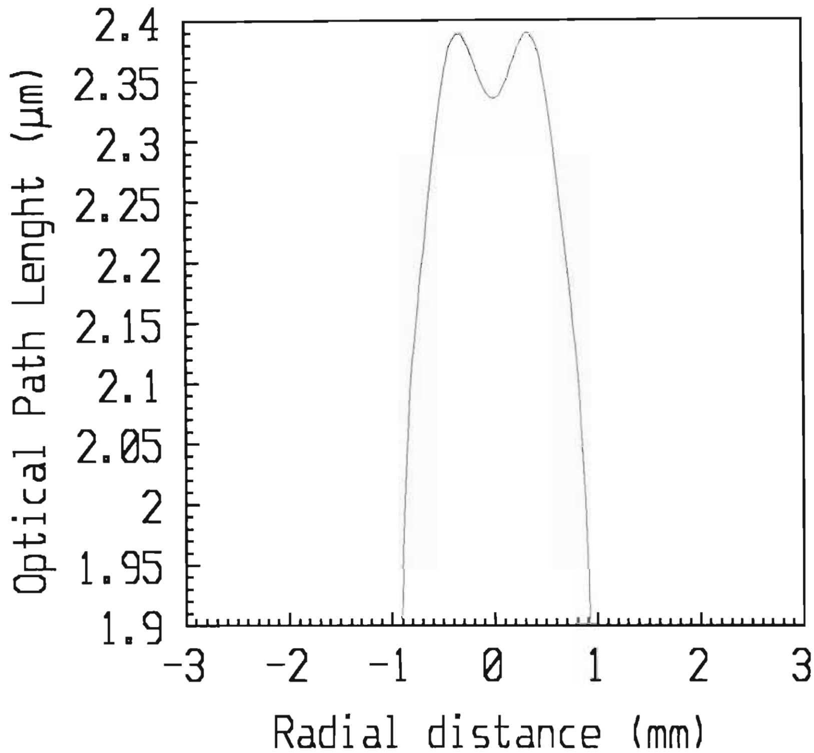

Fig.5.1.1 OPL radial profile from interferogram in fig.3.3.7. Delay=2.1μs after the shock collision. 8th order polynomial.

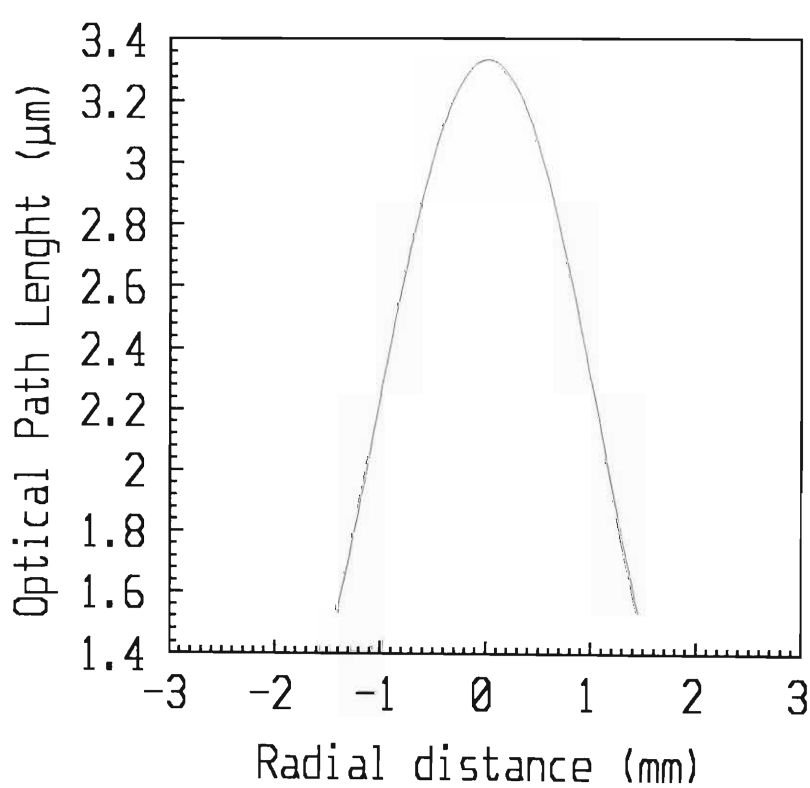

Fig.5.1.2 OPL radial profile from interferogram in fig.3.3.8. Delay=2.7μs after the shock collision. 4th order polynomial

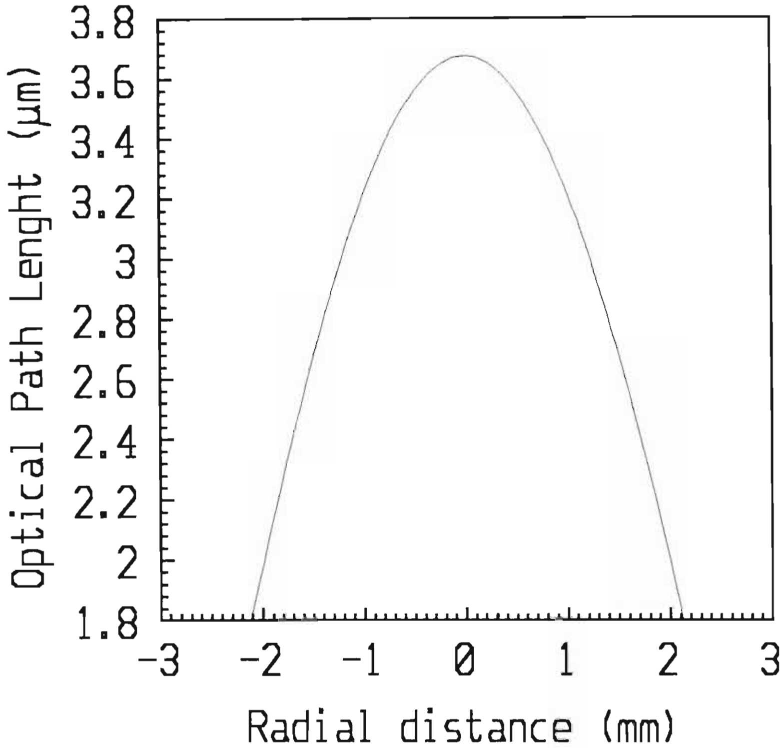

Fig.5.1.3 OPL radial profile from interferogram in fig.3.3.9. Delay=4.2μs after the shock collision. 4^{th} order polynomial.

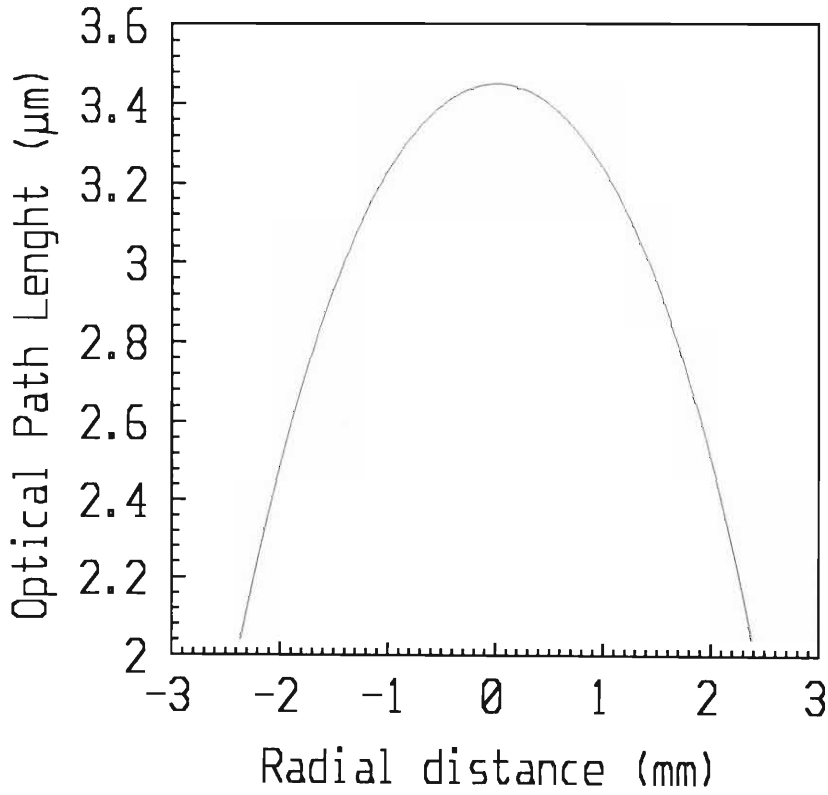

Fig.5.1.4 OPL radial profile from interferogram in fig.3.3.10 Delay=5.0μs after the shock collision. 4^{th} order polynomial.

5.1.1 FOCAL LENGTH RADIAL PROFILES

In the approximation of geometrical optics, when a light ray passes through a thin phase object, such as the colliding shock lens, its angular deflection coincides with the radial derivative of the optical path length (equation 3.3.5). By thin phase object we just mean that the deflection of the light ray within the phase object is negligible.

Due to the radial symmetry, the polynomial fit contains only the even coefficients, which are reported in table 3.3.1.

$$\tilde{n}(r) = a_0 + a_2 r^2 + a_4 r^4 + \ldots + a_{2n} r^{2n} \qquad 5.1.1$$

$$\theta(r) = \frac{\partial \tilde{n}}{\partial r} = 2a_2 r + 4a_4 r^3 + \ldots + 2na_{2n} r^{2n-1} \qquad 5.1.2$$

It is then straightforward to compute the CSL focal length from the OPL polynomial fit coefficients.

$$f(r) = -\frac{r}{\tan\left(\dfrac{\partial \tilde{n}}{\partial r}\right)} \qquad 5.1.3$$

From the equation 5.1.3 we find how the focal length of the device varies with the radial distance. This is a quantitative measurement of the longitudinal aberrations of the lens. For an ideal lens the focal length is independent of r. If we stop the polynomial expansion to the second order in equations 5.1.1 we have an ideal lens for paraxial rays, while the higher expansion terms introduce longitudinal aberrations. In the next four figures we show the radial focal length profiles. First, we can note from figure 5.1.5 that the profile in figure 5.1.1 does not focus at all. The focal length varies too sharply with the radial distance. Moreover, in the central region, due to the local negative curvature of the OPL (the 'hole' in the density distribution), the CSL acts as a diverging lens. This profile was taken too early after the shock collision for focusing to occur.

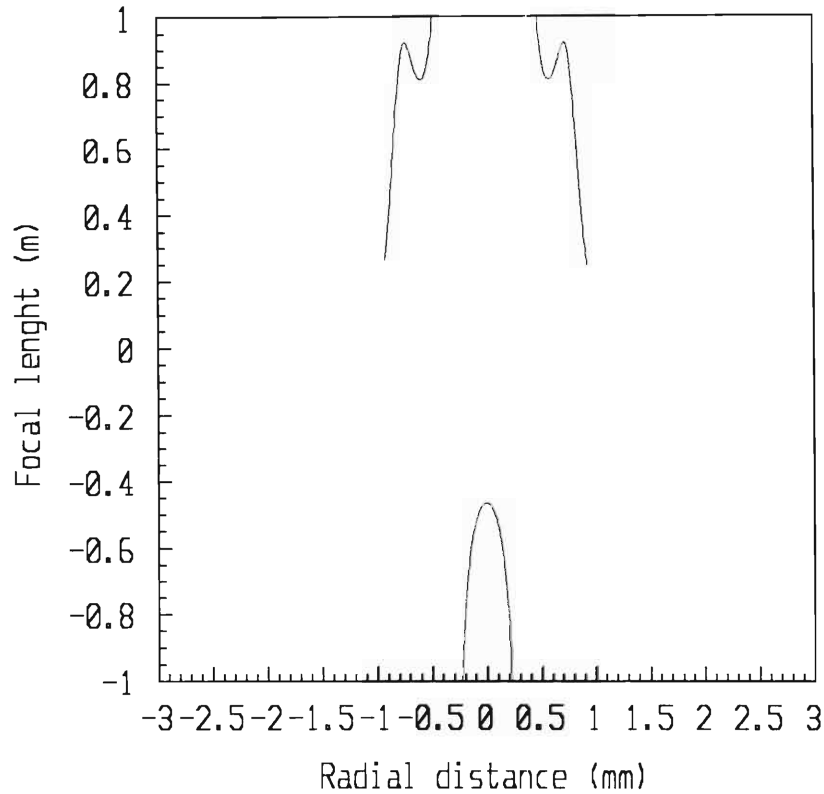

Fig.5.1.5 Focal length vs Radius (2.1μs after collision).

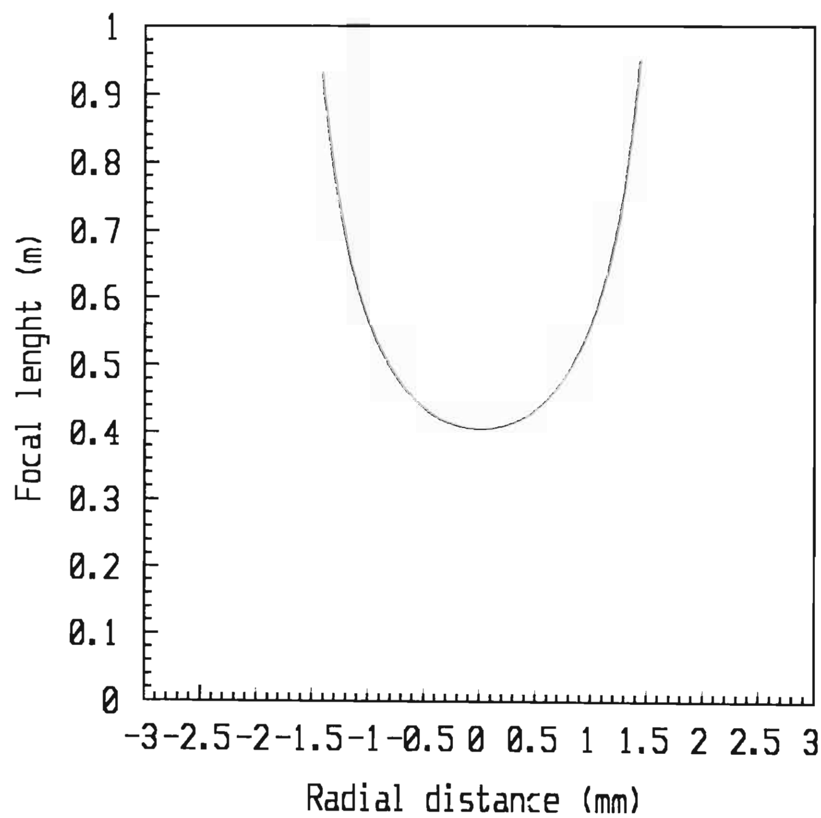

Fig.5.1.6 Focal length vs Radius (2.7μs after collision).

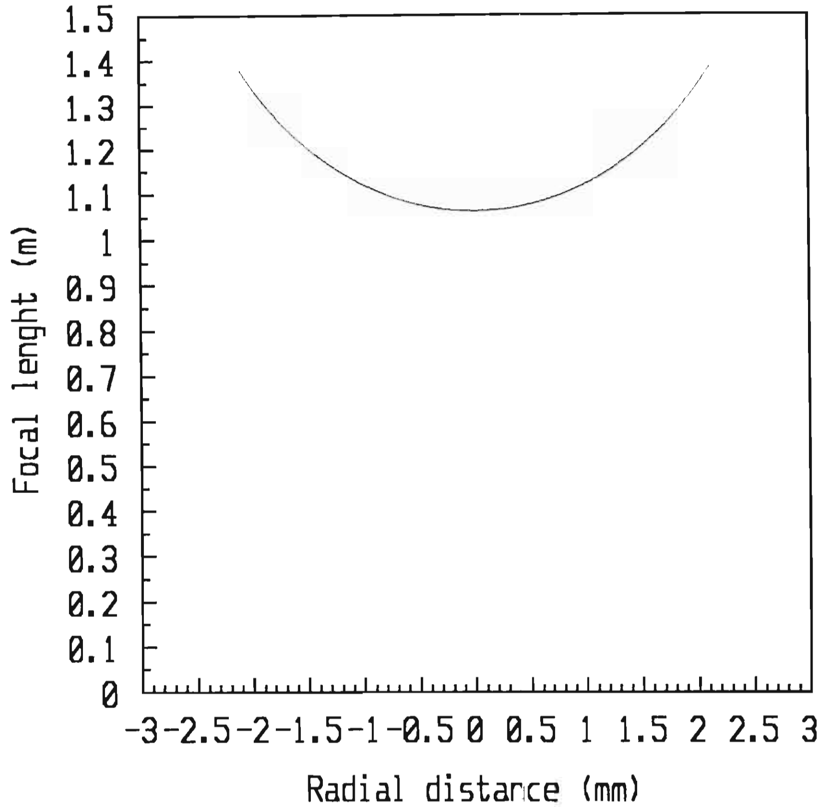

Fig.5.1.7 Focal length vs Radius (4.2μs after collision).

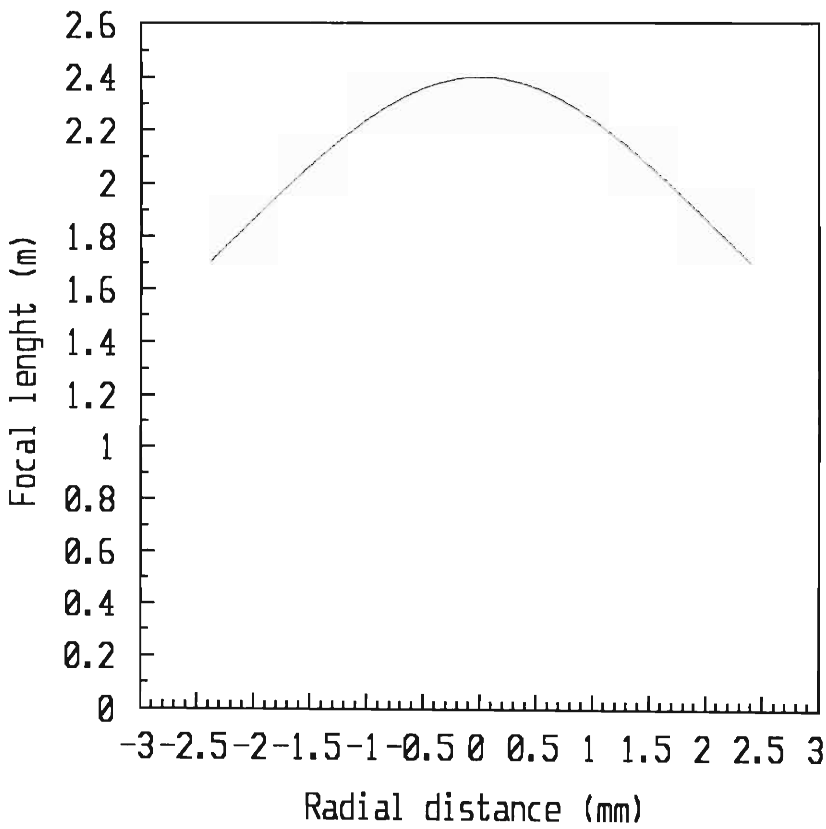

Fig.5.1.8 Focal length vs Radius (5.0μs after collision)

As the time passes, the density profile becomes smoother and the focal length increases, the radial profile, initially convex, becomes flatter and flatter, until about 5.0μs after collision when it becomes concave. We expect the optimum performances of the lens during this convexity transition period.

5.1.2 REFRACTIVE INDEX PROFILES

In order to compute the refractive index (or density) profile from the OPL profile we have the two following problems:

1) We already mentioned in section 3.3. that it is impossible to compute the refractive index three dimensional spatial profile from the interferograms, unless we set some very stringent hypotheses about the symmetry of the profile itself (such as radial or cylindrical).

2) If the fringes are discontinuous across the shock-front, only the relative value of the fringe-shift can be measured in the interferograms.

Concerning the first problem, our approach is the following: we take the refractive index to be constant along the rays' trajectories inside the cigar shaped graded index region.

As regards the second problem, we have little to do, and we have to accept that only the relative refractive index profile can be determined.

It follows that the results that we will be getting will be approximate because of the first statement and less than correct because of the second. The approximation that we introduce by taking the refractive index to be constant along the rays' trajectories is unavoidable. The error that is introduced by the discontinuity of the fringes across the shock-front could be avoided by a better measurement. However it is complex to solve the fringe pattern across the shock-front while retaining enough sensitivity where the density profile is smooth.

Given that, let us compute the refractive index profile. If the refractive index is constant along the trajectories, we have:

$$\tilde{n}(r) = 2\int_0^{L(r)} n(r,z)dz = 2n(r)L(r) \qquad 5.1.4$$

In figure 5.1.9, we report the geometry of the system.

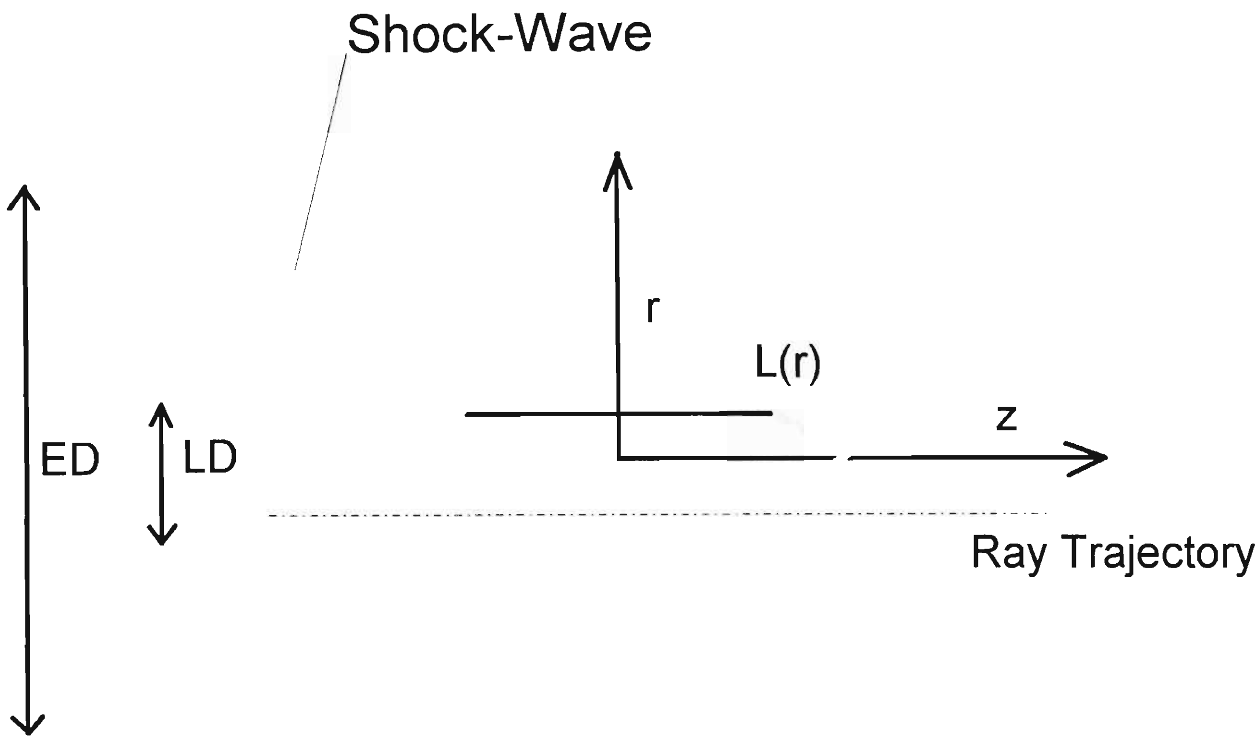

Fig.5.1.9 Calculation of the refractive index inside the CSL. The refractive index depends only on the radial distance r. Electrical diameter ED=3cm. Lens diameter LD.

From figure 5.1.9, it is easy to find a geometrical expression for the function L(r):

$$L(r) = 2\sqrt{\left(\frac{ED}{2} + \frac{LD}{2}\right)^2 - \left(\frac{ED}{2} + r\right)^2} \qquad 5.1.5$$

Equations 5.1.5 and 5.1.4 allow one to compute the approximate value of the refractive index difference from unity inside the CSL. The computed quantity is proportional to the average gas density at the position **r**.
In the next four figures (5.1.10 to 5.1.13) we show the refractive index radial profiles. The fringe discontinuity across the shock-front is significant in the first two interferograms, where the shock-front is more energetic, while in the last two interferograms we are quite confident that the measured value of the refractive index is close to the real one. Near to the edges of the lens we note a sharp increase of the refractive index. This effect can be understood by referring to the single spherical shock radial density profile, shown in figure 3.3.4, as the shock-tail of the expanding cylindrical shock. In the light of these results it is evident that the 'cigar' geometry plays a vital role in the performances of the CSL. The refractive index profiles shown in the next four pictures can focus light only when 'wrapped' in the geometry of the colliding shock lens. The approximation that we made by letting the refractive index be constant in **z** is essential for the calculation of the refractive index and we cannot calculate anything without it. Through this hypothesis we discovered the importance of the 'cigar' geometry of the colliding shock lens. However, we expect the refractive index to be a function of **z** too, and our hypothesis must be regarded as a zero-order approximation. The real experimental quantity that we measure is the fringe shift, which is the refractive index integral along the rays' trajectories. Gas-dynamic simulations of colliding shocks, and their comparison with the experimental results, can give a deeper insight into the detailed spatial structure of the gas density distribution [Buccellato B 1994].

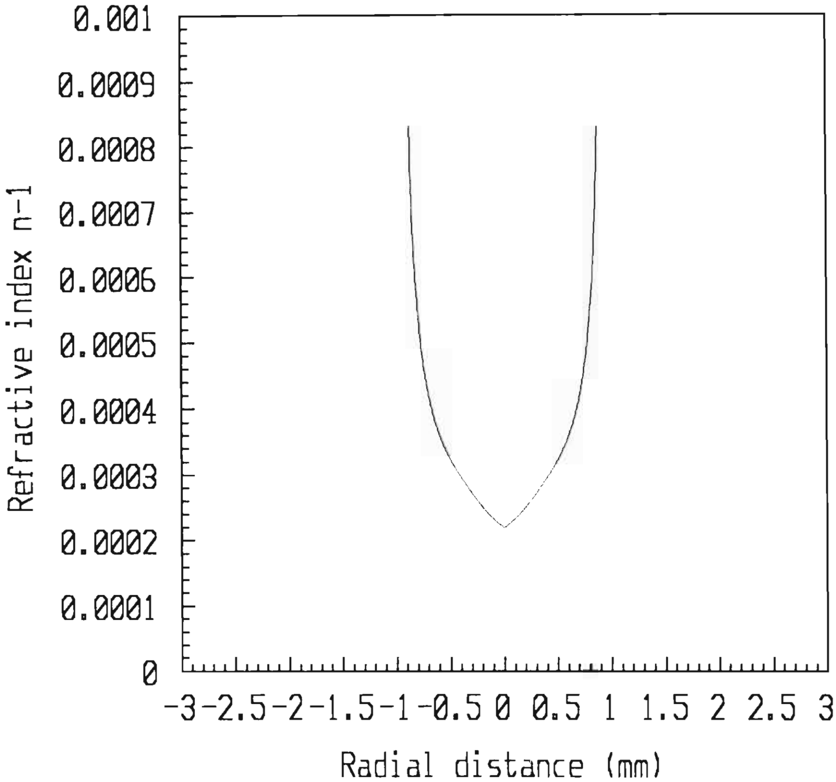

Fig 5.1.10 Refractive index profile 2.1μs after collision

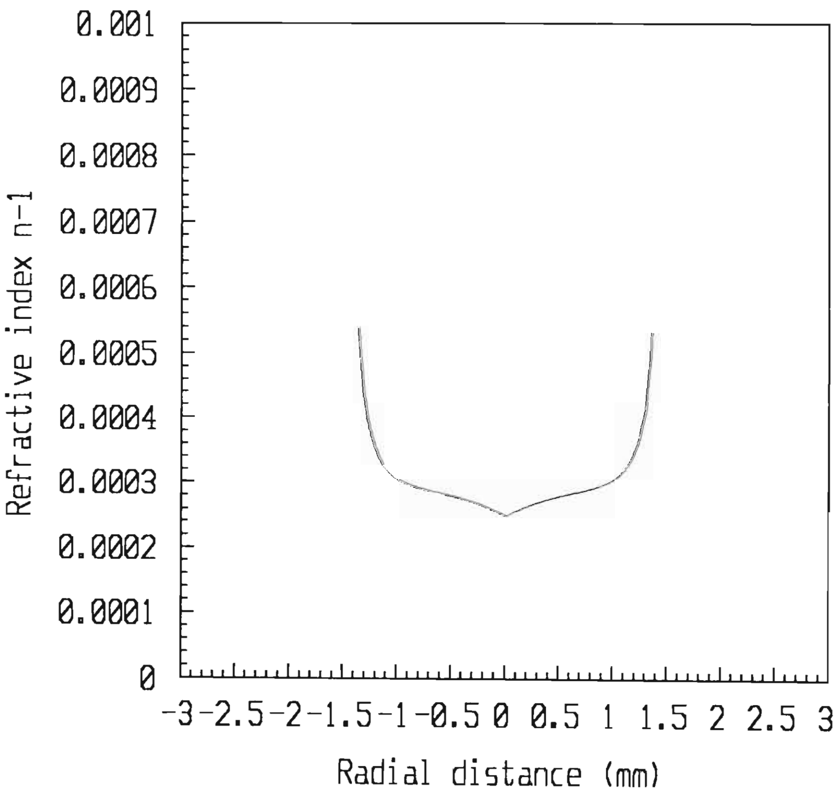

Fig 5.1.11 Refractive index profile 2.7μs after collision

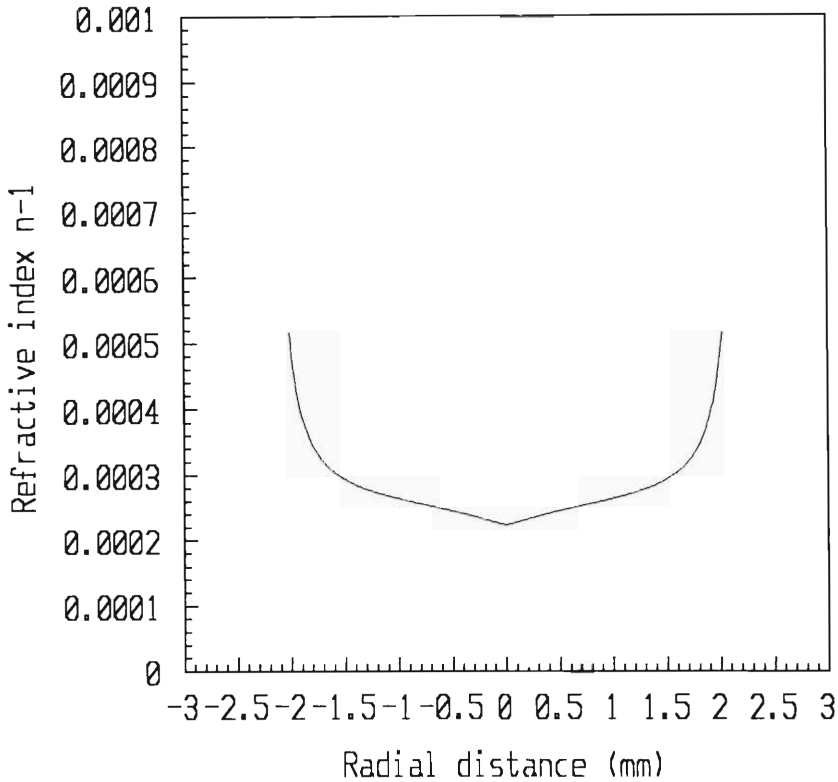

Fig 5.1.12 Refractive index profile 4.2μs after collision

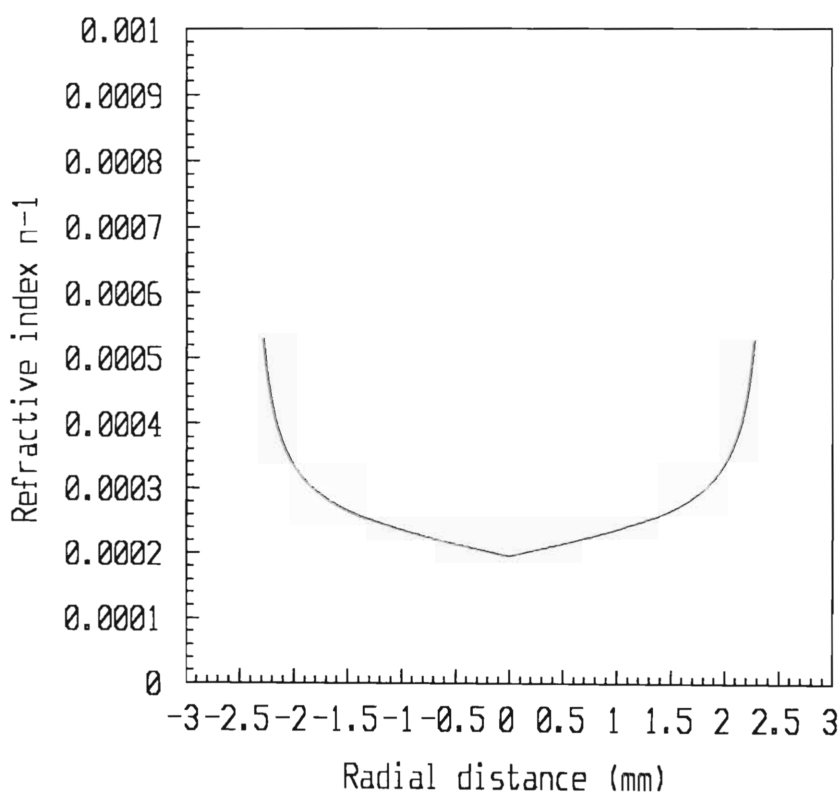

Fig 5.1.13 Refractive index profile 5.0μs after collision

5.2 REFRACTIVE FRINGES AND RADIAL INTENSITY PROFILES

In this section we will perform some ray tracing into the OPL radial profiles, or better into the polynomial fits of figures 5.1.1 to 5.1.4. The angular deflection of the light rays as they go through the central region of the CSL is simply given by the gradient of the radial OPL profile. In this respect we consider the refractive index distribution to be squeezed on a thin disk avoiding the solution of the ray equations in a graded index medium. The radial intensity profiles at any image plane after the CSL for an input laser beam are numerically computed with the help of diffraction and refraction theory. As an initially plane wave-front is propagated through the OPL radial profile a radial phase term is added and the wave-front is consequently curved. The wave-front is propagated through a plane aperture, due to the sharp refractive index discontinuity introduced by the shock-fronts, onto the colliding shock plane. The result of this computation is the fringe pattern for a laser beam which is diffraction limited by the aperture of the colliding shock lens. In order to include in our description the effect of the divergence of the input laser beam, finally a spatial averaging on the image plane can be included. For a better comparison with the experimental results, we utilised the laser beam parameters (wavelength and divergence) of the spatially filtered and expanded nitrogen laser described in Chapter 3.

5.2.1 DIVERGENCE AND DIFFRACTION

The divergence of an expanded and spatially filtered laser beam can be estimated from the spatial filter parameters. The spatial filter geometry is shown in figure 5.2.1. We can imagine the pinhole Φ as a spatially incoherent source of light. The filtered and expanded nitrogen laser beam divergence is then:

$$\Delta\theta^{div} = \frac{\Phi_{sp}}{f_{sp}} = \frac{50 \cdot 10^{-6}}{0.15} = 3.3 \cdot 10^{-4}\,\text{rad} \qquad 5.2.1$$

If we focus such laser beam with an ideal, aberration free lens of focal length f, the minimum spot diameter at the focus is:

$$\Phi^{div} = \Delta\theta^{div} f \qquad 5.2.2$$

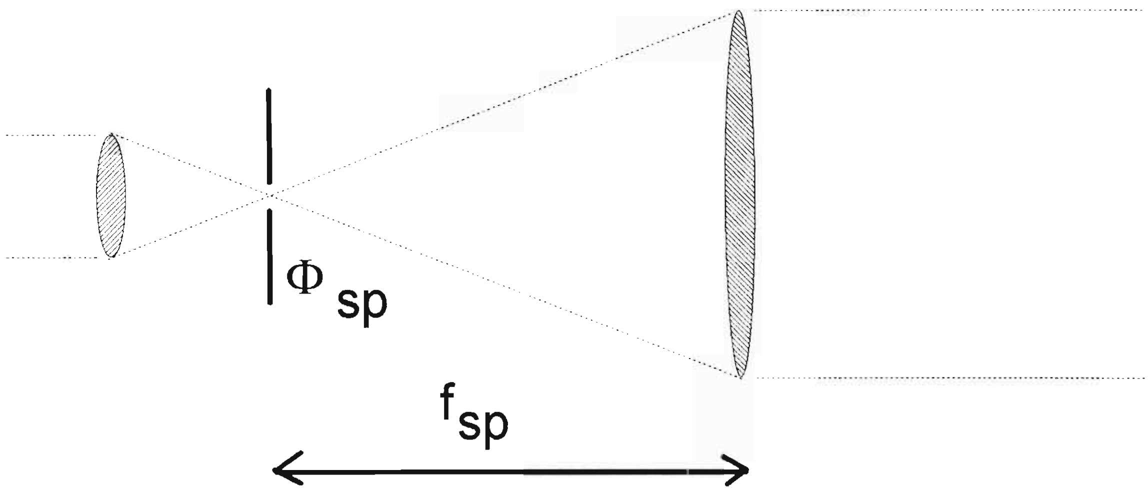

Fig.5.2.1 Nitrogen laser spatial filter and expansion optics. $\mathbf{f_{sp}=15cm}$, $\mathbf{\Phi_{sp}=50\mu m}$.

Let us consider diffraction. For a circular beam. the diffraction theory (1.6) tells us that:

$$\Delta\theta^{diff} = \frac{2.44\lambda}{d} \qquad \lambda = 337nm \qquad 5.2.3$$

$$\Phi^{diff} = \Delta\theta^{diff} f \qquad 5.2.4$$

The minimum spot size taking only diffraction into account depends on the beam or the lens diameter, the smallest of the two, that we call **d**.

The minimum spot size due to divergence is constant in **d**. Both the diffraction limited and divergence limited spot diameters increase linearly with the focal length. At small diameters **d** the effect of diffraction will be larger than the effect of divergence, while at larger diameters **d**, it will be the opposite. We call $\mathbf{d}^*$ the lens diameter at which the two effects are equal:

$$d^* = \frac{2.44\lambda}{\Delta\theta^{div}} = 2.5 \cdot 10^{-3}\,mm \qquad 5.2.5$$

We can separate the two effects by saying that for diameters which are smaller than $\mathbf{d}^*$, the focal spot size is limited by diffraction, while at larger diameters the focal spot size is limited by divergence. Consider now the colliding shock lens as an ideal aberration free lens. Taking into account the lens diameter, we note that for the small CSL (described in section 3.2) we had to perform a diffraction analysis, while for the big enclosed CSL (section 3.3) we should rather take into account the divergence of the probe laser beam. Given our intermediate operating conditions, both the effect of diffraction and divergence must be taken into account.

5.2.2 FRAUNHOFER DIFFRACTION THEORY OF THE COLLIDING SHOCK LENS

In Chapter 1 we found the Fraunhofer formula for the diffraction produced by an aperture on a plane screen. We shall apply the diffraction theory in order to compute the intensity profile and the fringe pattern at any distance from the CSL, including the effect of the longitudinal aberration in our discussion. In figure 5.2.2 we show the geometry of the system. According to the diffraction theory [Guenther 1990] each point **P0** of the source generates a spherical wave-front. The electric field at the lens plane depends on the source geometry and on the distance **r**:

$$E(x_L, y_L) = \frac{iA}{\lambda r'} \iint f(x_S, y_S) \exp\left(-i\vec{k} \cdot \vec{r}\right) dx_S dy_S \qquad 5.2\ 6$$

In the hypothesis that the diameter of the aperture is much larger than the distance between the source and the aperture, we can introduce the following approximation (the sagittal approximation):

$$r \cong r' + \frac{(x_L - x_S)^2}{2r'} + \frac{(y_L - y_S)^2}{2r'} \qquad 5.2.7$$

The electric field at the lens plane can then be rewritten as:

$$E(x_L, y_L) = \frac{iA}{\lambda r'} \exp(-ikr) \iint f(x_S, y_S) \exp\left(-ik\frac{(x_S - x_L)^2}{r'} - ik\frac{(y_S - y_L)^2}{r'}\right) dx_S dx_S$$

5.2.8

The passage through the lens introduces an additional phase shift that renders the wave-front curved.
The phase shift at each point coincides with the optical path length (or OPL) radial profile. As reported earlier in this thesis we do approximate the OPL radial profile with a fourth order polynomial containing only even terms. As a result, the electric field after the beam has passed through the CSL can be expressed as:

$$\Psi(x_L, y_L) = E(x_L, y_L) \exp\left[ika_2\left(x_L^2 + y_L^2\right) + ika_4\left(x_L^2 + y_L^2\right)^2\right] \qquad 5.2.9$$

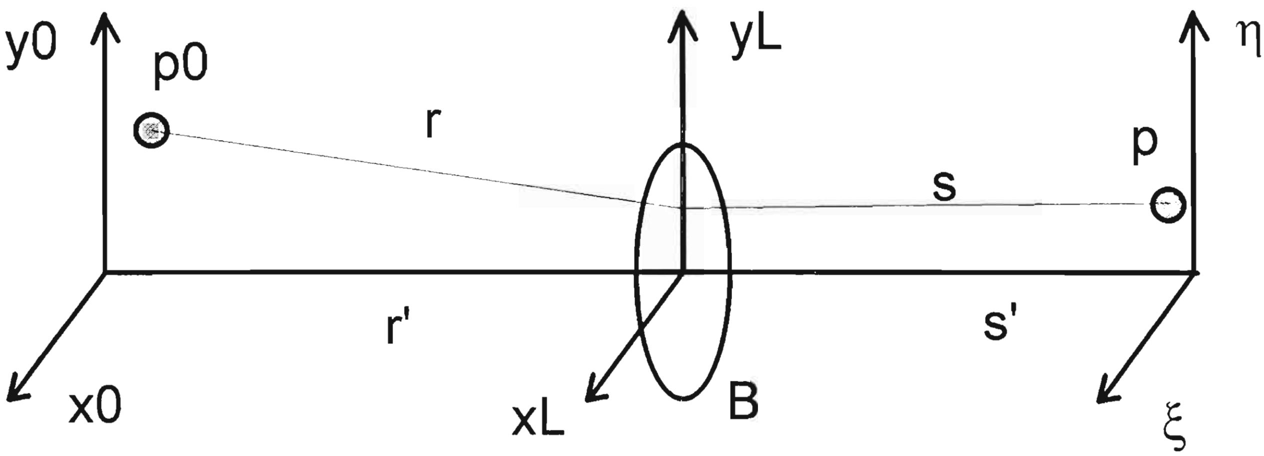

Fig 5.2.2 Geometry of the diffraction from the CSL.

Our goal is to compute the electric field at a point **P** in the η,ξ plane at the distance **s'** from the CSL. Then we propagate the expression for the electric field in equation 5.2.9 of the distance s:

$$U(\eta,\xi) = \iint f_L(x_L, y_L)\Psi(x_L, y_L)\exp\left(-ik\frac{(x_L-\xi)^2}{s'} - ik\frac{(x_L-\xi)^2}{s'}\right)dx_L dy_L \qquad 5.2.10$$

From equation 5.2.10 on we will neglect the normalisation coefficients in front of the propagation integrals. The latter can be easily computed as a final step using the energy conservation condition.

The case of a laser beam, or a well collimated beam, is well represented by a point source at a large distance from the lens. In this case we can imagine that **r'** goes to infinity and the source shape function becomes a two dimensional Dirac delta function:

$$f_S(x_S, y_S) = \delta(x_S, y_S) \qquad 5.2.11$$

The hypothesis of a point source greatly simplifies our calculations:

$$U(\eta,\xi) = \iint \exp\left[-ik(x_L^2 + y_L^2)\left(\frac{1}{2s'} + \frac{1}{2r'} - a_2\right)\right]\exp\left[ik(x_L^2 + y_L^2)^2 a_4\right]$$
$$\cdot\exp\left(ik\frac{x_L\xi}{2s'}\right)\exp\left(ik\frac{x_L\eta}{2s'}\right)f_L(x_L, y_L)dx_L dy_L \qquad 5.2.12$$

In equation 5.2.12 we notice that in the case that the fourth order coefficient of the wave-front curvature is zero ($a_4=0$), the planes at s' and at **r'** are conjugate planes if:

$$\frac{1}{2r'} + \frac{1}{2s'} = a_2\left(=\frac{1}{2f}\right) \qquad 5.2.13$$

In other words, an aberration free lens produces into the conjugate plane of a point source the two dimensional Fourier transform of the lens transmission function.

In our case, given that the lens it is not aberration-free, we cannot define the two conjugate planes and eliminate the second and fourth order radial dependencies of the exponential inside the integral of equation 5.2.12. The result is not straightforward and the intensity pattern at the plane η,ξ must be computed numerically.
In our case the lens is circular having a radius **R** defined by the expanding shock-front. We rewrite equation 5.2.12 in polar coordinates:

$$U(\rho) = \int_0^{2\pi} d\theta \int_0^R \exp\left[-ikr^2\left(\frac{1}{2s'} + \frac{1}{2r'} - a_2\right)\right]\exp\left(ika_4 r^4\right) \cdot \exp\left[i\frac{k}{2s'}\rho r(\cos\theta\cos\varphi + \sin\theta\sin\varphi)\right] r dr \qquad 5.2.14$$

The integration in θ can be performed analytically, to give the following one-dimensional integral:

$$U(\rho) = \int_0^R \exp\left(i\alpha r^2\right)\exp\left(i\beta r^4\right) \cdot J_0(\gamma\rho r) r dr \qquad 5.2.15$$

Where $\mathbf{J_0}$ is the first of the Bessel function and:

$$\alpha = -k\left(\frac{1}{2r'} + \frac{1}{2s'} - a_2\right)$$
$$\beta = ka_4 \qquad \gamma = \frac{k}{2s'} \qquad 5.2.16$$

By taking the square of the integral 5.2.15 we obtain the intensity pattern:

$$I(\rho) = \left|\int_0^R \cos\left(\alpha r^2 + \beta r^4\right) J_0(\gamma\rho r) r dr\right|^2 + \left|\int_0^R \sin\left(\alpha r^2 + \beta r^4\right) J_0(\gamma\rho r) r dr\right|^2 \qquad 5.2.17$$

The integration in 5.2.17 can be accomplished numerically by any of the standard methods. We stress the fact that the sine and cosine terms in 5.2.17 do oscillate very rapidly. Consequently it is opportune to utilise the simplest integration method in order to evaluate the function in the largest number of points as possible whilst keeping the computation time short.

Due to the lens longitudinal aberration we cannot unequivocally define a focal plane for the CSL. We have two possible choices. One is to define the focal plane as the plane at which the intensity pattern presents the maximum peak intensity at the centre. The second would be define the focal plane as the plane where the maximum amount of energy is focused within a given finite radius, say **R***. While the latter option could be more interesting from the point of view of some of the potential applications, the first criterion has the advantage of the simplicity. Moreover it will not produce results much different from the second, if the radius **R*** is small enough. On the same graph we report for comparison the intensity pattern due to an ideal, aberration free, lens having the same focal length.

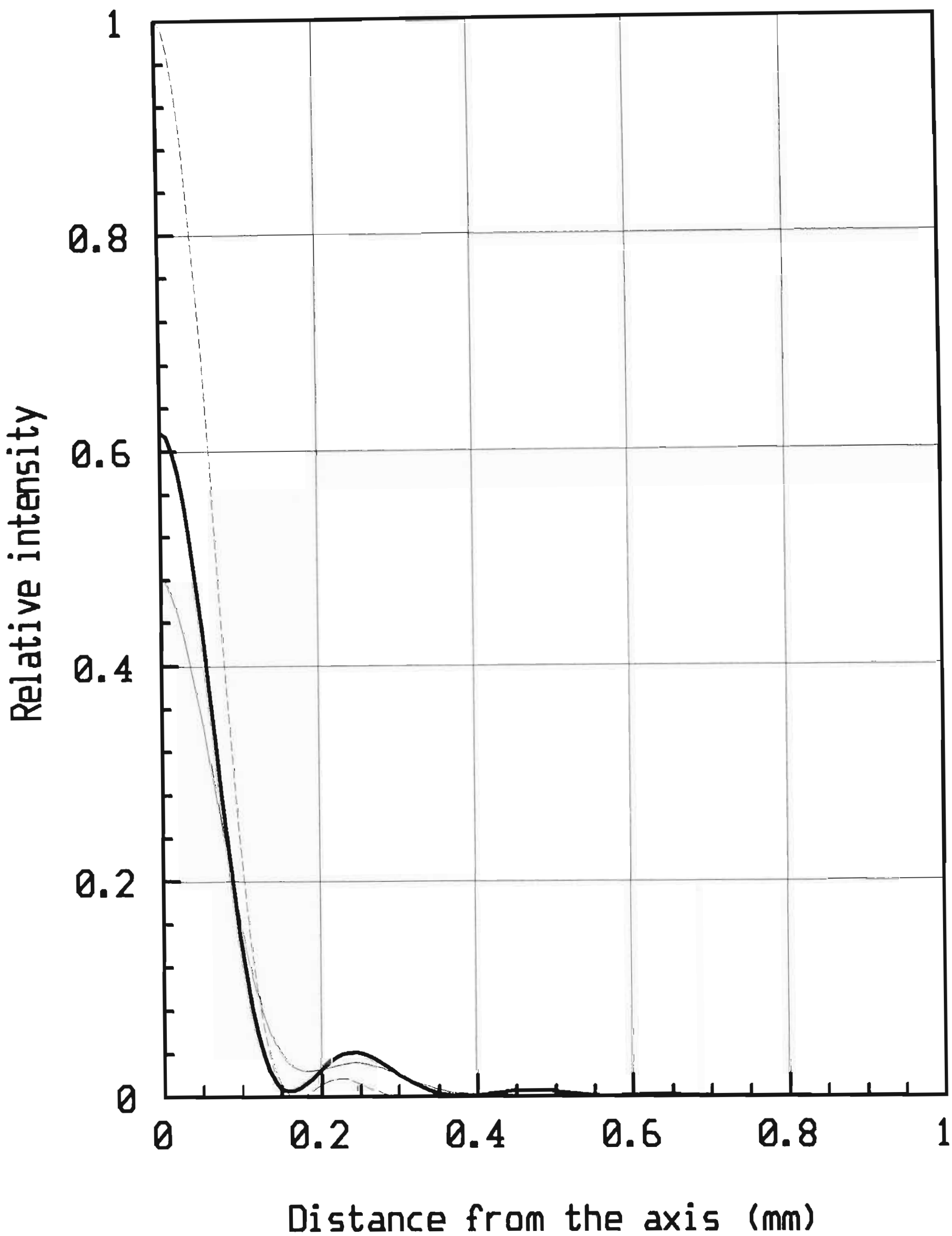

Fig 5.2.3 Intensity in the focal plane of the CSL, solid line. Lens diameter = 2.6mm. Focal length = 53.0cm. The Airy pattern of an equivalent diffraction limited lens is reported for comparison, dashed line. The thin solid line trace shows the intensity profile when the divergence of the probe laser beam is taken into account.

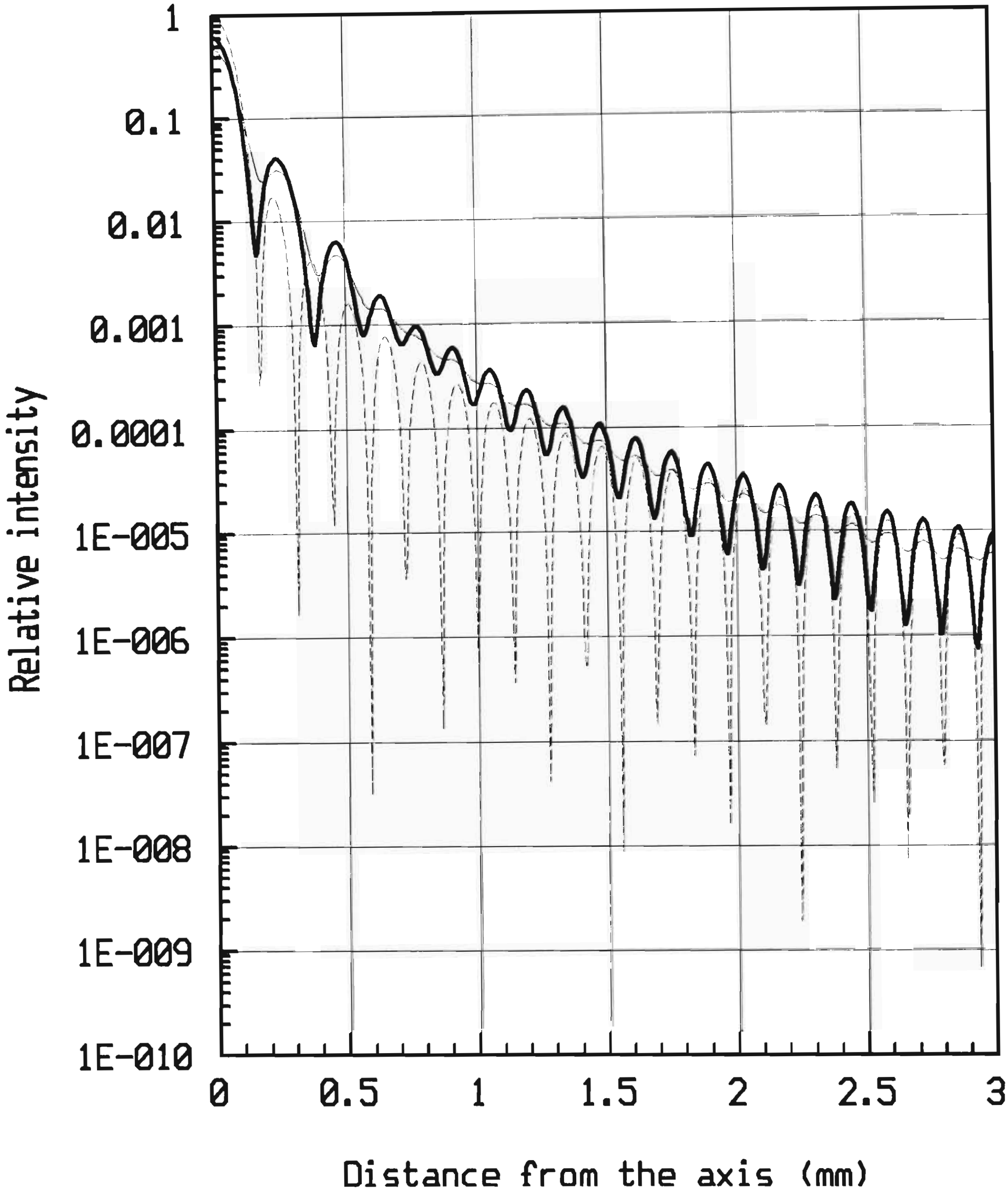

Fig 5.2.4 Intensity logarithm in the focal plane of the CSL, solid line. Lens diameter = 2.6mm. Focal length = 53.0cm. The Airy pattern of an equivalent diffraction limited lens is reported for comparison, dashed line. Note that the Airy pattern is zero at some distances from the optical axis and the log should diverge. This does not happen because of the numerical algorithm utilised to compute the Bessel function J_1. The thin solid line trace shows the intensity profile when the divergence of the probe laser beam is taken into account.

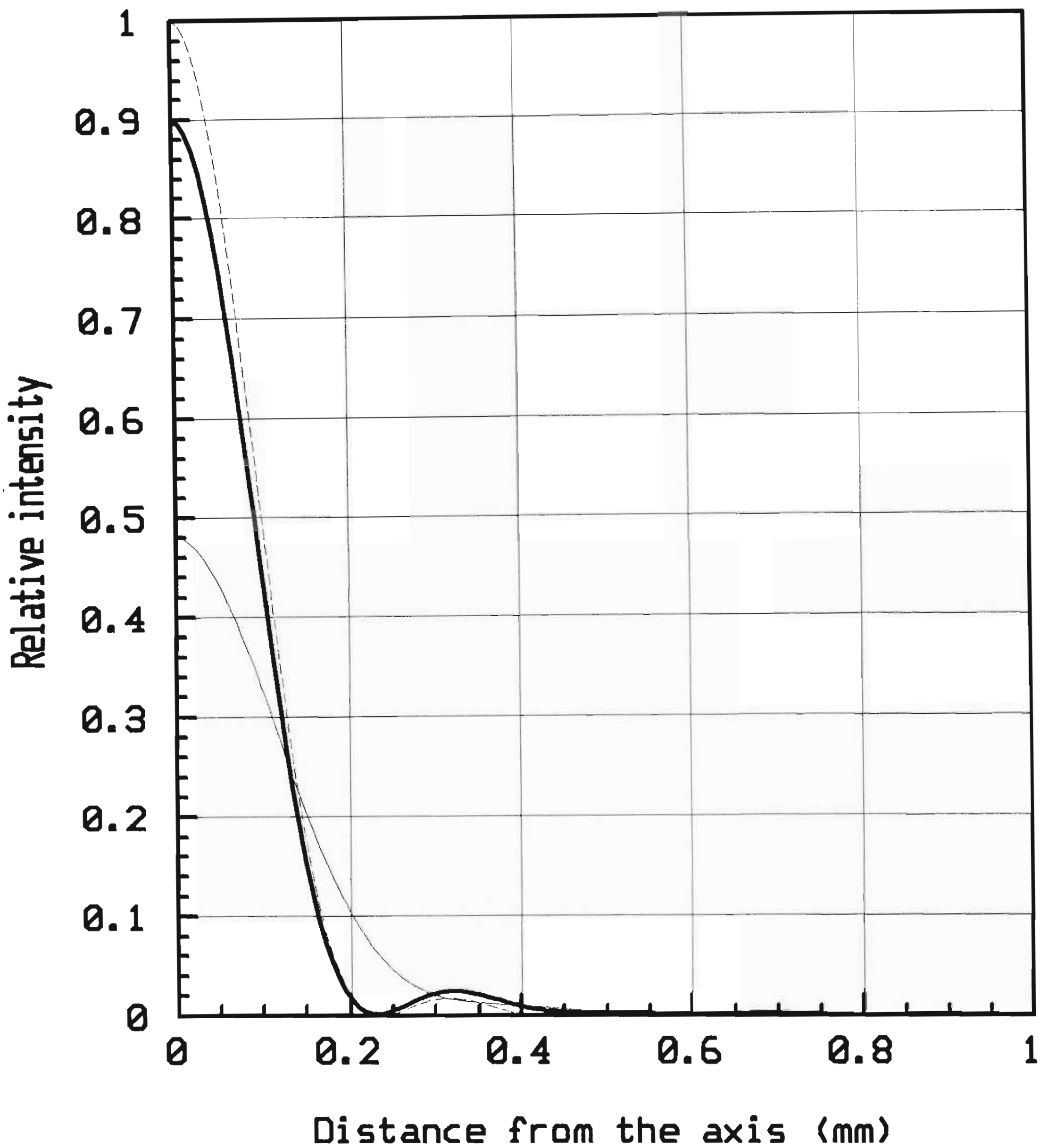

Fig 5.2.5 Intensity in the focal plane of the CSL, solid line. Lens diameter = 4.2mm. Focal length = 120.0cm. The Airy pattern of an equivalent diffraction limited lens is reported for comparison, dashed line. The thin solid line trace shows the intensity profile when the divergence of the probe laser beam is taken into account.

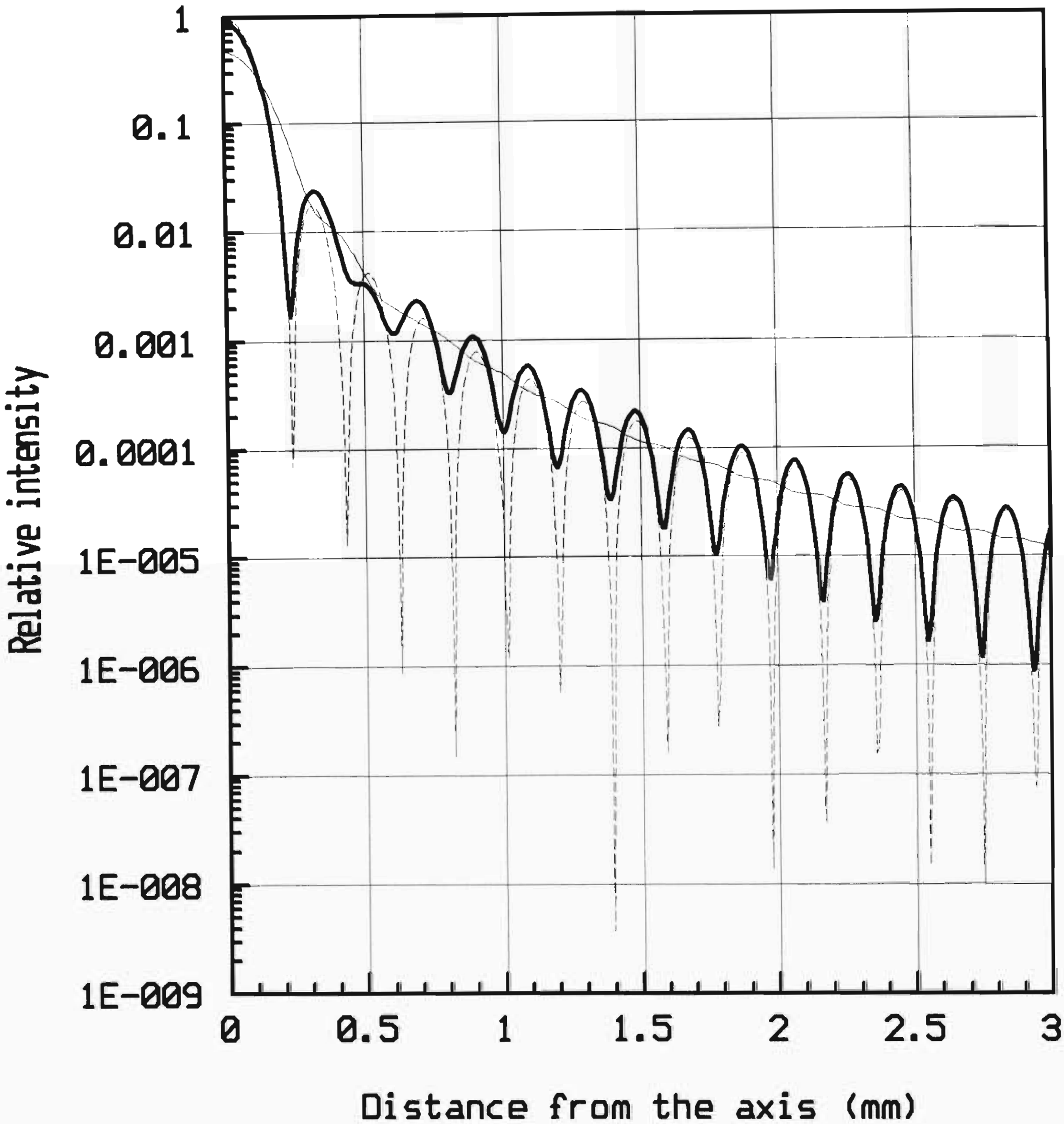

Fig 5.2.6 Intensity logarithm in the focal plane of the CSL, solid line. Lens diameter = 4.2mm. Focal length = 120.0cm. The Airy pattern of an equivalent diffraction limited lens is reported for comparison, dashed line. The thin solid line trace shows the intensity profile when the divergence of the probe laser beam is taken into account.

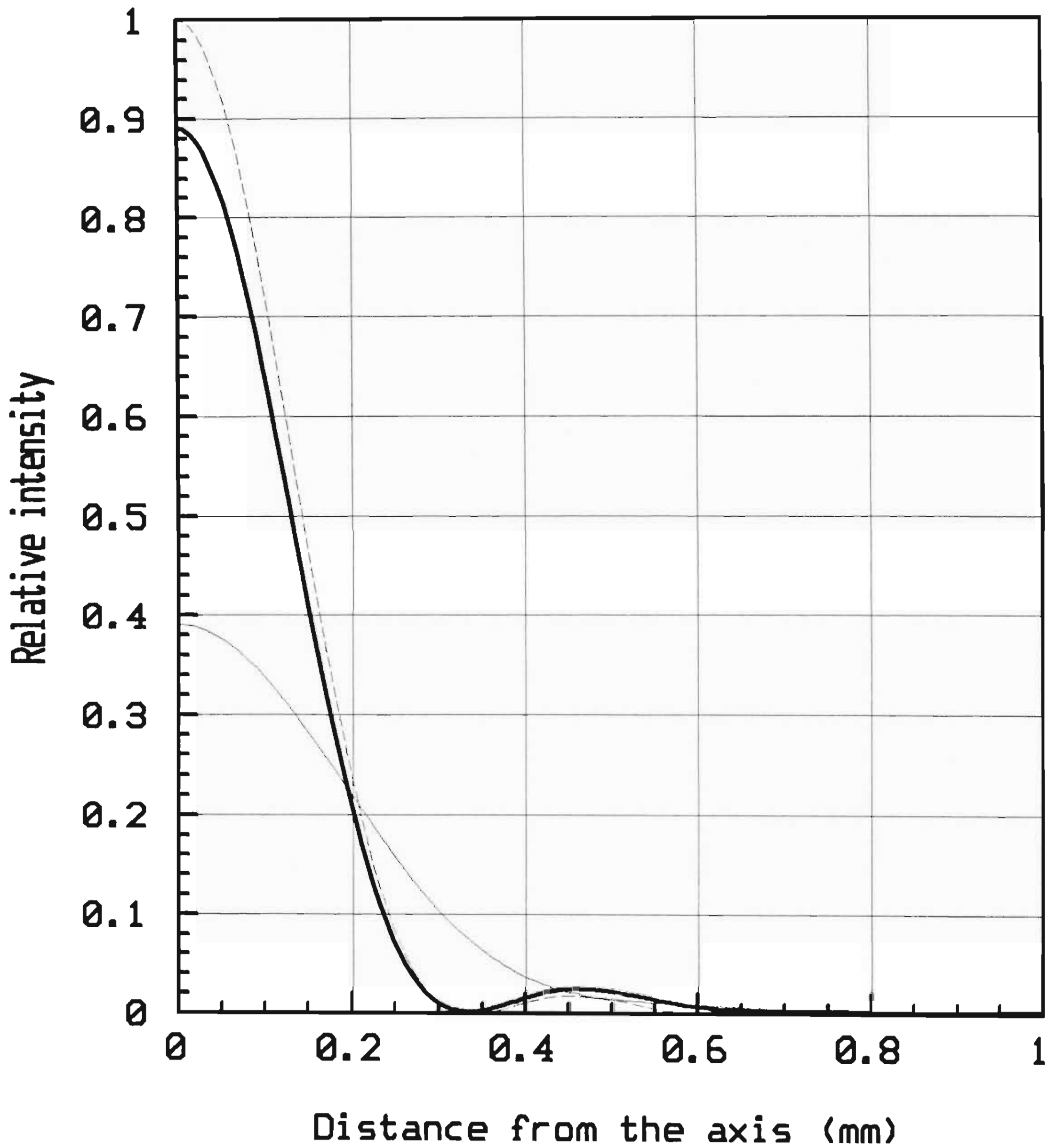

Fig 5.2.7 Intensity in the focal plane of the CSL, solid line. Lens diameter = 4.8mm. Focal length = 197.0cm. The Airy pattern of an equivalent diffraction limited lens is reported for comparison, dashed line. The thin solid line trace shows the intensity profile when the divergence of the probe laser beam is taken into account.

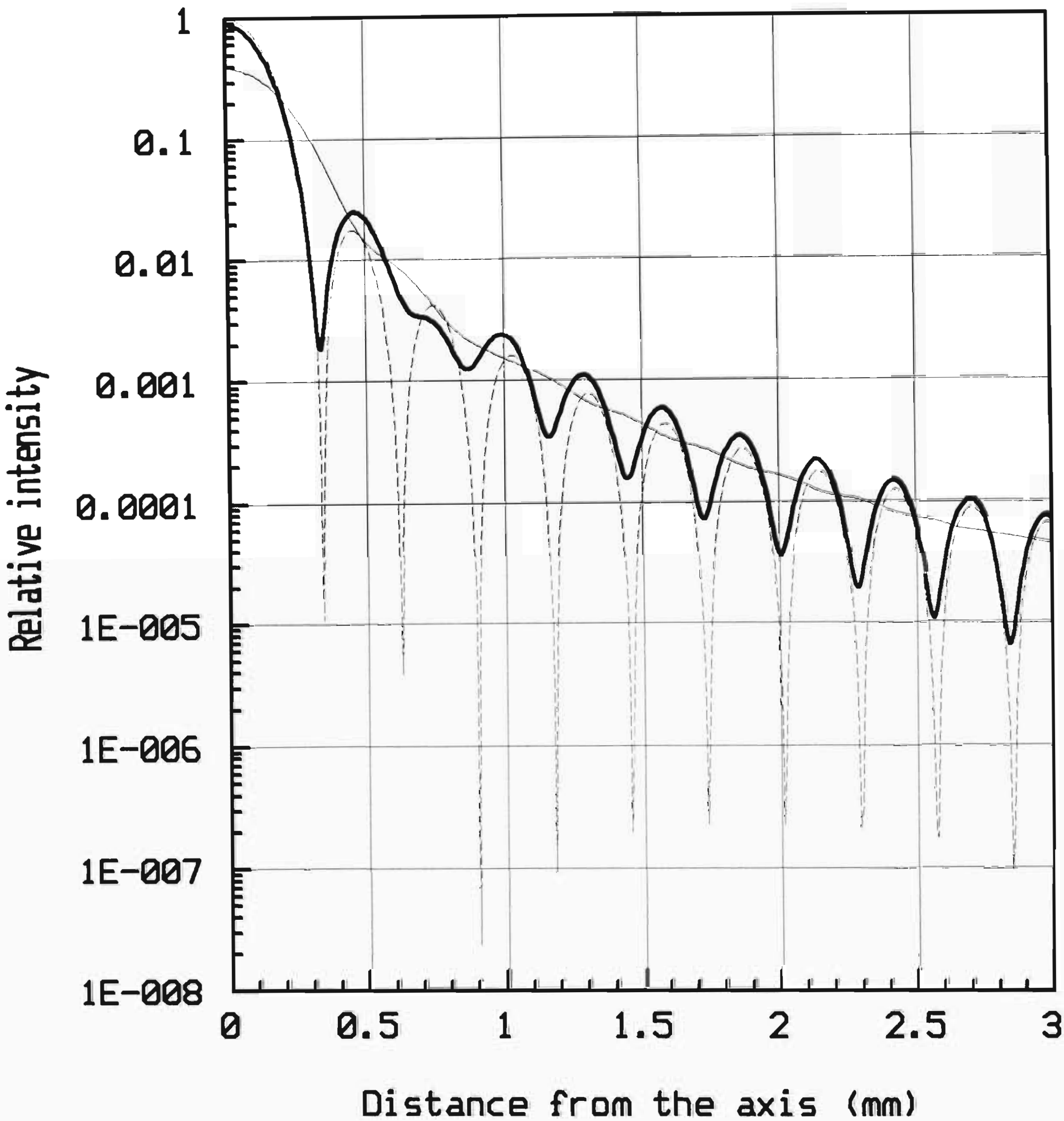

Fig 5.2.8 Intensity logarithm in the focal plane of the CSL, solid line. Lens diameter = 4.8mm. Focal length = 197.0cm. The Airy pattern of an equivalent diffraction limited lens is repcrted for comparison, dashed line. The thin solid line trace shows the intensity profile when the divergence of the probe laser beam is taken into account.

5.2.3 THE EFFECT OF THE LASER BEAM DIVERGENCE ON THE INTENSITY PROFILE

Finally we can perform an averaging in the image plane in order to take into account the divergence of the input laser beam. We can imagine substituting the input plane wave with an angular distribution of mutually incoherent plane waves. Since, by definition the plane waves travelling at different angles do not have any precise mutual phase relation, they do not create any interference pattern on an observable timescale. Consequently a spatial averaging onto the image plane will be sufficient to account for the phenomenon. The spatial averaging must take accurately into account the cylindrical geometry of the system, in order to preserve the total energy.

The intensity angular distribution that we have chosen is a normalised cosine distribution of the opportune width. Such angular distribution often well represents the output of a multimode laser beam.

$$
\begin{aligned}
I(\theta) &= \frac{1}{2\pi}\cos\left(\frac{\pi\theta}{2\Delta\theta^{div}}\right) \qquad |\theta| < \Delta\theta^{div} \\
I(\theta) &= 0 \qquad\qquad\qquad\qquad\quad |\theta| > \Delta\theta^{div}
\end{aligned}
\qquad 5.2.12
$$

The third curve shown in figure 5.2.3 to figure 5.2.8, the thin solid curve, shows the radial intensity plot on the focal plane when the effect of a laser divergence of 0.25 mrad is taken into account.

The programs performing the diffraction integral computation first and then the final spatial averaging onto the focal plane are written in Pascal and run on a PC. The listing are in Appendix C.

CHAPTER 6:
THE ELLIPTICAL COLLIDING SHOCK LENS

In chapter 3 and 5, and in [Buccellato B 1993], it has recently been demonstrated that the central collision of several shock-waves in a gaseous medium can generate a density and refractive index distribution that can efficiently focus laser light into a sharp focus. In this chapter we demonstrate how, by shaping the imploding shock-front, we can generate an elliptical lens, useful for line focusing applications.
The working principle relies on the refractive properties of non-uniform gas density distributions and on the gas-dynamic interaction of multiple shock waves in order to obtain a gas density distribution suitable for focusing. The CSL presents several advantages over an equivalent f-number solid state device, such as the high breakdown threshold and the damage resistance, besides its being a varifocal device.
An other advantage of the CSL over a conventional solid state device consists on the possibility of shaping the geometry of the imploding shock-front in order to obtain geometries which are different from the cylindrically symmetric one. If the CSL is utilised to focus a collimated laser beam on a flat target, the shaping of the imploding shock-front results in a different spatial distribution of the irradiance on target.
When we create a density distribution whose cross section is an ellipse, we can focus a laser beam into a line focus, suitable for some applications such as x-ray lasers.

6.1 ELLIPTICAL LENS THEORY

6.1.1 GEOMETRICAL OPTICS DESCRIPTION

We have shown in chapter 1 [Marchand 1978] how a radially symmetric parabolic refractive index profile such as,

$$n(r) = n_0 - \alpha^2 r^2 \qquad 6.1.1$$

can produce a sharp focus. If we let the refractive index contour line be elliptical rather than circular, thus loosing the cylindrical symmetry, the refractive index profile becomes:

$$n(x,y) = n_0 - \alpha_x^2 x^2 - \alpha_y^2 y^2 \qquad 6.1.2$$

In the latter case, we can solve analytically the ray equations, such as for the uni-dimensional case:

$$\frac{\partial^2 x}{\partial z^2} = \frac{\partial n}{\partial x}$$
$$\frac{\partial^2 y}{\partial z^2} = \frac{\partial n}{\partial y} \qquad 6.1.3$$

And we get two independent equations for the rays' deflection along the two directions x and y.

$$\theta_x(x) = -2\alpha_x^2 x = -\frac{x}{f_x}$$
$$\theta_y(y) = -2\alpha_y^2 y = -\frac{y}{f_y} \qquad 6.1.4$$

Equation 6.1.4 tells us that there are two stigmatic foci at two different distances from the elliptical lens. The ratio between the distances of the two foci equals the eccentricity of the elliptical profile. In this sections we briefly analysed the performances of an elliptical GRIN lens in the paraxial ray optics approximation. The detailed paraxial diffraction theory of the elliptical CSL can be found in the next paragraph.

6.1.2 THE ELLIPTICAL CSL DIFFRACTION THEORY

In Chapter 1 we found the Fraunhofer formula for the diffraction produced by an aperture on a plane screen. This theory allows one to compute the intensity profile in the focal plane when a lens is uniformly illuminated by laser light. In chapter 5 we did apply such a theory in order to compute the intensity profile in the focal plane of the CSL, whilst taking the CSL longitudinal aberrations into account. We shall now apply the Fraunhofer theory to the elliptical CSL. In figure 5.2.2 the geometry of the system is

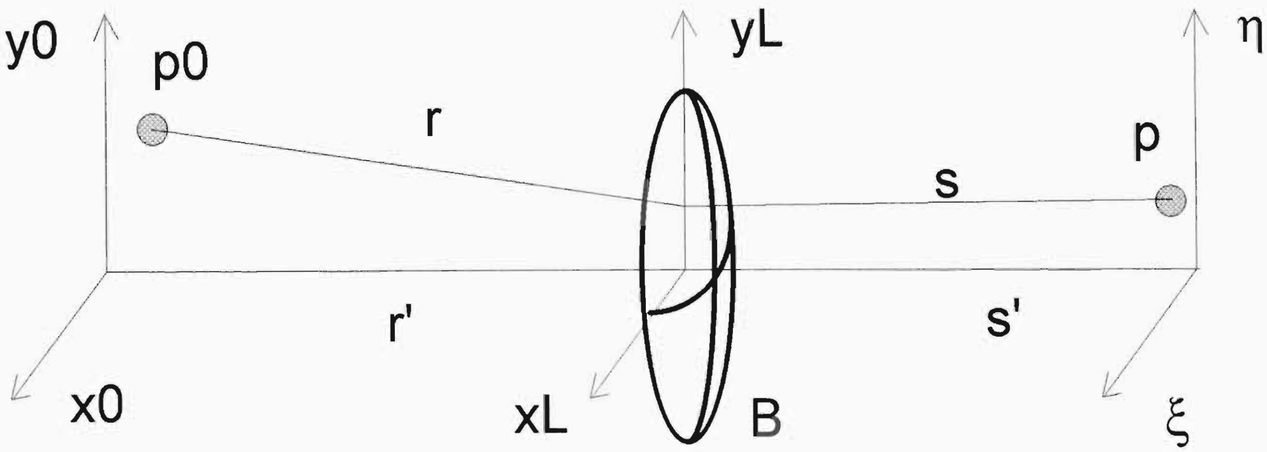

Fig 6.1.1 Geometry of the diffraction from the elliptical CSL.

reported. The calculation proceeds as in chapter 5 up to equation 5.1.8, when the wave-front reaches the CSL.

$$E(x_L, y_L) = \frac{iA}{\lambda r'} \exp(-ikr) \iint f(x_S, y_S) \exp\left(-ik\frac{(x_S - x_L)^2}{r'} - ik\frac{(y_S - y_L)^2}{r'}\right) dx_S dx_S$$

6.1.5

The function $f(x_S,y_S)$ is the source shape. The passage through the lens introduces an additional phase shift that renders the wave-front curved. In the actual case the wave-front is a two dimensional paraboloid, with an elliptical cross-section.
The phase shift at each point of the CSL plane coincides with the optical path length (or OPL). In the case of the elliptical CSL, the OPL is a function of x and y and is given by equation 6.1.2. The electric field after the beam has passed through the CSL can be expressed as:

$$\Psi(x_L, y_L) = E(x_L, y_L) \exp\left[ik\left(\alpha_x^2 x_L^2 + \alpha_y^2 y_L^2\right)\right] \qquad 6.1.6$$

In the η,ξ plane at the distance s' from the CSL the expression for the electric field in given, as in equation 5.2.10, by equation 6.1.7. As in chapter 5 we neglect the numerical coefficients in front of the electric field expressions.

$$U(\eta,\xi) = \iint f_L(x_L, y_L)\Psi(x_L, y_L) \exp\left(-ik\frac{(x_L - \xi)^2}{s'} - ik\frac{(x_L - \xi)^2}{s'}\right) dx_L dy_L \qquad 6.1.7$$

Where the function $f_L(x_L,y_L)$ is the aperture function of the elliptical lens. The case of a laser beam, or a well collimated beam, it is well represented by a point source at a large distance from the lens. In this case we can imagine that r' goes to infinity and the source shape function becomes a two dimensional Dirac delta function:

$$f_S(x_S, y_S) = \delta(x_S, y_S) \qquad 6.1.8$$

The hypothesis of a point source greatly simplifies our calculations:

$$U(\eta,\xi) = \iint \exp\left[-ikx_L^2\left(\frac{1}{2s'}+\frac{1}{2r'}-\alpha_x^2\right)\right]\exp\left[-iky_L^2\left(\frac{1}{2s'}+\frac{1}{2r'}-\alpha_y^2\right)\right]$$
$$\cdot\exp\left(ik\frac{x_L\xi}{2s'}\right)\exp\left(ik\frac{x_L\eta}{2s'}\right)f_L(x_L,y_L)dx_L dy_L \qquad 6.1.9$$

Making use of the relations 6.1.4 we can show that there are two stigmatic focal planes, at the positions:

$$\frac{1}{2r'}+\frac{1}{2s'}=\alpha_x^2=\frac{1}{2f_x}$$
$$\frac{1}{2r'}+\frac{1}{2s'}=\alpha_y^2=\frac{1}{2f_y} \qquad 6.1.10$$

If the eccentricity of the ellipse is set to one, the lens becomes circular and we can define two conjugate planes such as for an aberration free lens.

In our case, we can define two sets of conjugate planes corresponding to the two stigmatic foci. Let us chose the plane corresponding to the first of the two foci, at which:

$$\frac{1}{2r'}+\frac{1}{2s'}=\frac{1}{2f_x} \qquad 6.1.11$$

By introducing polar coordinates both in the lens and in the 'first focal' plane the electric field expression becomes:

$$U(\rho,\psi)=\int_0^{2\pi}\int_0^{R(\theta)}\exp\left[iky_L^2\left(\frac{1}{f_y}-\frac{1}{f_x}\right)\right]\cdot\exp\left(ik\frac{r\rho\cos\theta\cos\psi}{f_x}\right)\exp\left(ik\frac{r\rho\sin\theta\sin\psi}{f_x}\right)rdrd\theta$$
$$R(\theta)=a_x+\left(a_y-a_x\right)\cos\theta$$

6.1.12

Where A and B are the two semiaxes of the CSL. The double integral appearing in equation 6.1.12 can be evaluated numerically but its solution is time consuming. Thus we only evaluated the function $U(\rho,\psi)$ along two perpendicular axes into the 'first focal' plane (see figure 6.1.1) $\psi=0$ and $\psi=\pi/2$.

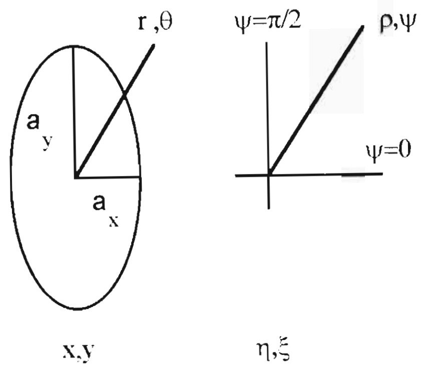

Fig.6.1.2 Elliptical lens plane and first focal plane.

The equation 6.1.12 there becomes:

$$U(\rho,0) = \int_0^{2\pi}\int_0^{R(\theta)} \exp\left[ik(r\sin\theta)^2\left(\frac{1}{f_y}-\frac{1}{f_x}\right)\right]\cdot \exp\left(ik\frac{r\rho\cos\theta}{f_x}\right) r\,dr\,d\theta \qquad 6.1.13$$

$$R(\theta) = a_x + (a_y - a_x)\cos\theta$$

$$U\left(\rho,\frac{\pi}{2}\right) = \int_0^{2\pi}\int_0^{R(\theta)} \exp\left[ik(r\sin\theta)^2\left(\frac{1}{f_y}-\frac{1}{f_x}\right)\right]\cdot \exp\left(ik\frac{r\rho\sin\theta}{f_x}\right) r\,dr\,d\theta \qquad 6.1.14$$

$$R(\theta) = a_x + (a_y - a_x)\cos\theta$$

The two integrals can be solved numerically as a function of ρ, by expressing the complex exponential as a sine and cosine function as done in chapter 5. Finally by taking the square of the function U, we obtain the intensity pattern along the two directions into the focal plane. In figure 6.1.3 we report the results of the numerical calculation. For the latter

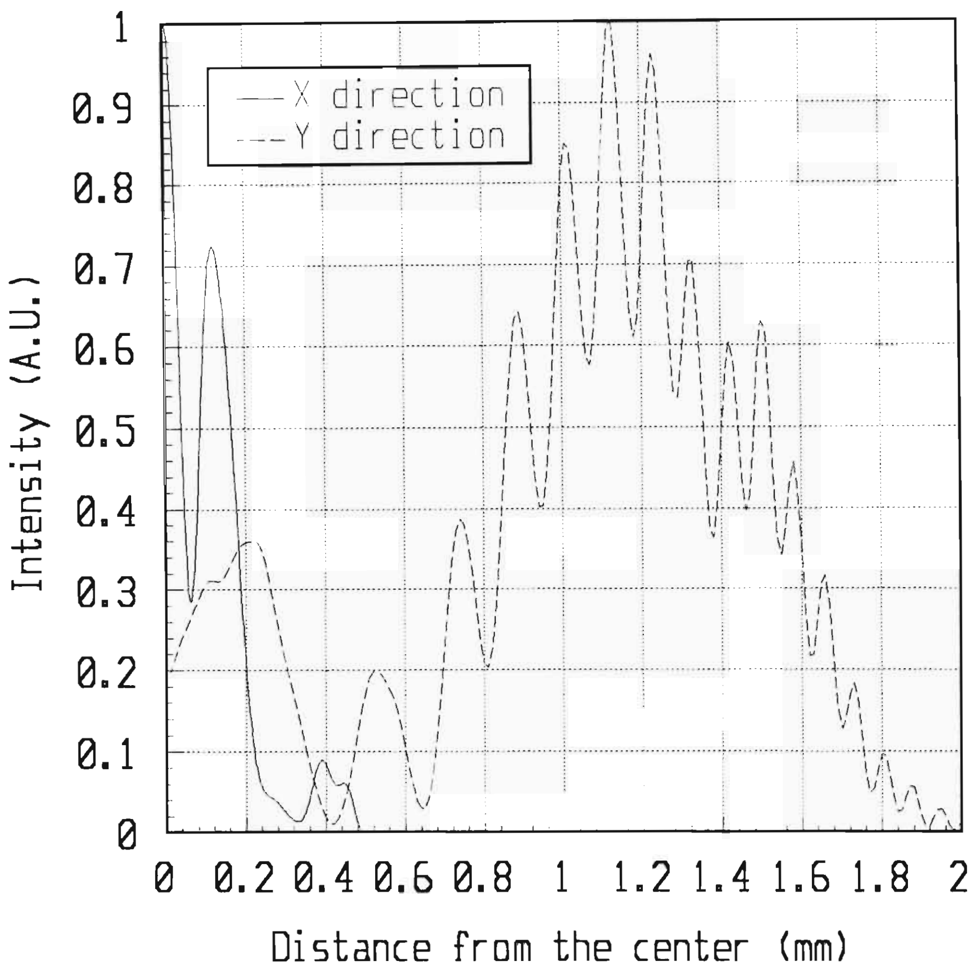

Figure 6.1.3 Computed diffraction pattern in the first focal plane. f_x=0.5m, Eccentricity=4.0, a_x=0.62mm.

calculation we chose the correct experimental values for the system parameters such as semiaxes, eccentricity and focal distance. The numerical programs utilised for this calculation are listed in appendix D.
The scale in the previous picture is not the same along the two directions and can be found by scaling one curve respect to the other until the values at the zero position do coincide. We immediately note that intensity is not uniform along the direction of the line focus This device is then more properly speaking a 'two foci' device, rather than a 'line focus' device. Agreement with the measured intensity pattern can be found in the next paragraphs where we introduce the experimental results.

6.1.2 THE ELLIPTICAL CSL

Suppose now that we are able to generate an expanding elliptical shock-front having the semiaxis a_x and a_y, and consequently the eccentricity ε:

$$\varepsilon = \frac{a_x}{a_y} \qquad 6.1.15$$

We can reasonably presume the density (and refractive index) contour lines to be parallel to the shock-front, thus having the same eccentricity. By placing the electric arc explosion equi-spaced along some curve, we can obtain that, after the central collision, the shock-front emerges with an elliptical profile.
In order to find such a curve, we should solve in theory both a simple geometrical and a complex gas-dynamic problem. The velocity of the single unperturbed expanding spherical shock wave caused by a single arc explosion decreases according to a power law, converging on the sound speed ($M_0=1$) at large distance from the explosion centre. Under this hypothesis, that is when the shock velocity varies only with the distance from the explosion centre, if we equi-space the shock launching points on the arc of an ellipse, the shock-front will expand after the central collision with an elliptical profile.
When several shock waves come together and overlap while converging towards the centre, they do interfere and their velocity varies. During this phase, some distortion of the shock-front from the elliptical profile could be expected if the shock energy is high ($M_0>>1$). In our conditions,

supported by the experimental results, we expect the latter effect to be negligible.

Let us consider the curve defined by the envelope of all the spherical shocks generated by the point explosions in air. Each point of such a curve moves in time towards the direction defined by the normal of the curve itself. Let the arc explosions be equi-spaced along the arc of an ellipse with semiaxis $\mathbf{d_x}$ and $\mathbf{d_y}$. During the propagation of the shock-front, we note that the eccentricity of the ellipse is not conserved at some times the shock-front is not even an ellipse (figure 6.1.4 and 6.2.3c).

Let the semiaxes of the ellipse we want to generate be $\mathbf{a_x}$ and $\mathbf{a_y}$, the semiaxes of the initial shock-front must be:

$$\begin{aligned} d_x &= A - a_x \\ d_y &= A - a_y \end{aligned} \qquad 6.1.17$$

Where A can be chosen within a useful range according to physical criteria. The lens cannot be too large or else the shock waves loose too much energy before the collision, and certainly must not be smaller than the ellipse that we want to generate. Basing our assumptions on experience gained with cylindrically symmetric CSL devices we choose the following values:

$$\begin{aligned} a_x &= 2\text{mm} \\ a_y &= 4\text{mm} \\ A &= 17\text{mm} \end{aligned}$$

In figure 6.1.4 we show a geometrical construction that represents the collision and successive expansion of the elliptical wave-front at different times from the arc explosion. The program utilised to generate this construction is in appendix D.

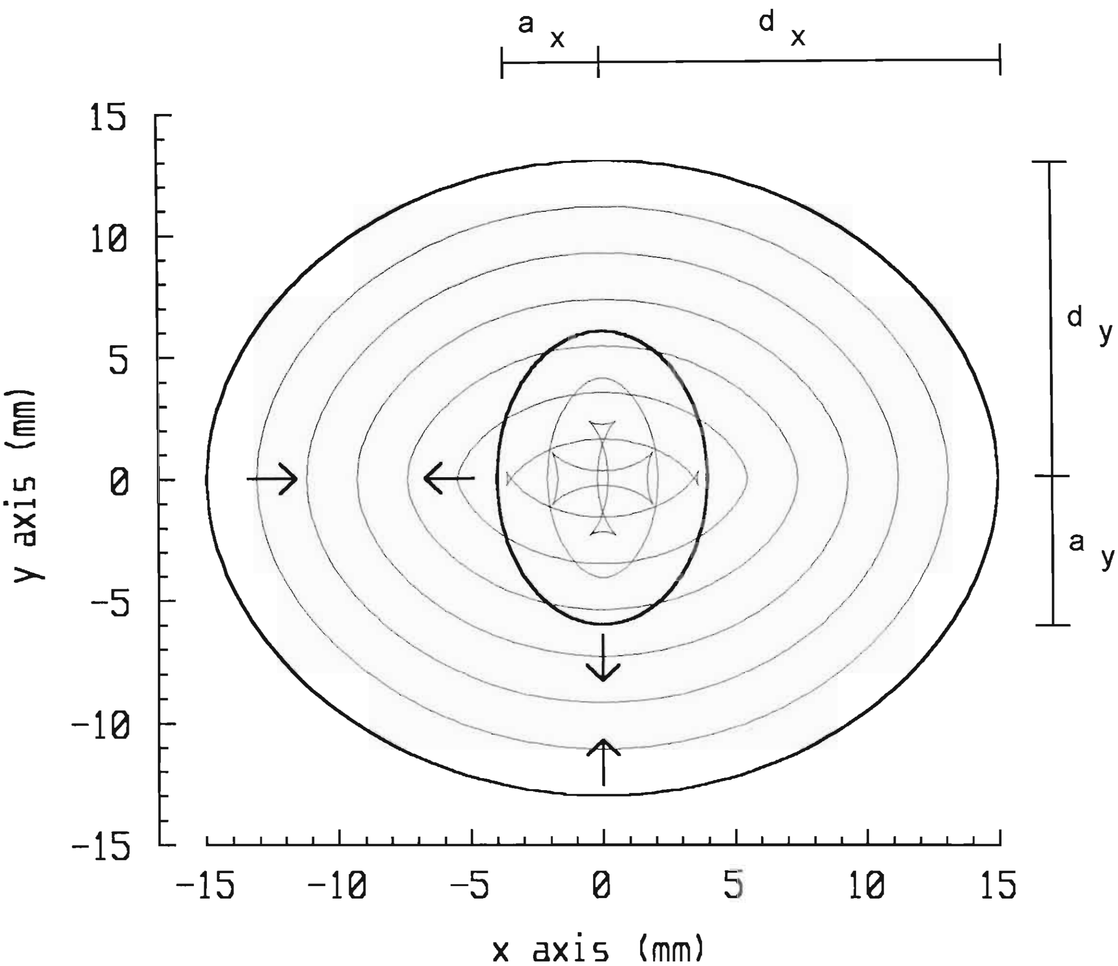

Fig.6.1.4 Converging elliptical wave-front. Geometrical construction in the hypothesis of constant shock velocity.

6.2 EXPERIMENT

6.2.1 EXPERIMENTAL SET-UP

The elliptical CSL has been designed with equi-spaced discharge electrodes. The distance between each couple of electrodes and the next was kept constant. The experimental set-up has already been described in chapter 3, it briefly consist of an arc discharge circuit which is electronically triggered via a spark-gap and of spatially filtered probe nitrogen laser which is electronically synchronised via a variable delay. The discharge circuit, together with a sketch of the elliptical CSL is shown in figure 6.2.1. The discharge capacitor value was chosen to be C=100nF and the gap between opposing electrodes G=1mm. The discharge electrodes are connected in series in order to ensure simultaneous arcing. The recording apparatus consists of a TV camera and an Oculus 200 frame grabber, connected to a personal computer. By using a 20cm focal length lens, the camera can image any object plane, including the shock collision plane. A sketch of the experimental set-up is reported in figure 6.2.2.

6.1.2 EXPERIMENTAL RESULTS

In figure 6.2.3 we report a sequence of the elliptical shock-front convergence, imaged onto the shock collision plane. In figure 6.2.4, 6.2.5 and 6.2.6, we show the intensity pattern of three stigmatic line foci at three different delays and distances from the elliptical CSL.
As seen in the pervious section, according to the elliptical CSL theory, at any fixed time delay there are two stigmatic line foci. In figure 6.2.4 we only show the first of the two foci, f_x, the one closer to the lens.
In figure 6.2.5 we report the time evolution of the two semiaxes a_x and a_y. We note that the elliptical CSL is a varifocal device, whose 'diameters' and aspect ratio vary sharply with time on the μs time-scale.

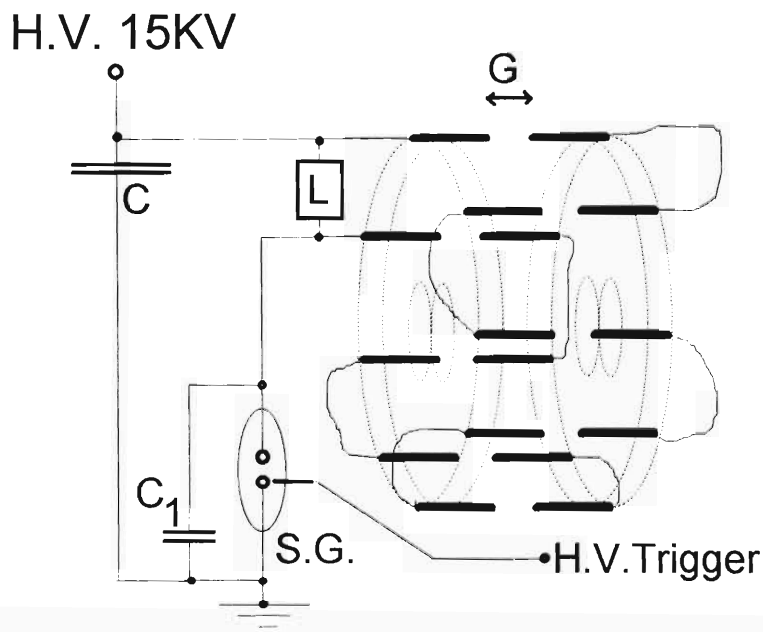

Figure 6.2.1. The elliptical Colliding Shock Lens. Consists of a CSL where the discharge pins are equi-spaced along the arc of an ellipse rather then along the arc of a circle. Discharge circuit. L=10H, C=100nf, C_1=1nf, G=1mm.

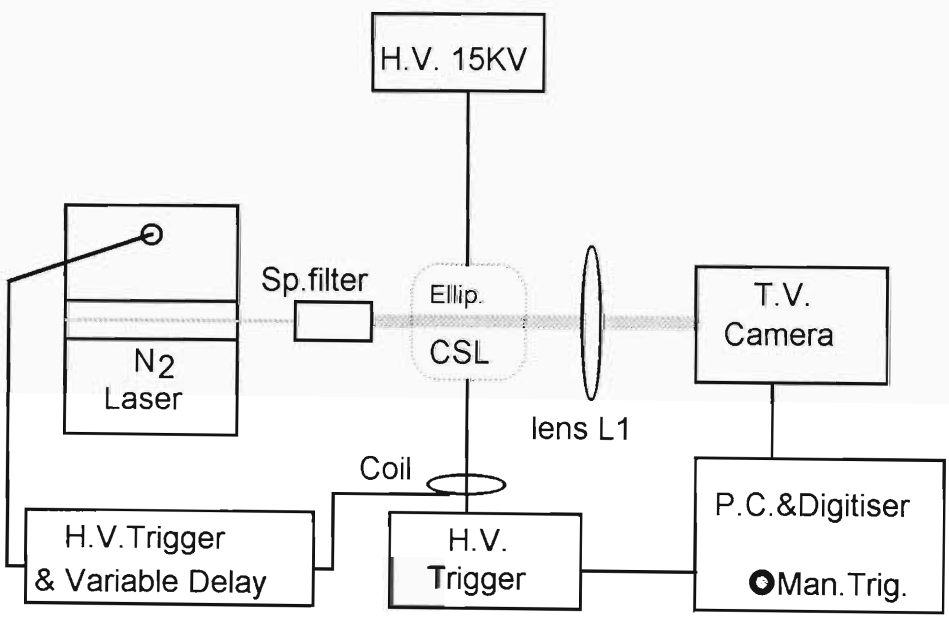

Figure 6.2.2 Experimental set-up for the focusing experiment of the elliptical CSL.

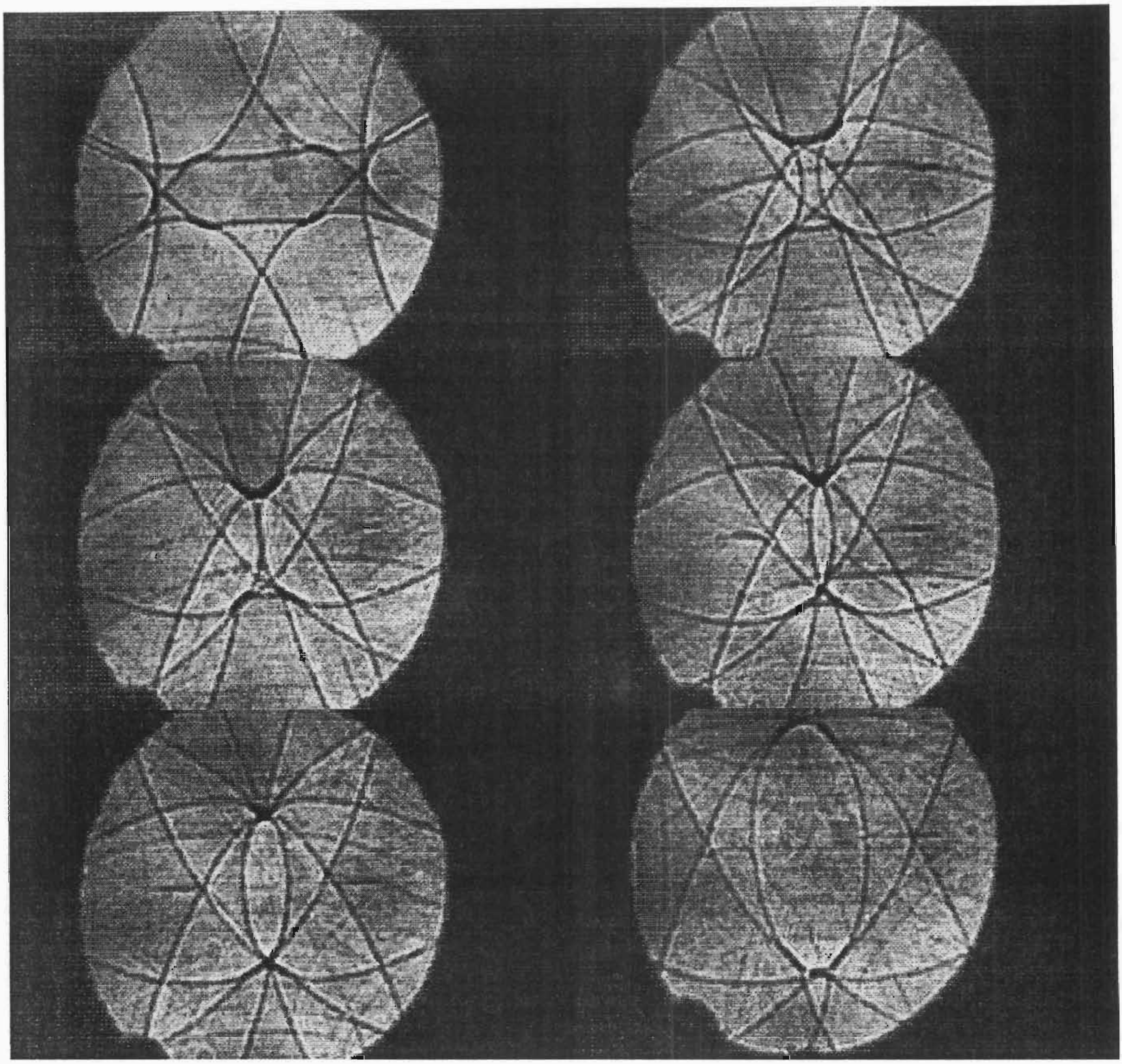

Figure 6.2.3 The elliptical colliding shock lens imaged onto the shock collision plane. From left to right and up to down: a)Delay=23.3μs, b)Delay=28.2μs, c)Delay=29.0μs, d)Delay=29.2μs, e)Delay=30.0μs, f)Delay=32.8μs. The shock collision is at Delay=29.0μs.

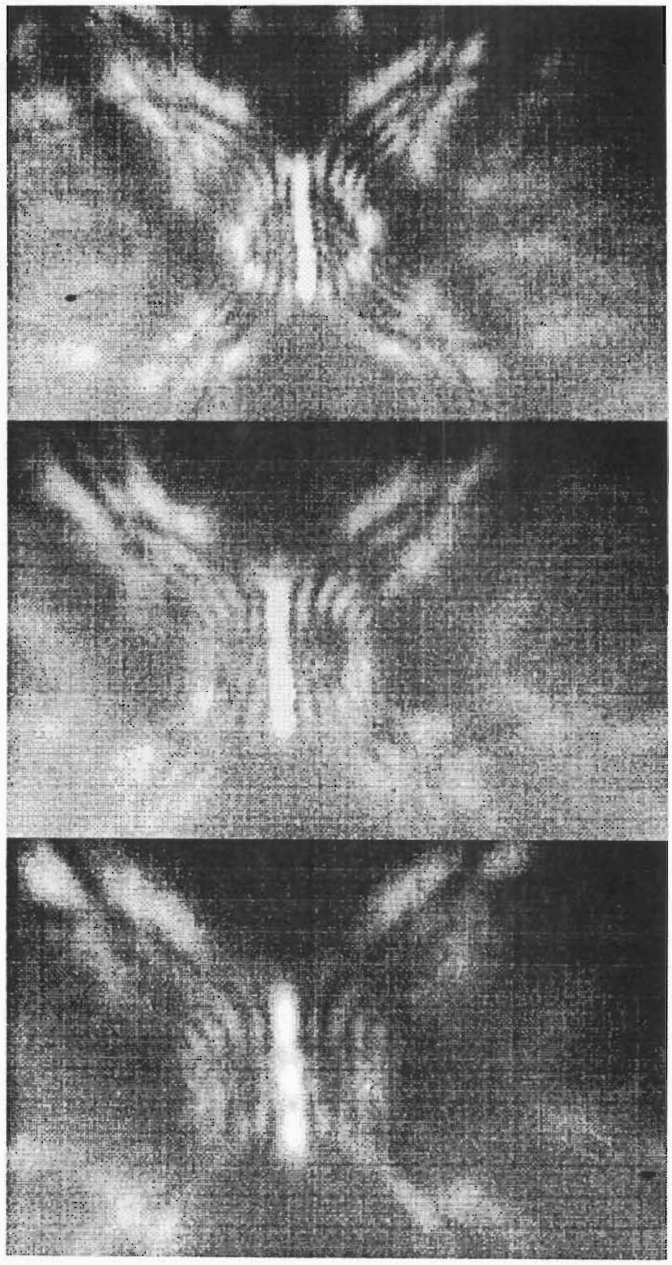

Fig.6.2.4 Images of the first focal plane. From the top down:

a) $f_x=0.5m$, Delay=$30\mu s$,

b) $f_x=0.9m$, Delay=$30.9\mu s$,

c) $f_x=1.5$, Delay=$31.5\mu s$.

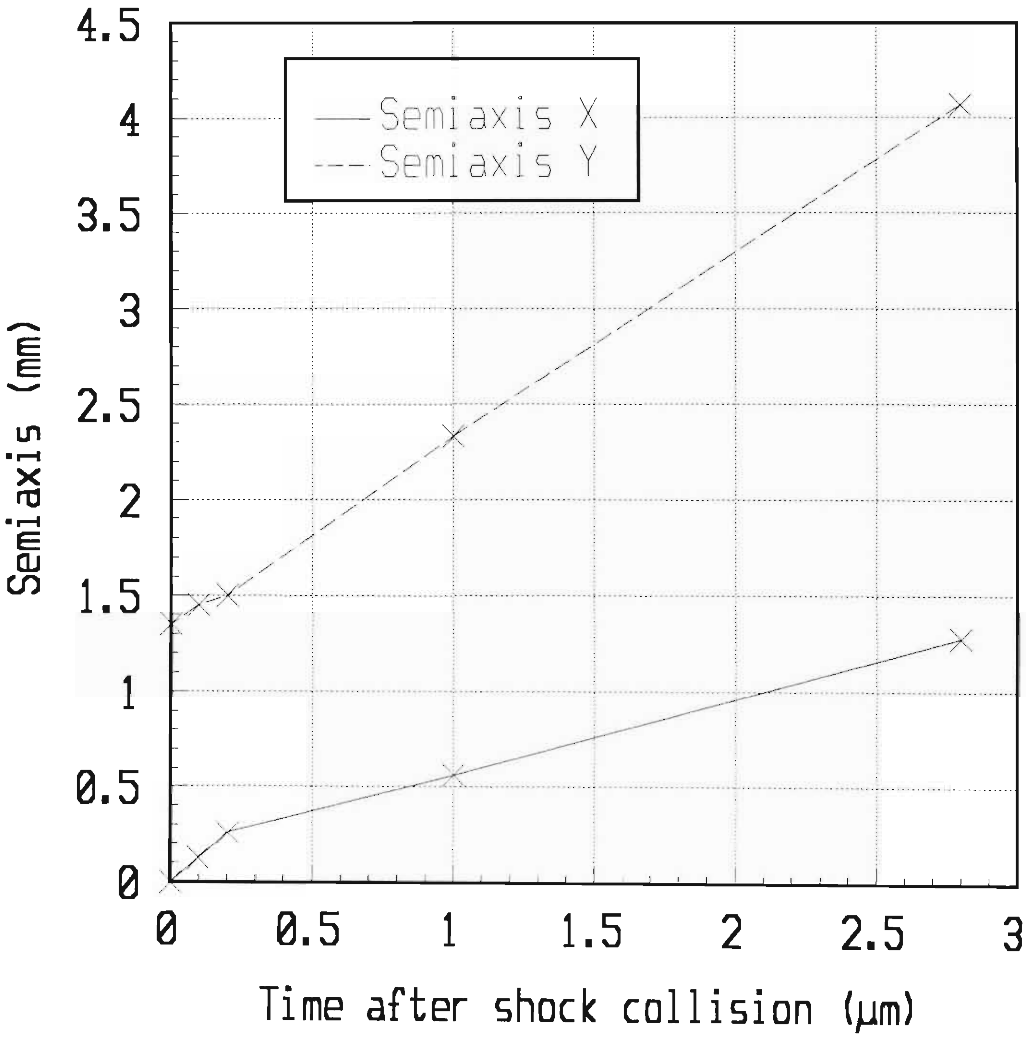

Figure 6.2.5 Time evolution of the elliptical CSL semiaxis.

6.3 CONCLUSIONS

In chapter 3 we characterised the CSL and its performances. One of the possible advantages over a solid state lens resulted that its focal length varies with time. In this chapter we stress another feature of the CSL. The possibility of varying the shape. In order to demonstrate this possibility we made an elliptical CSL. An elliptical lens, according to the diffraction theory, gives at the focal plane something which lies in between a "line focus" and a "two foci" or two lobed intensity distribution. The experiment confirmed this prediction.

This is only a first step, and CSL with different initial shock-front shapes can give a whole range of spatial intensity distributions in the focal plane. As discussed earlier in this thesis the main advantage of a CSL over an equivalent solid state device is the radiation resistance.

CONCLUSIONS

Gas lenses were first proposed in 1960's as light wave guides. The discovery of fibre-optics with their superior performances and reliability, interrupted the early research on these devices. The early devices were basically thermal gradient gas lenses. In a gas lens, the wave-front is shaped by a refractive index gradient distributed over a volume, rather than by the refraction at an interface such as in conventional solid state lenses. The gas lenses are GRIN lenses.

As we have seen in chapter 2, a spinning pipe gas lens, a thermal gradient gas lens, typically has a long focal length and a fairly high numerical aperture.

In a thermal gradient gas lens, the refractive index radial gradient that allows focusing to occur, follows the local structure of the temperature: The higher the temperature, the lower the gas density and the lower the refractive index. Such devices are in general bulky and heavy, and are sensitive to the surrounding conditions. Still air is a necessary condition for steady operations. The main advantage of a spinning pipe gas lens is the lack of reflective surfaces (or AR coatings) and the very high laser damage threshold.

As seen in chapter 4, the spinning pipe gas lens, can be employed advantageously during high power laser intracavity operations.

In chapter 3 we have introduced a novel type of gas lens: The Colliding Shock Lens (CSL). In this device, shock waves are utilised to compress a gas in a central dense core. The radial density gradient inside this core can focus the light of a laser beam to an almost diffraction limited focal spot. The Colliding Shock Lens has been rep-rated up to 10Hz but there is no physical limit to repetition rates up to few KHz.

In our geometry we make use of the non-linear properties of the interaction between shock-waves in order to produce a cylindrically symmetric high density core, starting from a polygonally shaped imploding shock-front. After the central implosion of the shocks, a cylindrically symmetric expanding density distribution occurs. Typically the CSL focal length and diameter vary on the μs time-scale.

The CSL can be utilised as a high power electro-optical switch. In chapter 4 we presented a novel type of Q-switching technique that merge together the advantages of intracavity optical gas elements and of telescopic cavities.
In chapter 5 we analysed in detail the optical performances of the CSL during its time evolution. The analysis is performed onto the interferograms that we recorded during an experiment reported in chapter 3. Our numerical analysis confirmed the optical performances of the CSL. At the optimum distance from the CSL, and at the corresponding optimum delay from the central shock collision, the CSL is really a diffraction limited device.
Finally in chapter 6 we exploited another interesting property of the CSL: the possibility of varying the implosion geometry. By shaping the imploding shock-front we can vary the shape of the lens and the optical properties change as well. In order to test the concept we made an elliptical CSL.
According to the Fraunhofer diffraction theory, an aberration free elliptical lens has two stigmatic "focal planes". The intensity pattern in the first "focal plane" is something in between a line focus and a two lobed focus, which is observed experimentally.
In conclusion we have demonstrated that the gas lenses are remarkably flexible devices. They can be operated both continuously and pulsed, both at low and high repetition rate. While the continuous gas lenses, the thermal gradient devices, require particularly still operating conditions, the pulsed devices (the CSL), do not and can be operated in repetitive mode. The main difficulty that one encounters is the improvement of the numerical aperture of the devices, that is increasing the aperture while keeping a short focal length and a consistent optical quality. This is more a physical than a technological problem. since as the density gradient increases so does the perpendicular gas flow and the gas distribution becomes more and more difficult to control.
A combination of pulsed devices with different geometries and continuous gas lenses, can perform a wide spectrum of operations on a high power laser wave front.

THE BIBLIOGRAPHY

Anan'ev Yu.A.; 'Unstable resonators and their applications (review)'; Soviet Journal of Quantum Electronics; **6** (1972) 565.

Ashcrofr N.W., Mermin N.D.; Solid State Physics; HRW International Editions; Philadelphia, 1976.

Bejan A.; Convection Heat Transfer; J. Wiley & Sons; New York, 1984.

Beck A.C.; 'An experimental gas lens optical transmission line'; IEEE Transactions on microwave theory and techniques; February (1967) 433.

Born M., Wolf E.; Principles of Optics; Pergamon Press, Oxford; Sixt edition 1993.

Bockasten K.; 'Transformation of observed radiances into radial distribution of the emission of a plasma'; Journal of the Optical Society of America; **51** (1961) 943

Bransden B.H, Joachain C.J, Physics of Atoms and Molecules, Longman, Londom (1983).

Buccellato R., Michaelis M.M.,Dempers C.A.,Prause A., Cunningham P.F; 'Pulsed gas lenses'; Optics and Laser Technology **25** (1993) 247.

Buccellato R., Lisi N., Michaelis M.M.; 'The colliding shock lens'; Optics Communications; **101** (1993) 350.

Buccellato R.; PhD Thesis, University of Natal (1994).

Courant R., Friedrichs K.O.; Supersonic Flow and Shock Waves; Interscience, New York; 1948.

CRC Handbook of chemistry and physics, 75th edition, 1995.

Cunningham P.F., Campbell R.N., Michaelis M.; 'Refractive fringe diagnostic of a ruby-laser produced plasma using a short pulse, short wavelength nitrogen laser'; Journal of Physics E: Scientific Instruments **19** (1986) 957.

Edlen B.; 'Refractive index of air'; Metrologia **2** (1966) 71.

Einstein A., Phys. Z., **18** (1917) 128.

Gloge D.; 'Deformation of gas lenses by gravity'; Bell Sys Tech J **46** (1967) 357.

Gower M.C.; 'KrF laser induced breakdown of gases'; Optics Communications; **36** (1981) 43.

Guenther R.; Modern Optics; J. Wiley & Sons; New York, 1990.

Guderley G.; Luftfahrt-forschung; **19** (1942) 302.

Hamamoto M., Muraoka K., Akazaki M.; 'Simultaneous recording of a two-wavelength interferometer outputs of an atmospheric impulse breakdown process'; Japanese Journal of Applied Physics; **20** (1981) 443.

Hanna D.C., Sawyers C.G. & Yuratich M.A.; 'Telescopic resonators for large-volume TEM_{00}-mode operation'; Optical and Quantum Electronic; **13** (1981) 493.

Koechner W.; Solid state laser engineering; Springer Verlagh, New York; Second Edition, 1988.

Kogelnik H., Li T.; 'Laser beams and resonators'; Applied Optics; **5** (1966) 1550.

Korad Model K1 ruby laser head (1975).

Landenburg; Zeits. fur Phys. **4** (1921) 451.

Landenburg; Zeits. fur Phys. **48** (1928) 15.

Lisi N., Buccellato R., Michaelis M.M.; 'Optical quality and temperature profile of a spinning pipe gas lens'; Optics and Laser Technology **26** (1994) 25.

Lisi N., Michaelis M.M., Kuppen M., Prause A., R.Buccellato; 'The colliding shock lens as an intracavity Q-switching element'; Applied Optics, **34** (1995) 942.

Loudon R.; The quantum theory of light; Clarendon Press, Oxford; Second edition 1983.

Marchand L.; Graded Index Optics; J. Wiley & Sons, New York; 1972.

Marcuse D.; Light Transmission Optics; Van Norstrand Reinhold, NY 1972.

Marcuse D.; 'Theory of a thermal gradient gas lens'; IEEE Transaction on Microwave Theory and Techniques; **MTT-13** (1965) 734.

Matsuo H. & Nakamura Y.; 'Cylindrically converging blast waves in air'; J. Appl. Phys. **52** (1981) 4503.

Melles Griot Catalogue 1992.

Michaelis M.M., Cunningham P.F., Cazalet R.S., Waltham J.A. & Nottcutt M., 'Gas lens applications'; Laser and Particle Beams **9** (1991) 641.

Michaelis M.M., Dempers C.A., Kosch M., Prause A., Notcutt M., Cunningham P.F. & Waltham J.A.; 'A gas-lens telescope'; Nature **353** (1991) 547.

Michaelis M.M., Willi O.; 'Refractive fringe diagnostics of laser produced plasmas'; Optics Communications; **36** (1981) 153.

Michaelis M.M., Waltham J.A., Cunningham P.F.; 'Refractive fringe diagnostics of spherical shocks'; Optics and Laser Technology **23** (1991) 283.

Michaelis M.M., Lisi N., Kuppen M., Buccellato R., Prause A.; 'Applications of the colliding shock lens'; Laser and Particle Beams **12** (1994) 531.

Michaelis M.M., Notcutt M., Cunningham P.F.; 'Drilling by gas lens focused laser'; Optics Communications; **59** (1991) 369.

Mitchell A.C.G. Zemansky M.W; Resonance radiation and excited atoms; Cambridge Univ. Press (1971).

Notcutt M., Michaelis M.M., Cunningham P.F., Waltham J.A.; 'Spinning pipe gas lens'; Optics and Laser Technology **20** (1988) 243.

Practical Temperature Measurements, Hewlett Pakard, Application Note 290, 8.

Raizer Yu.P.; Gas Discharge Physics; Springer Verlag (1990).

Routledge P.A., Berry A.J. & King T.A.; 'A Flashlamp pumped dye laser in a telescopic resonator configuration'; Optica Acta; **33** (1986) 445.

Schwendeman D.W. & Whitham G.B.; 'On converging shock waves'; Proc. R. Soc. Lond. A **413** (1987) 297.

Sharma A, Kumar D.V., Ghatak A.K.; 'Tracing rays through graded-index media: a new method'; Applied Optics; **21** (1982) 984.

Siegman A.E.; Lasers; University Science Book, Mill Valley, California (1986).

Siegman A.E.; 'Unstable optical resonators'; Applied Optics; **13** (1974) 353.

Statz H., Tang C.L.; 'Problem of mode deformation in optical masers'; Journal of Applied Physics; **36** (1965) 1816.

Statz H., Tang C.L.; 'Multimode oscillations in solid-state masers'; Journal of Applied Physics; **35** (1954) 1377.

Steier W.H.; 'Measurements on a thermal gradient gas lens'; IEEE Transaction on Microwave Theory and Techniques **MTT-13** (1965) 740.

Taylor G.I.; 'The air wave surrounding an expanding sphere'; Proc. R. Soc. Lond. A; **186** (1946) 272.

Xie B.L., Xia S.J. & Chow Q.T.; 'Varifocal gas lens'; Chinese Physiscs Letters **2** (1985) 509.

Waltham J.A., Cunningham P.F., Michaelis M.M., Campbell R.N., Notcutt M.; 'The application of the refractive fringe diagnostic to shocks in air'; Optics and Laser Technology; **19** (1987) 203.

Zel'dovich Ya.B.,Raizer Yu.P.; Physics of Shock Waves and High Temperature Hydrodynamic Phenomena; Vol 1, Academic Press NY (1966).

ADDENDUM

Slyusarev C.G.; Aberration and optical design theory; Adam Hilger; Bristol (1984).

Weltford W.T.; Aberrations of the symmetrical optical system; Academic Press; London (1974).

APPENDIX A

In this appendix we report the listing of the program utilised in Chapter 2. The program solves the rays trajectories inside the spinning pipe gas lens. The measured refractive index profile is utilised. Given a point source or a combination of several point sources of white light at any object plane, the program computes the intensity profile at any image plane after the exit of the pipe. In chapter 2 we imaged a single point source. The program can give several other graphic outputs.

```
(**********************************************************)
(* Ray tracing through a thermal gradient gas lens:          *)
(* Paraxial rays approximation.                              *)
(* The program requires The refractivity index of the gas, at a  *)
(* given temperature, and the two dimensional                *)
(* temperature spatial profile in a plane containing the optical *)
(* axis.                                                     *)
(* The system has not cylindrical symmetry                   *)
(**********************************************************)

Program rtglexp;

uses
   crt,graph;

const
   nr=6;
   nz=17;
   maximpoint=2000;
   maxlaspoint=200;
   npoint = 2;          (* Points of the object *)
   nimagi = 990;
   diam = 1.0;          (* Diameter of the diaphragm in front of the lens *)

type
   glnarray = array [1..4] of real;
   datar = array [1..nr] of real;
   dataz = array [1..nz] of real;
   datat = array [1..3,1..nz,1..nr] of real;

var
   maino, laso,imo:integer;
   nray,nstep,nimag:integer;
   d,deltar,l,dz,t0,n0,objang,objdist:real;
   distz,distr:array[1..200] of real;
   distx,disty,gradx,grady:array[1..maximpoint] of real;
   rdata:datar;
   zdata:dataz;
   tdata,dtdata:datat;
   nfile,cf,control:string;

(******************************)
(*** Initialize to 0 all vectors ***)
(******************************)

procedure initialize;

var
  i,j,k:integer;
```

```
begin
   for i:=1 to maxlaspoint do
   begin
      distz[i]:=0.0;
      distr[i]:=0.0;
   end;
   for i:=1 to maximpoint do
   begin
      distx[i]:=0.0;
      disty[i]:=0.0;
      gradx[i]:=0.0;
      grady[i]:=0.0;
   end;
   for i:=1 to nr do
     rdata[i]:=0.0;
   for i:=1 to nz do
     zdata[i]:=0.0;
   for k:=1 to 3 do
      for j:=1 to nz do
         for i:=1 to nr do
           tdata[k,j,i]:=0.0;
end;

(******************************)
(*** Loading Experimental data ***)
(******************************)

Procedure loadexpdata;

var
   ft:text;
   k,i,j:integer;

begin
   assign(ft,'c:\data\tempe.dat');
   reset(ft);
   for j:=1 to nr do
      readln (ft,rdata[j]);
   for i:=1 to nz do
      readln (ft,zdata[i]);
   for k:=2 downto 1 do
      for i:=1 to nz do
         for j:=1 to nr do
            readln (ft,tdata[k,i,j]);
   d:=2*rdata[nr];
   l:=zdata[nz];
   close(ft);
end;


(**********************************************)
(************ Derivative of the refractive *********)
(************ index profile                *********)
(**********************************************)

procedure dnxy(xx,yy,zz:real; var dndx,dndy:real);

var
   t,dtdy,dtdx:real;


procedure temp(ax,ay,az:real; var at,adtdx,adtdy:real);


var
   ar,dt,dy1,dyn,at1:real;
   ydata,ddy:datar;

(********************************)
(*** 2-D interpolation subroutine ***)
(********************************)

PROCEDURE spline(x,y: datar; n: integer; yp1,ypn: real;
         VAR y2: datar);

VAR
   i,k: integer;
   p,qn,sig,un: real;
   u: datar;
```

```
BEGIN
   IF (yp1 > 0.99e30) THEN BEGIN
      y2[1] := 0.0;
      u[1] := 0.0
   END ELSE BEGIN
      y2[1] := -0.5;
      u[1] := (3.0/(x[2]-x[1]))*((y[2]-y[1])/(x[2]-x[1])-yp1)
   END;
   FOR i := 2 to n-1 DO BEGIN
      sig := (x[i]-x[i-1])/(x[i+1]-x[i-1]);
      p := sig*y2[i-1]+2.0;
      y2[i] := (sig-1.0)/p;
      u[i] := (y[i+1]-y[i])/(x[i+1]-x[i])
         -(y[i]-y[i-1])/(x[i]-x[i-1]);
      u[i] := (6.0*u[i]/(x[i+1]-x[i-1])-sig*u[i-1])/p
   END;
   IF (ypn > 0.99e30) THEN BEGIN
      qn := 0.0;
      un := 0.0
   END ELSE BEGIN
      qn := 0.5;
      un := (3.0/(x[n]-x[n-1]))*(ypn-(y[n]-y[n-1])/(x[n]-x[n-1]))
   END;
   y2[n] := (un-qn*u[n-1])/(qn*y2[n-1]+1.0);
   FOR k := n-1 DOWNTO 1 DO BEGIN
      y2[k] := y2[k]*y2[k+1]+u[k]
   END
END;


PROCEDURE splint(xa,ya,y2a: datar; n: integer;
               x: real; VAR y,dy: real);

VAR
   klo,khi,k: integer;
   h,b,a: real;

BEGIN
   klo := 1;
   khi := n;
   WHILE (khi-klo > 1) DO BEGIN
      k := (khi+klo) DIV 2;
      IF (xa[k] > x) THEN khi := k ELSE klo := k
   END;
   h := xa[khi]-xa[klo];
   a := (xa[khi]-x)/h;
   b := (x-xa[klo])/h;
   y := a*ya[klo]+b*ya[khi]+
      ((a*a*a-a)*y2a[klo]+(b*b*b-b)*y2a[khi])*(h*h)/6.0;
   dy := (ya[khi]-ya[klo])/h-(3*sqr(a)-1.0)/6.0*h*y2a[klo]+
        (3*sqr(b)-1.0)/6.0*h*y2a[khi];
END;


procedure interlin(bx,by,bz,br:real; var bydata:datar);

const pi=3.14159;

var
   ik,jk,jj:integer;
   th:real;
   ydata1,ydata2,ydata3:datar;

begin
   ik:=nz-1;
   jk:=nr-1;
   while ((ik>1)and(not(((bz>=zdata[ik]) and (bz<zdata[ik+1]))))) do
      dec(ik);
   while ((jk>1)and(not(((br>=rdata[jk]) and (br<rdata[jk+1]))))) do
      dec(jk);
   for jj:=1 to nr do
   begin
      ydata1[jj]:=tdata[1,ik,jj]+(tdata[1,ik+1,jj]-tdata[1,ik,jj])/
              (zdata[ik+1]-zdata[ik])*(bz-zdata[ik]);
      ydata2[jj]:=tdata[2,ik,jj]+(tdata[2,ik+1,jj]-tdata[2,ik,jj])/
              (zdata[ik+1]-zdata[ik])*(bz-zdata[ik]);
      ydata3[jj]:=(ydata1[jj]+ydata2[jj])/2.0;
   end;
   if by<>0.0 then
   begin
```

```
    th:=arctan(abs(bx/by));
    if ((bx>=0.0)and(by>0.0)) then
       for jj:=1 to nr do
          bydata[jj]:=ydata1[jj]+(ydata3[jj]-ydata1[jj])
          *th/pi*2.0
    else if ((bx>=0.0)and(by<0.0)) then
       for jj:=1 to nr do
          bydata[jj]:=ydata2[jj]+(ydata3[jj]-ydata2[jj])
          *th/pi*2.0
    else if ((bx<=0.0)and(by<0.0)) then
       for jj:=1 to nr do
          bydata[jj]:=ydata2[jj]+(ydata3[jj]-ydata2[jj])
          *th/pi*2.0
    else if ((bx<=0.0)and(by>0.0)) then
       for jj:=1 to nr do
          bydata[jj]:=ydata1[jj]+(ydata3[jj]-ydata1[jj])
          *th/pi*2.0;
  end
  else if by=0.0 then
     for jj:=1 to nr do
        bydata[jj]:=ydata3[jj];
end;

begin
   ar:=sqrt(sqr(ax)+sqr(ay));
   interlin(ax,ay,az,ar,ydata);
   dy1:=0.0;
   dyn:=0.0;
   spline(rdata,ydata,nr,dy1,dyn,ddy);
   splint(rdata,ydata,ddy,nr,ar,at,dt);
   if ar<>0.0 then
   begin
      adtdx:=dt*ax/ar;
      adtdy:=dt*ay/ar;
   end
   else
   begin
      adtdx:=0.0;
      adtdy:=0.0;
   end;
end;


begin
   temp(xx,yy,zz,t,dtdx,dtdy);
   dndx:=-(n0-1.0)*t0/sqr(t)*dtdx;
   dndy:=-(n0-1.0)*t0/sqr(t)*dtdy;
end;


(****************************)
(*** Differential equations ***)
(*** definition             ***)
(****************************)

Procedure derivs(x:real; y:glnarray; var dydx:glnarray);

var
   dndx,dndy:real;

begin
   dnxy(y[1],y[3],x,dndx,dndy);
   dydx[2]:=dndx;
   dydx[1]:=y[2];
   dydx[4]:=dndy;
   dydx[3]:=y[4];
end;

(***********************)
(*** Runge Kutta fourth ***)
(*** order method       ***)
(***********************)

PROCEDURE rk4(var y:glnarray; dydx: glnarray; n: integer; x,h: real);

VAR
   i: integer;
   xh,hh,h6: real;
   dym,dyt,yt: glnarray;
```

```
BEGIN
   hh := h*0.5;
   h6 := h/6.0;
   xh := x+hh;
   FOR i := 1 to n DO BEGIN
      yt[i] := y[i]+hh*dydx[i]
   END;
   derivs(xh,yt,dyt);
   FOR i := 1 to n DO BEGIN
      yt[i] := y[i]+hh*dyt[i]
   END;
   derivs(xh,yt,dym);
   FOR i := 1 to n DO BEGIN
      yt[i] := y[i]+h*dym[i];
      dym[i] := dyt[i]+dym[i]
   END;
   derivs(x+h,yt,dyt);
   FOR i := 1 to n DO BEGIN
      y[i] := y[i]+h6*(dydx[i]+dyt[i]+2.0*dym[i])
   END
END;


(****************************************)
(*** Initial data entry for a laser beam ***)
(****************************************)

Procedure datalasentry;

var
   ii: integer;
   nrays,nsteps: string;

begin
   ii:=1;
   writeln;
   writeln('Parameters for the ray tracing computation');
   writeln;
   write('How many rays (/2)        [',nray,'] Nray  = ');readln(nrays);
   if length(nrays)<>0 then val(nrays,nray,ii);
   write('Steps for each trajectory  [',nstep,'] Nstep  = ');readln(nsteps);
   if length(nsteps)<>0 then val(nsteps,nstep,ii);
end;

(**********************************)
(*** Initial data entry for imaging ***)
(**********************************)

Procedure dataimentry;

var
   ii: integer;
   nsteps,objangs,objdists: string;

begin
   ii:=1;
   writeln;
   writeln('Parameters of the imaging');
   writeln;
   write('Angular dimension of the object  (rad)  [',
   objang,'] objang = ');readln(objangs);
   if length(objangs)<>0 then val(objangs,objang,ii);
   writeln;
   write('Distance of the object           (cm)   [',
   trunc(objdist),'] (cm) objdist = ');readln(objdists);
   if length(objdists)<>0 then val(objdists,objdist,ii);
   writeln;
   writeln('Enter parameters for the ray tracing computation');
   writeln;
   write('Steps for each trajectory  [',nstep,'] Nstep  = ');readln(nsteps);
   if length(nsteps)<>0 then val(nsteps,nstep,ii);
end;

(********************************)
(*** Setting the defaults values ***)
(********************************)

procedure setdefaultval;

begin
```

```
   n0:=1.000293;
   t0:=273.3;
   nray:=10;
   nstep:=10;
   objang:=1.0e-3;
   objdist:=1.0e8;
end;

(************************)
(*** setting more values ***)
(************************)

procedure setmoreval;

begin
   deltar:=d/2.0/nray;
   dz:=l/nstep;
end;

(********************)
(*** Begin graphics ***)
(********************)

procedure begraph;

var
   grdriver,grmode:integer;

begin
   grdriver:=vga; grmode:=vgahi;
   initgraph(grdriver,grmode,'c:\tp6');
   setviewport(10,10,630,470,false);
   rectangle(0,0,620,460);
end;

(*******************)
(*** End Graphics ***)
(*******************)

procedure endgraph;

begin
   closegraph;
   restorecrtmode;
end;

(****************************************)
(*** Procedure to convert physical values ***)
(*** in screen cohordinates               ***)
(****************************************)

procedure convert(xmin,ymin,xmax,ymax,a,b:real; var na,nb:integer);

begin
   na:=round((a-xmin)/(xmax-xmin)*620);
   nb:=460-round((b-ymin)/(ymax-ymin)*460);
end;


(*******************************)
(*** determination of minimum   ***)
(*** and maximum focal distance ***)
(*******************************)

procedure zmaxmin(var max,min:real);

var
   i:integer;

begin
   max:=distz[1];
   min:=distz[1];
   for i:=1 to nray do
   begin
      if distz[i]>max then max:=distz[i];
      if distz[i]<min then min:=distz[i];
   end;
end;

(***************************)
```

```
(*** Rays trajectories of an ***)
(*** input laser beam        ***)
(*****************************)

procedure drawlasray;

var
   r,drdz:glnarray;
   gr,gz,j,i:integer;
   mr:string[40];
   disp,z:real;

begin
   begraph;
   line(0,230,620,230);
   outtextxy(200,462,' Rays trajectory in the lens');
   str(d:0:2,mr);
   mr:=concat('lens diameter = ',mr,' cm');
   outtextxy(1,-8,mr);
   for i:=1 to 2*nray-1 do
   begin
      z:=dz;
      r[3]:=-d/2.0+i*deltar;
      r[2]:=0.0;
      r[1]:=0.0;
      r[4]:=0.0;
      drdz[1]:=0.0;
      drdz[2]:=0.0;
      drdz[3]:=0.0;
      drdz[4]:=0.0;
      convert(0,-d/2,1,d/2,z,r[3],gz,gr);
      moveto(0,gr);
      for j:=1 to nstep do
      begin
         z:=0.0+j*dz;
         derivs(z,r,drdz);
         rk4(r,drdz,4,z,dz);
         convert(0,-d/2,1,d/2,z,r[3],gz,gr);
         lineto(gz.gr);
      end;
      disp:=0.7e-1;
      r[3]:=r[3]+disp;
      if r[4]<>0 then distz[i]:=-r[3]/r[4]
      else distz[i]:=0.0;
      distr[i]:=r[3];
      if distz[i]>10000.0 then distz[i]:=10000.0;
   end;
   repeat until readkey=' ';
   endgraph;
end;

(************************)
(*** Laser focusing file ***)
(************************)

procedure lasfile;

var
   flas:text;
   con,lasf,lasfs:string[8];
   lasf1:string;
   i:integer;

begin
   clrscr;
   lasf:='lasfocus';
   write('do you want the data to a file y/[n]');
   readln(con);
   if con='y' then
   begin
      write('Enter filename  [',lasf,'] ');
      readln(lasfs);
      if length(lasfs)<>0 then lasf:=lasfs;
      lasf1:=concat('c:\data\',lasf,'.dat');
      assign(flas,lasf1);
      rewrite(flas);
      for i:=1 to 2*nray-2 do
         writeln(flas,distr[i],' ',distz[i]);
      close(flas);
   end;
```

```
end;

(*************************)
(*** Focus drawing for an  ***)
(*** input laser beam      ***)
(*************************)

procedure drawlasfocus;

var
nz,nr,nz0,nr0,i:integer;
mmin,mmax:string[12];
mr:string[40];
max,min:real;

begin
   clrscr;
   begraph;
   line(0,230,620,230);
   zmaxmin(max,min);
   for i:=1 to 2*nray-2 do
   begin
      if (distz[i]>0.0) then
      begin
         convert(0,-d/2,max,d/2,0,distr[i],nz0,nr0);
         convert(0,-d/2,max,d/2,distz[i],0,nz,nr);
         line(nz0,nr0,nz,nr);
         convert(0,-d/2,max,d/2,distz[i],0,nz,nr);
         convert(0,-d/2,max,d/2,max,-distr[i]*(max-distz[i])/distz[i],nz0,nr0);
         line(nz0,nr0,nz,nr);
      end;
   end;
   str(max:0:2,mmax);
   mmax:=concat(mmax,' cm');
   outtextxy(540,462,mmax);
   str(0.0:0:2,mmin);
   mmin:=concat(mmin,' cm');
   outtextxy(1,462,mmin);
   outtextxy(200,462,' Rays trajectory after the lens');
   str(d:0:2,mr);
   mr:=concat('lens diameter = ',mr,' cm');
   outtextxy(1,-8,mr);
   repeat until readkey=' ';
   endgraph;
end;


(*********************************)
(*** istogram of the focal distance ***)
(*** for an input laser beam        ***)
(*********************************)

procedure drawlasisto;

var
numax,dz,z1,z2,max,min,yisto,yisto1:real;
nisto,is,istmax,i,nz1,nz2,nnl,nnr:integer;
mmax,mmin:string[12];
num:array[1..50] of real;

(************************************************)
(*** Setting parameters for the istogram of the focus ***)
(************************************************)

procedure istotitle;

var
   mins,maxs,nistos,yistos:string;
   istr:integer;

begin
   writeln;
   writeln(' Histogram Of The Laser Rays Along Z ');
   writeln;
   write('For which Y value you want the istogram   Y = [',yisto,'] cm ');
   readln(yistos);
   if length(yistos)<>0 then val(yistos,yisto,istr);
   write('how many intervals          ( < 50 ) Nisto = [',
        nisto,'] ');
   readln(nistos);
```

```
   if length(nistos)<>0 then val(nistos,nisto,istr);
   write('Minimum value in the z axis            Min = [',
        min,'] cm  ');
   readln(mins);
   if length(mins)<>0 then val(mins,min,istr);
   write('Maximum value in the z axis            Max = [',
        max,'] cm  ');
   readln(maxs);
   if length(maxs)<>0 then val(maxs,max,istr);
end;

begin
   zmaxmin(max,min);
   if min<0.0 then min:=0.0;
   numax:=0.0;
   nisto:=nray;
   yisto:=0.0;
   yisto1:=0.0;
   istotitle;
   for i:=1 to 2*nray-2 do
      distz[i]:=distz[i]*((distr[i]-yisto)/(distr[i]-yisto1));
   dz:=(max-min)/nisto;
   yisto1:=yisto;
   for is:=1 to nisto do
   begin
      num[is]:=0.0;
      z1:=min+(is-1)*dz;
      z2:=z1+dz;
      for i:=1 to 2*nray-2 do
         if (((distz[i]>0.0)and(distz[i]>=z1)and((distz[i]<z2))))
          then num[is]:=num[is]+1.0;
      if num[is]>numax then
      begin
         numax:=num[is];
         istmax:=is;
      end;
   end;
   numax:=numax+1.0;
   begraph;
   for is:=1 to nisto do
      if num[is]<>0.0 then
      begin
         z1:=min+(is-1)*dz;
         z2:=z1+dz;
         convert(min,0.0,max,numax,z1,0.0,nz1,nnl);
         convert(min,0.0,max,numax,z2,num[is],nz2,nnr);
         setfillstyle(1,2);
         bar3d(nz1,nnl,nz2,nnr,1,false);
      end;
   str(max:0:2,mmax);
   mmax:=concat(mmax,' cm');
   outtextxy(540,462,mmax);
   str(min:0:2,mmin);
   mmin:=concat(mmin,' cm');
   outtextxy(1,462,mmin);
   outtextxy(200,462,' Focal distance');
   outtextxy(1,-8,' Rays density at the focus (histogram) ');
   repeat until readkey=' ';
   endgraph;
end;

(***************************)
(*** Rays trajectories of an  ***)
(*** input image              ***)
(***************************)

procedure drawray;


var
   r,drdz,fi:glnarray;
   gr,gz,j,i,k,k1:integer;
   mr:string[40];
   thd,z:real;
   xo,yo:array [1..npoint] of real;
   x,y:array [1..nimagi] of real;

(***********************)
(*** Initialize variables ***)
(***********************)
```

```
procedure inima;

var
   i:integer;

begin
   for i:=1 to npoint do
   begin
      xo[i]:=0.0;
      yo[i]:=0.0;
   end;
   for i:=1 to nimagi do
   begin
      x[i]:=0.0;
      y[i]:=0.0;
   end;
end;

(********************************)
(*** Define the object and the grid ***)
(*** at the entrance of the lens    ***)
(*** The grid is a random mesh of  ***)
(*** Points.                        ***)
(********************************)

procedure objgrid;

var
   nn,ii,jj,li,lo:integer;
   dxy,dim:real;

begin
   dim:=objang*objdist;
   if npoint=1 then
   begin
      yo[1]:=0.0;
      xo[1]:=0.0;
   end
   else
      for lo:=1 to npoint do
      begin
         yo[lo]:=(lo-1)*dim/(npoint-1);
         xo[lo]:=0.0;
      end;
   li:=1;
   randomize;
   repeat
      x[li]:=random(round(diam*1.0e4))/1.0e4-diam/2.0;
      y[li]:=random(round(diam*1.0e4))/1.0e4-diam/2.0;
      if ( sqr(x[li]) + sqr(y[li]) <= sqr(diam/2) ) then inc(li);
   until li=nimagi;
end;

(******************************************)
(*** initial conditions for the imaging ***)
(******************************************)

procedure inipos(llo,lli:integer; var ar:glmarray);

var
   x1,y1,z1,x2,y2,z2,ddx,ddy,ddz:real;

begin
   x1:=xo[llo];
   y1:=yo[llo];
   z1:=-objdist;
   x2:=x[lli];
   y2:=y[lli];
   z2:=0.0;
   ddx:=(x2-x1);
   ddy:=(y2-y1);
   ddz:=(z2-z1);
   ar[1]:=x2;
   ar[2]:=ddx/ddz;
   ar[3]:=y2;
   ar[4]:=ddy/ddz;
end;

(*****************************)
```

```
begin
   inima;
   objgrid;
   begraph;
   outtextxy(200,462,' Rays trajectory in the lens');
   str(d:0:2,mr);
   mr:=concat('lens diameter = ',mr,' cm');
   outtextxy(1,-8,mr);
   k1:=1;
   for i:=1 to npoint do
   begin
      for j:=1 to nimagi do
      begin
         inipos(i,j,r);
         z:=0.0;
         thd:=(1.0-random(2))*1.22*6.0e-7/diam*100/sqrt(2);
         drdz[1]:=r[2]+thd;
         drdz[2]:=0.0;
         drdz[3]:=r[4]+thd;
         drdz[4]:=0.0;
         convert(0,-d,l,d,z,r[3],gz,gr);
         moveto(0,gr);
         for k:=1 to nstep+1 do
         begin
            z:=(k-1)*dz;
            derivs(z,r,drdz);
            rk4(r,drdz,4,z,dz);
            if (sqr(r[1])+sqr(r[3]))>=sqr(d/2.0) then
            begin
               r[1]:=d;
               r[2]:=0.0;
               r[3]:=d;
               r[4]:=0.0;
            end
            else
            begin
               convert(0,-d,l,d,z,r[3],gz,gr);
               lineto(gz,gr);
            end;
         end;
         if (sqr(r[1])+sqr(r[3]))<sqr(d/2.0) then
         begin
            distx[k1]:=r[1];
            gradx[k1]:=r[2];
            disty[k1]:=r[3];
            grady[k1]:=r[4];
            inc(k1);
         end;
      end;
      nimag:=k1-1;
   end;
   repeat until readkey=' ';
   endgraph;
end;

(*********************)
(*** Image drawing ***)
(*********************)

procedure drawimag(imdist:real);

var
   i,gx,gy:integer;
   ximag,yimag,ximagmax,yimagmax,ximagmin,yimagmin,
   x1min,x1max,y1min,y1max,a:real;

(************)
(*** Axis ***)
(************)

procedure axis;

var
   gx1,gy1,gx2,gy2:integer;
   ximagmins,ximagmaxs,yimagmins,yimagmaxs,imdists:string[100];

begin
   convert(x1min,y1min,x1max,y1max,ximagmin,0,gx2,gy2);
   convert(x1min,y1min,x1max,y1max,ximagmax,0,gx1,gy1);
```

```
    line (gx2,gy2,gx1,gy1);
    convert(x1min,y1min,x1max,y1max,ximagmin,yimagmin,gx2,gy2);
    convert(x1min,y1min,x1max,y1max,ximagmax,yimagmin,gx1,gy1);
    line (gx2,gy2,gx1,gy1);
    convert(x1min,y1min,x1max,y1max,ximagmax,yimagmax,gx2,gy2);
    line (gx1,gy1,gx2,gy2);
    convert(x1min,y1min,x1max,y1max,ximagmin,yimagmax,gx1,gy1);
    line (gx2,gy2,gx1,gy1);
    convert(x1min,y1min,x1max,y1max,ximagmin,yimagmin,gx2,gy2);
    line (gx1,gy1,gx2,gy2);
    str(ximagmin:8:2,ximagmins);
    str(yimagmin:8:2,yimagmins);
    str(ximagmax:8:2,ximagmaxs);
    str(yimagmax:8:2,yimagmaxs);
    str(imdist:8:2,imdists);
    ximagmins:=concat('Minimum x =',ximagmins,' cm');
    ximagmaxs:=concat('Maximum x =',ximagmaxs,' cm');
    yimagmins:=concat('Minimum y =',yimagmins,' cm'),
    yimagmaxs:=concat('Maximum y =',yimagmaxs,' cm');
    imdists:=concat('Distance from the lens =',imdists,' cm');
    outtextxy(10,462,ximagmins);
    outtextxy(240,-8,ximagmaxs);
    outtextxy(210,462,yimagmins);
    outtextxy(440,-8,yimagmaxs);
    outtextxy(10,8,imdists);
 end;

 (**********)

 begin
    ximagmin:=0.0;
    ximagmax:=0.0;
    yimagmin:=0.0;
    yimagmax:=0.0;
    for i:=1 to nimag do
    begin
       ximag:=distx[i]+gradx[i]*imdist;
       yimag:=disty[i]+grady[i]*imdist;
       if ximag>ximagmax then ximagmax:=ximag;
       if ximag<ximagmin then ximagmin:=ximag;
       if yimag>yimagmax then yimagmax:=yimag;
       if yimag<yimagmin then yimagmin:=yimag;
    end;
    a:=(yimagmax-yimagmin)/2;
    if (2*(ximagmax-ximagmin)/2)>1.5*a then a:=(ximagmax-ximagmin)/2;
    x1min:=(ximagmin+ximagmax)/2-2*a;
    x1max:=(ximagmin+ximagmax)/2+2*a;
    y1min:=(yimagmin+yimagmax)/2-1.5*a;
    y1max:=(yimagmin+yimagmax)/2+1.5*a;
    cleardevice;
    axis;
    for i:=1 to nimag do
    begin
       ximag:=distx[i]+gradx[i]*imdist;
       yimag:=disty[i]+grady[i]*imdist;
       convert(x1min,y1min,x1max,y1max,ximag,yimag,gx,gy);
       circle(gx,gy,4);
    end;
end;

(*************)
(*** defdist ***)
(*************)

Procedure defdist;

var con:string;
    ii:integer;
    imdists:string;
    imdist:real;

begin
   imdist:=0.0;
   begraph;
   drawimag(imdist);
   repeat until readkey=' ';
   endgraph;
   repeat
      writeln;
      writeln(' Press q to stop, any other key to define a new distance');
```

```
      con:=readkey;
      if con='q' then exit;
      writeln;
      writeln('          Distance of the image plane from the lens     ');
      write('         [',(imdist),'] (cm) Imdist = ');readln(imdists);
      if length(imdists)<>0 then val(imdists,imdist,ii);
      begraph;
      drawimag(imdist);
      repeat until readkey=' ';
      endgraph;
   until 1=0;
   endgraph;
end;

(*******************)
(***  WEIRD TRIP ***)
(*******************)

procedure trip;

var
   i:integer;
   imdist,m:real;
   as:string;

(***************)
(*** Trip title ***)
(***************)

Procedure triptitle;

begin
   clrscr;
   writeln;
   writeln('This is a serious trip.    Press - to slow down  ');
   writeln('                           Press + to accelerate     ');
   writeln('                       Press z to change direction   ');
   writeln('                   Press s to stop                 ');
   writeln('               Press spacebar to restart             ');
   writeln('           Press q to quit                         ');
   writeln(' Now spacebar to start ');
   repeat until readkey=' ';
end;

begin
   m:=3.0;
   imdist:=0.0;
   begraph;
   repeat
      if keypressed then
      begin
         as:=readkey;
         if as='+' then m:=m*2.0
         else if as='-' then m:=m/2.0
         else if as='z' then m:=-m
         else if as='s' then repeat until readkey=' ';
      end;
      imdist:=imdist+m;
      drawimag(imdist);
   until as='q';
   endgraph;
end;

(***********************)
(*** Intensity Histogram ***)
(***********************)

procedure istoimag(istdist,xistmin,xistmax,yistmin,yistmax:real);

const
   nc=14;

var
   i,gx,gy,nmax,gx1,gy1,ncol,kx,ky:integer;
   a,dxbox,dybox,xbox,ybox,xist,yist,x1box,y1box,x1min:real;
   x1max,y1min,y1max:real;
   nist:array[1..nc+1,1..nc+1] of integer;

(**************)
(*** Axisisto ***)
```

```
(**************)

procedure axisisto;

var
   gx1,gy1,gx2,gy2:integer;
   xistmins,xistmaxs,yistmins,yistmaxs,istdists:string[100];

begin
   convert(x1min,y1min,x1max,y1max,xistmin,0,gx2,gy2);
   convert(x1min,y1min,x1max,y1max,xistmax,0,gx1,gy1);
   line (gx2,gy2,gx1,gy1);
   convert(x1min,y1min,x1max,y1max,xistmin,yistmin,gx2,gy2);
   convert(x1min,y1min,x1max,y1max,xistmax,yistmin,gx1,gy1);
   line (gx2,gy2,gx1,gy1);
   convert(x1min,y1min,x1max,y1max,xistmax,yistmax,gx2,gy2);
   line (gx1,gy1,gx2,gy2);
   convert(x1min,y1min,x1max,y1max,xistmin,yistmax,gx1,gy1);
   line (gx2,gy2,gx1,gy1);
   convert(x1min,y1min,x1max,y1max,xistmin,yistmin,gx2,gy2);
   line (gx1,gy1,gx2,gy2);
   str(xistmin:8:2,xistmins);
   str(yistmin:8:2,yistmins);
   str(xistmax:8:2,xistmaxs);
   str(yistmax:8:2,yistmaxs);
   str(istdist:8:2,istdists);
   xistmins:=concat('Minimum x =',xistmins,' cm');
   xistmaxs:=concat('Maximum x =',xistmaxs,' cm');
   yistmins:=concat('Minimum y =',yistmins,' cm');
   yistmaxs:=concat('Maximum y =',yistmaxs,' cm');
   istdists:=concat('Distance from the lens =',istdists,' cm');
   outtextxy(10,462,xistmins);
   outtextxy(240,-8,xistmaxs);
   outtextxy(210,462,yistmins);
   outtextxy(440,-8,yistmaxs);
   outtextxy(10,8,istdists);
end;

(************************)
(* Procedure setnikcolor ***)
(************************)

Procedure setnikcolor(nc:integer);

var
   nc1:integer;

begin
   if control='c' then
      if nc=0 then nc1:=0
      else if nc=1 then nc1:=8
      else if nc=2 then nc1:=6
      else if nc=3 then nc1:=7
      else if nc=4 then nc1:=1
      else if nc=5 then nc1:=9
      else if nc=6 then nc1:=3
      else if nc=7 then nc1:=11
      else if nc=8 then nc1:=2
      else if nc=9 then nc1:=10
      else if nc=10 then nc1:=5
      else if nc=11 then nc1:=13
      else if nc=12 then nc1:=4
      else if nc=13 then nc1:=12
      else if nc=14 then nc1:=14
      else if nc=15 then nc1:=15;
   if control='g' then
      if nc=0 then nc1:=0
      else if nc=1 then nc1:=11
      else if nc=2 then nc1:=13
      else if nc=3 then nc1:=12
      else if nc=4 then nc1:=2
      else if nc=5 then nc1:=5
      else if nc=6 then nc1:=4
      else if nc=7 then nc1:=1;
   setcolor(nc1);
   setfillstyle(1,nc1);
end;

(************************)
(*** Procedure colorscale ***)
```

```
(************************)

Procedure colorscale;

var
   i:integer;

begin
   if control='c' then
      for i:=0 to 15 do
      begin
         setnikcolor(i);
         bar(20,400-10*i,30,400-10*i-10);
      end
   else if control='g' then
      for i:=0 to 7 do
      begin
         setnikcolor(i);
         bar(20,400-10*i,30,400-10*i-10);
      end;
end;

(*************************************)
(*** Writes on file the histogram values ***)
(*************************************)

procedure writefile;

var
   nfileb:string,
   fhis:text;
   ntot,i,j:integer;

begin
   ntot:=0;
   for i:=1 to nc+1 do
      for j:=1 to nc+1 do
         ntot:=ntot+nist[i,j];
   nfileb:=concat('c:\data\',nfile,'.dat');
   assign(fhis,nfileb);
   rewrite(fhis);
   writeln(fhis,'\  Total energy in the field =',ntot,'/',nimag);
   writeln(fhis,nc+1,' ',nc+1);
   write(fhis,0.0,' ');
   for i:=1 to nc+1 do
      write(fhis,xistmin+(i-0.5)*dxbox,' ');
   writeln(fhis);
   for j:=1 to nc+1 do
   begin
      write(fhis,yistmin+(j-0.5)*dybox,' ');
      for i:=1 to nc+1 do
         write(fhis,nist[i,j]/nmax,' ');
      writeln(fhis);
   end;
   close(fhis);
end;

(**********)

begin
   nmax:=0;
   cleardevice;
   for kx:=1 to nc+1 do
      for ky:=1 to nc+1 do
         nist[kx,ky]:=0;
   dxbox:=(xistmax-xistmin)/(nc+1);
   dybox:=(yistmax-yistmin)/(nc+1);
   for kx:=1 to nc+1 do
   begin
      xbox:=xistmin+(kx-1)*dxbox;
      for ky:=1 to nc+1 do
      begin
         ybox:=yistmin+(ky-1)*dybox;
         for i:=1 to nimag do
         begin
            xist:=distx[i]+gradx[i]*istdist;
            yist:=disty[i]+grady[i]*istdist;
            if (xist>xbox) and (xist<xbox+dxbox) and (yist>ybox)
              and (yist<ybox+dybox) then nist[kx,ky]:=nist[kx,ky]+1;
            if nist[kx,ky]>=nmax then nmax:=nist[kx,ky];
```

```
      end;
    end;
  end;
  if cf='y' then writefile;
  a:=(yistmax-yistmin)/2;
  if (2*(xistmax-xistmin)/2)>1.5*a then a:=(xistmax-xistmin)/2;
  x1min:=(xistmin+xistmax)/2-2*a;
  x1max:=(xistmin+xistmax)/2+2*a;
  y1min:=(yistmin+yistmax)/2-1.5*a;
  y1max:=(yistmin+yistmax)/2+1.5*a;
  cleardevice;
  colorscale;
  for kx:=1 to nc+1 do
  begin
    xbox:=xistmin+(kx-1)*dxbox;
    x1box:=xistmin+kx*dxbox;
    for ky:=1 to nc+1 do
    begin
      ybox:=yistmin+(ky-1)*dybox;
      y1box:=yistmin+ky*dybox;
      convert(x1min,y1min,x1max,y1max,xbox,ybox,gx,gy);
      convert(x1min,y1min,x1max,y1max,x1box,y1box,gx1,gy1);
      if control='c' then ncol:=round(nist[kx,ky]*15.0/nmax)
      else if control='g' then ncol:=round(nist[kx,ky]*7.0/nmax);
      setnikcolor(ncol);
      bar(gx,gy,gx1,gy1);
    end;
  end;
  setcolor(white);
  axisisto;
  repeat until readkey=' ';
end;

(**************)
(*** dististo ***)
(**************)

Procedure dististo;

var
   con:string;
   ii:integer;
   istdists,xistmins,xistmaxs,yistmins,yistmaxs,controls,cfs:string;
   istdist,xistmin,xistmax,yistmin,yistmax:real;

begin
  istdist:=0.0;
  xistmin:=-1.0;
  xistmax:=1.0;
  yistmin:=-1.0;
  yistmax:=1.0;
  control:='g';
  cf:='n';
  repeat
    clrscr;
    writeln;
    writeln(' Press q to stop, any other key to define a new distance');
    con:=readkey;
    if con='q' then exit;
    writeln;
    writeln('          Distance of the Histogram plane from the lens      ');
    write('          [',(istdist),'] (cm) Histogram distance = ');
    readln(istdists);
    if length(istdists)<>0 then val(istdists,istdist,ii);
    writeln;
    writeln('          Minimum X value');
    write('          [',(xistmin),'] (cm) Minimum X = ');
    readln(xistmins);
    if length(xistmins)<>0 then val(xistmins,xistmin,ii);
    writeln;
    writeln('          Maximum X value');
    write('          [',(xistmax),'] (cm) Maximum X = ');
    readln(xistmaxs);
    if length(xistmaxs)<>0 then val(xistmaxs,xistmax,ii);
    writeln;
    writeln('          Minimum Y value');
    write('          [',(yistmin),'] (cm) Minimum y = ');
    readln(yistmins);
    if length(yistmins)<>0 then val(yistmins,yistmin,ii);
    writeln;
```

```
      writeln('         Maximum Y value');
      write('           [',(yistmax),'] (cm) Maximum Y = ');
      readln(yistmaxs);
      if length(yistmaxs)<>0 then val(yistmaxs,yistmax,ii);
      writeln;
      write(' False colors (c) or Grayscale (g) [',(control),'] ');
      readln(controls);
      if length(controls)<>0 then control:=controls;
      write('Do you want a file of the histogram [',cf,'] ');
      readln(cfs);
      if length(cfs)<>0 then cf:=cfs;
      if cf='y' then
         repeat
            writeln;
            write('Enter name of the file  ');
            readln(nfile);
         until length(nfile)<>0;
      begraph;
      istoimag(istdist,xistmin,xistmax,yistmin,yistmax);
      endgraph;
   until 1=0;
end;


(***********************************)
(* Menu selection of the program options *)
(***********************************)

procedure mainmenu;

begin
   clrscr;
   writeln;
   writeln('                    RAY TRACING OF A GAS LENS ');
   writeln;
   writeln('Select one of the following option');
   writeln;
   writeln('Laser beam through the vertical section (1)');
   writeln;
   writeln('Imaging through the gas lens           (2)');
   writeln;
   writeln('End main menu                          (3)');
   writeln;
   write('option ? ');readln(maino);
end;

procedure lasmenu;

begin
   clrscr;
   writeln;
   writeln('                    LASER THROUGH A GAS LENS ');
   writeln;
   writeln('Select one of the following option');
   writeln;
   writeln('Laser beam focusing (after the lens)          (1)');
   writeln;
   writeln('Histogram of the intensity on the optical axis (2)');
   writeln;
   writeln('End laser menu                                (3)');
   writeln;
   write('option ? ');readln(laso);
end;


procedure immenu;

begin
   clrscr;
   writeln;
   writeln('                  IMAGING THROUGH A GAS LENS ');
   writeln;
   writeln('Select one of the following option');
   writeln;
   writeln('Image projection on a particular plane           (1)');
   writeln;
   writeln('Intensity histogram on a particular plane        (2)');
   writeln;
   writeln('Trip along the optical axis looking at the image (3)');
   writeln;
```

```
   writeln('End imaging menu                                    (4)');
   writeln;
   write('option ? ');readln(imo);
end;


(********************)
(*** MAIN PROGRAM ***)
(********************)

begin
   clrscr;
   initialize;
   loadexpdata;
   setdefaultval;
   repeat
      mainmenu;
      if maino=1 then
      begin
         datalasentry;
         setmoreval;
         drawlasray;
         repeat
            lasmenu;
            if laso=1 then
            begin
               lasfile;
               drawlasfocus;
            end
            else if laso=2 then drawlasisto
         until laso=3;
      end
      else if maino=2 then
      begin
         dataimentry;
         setmoreval;
         drawray;
         repeat
            immenu;
            if imo=1 then defdist
            else if imo=2 then dististo
            else if imo=3 then trip;
         until imo=4;
       end;
   until maino=3;
End.
```

APPENDIX B

The program listed below was utilised in chapter 4 to model the colliding shock q-switching of a ruby laser. At each time after the shock collision the focal length and the CSL diameter are calculated and the resonator geometry is solved by utilising ray matrix optics. At each time the resonator configuration, the cavity magnification and the losses are known, so that the rate equation for the population inversion and the photon density can be solved numerically. A Runge Kutta algorithm with variable step size is utilised.

```
(******************************************)
(*** This program solves the rate equations ***)
(*** for the q-switched ruby laser          ***)
(*** Computing the losses for the cavity    ***)
(*** with the CSL                           ***)
(******************************************)

Program qswi;

uses crt,graph;

const
   d1=75.0e-2;          (* distance between OC and lens (m)          *)
   d2=250.0e-2;         (* distance between lens and CSL             *)
   d3=10.0e-2;          (* distance between CSL and FR               *)
   f1=200.0e-2;         (* focal length of the lens in the cavity    *)
   tmax=10.0e-6;        (* maximum time to solve the laser equation  *)
   tiniwr=3.0e-6;       (* initial data writing time                 *)
   tfinwr=10.0e-6;      (* final data writing time                   *)
   nruby=1.75;          (* Ruby refractive index                     *)
   cl=3.0e10;           (* cm/s                                      *)
   s21=2.5e-20;         (* stimulated emission cross section (cm2)   *)
   lres=d1+d2+d3;       (* resonator length                          *)
   lrod=10.4e-2;        (* rod length                                *)
   gamma=1.5;           (* level degeneracy                          *)
   ni=1.58e19;          (* Cr ion density cm-3                       *)
   tr=2.0*100*lres/cl;  (* round trip time (s)                       *)
   nloss=500;           (* number of time point to compute the losses *)
   refl1=0.45;          (* Output coupler reflectivity               *)
   hplank=6.63e-34;     (* plank constant                            *)
   dtstart=1.0e-9;      (* initial guess for the RK4 time step       *)
   rruby=0.5e-2;        (* Radius of the ruby rod                    *)
   ntime=400;           (* Number of output points                   *)
   tsw=4.0e-6;          (* Switching time                            *)
   los=0.27;            (* Diffraction, Reflections, Scattering losses *)
   ininver=ni*0.33;     (* Initial population inversion              *)
   nshell=30;           (* Number of shells                          *)
   dr=rruby/nshell;     (* Radial increment                          *)

type
   glnarray = ARRAY [1..2] OF double;
   arrtime = array [1..nloss] of double;
   result = array [1..ntime+1] of double;
   mat=array[1..2,1..2] of double;
   ray=array[1..2] of double;
   shell=array[1..nshell] of double;

var
   arrloss: arrtime;
   time,inten,lost,intave:result;
   ener,epsi,lcoup,t,las1,las2,int,dt:double;
   j,k:integer;
   intmax,ene,tlas,radius:shell;
   las,dlasdt:glnarray;
   a,b,c,d,e,f,g,h,i,mtot,firhalf,sechalf:mat;
```

```
  nf1,nf2,nf3:text;
  nfile1,nfile2,nfile3:string;

(***********************)
(*** Matrix 2*2 product ***)
(***********************)

procedure prod(x,y:mat; var pro:mat);

begin
  pro[1,1]:=x[1,1]*y[1,1]+x[1,2]*y[2,1];
  pro[1,2]:=x[1,1]*y[1,2]+x[1,2]*y[2,2];
  pro[2,1]:=x[2,1]*y[1,1]+x[2,2]*y[2,1];
  pro[2,2]:=x[2,1]*y[1,2]+x[2,2]*y[2,2];
end;

(**********************)
(*** Procedure equalm ***)
(**********************)

procedure equalm(m1:mat; var m2:mat);

begin
  m2[1,1]:=m1[1,1];
  m2[1,2]:=m1[1,2];
  m2[2,1]:=m1[2,1];
  m2[2,2]:=m1[2,2];
end;

(*********************)
(*** Procedure equalr ***)
(*********************)

Procedure equalr(r1:ray; var r2:ray);

begin
  r2[1]:=r1[1];
  r2[2]:=r1[2];
end;

(***************************)
(*** Procedure set m to idm ***)
(***************************)

procedure idm(var m:mat);

begin
  m[1,1]:=1.0;
  m[1,2]:=0.0;
  m[2,1]:=0.0;
  m[2,2]:=1.0;
end;

(********************************)
(*** Propagate a ray of matrix mz ***)
(********************************)

procedure propagm(m:mat; x:ray; var x1:ray);

begin
  x1[1]:=x[1]*m[1,1]+x[2]*m[1,2];
  x1[2]:=x[1]*m[2,1]+x[2]*m[2,2];
end;

(**********************************************)
(*** Define resonator matrix for the constant optics ***)
(**********************************************)

procedure defmatrix;

var
  j:integer;

begin
  for j:=1 to 2 do
  begin
    a[j,j]:=1.0;
    b[j,j]:=1.0;
    c[j,j]:=1.0;
    d[j,j]:=1.0;
```

```
      e[j,j]:=1.0;
      f[j,j]:=1.0;
      g[j,j]:=1.0;
      h[j,j]:=1.0;
      i[j,j]:=1.0;
   end;
   a[2,1]:=0.0;
   a[1,2]:=d1;
   c[2,1]:=0.0;
   c[1,2]:=d2;
   e[2,1]:=0.0;
   e[1,2]:=2.0*d3;
   b[1,2]:=0.0;
   b[2,1]:=-1.0/f1;
   h[1,2]:=b[1,2];
   h[2,1]:=b[2,1];
   g[1,2]:=c[1,2];
   g[2,1]:=c[2,1];
   i[1,2]:=a[1,2];
   i[2,1]:=a[2,1];
end;

(******************************)
(*** CSL focal length Vs. Time ***)
(******************************)

function f2(time:double):double;

var
   fl,tl:array[0..4] of double;
   j:integer;

begin
   tl[0]:=tsw;
   fl[0]:=0.0;
   tl[1]:=tsw+2.7e-6;
   fl[1]:=0.4;
   tl[2]:=tsw+3.2e-6;
   fl[2]:=0.5;
   tl[3]:=tsw+4.4e-6;
   fl[3]:=0.91;
   tl[4]:=tsw+4.7e-6;
   fl[4]:=1.3;
   if time<=tsw then
      f2:=1.0e10
   else if time>=tl[4] then
      f2:=fl[4]+(fl[4]-fl[3])/(tl[4]-tl[3])*(time-tl[4])
   else for j:=0 to 3 do
      if (time>=tl[j])and(time<tl[j+1]) then
         f2:=fl[j]+(fl[j+1]-fl[j])/(tl[j+1]-tl[j])*(time-tl[j]);
end;

(************************)
(*** Variable lens matrix ***)
(************************)

procedure varlens(a:double);

begin
   d[1,2]:=0.0;
   d[2,1]:=-1.0/f2(a);
   f[1,2]:=d[1,2];
   f[2,1]:=d[2,1];
end;

(*************************)
(*** CSL diameter Vs. time ***)
(*************************)

function df2(time:double):double;

const
   ddf2dt=7.5e-3/8.4e-6;    (* CSL diameter time gradient *)

begin
   if time<tsw then
      df2:=1.0e-2
   else
      df2:=ddf2dt*(time-tsw);
end;
```

```
(**************************)
(*** Procedure find FirHalf ***)
(**************************)

Procedure findfirhalf;

begin
   prod(b,a,firhalf);
   prod(c,firhalf,firhalf);
   prod(d,firhalf,firhalf);
end;

(**************************)
(*** Procedure find SecHalf ***)
(**************************)

Procedure findsechalf;

begin
   prod(g,f,sechalf);
   prod(h,sechalf,sechalf);
   prod(i,sechalf,sechalf);
end;

(************************)
(*** Procedure find Mtot ***)
(************************)

Procedure findmtot;

begin
   prod(b,a,mtot);
   prod(c,mtot,mtot);
   prod(d,mtot,mtot);
   prod(e,mtot,mtot);
   prod(f,mtot,mtot);
   prod(g,mtot,mtot);
   prod(h,mtot,mtot);
   prod(i,mtot,mtot);
end;

(*************************************)
(*** This procedure solves the resonator ***)
(*** In matrix algebra                 ***)
(*************************************)

procedure reso(t:double; x:double; var loss:double);

var
   abs1,abs2,aa,trans,trans1,trans2,trans3,x1,x2,x3,m,mag,dthdx:double;
   rentr,rexit:ray;
   cond1,cond2,cond3:boolean;
   nm,mi:integer;

begin
   defmatrix;
   varlens(t);
   aa:=df2(t)/2;
   nm:=10;
   findmtot;
   findfirhalf;
   findsechalf;
   m:=0.5*(mtot[1,1]+mtot[2,2]);
   if abs(m)>=1 then
   begin
      if m=1 then
         dthdx:=0.0
      else
      begin
         if m>1 then mag:=m+sqrt(sqr(m)-1);
         if m<-1 then mag:=m-sqrt(sqr(m)-1);
         dthdx:=(mag-mtot[1,1])/mtot[1,2];
      end;
      rentr[1]:=x;
      rentr[2]:=dthdx*rentr[1];
      propagm(firhalf,rentr,rexit);
      x1:=abs(rexit[1]);
      cond1:=x1>aa;
      if cond1 then
```

```
      begin
         rexit[1]:=aa*rexit[1]/x1;
         rexit[2]:=rexit[2]*aa/x1;
      end;
      propagm(e,rexit,rexit);
      x2:=abs(rexit[1]);
      cond2:=x2>aa;
      if cond2 then
      begin
         rexit[1]:=aa*rexit[1]/x2;
         rexit[2]:=rexit[2]*aa/x2;
      end;
      propagm(sechalf,rexit,rexit);
      x3:=abs(rexit[1]);
      cond3:=x3>x;
      if cond1 then
         trans1:=sqr(aa)/sqr(x1)
      else trans1:=1;
      if cond2 then
         trans2:=sqr(aa)/sqr(x2)
      else trans2:=1;
      if cond3 then
         trans3:=sqr(x)/sqr(x3)
      else trans3:=1;
      trans:=trans1*trans2*trans3;
   end
   else if abs(m)<1 then
   begin
      rexit[1]:=x;
      rexit[2]:=0;
      trans:=1;
      for mi:=1 to nm do
      begin
         propagm(firhalf,rexit,rexit);
         x1:=abs(rexit[1]);
         cond1:=x1>aa;
         if cond1 then
         begin
            rexit[1]:=rexit[1]*aa/x1;
            rexit[2]:=rexit[2]*aa/x1;
         end;
         propagm(e,rexit,rexit);
         x2:=abs(rexit[1]);
         cond2:=x2>aa;
         if cond2 then
         begin
            rexit[1]:=rexit[1]*aa/x2;
            rexit[2]:=rexit[2]*aa/x2;
         end;
         propagm(sechalf,rexit,rexit);
         x3:=abs(rexit[1]);
         cond3:=x3>x;
         if cond3 then
         begin
            rexit[1]:=rexit[1]*x/x3;
            rexit[2]:=rexit[2]*x/x3;
         end;
         cond1:=x1>aa;
         cond2:=x2>aa;
         cond3:=x3>x;
         if cond1 then
            trans1:=sqr(aa)/sqr(x1)
         else trans1:=1;
         if cond2 then
            trans2:=sqr(aa)/sqr(x2)
         else trans2:=1;
         if cond3 then
            trans3:=sqr(x)/sqr(x3)
         else trans3:=1;
         trans:=trans*trans1*trans2*trans3;
      end;
   end;
   loss:=1-trans;
end;

(*****************************************************)
(*** Procedure to calculate the losses at different times ***)
(*****************************************************)

procedure lossarrcal(rr:double);
```

```
var
   a,tl,dtl:double;
   k:integer;

begin
   dtl:=tmax/nloss;
   for k:=1 to nloss do
   begin
      tl:=k*dtl;
      reso(tl,rr,a);
      arrloss[k]:=a;
   end;
end;

(*******************************************)
(*** Function to interpolate the array arrloss ***)
(*******************************************)

function closs(t:double):double;

var
   tl,tl1,dtl:double;
   k:integer;

begin
   closs:=0.0;
   dtl:=tmax/nloss;
   if t<dtl then closs:=arrloss[1]
   else
      for k:=1 to nloss-1 do
      begin
         tl:=k*dtl;
         tl1:=(k+1)*dtl;
         if (t>=tl) and (t<tl1) then
            closs:=arrloss[k]+(arrloss[k+1]-arrloss[k])/dtl*(t-tl);
   end;
end;

(****************************)
(*** Define the rate equations ***)
(****************************)

PROCEDURE derivs(x:double; y:glnarray; VAR dydx:glnarray);

var
   sp21,loss:double;

begin
    sp21:=y[1]*1.0e-6;
    loss:=closs(x)-ln(refl1)+los;
    dydx[1]:=-y[2]*s21*cl/nruby*gamma*y[1];
    dydx[2]:=y[2]*(s21*y[1]*cl/nruby*lrod/lres-loss/tr)+sp21;
end;

(***************************)
(*** Runge Kutta fourth order ***)
(***************************)

PROCEDURE rk4(y,dydx: glnarray; n: integer; x,h: double; VAR yout: glnarray);

VAR
   i: integer;
   xh,hh,h6: double;
   dym,dyt,yt: glnarray;

BEGIN
   hh := h*0.5;
   h6 := h/6.0;
   xh := x+hh;
   FOR i := 1 to n DO BEGIN
      yt[i] := y[i]+hh*dydx[i]
   END;
   derivs(xh,yt,dyt);
   FOR i := 1 to n DO BEGIN
      yt[i] := y[i]+hh*dyt[i]
   END;
   derivs(xh,yt,dym);
   FOR i := 1 to n DO BEGIN
      yt[i] := y[i]+h*dym[i];
```

```
      dym[i] := dyt[i]+dym[i]
   END;
   derivs(x+h,yt,dyt);
   FOR i := 1 to n DO BEGIN
      yout[i] := y[i]+h6*(dydx[i]+dyt[i]+2.0*dym[i])
   END
END;

(*****************************)
(*** Procedure saveresult to file ***)
(*****************************)

Procedure saveresult(k:integer; tt,ii,ll:result; var nf:text);

var
   j:integer;

begin
   if K=1 then
     for j:=1 to ntime do
        writeln(nf,tt[j]-tsw,' ',ii[j],' ',ll[j]);
end;

(************************************)
(*** Procedure to save radial information ***)
(************************************)

Procedure saveradial(ra,en,inm,tl:shell; entot:double; var nf:text);

var
   k:integer;

begin
   writeln(nf);
   for k:=1 to nshell do
   begin
      writeln(nf,'\ ',k,' Ene= ',en[k],' Intmax=',inm[k]);
      writeln(nf,'\ ',k,' Tlas=',tl[k]-tsw,' radius=',ra[k]);
      writeln(nf,ra[k],' ',en[k],' ',inm[k],' ',tl[k]-tsw);
   end;
end;


(*************************)
(*** Procedure to open file ***)
(*************************)

Procedure open(var nf:text; var nfile:string);

var
   nfile1:string;

begin
   nfile1:=concat('c:\data\',nfile,'.dat');
   assign(nf,nfile1);
   rewrite(nf);
end;

(**********************************)
(*** Procedure to initialize data values ***)
(**********************************)

procedure initialize1;
begin
   nfile1:='modecmax';
   nfile2:='modecrad';
   open(nf1,nfile1);
   lcoup:=(1.0-refl1)/(1.0+refl1)*sqr(cl)*hplank/0.693e-4;
   ener:=0.0;
   for j:=1 to ntime+1 do
   begin
      time[j]:=tiniwr+(tfinwr-tiniwr)/ntime*(j-1);
      inten[j]:=0.0;
      intave[j]:=0.0;
      lost[j]:=0.0;
   end;
end;

(**********************************)
(*** Procedure to initialize data values ***)
```

```
(*************************************)

Procedure initialize2;

begin
   radius[k]:=k*dr;
   intmax[k]:=0.0;
   ene[k]:=0.0;
   tlas[k]:=tsw;
   las[1]:=ininver;             (* Initial inversion *)
   las[2]:=0;                   (* initial intensity *)
   j:=1;
   dt:=dtstart;
   t:=0.0;
end;

(******************)
(*** Main program ***)
(******************)

Begin
   initialize1;
   for k:=1 to nshell do
   begin
      initialize2;
      lossarrcal(radius[k]);
      while (t<tmax) do
      begin
         las1:=las[1];
         las2:=las[2];
         derivs(t,las,dlasdt);
         rk4(las,dlasdt,2,t,dt,las);
         int:=las[2]*lcoup;
         if int>intmax[k] then
         begin
            intmax[k]:=int;
            tlas[k]:=t;
         end;
         ene[k]:=ene[k]+int*dt;
         if (las1=0.0) or (las2=0.0) then epsi:=0
         else epsi:=1.0e1*abs(((las[1]-las1)/las1+abs(las[2]-las2)/las2)/2.0);
         dt:=(dtstart/(0.08+epsi)+dt)/2;
         if (t>time[j]) and (t<time[j+1]) then
         begin
            inten[j]:=int;
            if k=1 then
               intave[j]:=intave[j]+inten[j]*sqr(radius[1])/sqr(rruby)
            else
               intave[j]:=intave[j]+inten[j]*
                     (sqr(radius[k])-sqr(radius[k-1]))/sqr(rruby);
            lost[j]:=closs(t);
            writeln(time[j],inten[j]);
            inc(j);
         end;
         t:=t+dt;
      end;
      if k=1 then
         ener:=ener+ene[1]*pi*sqr(radius[1])*1.0e4
      else
         ener:=ener+ene[k]*pi*(sqr(radius[k])-sqr(radius[k-1]))*1.0e4;
      writeln(k);
      writeln('Laser Pulse Energy =',ene[k],' J/cm2 ');
      writeln('laser pulse at time t =',tlas[k]-tsw);
      saveresult(k,time,inten,lost,nf1);
   end;
   close(nf1);
   writeln('Energy =',ener);
   open(nf2,nfile2);
   saveradial(radius,ene,intmax,tlas,ener,nf2);
   close(nf2);
end.
```

APPENDIX C

The following program was utilised in chapter 5 to compute the diffraction pattern due to the colliding shock lens. Both the refraction due to the refractive index profile experimentally measured and the diffraction from the circular aperture of the CSL are taken into account.

```
(**************************************************)
(*** This program computes the diffraction pattern due ***)
(*** to the Colliding Shock Lens at any image plane     ***)
(**************************************************)

program difcsl;

uses
   crt, graph;

const
   a2=0.21;
   a4=7.41e3;
   rmax=2.4e-3;
   nr=5000;
   pmax=3.0e-3;
   np=400;
   lambda=0.337e-6;

var
   r,r1,p,dr,dp,r24,rj,alfa,beta,gamma,intc,ints,intmax,zmax:double;
   intint,intref,norm:double;
   fl:text;
   ip,ir:integer;
   int,ref:array[1..np] of double;

FUNCTION bessj0(x: double): double;

VAR
   ax,xx,z: double;  y,ans,ans1,ans2: double;

BEGIN
   IF (abs(x) < 8.0) THEN BEGIN
      y := sqr(x);
      ans1 := 57568490574.0+y*(-13362590354.0+y*(651619640.7
         +y*(-11214424.18+y*(77392.33017+y*(-184.9052456)))));
      ans2 := 57568490411.0+y*(1029532985.0+y*(9494680.718
         +y*(59272.64853+y*(267.8532712+y*1.0))));
      bessj0 := ans1/ans2 END
   ELSE BEGIN
      ax := abs(x); z := 8.0/ax; y := sqr(z); xx := ax-0.785398164;
      ans1 := 1.0+y*(-0.1098628627e-2+y*(0.2734510407e-4
         +y*(-0.2073370639e-5+y*0.2093887211e-6)));
      ans2 := -0.1562499995e-1+y*(0.1430488765e-3
         +y*(-0.6911147651e-5+y*(0.7621095161e-6
         -y*0.934945152e-7)));
      ans := sqrt(0.636619772/ax)*(cos(xx)*ans1-z*sin(xx)*ans2);
      bessj0 := ans END
END;

FUNCTION bessj1(x: double): double;
VAR
   ax,xx,z: double;  y,ans,ans1,ans2: double;
FUNCTION sign(x: double): double;
   BEGIN
      IF x >= 0.0 THEN sign := 1.0
      ELSE sign := -1.0;
   END;
BEGIN
   IF (abs(x) < 8.0) THEN BEGIN
      y := sqr(x);
```

```
      ans1 := x*(72362614232.0+y*(-7895059235.0+y*(242396853.1
         +y*(-2972611.439+y*(15704.48260+y*(-30.16036606))))));
      ans2 := 144725228442.0+y*(2300535178.0+y*(18583304.74
         +y*(99447.43394+y*(376.9991397+y*1.0))));
      bessj1 := ans1/ans2  END
   ELSE BEGIN
      ax := abs(x); z := 8.0/ax; y := sqr(z); xx := ax-2.356194491;
      ans1 := 1.0+y*(0.183105e-2+y*(-0.3516396496e-4
         +y*(0.2457520174e-5+y*(-0.240337019e-6))));
      ans2 := 0.04687499995+y*(-0.2002690873e-3
         +y*(0.8449199096e-5+y*(-0.88228987e-6+y*0.105787412e-6)));
      ans := sqrt(0.636619772/ax)*(cos(xx)*ans1
         -z*sin(xx)*ans2)*sign(x);
      bessj1 := ans  END
END;

(****************************************)
(*** Finds the normalisation of the integral ***)
(****************************************)

procedure normint(var iintmax:double);

var
   iints,iintc,rr,rr24,rrj:double;
   iir:integer;

begin
   iintc:=0.0;
   iints:=0.0;
   for iir:=1 to nr do
   begin
      rr:=iir*dr;
      rr24:=alfa*sqr(rr)+beta*sqr(sqr(rr));
      rrj:=p*rr*gamma;
      iintc:=iintc+1e10*cos(rr24)*rr;
      iints:=iints+1e10*sin(rr24)*rr;
   end;
   iintmax:=sqr(iints)+sqr(iintc);
end;

(****************************************************)
(*** Finds the intensity at the centre of the intensity pattern ***)
(****************************************************)

procedure findI0(z:double; var I0:double);

var
   ir:integer;
   intc,ints,r,r24,alfa,beta,gamma:double;

begin
   alfa:=2*pi/lambda*(a2-0.5/z);
   beta:=2*pi/lambda*a4;
   gamma:=pi/lambda/z;
   intc:=0.0;
   ints:=0.0;
   for ir:=1 to nr do
   begin
      r:=ir*dr;
      r24:=alfa*sqr(r)+beta*sqr(sqr(r));
      intc:=intc+1e10*cos(r24)*r;
      ints:=ints+1e10*sin(r24)*r;
   end;
   I0:=sqr(ints)+sqr(intc);
end;

(*********************************************************)
(*** Finds the focus as the plane with maximum central intensity ***)
(*********************************************************)

procedure findzmax(var zmax:double);

var
   i,nz:integer;
   za,zb,z1,z2,dz,I1,I2,Imax:double;

begin
   imax:=0.0;
   nz:=10;
   za:=1.0;
```

```
  zb:=3.0;
  dz:=(zb-za)/nz;
  for i:=1 to nz+1 do
  begin
    z1:=za+(i-1)*dz;
    findi0(z1,i1);
    if i1>imax then
    begin
      imax:=i1;
      zmax:=z1;
    end;
  end;
  z1:=zmax-dz;
  z2:=zmax+dz;
  while abs(z1-z2)>1.0e-4 do
  begin
    findI0(z1,I1);
    findI0(z2,I2);
    writeln('z1 =',z1,' I1 =',i1);
    writeln('z2 =',z2,' I2 =',i2);
    writeln;
    if I1>=I2 then
      z2:=z1+abs(z1-z2)/2
    else if I1<I2 then
      z1:=z1+abs(z1-z2)/2;
  end;
  zmax:=(z1+z2)/2;
end;



(*******************)
(*** Main program ***)
(*******************)

begin
  dp:=pmax/np;
  dr:=rmax/nr;
  findzmax(zmax);
  alfa:=2*pi/lambda*(a2-0.5 zmax);
  beta:=2*pi/lambda*a4;
  gamma:=pi/lambda/zmax;
  normint(intmax);
  intint:=0.0;
  intref:=0.0;
  for ip:=1 to np do
  begin
    p:=ip*dp;
    intc:=0.0;
    ints:=0.0;
    for ir:=1 to nr do
    begin
      r:=ir*dr;
      r24:=alfa*sqr(r)+beta*sqr(sqr(r));
      rj:=p*r*gamma;
      intc:=intc+1e10*cos(r24)*bessj0(rj)*r;
      ints:=ints+1e10*sin(r24)*bessj0(rj)*r;
    end;
    int[ip]:=(sqr(ints)+sqr(intc))/intmax;
    r1:=gamma*p*rmax;
    ref[ip]:=sqr(2.0*bessj1(r1)/r1);
    intint:=intint+int[ip]*p;
    intref:=intref+ref[ip]*p;
    writeln('at ',p,': ',int[ip],' ',ref[ip] );
  end;
  norm:=intref/intint;
  assign(f1,'c:\datacsl\14f.dat');
  rewrite(f1);
  writeln(f1,'\ Focal length =',zmax);
  writeln(f1,0.0,' ',1.0*norm,' ',1.0);
  for ip:=1 to np do
  begin
    writeln('at ',ip*dp,' = ',int[ip]*norm,' ',ref[ip] );
    writeln(f1,ip*dp,' ',int[ip]*norm,' ',ref[ip] );
  end;
  close(f1);
end.
```

The next program reads the output files written by the previous program and simulates the effect of the divergence of the laser on the intensity profile.

```
(**************************************************)
(*** This program computes the diffraction pattern due ***)
(*** to the Colliding Shock Lens at any image plane     ***)
(*** including the divergence of the laser beam          ***)
(**************************************************)

program difcslav;

uses dos,crt;

const
   np=400;

type
   arrival=array[1..np] of double;

var
   i:integer;
   fl,fla:text;
   l,dth,dr:double;
   r,int,ref,inta:arrival;

(************************************************)
(*** Procedure to average the fringe profile according ***)
(*** to the divergence of the laser                     ***)
(************************************************)

procedure calcave(int:arrival; var intave:arrival);

var
   ndr,i:integer;
   m,ii,jj:longint;
   nn,aa,rij2,rn2,intpr:double;

begin
   ndr:=round(l*dth/2.0/dr);
   if ndr=0 then ndr:=1;
   rn2:=ndr;
   for i:=1 to np-ndr-1 do
   begin
      nn:=1;
      intpr:=0.0;
      for ii:=-ndr to ndr do
         for jj:=-ndr to ndr do
         begin
            rij2:=sqrt(sqr(ii)+sqr(jj));
            if rij2<=rn2 then
            begin
               m:=round(sqrt( sqr(i+ii) + sqr(jj) ));
               if m=0 then m:=1;
               aa:=cos(rij2/rn2*pi/2);
               intpr:=intpr+int[m]*aa;
               nn:=nn+aa;
            end;
         end;
      intave[i]:=intpr/nn;
   end;
end;

(*******************)
(*** Main Program ***)
(*******************)

begin
   l:=1.97;
   dth:=3.3e-4;
   assign(fl,'c:\datacsl\14f.dat');
   reset(fl);
   readln(fl);
   for i:=1 to np do
```

```
  begin
    read(fl,r[i],int[i],ref[i]);
    writeln('at ',r[i],' = ',int[i],' ',ref[i]);
  end;
  close(fl);
  dr:=r[2]-r[1];
  calcave(int,inta);
  for i:=1 to np do
  begin
    if inta[i]<1.0e-7 then inta[i]:=1.0e-7;
    writeln(r[i],' ',int[i],' ',inta[i]);
  end;
  assign(fla,'c:\datacsl\14fa.dat');
  rewrite(fla);
  for i:=1 to np do
    writeln(fla,r[i],' ',inta[i]);
  close(fla);
end.
```

APPENDIX D

The stigmatic focusing properties of the elliptical CSL are investigated with the help of the next two programs. Given that there is no circular symmetry, the calculation of the intensity pattern over the whole focal plane involves a two dimensional calculation and would be excessively time consuming. Consequently the calculation was performed only along the two axes parallel to the semi-axes of the elliptical CSL and perpendicular to the optical axis. The first of the two programs listed below computes the intensity profile along the x-axis and the second along the y-axis.

```
(*****************************************************)
(*** This program computes the diffraction pattern due ***)
(*** to the elliptical lens along the x-axis          ***)
(*** (perpendicular to the line focus)                 ***)
(*****************************************************)

program difell;

uses
  dos,crt,graph;

const
  ec=2.9;
  fx=1.5;
  fy=ec*fx;
  rmax=1.4e-3;
  nr=300;
  nth=67;
  pmax=0.5e-3;
  np=200;
  lambda=0.337e-6;

var
  a,arg,r,p,th,dr,dp,dth,alfa,beta,ralfa,rbeta,
  max,intc,ints,intthc,intths:double;
  fl:text;
  ip,ir,ith:integer;
  int:array[1..np] of double;

(************************)
(*** Function rm(theta) ***)
(************************)

function rm(theta:double):double;

begin
  rm:=rmax*(1+(ec-1)*sin(theta));
end;

(*******************)
(*** Main program ***)
(*******************)

begin
  a:=0.5*(1/fy-1/fx);
  dp:=pmax/np;
  dth:=2*pi/nth;
  beta:=2*pi/lambda*a;
  for ip:=1 to np do
  begin
    p:=ip*dp;
```

```
      alfa:=2*pi/lambda/fx*p;
      intc:=0.0;
      ints:=0.0;
      for ith:=1 to nth do
      begin
         intthc:=0.0;
         intths:=0.0;
         th:=ith*dth;
         dr:=rm(th)/nr;
         ralfa:=alfa*cos(th);
         rbeta:=beta*sqr(sin(th));
         for ir:=1 to nr do
         begin
            r:=ir*dr;
            arg:=ralfa*r+rbeta*sqr(r);
            intthc:=intthc+1e10*r*cos(arg);
            intths:=intths+1e10*r*sin(arg);
         end;
         intc:=intc+intthc;
         ints:=ints+intths;
      end;
      int[ip]:=sqr(ints*dr*dth/1.0e10)+sqr(intc*dr*dth/1.0e10);
      writeln('at ',p,':  ',int[ip]/int[1]);
   end;
   max:=int[1];
   for ip:=1 to np do
      if int[ip]>max then max:=int[ip];
   assign(fl,'c:\datacsl\difellx4.dat');
   rewrite(fl);
   for ip:=1 to np do
   begin
      writeln('at ',ip*dp,' = ',int[ip]/max);
      writeln(fl,ip*dp,'  ',int[ip]/max);
   end;
   close(fl);
end.




(*****************************************************)
(*** This program computes the diffraction pattern due ***)
(*** to the elliptical lens along the y-axis          ***)
(*** (parallel respect to the line focus)              ***)
(*****************************************************)

program difell;

uses
   dos,crt,graph;

const
   ec=2.9;
   fx=1.5;
   fy=ec*fx;
   rmax=1.4e-3;
   nr=300;
   nth=67;
   pmax=3.0e-3;
   np=300;
   lambda=0.337e-6;

var
   a,arg,r,p,th,dr,dp,dth,alfa,beta,ralfa,rbeta,
   max,intc,ints,intthc,intths:double;
   fl:text;
   ip,ir,ith:integer;
   int:array[1..np] of double;

(***********************)
(*** Function rm(theta) ***)
(***********************)

function rm(theta:double):double;

begin
   rm:=rmax*(1+(ec-1)*sin(theta));
end;

(*******************)
```

```
(*** Main program ***)
(*******************)

begin
   a:=0.5*(1/fy-1/fx);
   dp:=pmax/np;
   dth:=2*pi/nth;
   beta:=2*pi/lambda*a;
   for ip:=1 to np do
   begin
      p:=ip*dp;
      alfa:=2*pi/lambda/fx*p;
      intc:=0.0;
      ints:=0.0;
      for ith:=1 to nth do
      begin
         intthc:=0.0;
         intths:=0.0;
         th:=ith*dth;
         dr:=rm(th)/nr;
         ralfa:=alfa*sin(th);
         rbeta:=beta*sqr(sin(th));
         for ir:=1 to nr do
         begin
            r:=ir*dr;
            arg:=ralfa*r+rbeta*sqr(r);
            intthc:=intthc+1e10*r*cos(arg);
            intths:=intths+1e10*r*sin(arg);
         end;
         intc:=intc+intthc;
         ints:=ints+intths;
      end;
      int[ip]:=sqr(ints*dr*dth/1.0e10)+sqr(intc*dr*dth/1.0e10);
      writeln('at ',p,':  ',int[ip]/int[1]);
   end;
   max:=int[1];
   for ip:=1 to np do
      if int[ip]>max then max:=int[ip];
   assign(f1,'c:\datacsl\difelly4.dat');
   rewrite(f1);
   for ip:=1 to np do
   begin
      writeln('at ',ip*dp,' = ',int[ip]/max);
      writeln(f1,ip*dp,'  ',int[ip]/max);
   end;
   close(f1);
end.
```

App. D

The following program reconstruct the initial shockfront geometry that would generate an elliptical lens after the central implosion. We utilised the hypothesis is that the shock velocity is constant. Nevertheless, the calculation is performed numerically rather than analytically in order to have a more flexible tool. With little modifications it is possible to take into account of the shock velocity variations (of course not through gas dynamics) and to change the geometry from elliptical.

```
(*******************************************)
(*** Calculates the shockfront that generates  ***)
(*** an ellipse after collision                 ***)
(*******************************************)

program ellipse;

uses
   dos,crt,graph;

const
   n=50;
   nc=10;

var
   x,xmax,ymax,xell,yell: double;
   i,ii,ic,j,sigx,sigy,gx,gy: integer;
   a,b,c,cmax: double;
   angle,ypos,xpos: array [1..n+1] of double;
   fl:text;

(********************)
(*** Begin graphics ***)
(********************)

procedure begraph;

var
   grdriver,grmode:integer;

begin
   grdriver:=vga; grmode:=vgahi;
   initgraph(grdriver,grmode,'c:\tp');
   setviewport(10,10,630,470,false);
   rectangle(0,0,620,460);
end;

(******************)
(*** End Graphics ***)
(******************)

procedure endgraph;

begin
   closegraph;
   restorecrtmode;
end;

(*************************************)
(*** Procedure to convert physical values ***)
(*** in screen cohordinates              ***)
(*************************************)

procedure convert(xmin,ymin,xmax,ymax,a,b:real; var na,nb:integer);

begin
   na:=round((a-xmin)/(xmax-xmin)*620);
   nb:=460-round((b-ymin)/(ymax-ymin)*460);
end;
```

```
function dy1dx1(xx:double):double;

begin
   if xx>=a then dy1dx1:=1.0e10
   else dy1dx1:=sqr(b/a)*xx/sqrt(sqr(b)-sqr(b*xx/a));
end;

function y1(xx:double):double;

begin
   if xx>=a then y1:=0.0
   else y1:=sqrt(sqr(b)-sqr(b/a*xx));
end;

procedure selectsign(quad:integer; var sigx,sigy:integer);

begin
   if quad=1 then
   begin
      sigx:=-1;
      sigy:=-1;
   end
   else if quad=2 then
   begin
      sigx:=-1;
      sigy:=1;
   end
   else if quad=3 then
   begin
      sigx:=1;
      sigy:=1;
   end
   else if quad=4 then
   begin
      sigx:=1;
      sigy:=-1;
   end;
end;

begin
   a:=4.0;
   b:=6.0;
   cmax:=19.0;
   xmax:=0.0;
   ymax:=0.0;
   for i:=1 to n+1 do
   begin
      x:=(i-1)*a/n;
      angle[i]:=arctan(dy1dx1(x));
      ypos[i]:=y1(x);
      xpos[i]:=x;
   end;
   assign(fl,'c:\datacsl\ellip.dat');
   rewrite(fl);
   begraph;
   for ic:=1 to nc+1 do
   begin
      c:=(ic-1)*cmax/nc;
      writeln(fl);
      writeln(fl);
      writeln(fl,204,' ',ic);
      writeln(fl,'\ curve number  n = ',ic);
      for j:=1 to 4 do
      begin
         selectsign(j,sigx,sigy);
         for i:=1 to n+1 do
         begin
            if j mod 2 = 0 then ii:=n+2-i else ii:=i;
            xell:=-sigx*xpos[ii]+sigx*c*sin(angle[ii]);
            yell:=-sigy*ypos[ii]+sigy*c*cos(angle[ii]);
            if xell>xmax then xmax:=xell;
            if yell>ymax then ymax:=yell;
            writeln(fl,xell,' ',yell);
            convert(-cmax*1.4,-cmax,cmax*1.4,cmax,xell,yell,gx,gy);
            if i=1 then
               moveto(gx,gy)
            else
               lineto(gx,gy);
```

```
         end;
      end;
   end;
   close(f1);
   repeat until readkey=' ';
   endgraph;
   writeln('E  X semiaxis = ', xmax,'      Y semiaxis =', ymax);
   writeln('T  X semiaxis = ', c-a ,'      Y semiaxis =', c-b);
   repeat until readkey=' ';
end.
```

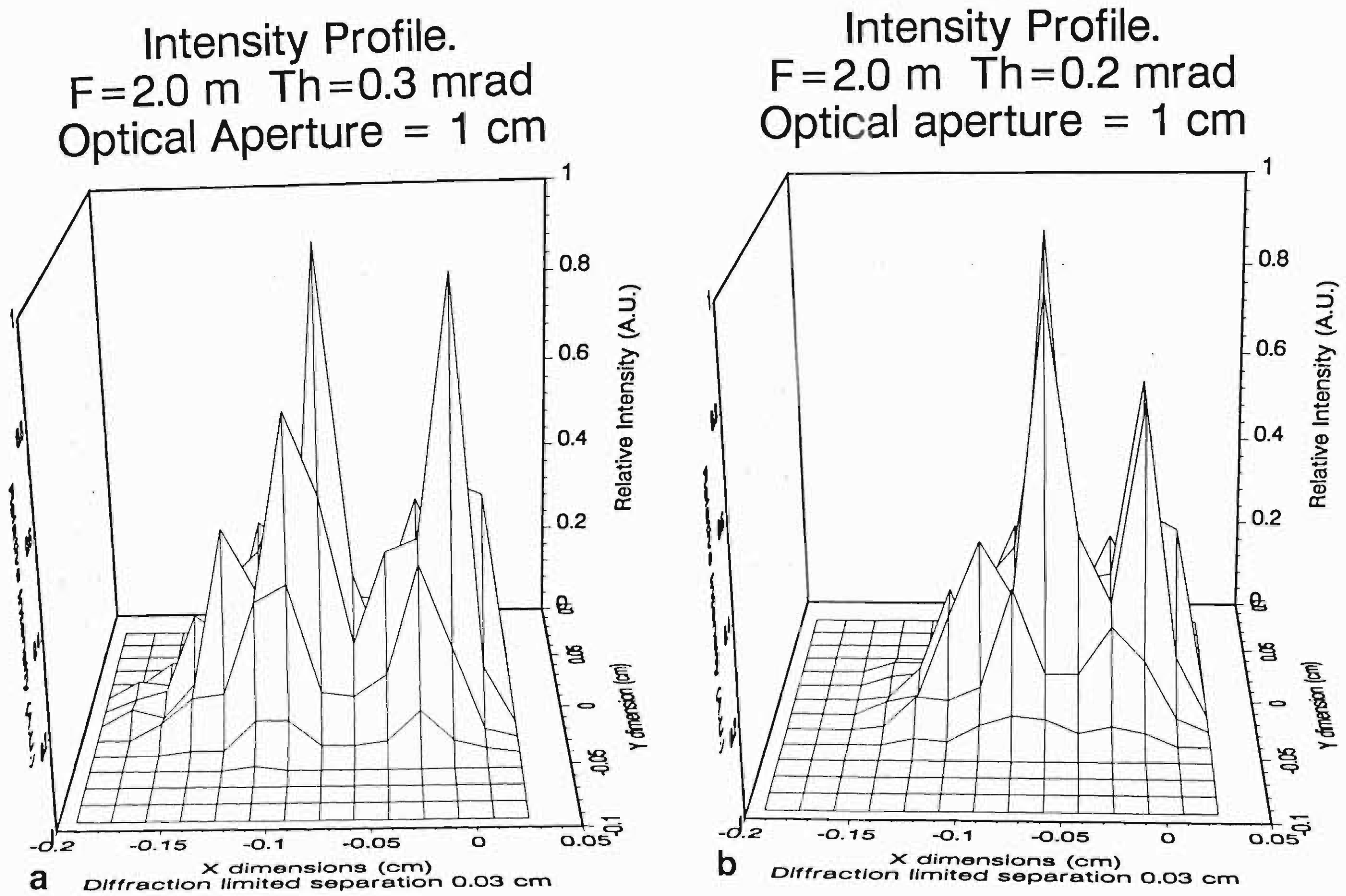

Fig. 3 Computed intensity profile for two point sources at infinity, optical aperture 1 cm: (a) angular separation 0.3 mrad; (b) angular separation 0.2 mrad

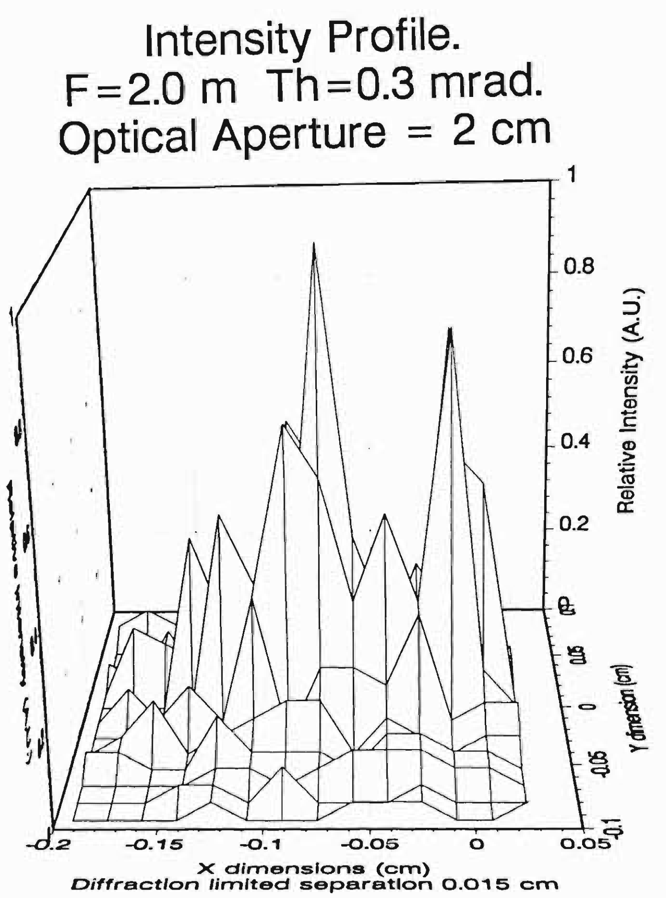

Fig. 4 Computed intensity profile for two point sources at infinity, optical aperture 2 cm, angular separation 0.3 mrad

(Fig. 3(b)), which is only about twice the diffraction limit. It can be easily seen that the outer rays are too weakly refracted to arrive in the same focus as the inner rays. Another feature, visible both in Fig. 3 and Fig. 4, is that the focus is displaced along the vertical, below the optical axis, due to the effect of gravity on the temperature distribution (see Fig. 2(b)).

Conclusions

Ray tracing through the measured refractive index profile of a spinning pipe gas lens, satisfactorily explains two important features: the decrease in optical quality as the optical aperture approaches that of the pipe, and the lowering of the image centre due to gravity. Reasonable numerical agreement is obtained.

References

1 **Marcuse D.**, Theory of thermal gradient gas lens, *IEEE Trans Microwave Theory and Techniques* **MTT-13** (1965) 734
2 **Nottcutt M., Michaelis M. M., Cunningham P. F., Waltham J. A.**, Spinning pipe gas lens, *Opt Laser Technol* **20** (1988) 243.
3 **Michaelis M. M., Dempers C. A., Kosch M., Prause A., Nottcutt, M., Cunningham P. F., Waltham J. A.**, A gas-lens telescope, *Nature* **353** (1991) 547
4 **Gloge D.**, *Bell Syst Tech J* **46** (1967) 357
5 **Steier W. H.**, Measurement of a thermal gradient gas lens, *IEEE Trans Microwave Theory and Techniques* **MTT-13** (1965) 740
6 *Practical Temperature Measurements*, Hewlett Packard, Application Note 290, 8
7 **Michaelis M. M., Cunningham P. F., Cazalet R. S., Waltham J. A., Nottcutt M.**, Gas lens applications, *Laser and Particle Beams* **9** (1991) 641

Optics Communications 101 (1993) 350–355
North-Holland

OPTICS
COMMUNICATIONS

Colliding shock lens

R. Buccellato, N. Lisi and M.M. Michaelis
Plasma Physics Research Institute, University of Natal, Durban, South Africa

Received 7 December 1992; revised manuscript received 8 March 1993

A pulsed colliding shock lens is developed where the shocks were generated by electric discharges. Near diffraction limited focusing was observed.

1. Introduction

Gas lenses have recently been shown to be more versatile than expected [1,2]. Continuous wave gas lenses have industrial potential and even show promise in astronomy [3]. In ref. [4] we consider a macroscopic pulsed gas lens that could be used as a final focusing element in a laser driven thermonuclear fusion experiment. In this article we describe a novel type of pulsed gas lens which would be suitable for operation in series with a small pulsed gas laser: the colliding shock lens (CSL).

2. Colliding shock lens principle

When two spherical shocks collide, the interaction depends on their strength [5]. At low Mach number (M_0) the waves simply pass unmodified through one another. At intermediate M_0 they pass but are somewhat delayed. At higher M_0, there is a period of stagnation during which the fronts merge into a high density plane slab, and at very high M_0 the collision generates turbulence. When several shocks are launched from explosion points placed on the arc of a circle, one might expect similar behaviour to that of the double shock interaction. Moreover, since many shocks now collide at one point, nonlinearities in the shock interaction are expected to occur at lower M_0 than for two colliding shocks. The regime of interest here, is at an intermediate M_0 when the fronts interact in a nonlinear but orderly manner.

When several spherical shocks, produced by arc discharges, expand from points equi-spaced on a circumference, a cylindrically symmetric converging shockfront is formed. Schwendeman and Whitham [6] have noted that converging cylindrical shocks with regular polygonal shaped cross-sections are stable and tend towards a circular cross-section. Converging cylindrically symmetric shock waves produce a condition of high pressure, temperature and density in the region of implosion. After the spherical shock converges to a point, a regular and stable [7] axi-symmetric cigar shaped expanding density distribution results. It is in this region that we expect the density distribution to act as a graded index lens.

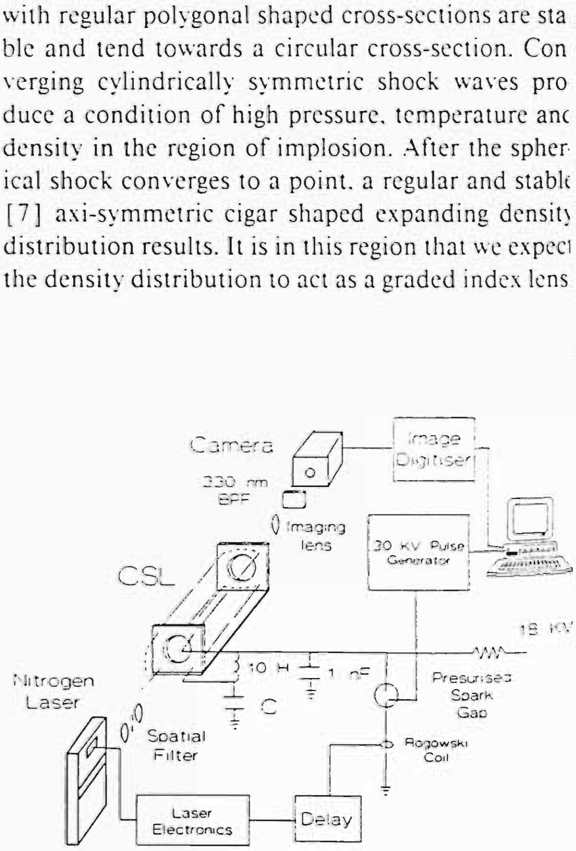

Fig. 1. Experimental setup.

3. Experimental setup

A schematic representation of the experimental setup, including the colliding shock lens, is shown in fig. 1. The spherical shocks were created at points equi-spaced on a circumference (diameter 11 mm) by eight pairs of opposing electrodes (for simplicity only four pairs of electrodes are shown in fig. 1). We utilized needles of diameter 0.85 mm and an arc gap spacing of 1 mm. The electrodes were mounted on two opposite plexiglass plates with a circular hole in the center (diameter 7.5 mm) allowing a laser beam to be directed along the axis of the CSL. The gaps were connected in series in order to have approximately simultaneous breakdown. A spatially filtered nitrogen laser beam (fwhm ≈ 1 ns) was directed through the collision region onto a T.V. camera face plate through an imaging lens and a nitrogen interference filter (330 nm, bandwidth 10 nm). A PC synchronised the triggering of the CSL with the image digitiser. A Rogowsky coil in the CSL circuitry triggered the nitrogen laser via a variable delay box. The value of the capacitor C determines the energy provided to the colliding shocks. A 5 nF capacitor was used.

4. Results

The CSL properties were investigated by recording images at different distances from the CSL and at different delays. Parasitic fringes were due to the interference filter.

A time sequence for the colliding shocks is given in fig. 2 ($M_0 \approx 1.5$). After the eight shocks have collided (figs. 2f, 2g) a high density expanding region

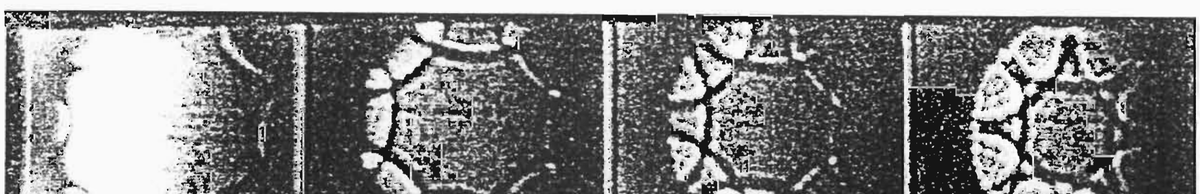

Fig. 2. Time sequence of an eight arc CSL imaged 19 cm from the CSL at (a) 3.2 μs, (b) 5 μs, (c) 6 μs, (d) 6.9 μs, (e) 8 μs, (f) 10 μs, (g) 10.4 μs, (h) 10.9 μs, (i) 11.3 μs, (j) 11.6 μs, (k) 11.8 μs, (l) 12.2 μs, (m) 12.4 μs, (n) 13.1 μs, (o) 14 μs, (p) 15.6 μs.

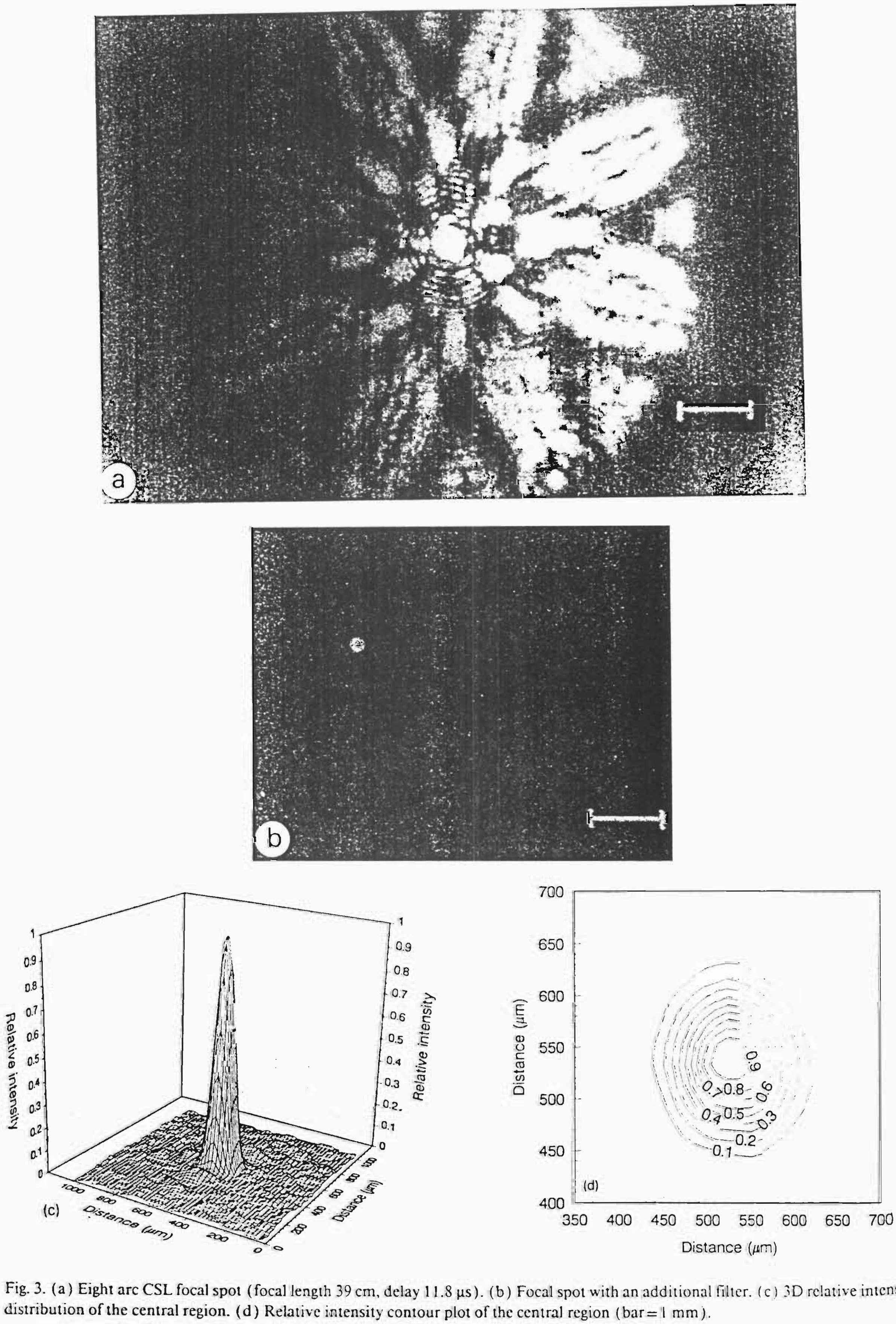

Fig. 3. (a) Eight arc CSL focal spot (focal length 39 cm, delay 11.8 μs). (b) Focal spot with an additional filter. (c) 3D relative intensity distribution of the central region. (d) Relative intensity contour plot of the central region (bar = 1 mm).

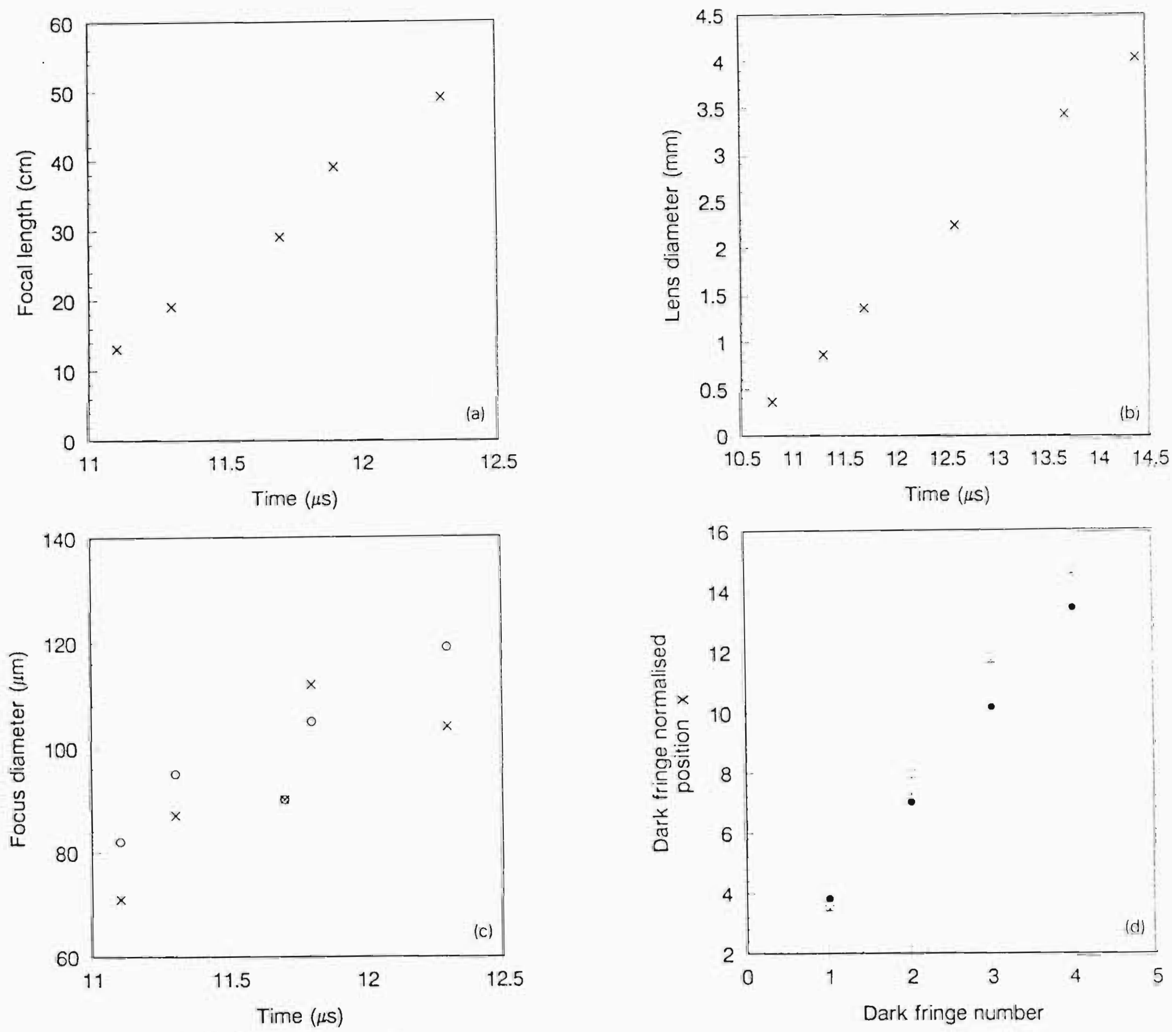

Fig. 4. (a) Focal length of eight arc CSL at different times after arcing. (b) Effective lens diameter. (c) Comparison of focus diameters (fwhm) with time, O: experimental focus diameter, ×: diffraction limit. (d) Dark fringe number versus dark fringe normalized position $x=(\pi D d_f)/(\lambda f)$. d_f is the dark fringe position, D, f are the lens diameter and focal length, respectively. ● Theoretical. □: lens diameter of 0.84 mm, focal length is 19.1 cm; ×: lens diameter of 1.3 mm and focal length of 39.1 cm.

is created (figs. 2h, 2p). Focusing is achieved in figs. 2h and 2i. Figures 2j–m show the typical diffraction pattern when focusing is achieved closer to the TV camera. Figure 3a shows the focusing obtained with the eight arc CSL (C=5 nF) at a distance of 39 cm. The image in fig. 3b was recorded with an addition filter (ND=1). A three-dimensional representation of the relative intensity of the central region is shown in fig. 3c and the associated contour plot is shown in fig. 3d. The fwhm focal spot diameter is 100 μm. The CSL is a varifocal lens in which the focal length increases with time: fig. 4a. The effective lens diameter was obtained by imaging on the shock collision plane. Due to the expansion of the shockfront after the collision, the effective lens diameter increases with time (fig. 4b). Consequently, the relative diffraction limited focal spot size is expected to vary with time and is consistent with the measured focal spot size (fig. 4c). The position of the rings surrounding the central spot (fig. 3a) is in reasonable agreement with

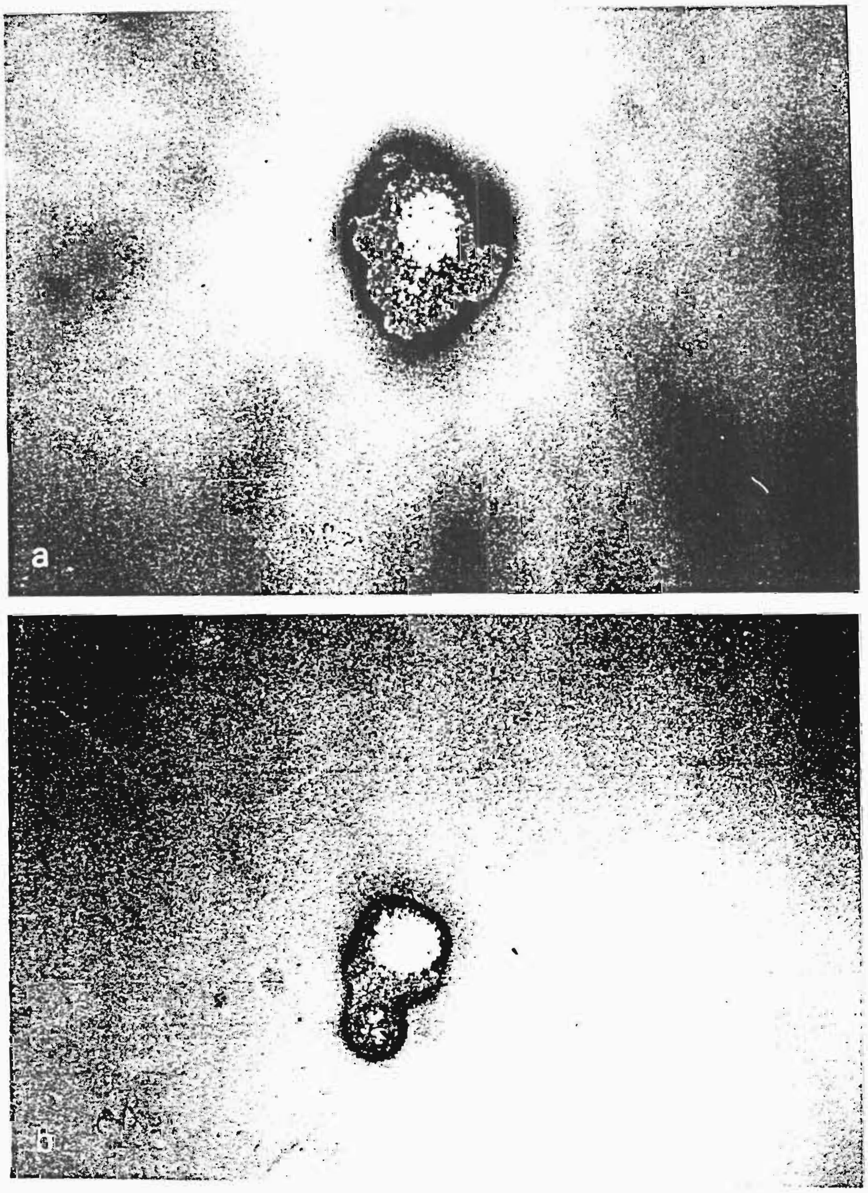

Fig. 5. (a) Eight arc CSL burn pattern (focal length 39 cm, delay 11.8 μs). (b) Equivalent glass lens burn pattern.

the theoretical Airy rings value (fig. 4d).

The CSL was used to focus a ruby laser beam (fwhm≈30 ns, $E \approx 0.5$ J) onto photographic paper in order to obtain a burn pattern. We chose a focal length of 39 cm. The diffraction limited ruby beam was directed through the lensing region and the burn pattern shown in fig. 5a was obtained. For comparison a glass convex lens of equal focal length was apertured to 1.5 mm. This is the effective aperture of the CSL. The burn pattern of fig. 5b was obtained. The secondary spot in the lower region of the burn patter is due to secondary reflections by the prisms used to direct the beam through the lens. The central burnt regions for both lenses were approximately 200 μm in diameter.

5. Conclusion

We have developed a novel type of focusing device, the colliding shock lens, where near diffraction limited focusing was observed. Although the useful aperture of this lens is small we are in the process of scaling up its dimensions.

Acknowledgements

Useful discussions were held with P.F. Cunningham and A. Prause. We thank W. de Beer, D. Davies and B. Buhrman for their technical assistance, and the Laser Applications and Research Institute of South Africa (LARISA) and the Foundation for Research and Development (FRD) for financial support.

References

[1] B.L. Xie, S.J. Xia and Q.T. Chow, Chinese Phys. Lett. 2 (1985) 509.

[2] M.M. Michaelis, P.F. Cunningham, R.S. Cazalet, J.Z. Waltham and M. Notcutt, Laser and Particle Beams 9 (1991) 641.

[3] M.M. Michaelis, C.A. Dempers, M. Kosch, A. Prause, M. Notcutt, P.F. Cunningham and J.A. Waltham, Nature 353 (1991) 547.

[4] R. Buccellato, M.M. Michaelis, C.A. Dempers, A. Prause and P.F. Cunningham, Optics and Laser Technology, to be published.

[5] R. Courant and K.O. Friedrichs, Supersonic flow and shock waves (Interscience, New York, 1948) p. 297.

[6] D.W. Schwendeman and G.B. Whitham, Proc. R. Soc. Lond. A 413 (1987) 297.

[7] H. Matsuo and Y. Nakamura, J. Appl. Phys. 52 (1981) 4503.

Colliding shock lens as an intracavity Q-switch element

N. Lisi, M. M. Michaelis, R. Buccellato, M. Kuppen, and A. Prause

We show how a varifocal pulsed gas lens, the colliding shock lens, can be used as an intracavity element to Q switch a ruby laser. By placement of the shock lens in tandem with a second lens, a giant pulse is obtained. The second lens may be a conventional glass lens or a continuous-wave gas lens.

The quality factor or Q switching of lasers is an important method of enhancing the power of pulsed lasers.[1] Mechanical Q switches and dye cell switches have generally been discarded in favor of triggerable opto-electronic devices based on rotation of polarization by the use of the Kerr or Pockels effect. In this paper we discuss another form of triggerable Q switching that makes use of a new kind of gas lens. This lens, the colliding shock lens (CSL),[2] was developed in our laboratory, in step with the recent revival of interest in gas-lens optics.[3,4]

The principle of colliding shock Q switching (CS-QS) relies on the insertion of a steady-state converging lens and of the rapidly varying CSL in a laser cavity. The CSL focal length and lens diameter increase with time over a few microseconds. When the CSL is switched off, the steady-state lens renders the cavity unstable. Only when the CSL is switched on and while the focal regions of the two lenses overlap does the laser cavity become stable and the losses low. If this condition is achieved when the population inversion is at its peak in the active medium, lasing occurs in the form of a giant pulse.

In the experiment designed to test the CS-QS concept, a commercial ruby laser (1975 Korad Model K1) was modified to incorporate additional Q-switching components. Figure 1(a) is a schematic of the experiment. The laser consists of a ruby head, full reflector R1, and output coupler R2. The Q-switching components are CSL L2, continuous lens L1, and fluorescence-sensing photodiode PD1.

The authors are with the Plasma Physics Research Institute, University of Natal, Durban, South Africa 4001.

Received 21 March 1994; revised manuscript received 9 September 1994.

0003-6935/95/060942-04$06.00/0.

The CSL consists of eight arc discharges, struck simultaneously between pairs of opposing points located on the arc of a circle as illustrated in Fig. 1(b). Each point explosion produces an expanding spherical shock wave. After the eight shock waves collide at the center of the circle, a cigar-shaped, high-density, axially symmetric core expands outward. Focusing is due to the radially symmetric density gradients within the expanding region. As the lens diameter increases, the density diminishes and the focal length increases as depicted in Fig. 2. The CSL used for these experiments was specially chosen for its fast switching and large optical aperture. It consists of a 5.0-cm-diameter cylinder closed at both ends. The end plates that carry the 16 pins that form the eight gaps are 1.0 cm apart. The gaps are set to 1.5 mm, and the diameter of the circle of pins is 3.0 cm. The central apertures are 1.0 cm in diameter. A 100-nF capacitor, charged to 17 kV, is connected to the eight gaps in series by a triggerable spark gap. This series connection ensures simultaneous arcing.

Lens L1 can be either a conventional solid-state device or a continuous-wave gas lens. The spinning-pipe gas lens[5] used in some experiments, consists of a 1.0-m-long, 2.0-cm-diameter heated tube, spun at 30 Hz. The rotation centrifuges warm air out of the two ends and causes cold air to be aspired along the axis. The resulting density and refractive-index gradient produces a long-focal-length lens, the quality of which fluctuates.[6] One can vary the focal length from 1.5 m to several meters (as measured from the center of the pipe) by changing the pipe temperature and rotation speed. The two flat end mirrors are a full reflector, $R_1 = 96\%$, and an output coupler, $R_2 = 45\%$.

The operation sequence for all CS-QS experiments is the following: First the ruby flash lamp is fired and the PD1 photodiode detects the fluorescence signal from the active medium. This signal is elec-

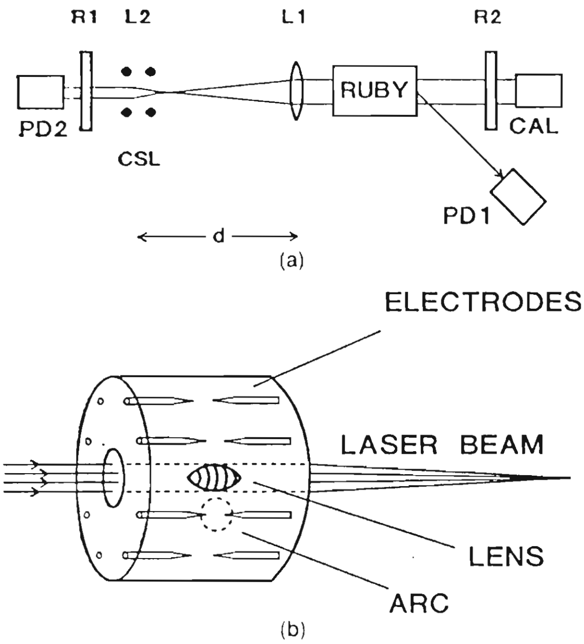

Fig. 1. (a) Schematic of the CS-QS experiment: PD's, photodiodes; CAL, calorimeter. (b) CSL geometry.

tronically delayed and used as a trigger for the CSL master spark-gap circuit. The signal from photodiode PD2, placed behind full reflector R_1, is read by a storage oscilloscope and yields the laser-pulse waveform. The laser-beam energy is measured with a calorimeter. A burn pattern of the attenuated beam at the focus of a lens can be used to measure the divergence of the beam.

The cavity is operated in three different modes described below in detail. Mode a maximizes the output energy and beam diameter. Mode b minimizes the Q-switched laser-pulse duration. Mode c explores the feasibility of a cavity with intracavity beam-expansion optics consisting entirely of gas.

The stability of the laser resonator can be determined in terms of the complex parameter m, which, in the formalism of the ray matrix optics, is half the trace of the round-trip resonator matrix.[7] For an unstable resonator, $abs(m) > 1$. In this case we define the magnification M as

$$M = \begin{cases} m + (m^2 - 1)^{1/2} & \text{if } m > 1 \text{ (positive branch)} \\ m - (m^2 - 1)^{1/2} & \text{if } m < -1 \text{ (negative branch),} \end{cases} \tag{1}$$

where M is the amplification of the beam cross section per round trip and can be related to the cavity losses. When $abs(m) < 1$, the cavity is stable, while $abs(m) = 1$ for a plane-parallel configuration, which corresponds to the confocal situation of the intracavity telescope.

In mode a, L1 is a 200-cm focal-length glass lens. The lens separation d is 250 cm. The condition $abs(m) = 1$ is achieved when $f_{CSL} = 50$ cm. The CSL lens aperture (d_{CSL}) is 3.0 mm (see Fig. 1), and the beam fills the ruby rod (10 mm). At slightly later times, the resonator becomes stable, and we expect lasing to occur. A drawback of this operating condition is that the cavity is long (3.0 m), as is consequently the rise time of the laser pulse. In this case the initial magnification of the resonator (before the CSL is operated) is low, $M = 2.8$. We must therefore operate the flash lamp below 4.3 kV to avoid free-running lasing. A 2.0-J laser pulse of a duration of 360 ns (FWHM) is observed 5 μs after the shock collision. Figure 3 shows the pulse waveform.

In mode b, L1 is a 50-cm focal-length glass lens ($d = 100$ cm). Again $m = 1$ is achieved when $f_l = 50$ cm, $d_{CSL} = 3.0$ mm, and the beam diameter on the output coupler is expected to be 3.0 mm. The initial magnification M is now 4.4, and free running is inhibited at any flash-lamp voltage. We operated the flash lamp at 4.5 kV. In this case we expect shorter

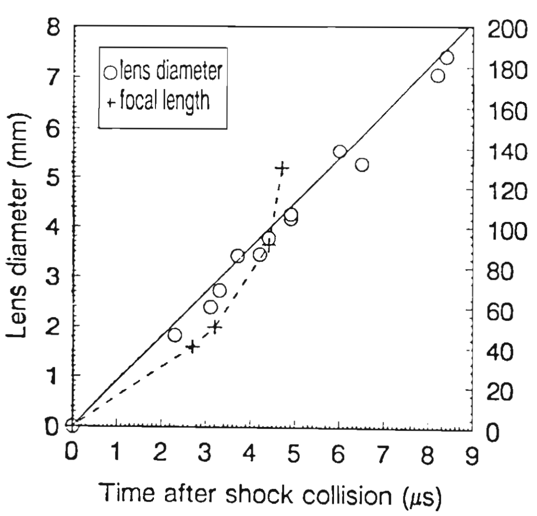

Fig. 2. CSL characteristics: Evolution of focal length and effective diameter after the shock collision.

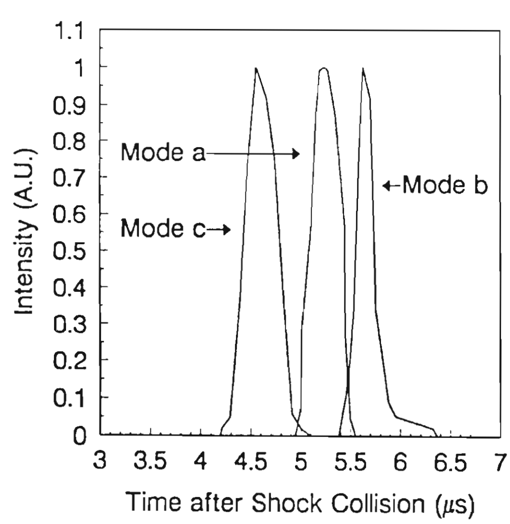

Fig. 3. Measured laser-pulse-intensity waveforms.

pulses and a very narrow beam together with lower energy. A 100-mJ pulse of a duration of 175 ns (FWHM) is observed 5.5 μs after the shock collision (see Fig. 3). On a few occasions when the CSL alignment appeared to be optimized, a pulse length of approximately 50 ns was observed.

In mode c, L1 is a spinning-pipe gas lens operated at a 200-cm focal length. For this all-gas Q switch, we expected similar performance to mode a. Figure 3 shows a 375-ns (FWHM) pulse 4.5 μs after the shock collision. However, the energy for this mode is now slightly higher (3.0 J). The absence of reflective losses in the cavity appears to outweigh the effect of spinning-pipe gas-lens aberrations.

In Table 1 we summarize the results of the experiment. The energy values reported in this paper are the maximum values obtained over a large number of experiments. Although the fluctuations are large, especially for mode c, which in this case is due to the unstable behavior of the spinning-pipe gas lens,[5] we noted that the operations do not critically depend on the cavity alignment and the gas-lens aberrations.

We now examine in greater detail the evolution of the cavity geometry after the CSL shocks have collided and how this affects the cavity losses. The losses can be split into two terms. The first term is constant and takes into account diffraction, surface reflections from lens L1, and the ruby-rod surface imperfections.

The second term depends on the cavity geometry and will vary explicitly with time. If no apertures are present in the cavity, the losses depend on only the parameter m and can be calculated according to the loss formula[1]

$$L = \begin{cases} 1 - 1/M^2 & \text{if } abs(m) > 1 \\ 0 & \text{if } abs(m) \leq 1, \end{cases} \tag{2}$$

where L is the fractional intensity loss of an input beam that is entering the output coupler and whose linear magnification over one round trip is M. The evolution of M and the corresponding L is shown in Fig. 4 for mode a.

A simple model of the laser system was developed.[8] Because of the presence of apertures in the cavity, such as the ruby-rod external diameter and the CSL aperture, the expression for the loss term is more complex than that given by Eq. (2) and depends on the input beam cross section. The expression for the loss term coincides with Eq. (2) only for light that is traveling close to the optical axis. This was taken into account in the calculation of the losses as a function of the distance from the optical axis, which was carried out with the formalism of matrix optics. The laser beam was subdivided into a collection of annular beams. The laser rate equations were solved for each annulus, using the fourth-order Runge Kutta numerical method with variable step size. Independently an approximate computation of the beam divergence is performed for the resonator geometry that exists when lasing is at its peak. We generate a uniform planar distribution of rays at the position of the ruby rod, and we follow the path of each of the rays for a given number of round trips, recording the values of their angle at the output coupler. These values are used to calculate the beam divergence.

Figure 5 shows the computed laser-beam-intensity waveform in the center of the beam for modes a, b, and c. The computed values of the laser energy, pulse length, beam diameter, and divergence are summarized in Table 2. The discrepancy between the measured and the computed pulse lengths can be

Table 1. Summary of the Results of the CS-QS Experiment[a]

Mode	E_{max} (J)	t_p (ns)	d (mm)	div (mrad)
a	2.0	360	8.0	1.0
b	0.1	175	2.0	3.3
c	3.0	375	8.0	1.4

[a] E_{max}, maximum recorded value of the output energy in the three different resonator geometries; t_p, typical pulse duration (FWHM); d, laser spot diameter; div, divergence.

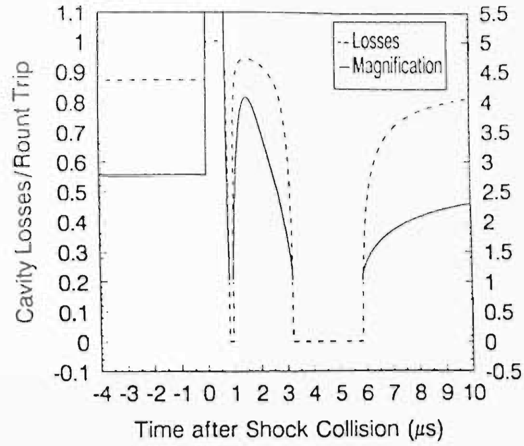

Fig. 4. Evolution of the cavity magnification M and losses L for the paraxial rays (mode a).

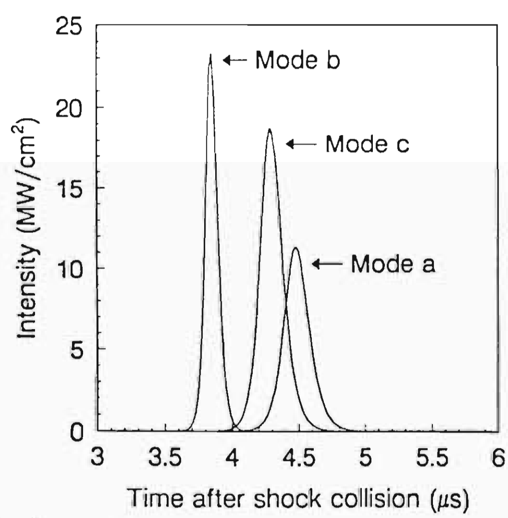

Fig. 5. Computed laser-pulse intensities in the center of the beam.

Table 2. Summary of the Computational Results of the CS-QS

Mode	E_{max} (J)	t_p (ns)	d (mm)	div (mrad)
a	2.0	225	10.0	1.0
b	0.13	105	2.8	4.0
c	3.0	200	10.0	0.9

attributed to the aberrations of the gas lenses, which are not included in the model.

In conclusion, we have demonstrated a novel Q-switching configuration that can use gas optics only. The advantages of the method are no damage threshold, both for high peak power and average power, and the absence of polarization and a polarizer. A major disadvantage is the necessity of having a long cavity, which results in a long laser pulse. Improvements in CSL design and performance may correct this problem.

We thank W. de Beer and D. Davies for unflagging technical support, P. Di Lazzaro, M. A. Hellberg, and M. H. Key for discussions, and the Foundation for Research and Development and the Laser Applications Research Institute of South Africa for financial support.

References

1. W. Koechner, *Solid-State Laser Engineering*, 2nd ed. (Springer-Verlag, Berlin, 1988), Chap. 8, p. 410.
2. R. Buccellato, N. Lisi, and M. M. Michaelis, "Colliding shock lens," Opt. Commun. **101**, 350–355 (1993).
3. M. M. Michaelis, C. A. Dempers, M. Kosch, A. Prause, M. Notcutt, P. F. Cunningham, and J. A. Waltham, "A gas telescope," Nature (London) **353**, 547–548 (1991).
4. B. L. Xie, S. J. Xia, and Q. T. Chow, "Gas varifocal lens," Chin. Phys. Lett. **2**, 509–512 (1985).
5. M. Notcutt, M. M. Michaelis, P. F. Cunningham, and J. A. Waltham, "Spinning pipe gas lens," Opt. Laser Technol. **20**, 243–250 (1988).
6. N. Lisi, R. Buccellato, and M. M. Michaelis, "Optical quality and temperature of a spinning pipe gas lens," Opt. Laser Technol. **26**, 25–27 (1994).
7. A. E. Siegman, *Lasers*, 2nd ed. (University Science, Mill Valley, Calif., 1986), Chap. 15, p. 599.
8. N. Lisi, "C.S.L. Q switch," Internal rep. (Department of Physics, University of Natal, Durban, South Africa, 4001, February 1993).

Laser and Particle Beams (1994), *vol.* 12, *no.* 3, *pp.* 531–538
Printed in the United States of America

Applications of the colliding shock lens

By M.M. MICHAELIS, N. LISI, R. KUPPEN, R. BUCCELLATO, AND A. PRAUSE
Department of Physics, University of Natal, Durban, South Africa

(Received 10 January 1994; accepted 19 January 1994)

The colliding shock lens is described briefly. Possible applications, industrial drilling and cutting, laser Q-switching and spatial filtering, ultrahigh-power applications, and "all gas lasers" are proposed. The time evolution, scaleability, and repetition rate operation are investigated.

1. Introduction

At a previous ECLIM, we described work with continuous gas lenses (Michaelis *et al.* 1991a). A novel pulsed gas lens has now been developed relying on the interaction of converging shocks in air. Here we report on the initial studies of the parameters of this lens undertaken to see which applications, if any, show promise. The article is divided into four parts: a brief description of the colliding shock lens (CSL); a list of potential applications suitable for the CSL; a study of the performance of various CSL designs; and concluding remarks.

2. The colliding shock lens

Gas lenses invented at Bell Labs in the early 1960s were soon discarded as bulky devices with a narrow field of view. A slight renewal of interest has resulted from a demonstration that they are able to focus laser light to drill holes (Notcutt *et al.* 1988; Michaelis *et al.* 1991a) or to generate laser-produced plasmas (Waltham *et al.* 1990). We have shown that they have sufficiently good optical quality to serve as objective lenses in telescopy (Michaelis *et al.* 1991b). We have also proposed that large aperture pulsed gas lenses could play an important part as the final focusing element in a laser-driven fusion reactor (Buccellato *et al.* 1993a). More recently (Buccellato *et al.* 1993b) we have described a different type of pulsed gas lens, the CSL.

The simplest CSL consists of 16 needles disposed in opposition on the arc of a circle (figure 1a). Eight electric arcs are struck between opposing points and generate eight shock waves that converge at the center. A cigar-shaped region of high gas density gradient results. If a pulsed laser is synchronized soon (500 ns) after the shock collision and directed through the center, it can produce a focus. Figures 1b and 1c show other CSL designs with different number of arcs and different diameters. We distinguish between the "electrical diameter," that of the circle of arcs, and the optical aperture, that of the effective lens. The optical aperture turns out to be an order of magnitude smaller than the electrical diameter. It is not yet clear whether the optical aperture will scale with the system geometry or with the typical shock width dimensions. The former would mean that the f-number could remain more or less constant with increasing optical aperture; the latter, that it does not scale at all. A first attempt at scaling up the first 1.2-cm electrical diameter device to 3 cm

 0263-0346/94 $5.00 + .00

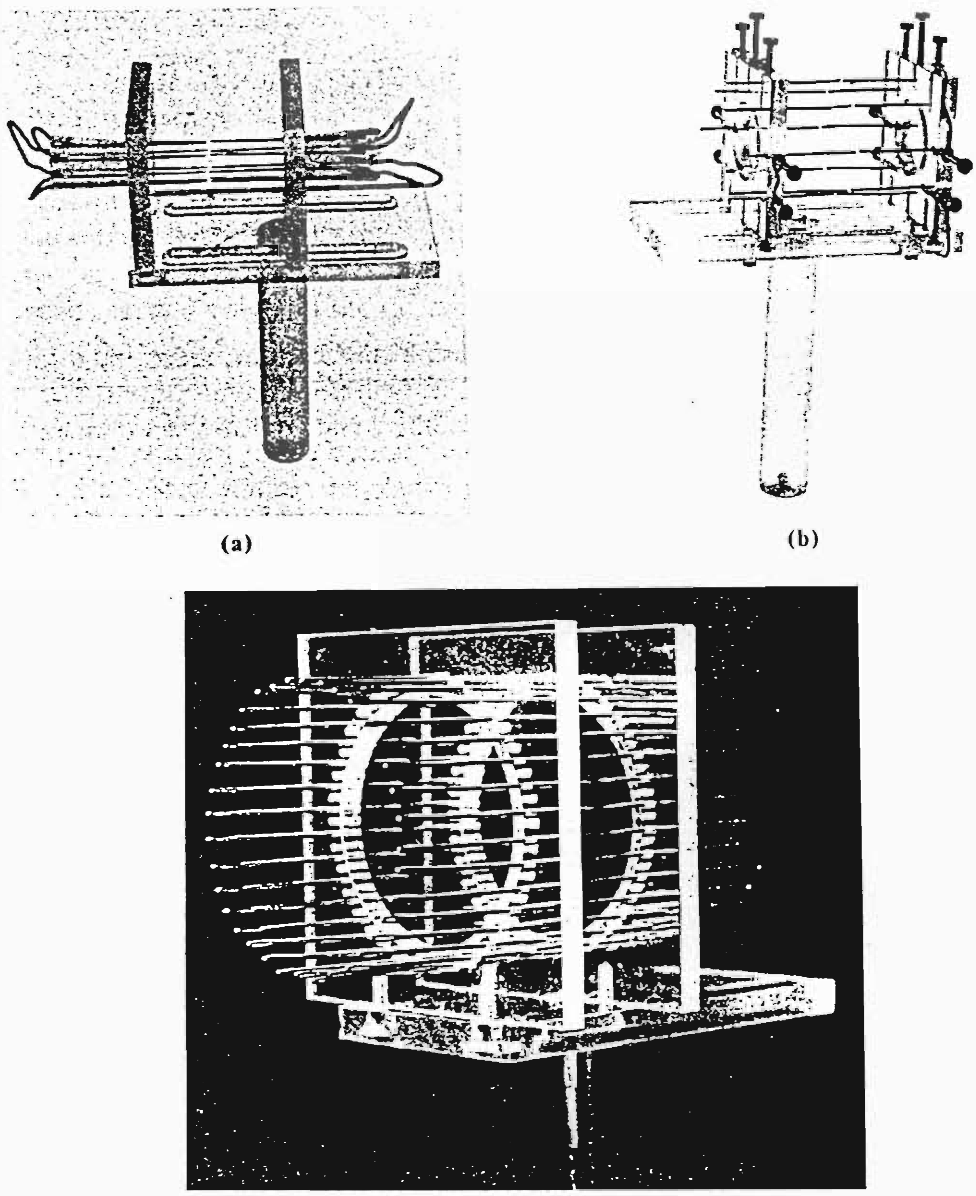

(a) (b)

(c)

FIGURE 1. Colliding shock lenses. (a) 16-pin, 8-arc device. Electric diameter 1.2 cm. Optical aperture 2 mm. (b) 3-cm electric diameter device. Optical aperture approximately 3 mm. (c) 36-pin, 3-cm electric diameter device.

(figure 1b) indicates that the truth lies somewhere in between. Increasing the number of pins (figure 1c) did not have any obvious effect.

Depending on the time at which the pulsed laser is fired with respect to the arcs, a variety of illumination patterns results; figure 2 shows a sequence obtained with an eight-arc device. The frames are taken directly with a lensless television camera disposed 40 cm away from the center of the lens. The first three frames show the shock waves propagating almost undisturbed through one another. The detailed illumination pattern (i.e., dark and bright rings, coarse and fine fringes) is best understood by referring to articles on refractive fringe diagnostics (Bacon *et al.* 1989; Michaelis *et al.* 1991c). The next frames show nonlinear interaction between the shock waves resulting in noncylindrically symmetric illumination pat-

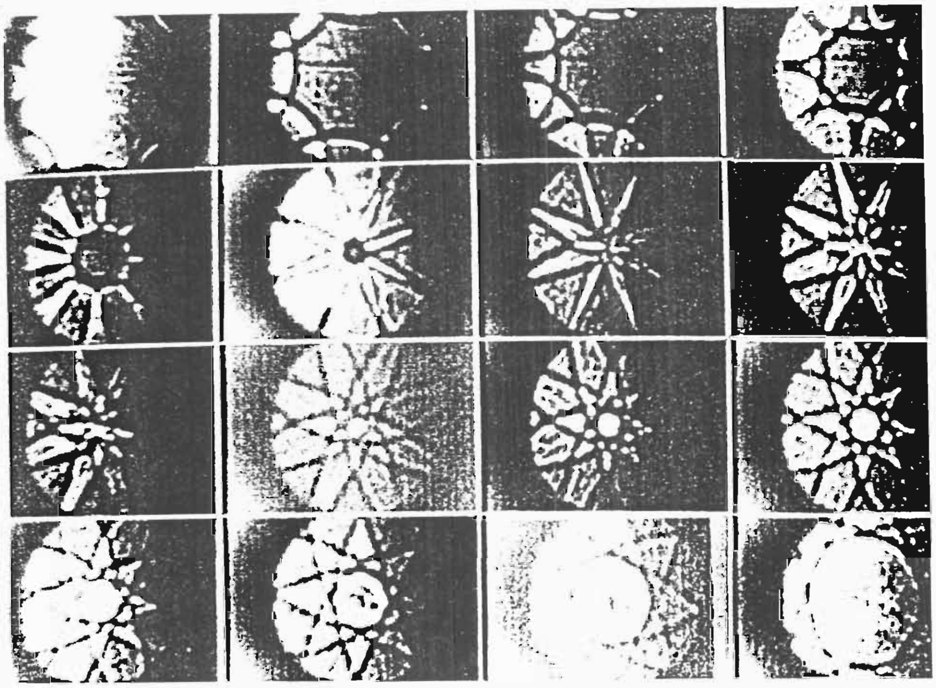

FIGURE 2. Illumination patterns 40 cm from the lens of figure 1a, at various times after the arcs: 3.2, 5, 6, 6.9, 8, 10, 10.4, 10.9, 11.3, 11.6, 11.8, 12.2, 12.4, 13.1, 14, 15.6 μs.

terns. The interesting point is that after the shocks have collided at the center, there is a cylindrically symmetric core. The shocks have forgotten where they originated. A sharp focus is seen in the seventh frame. An enlargement of the focal region (figure 3) shows an interesting set of Airy ring-like patterns centered on the strongly saturated focus.

3. Potential applications

3.1. *Drilling, cutting, and welding*

A good reason why lasers have not penetrated every industrial workshop is that their output windows and lenses are expensive and sensitive devices. We have already shown that CO_2 lasers coupled to gas lenses are capable of drilling through thick steel sheets (Michaelis *et al.* 1991a). However, the lenses we used were unwieldy CW devices with very long focal lengths (of the order of 80 cm.) The "dream" gas lens for this purpose would be a short focal length device (10 cm) capable of being "rep-rated" (100 Hz), with an optical aperture of at least 1 cm and minimal power consumption and weight.

3.2. *Q-switching and spatial filtering*

The combination of a CSL and a pinhole within the laser resonator could in principle serve to simultaneously Q-switch and spatially filter a laser oscillator. The pinhole would need to be under vacuum or, if the pulse is short enough, in helium gas to prevent breakdown. But Q-switching requires opening times of about 10–100 ns (Siegman 1986). For engineering applications, the focal length should not vary too quickly; whereas for Q-switching and beam handling (e.g., isolator) functions, fast switching is essential.

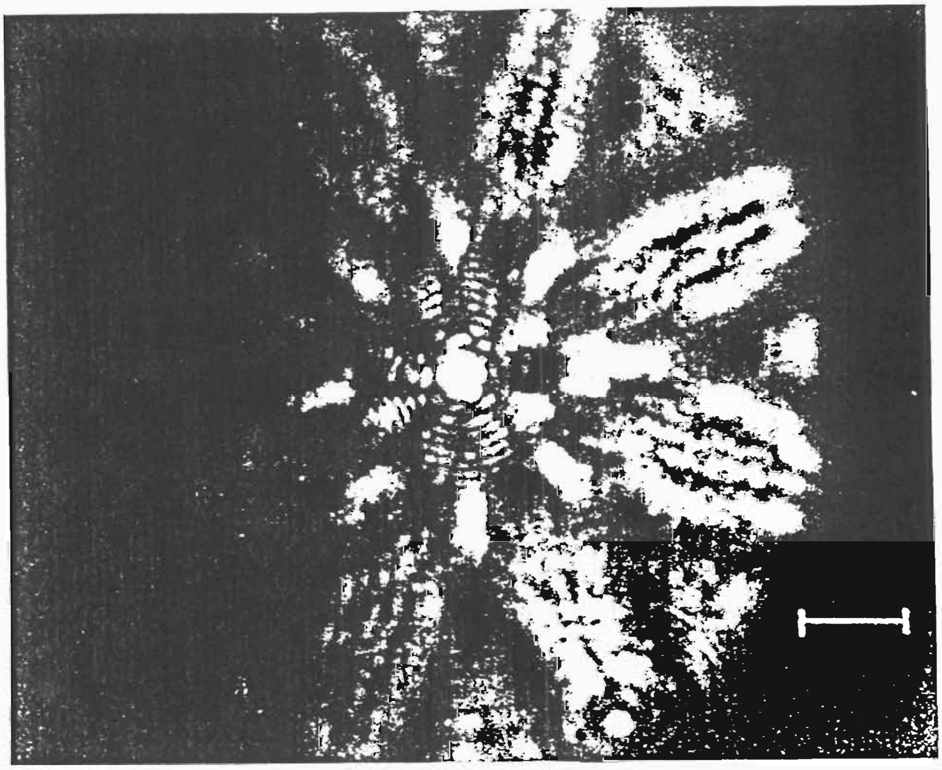

FIGURE 3. Magnified central region of 11.3-μs frame. (Bar = 1 mm)

3.3. *Ultrahigh-power and "all gas" lasers*

It is well known that even under clean room conditions lenses operating for pulse lengths of tens of nanoseconds start to fail at intensities in the GW/cm^2 range. Also, multiphoton processes at ultrahigh intensities render conventionally transmitting materials opaque or absorbing. We have previously pointed out that gas lenses could help alleviate these problems (Michaelis *et al.* 1991a). We foresee, without having the means to observe it, that very high powers may heat the gas and change the characteristics of the lens, just as in atmospheric "thermal blooming" (Barnard 1989). But for intermediate powers, the CSL could fill the present gap.

The final application we envisage is that of an "all gas" (or nearly all gas) system. Conventional pulsed gas laser systems are designed with beam diameters corresponding to the breakdown thresholds of solid optical components. A combination of aerodynamic windows and diverging and converging gas lenses could give gas laser design a new degree of freedom.

4. Performance of the CSL

All the applications listed above pose the following questions:

a. How good is the focus? Is it near diffraction limited?
b. How short is the focal length?
c. How quickly do CSLs switch, and how long do they last?
d. How large is the aperture, and is any light lost?
e. Can they be "rep-rated"? How much power do they consume?

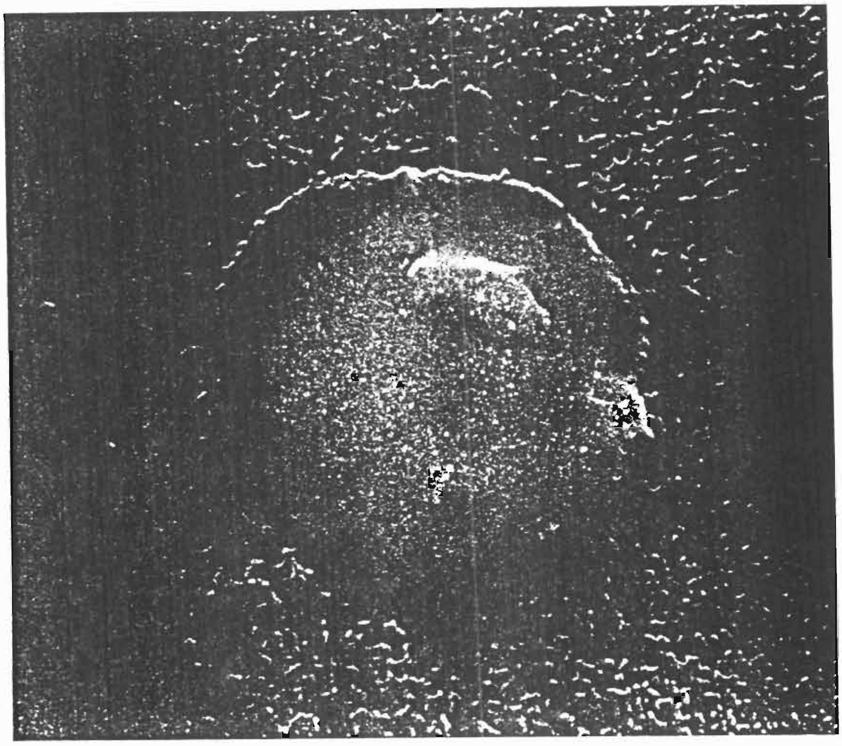

FIGURE 4. 130-μm burn pattern in aluminum foil obtained with lens of figure 1b.

a. From the very first experiments, we realized that this was somewhat surprisingly, given the limited number of arcs, an excellent lens. Figure 4 shows a burn pattern in aluminum foil obtained with an eight-arc lens. The optical aperture of the lens was 3 mm and the focal length 40 cm, so the diffraction limit would give a 130-μm hole. The central hole is approximately 130 μm.

b. The shortest focal length for an eight-arc device is about 20 cm. This is too long for many applications. We have already begun testing a double-ring device, and there is no apparent reason why several rings should not reduce the focal length to the 10-cm range.

c. For this purpose we have measured the switching ability. Our experimental apparatus is very simple and consists of a 10-mW HeNe laser followed by the CSL and a receiving photodiode at a distance L with a pinhole of diameter Φ immediately in front of it. We vary the distance L, the diameter Φ, and also the energy delivered to the shocks by changing the discharge capacitor. Figure 5 shows a typical switching time curve. In figure 6 we show how the switching rise time and the maximum signal vary with the pinhole size Φ at a fixed distance L, and in figure 7 we show how the same quantities vary with the focal length L for fixed Φ. As can be seen from switching curves like those in figure 5, the fall time of the signal is always comparable with the rise time (to within, say 50%), the latter being the critical quantity for Q-switching. The signals have been normalized to the signal produced by a 3-mm aperture, 50-cm focal length, spherical glass lens on the same photodiode and a pinhole $\Phi = 250$ μm. Figure 8 is like figure 6, but for a capacitor value of 1 μF. We believe that by increasing the shock energy we can make the switching faster.

The present CSL is thus a little too slow for Q-switching. But we have a concept for speeding it up that involves a multiple lens. Another problem in using this device for Q-switching is that it requires the presence of a pinhole in the cavity and the concomitant possibility of too high a radiation flux through it. Our idea is that this system could be worthwhile for cheaply Q-switching a small laser system.

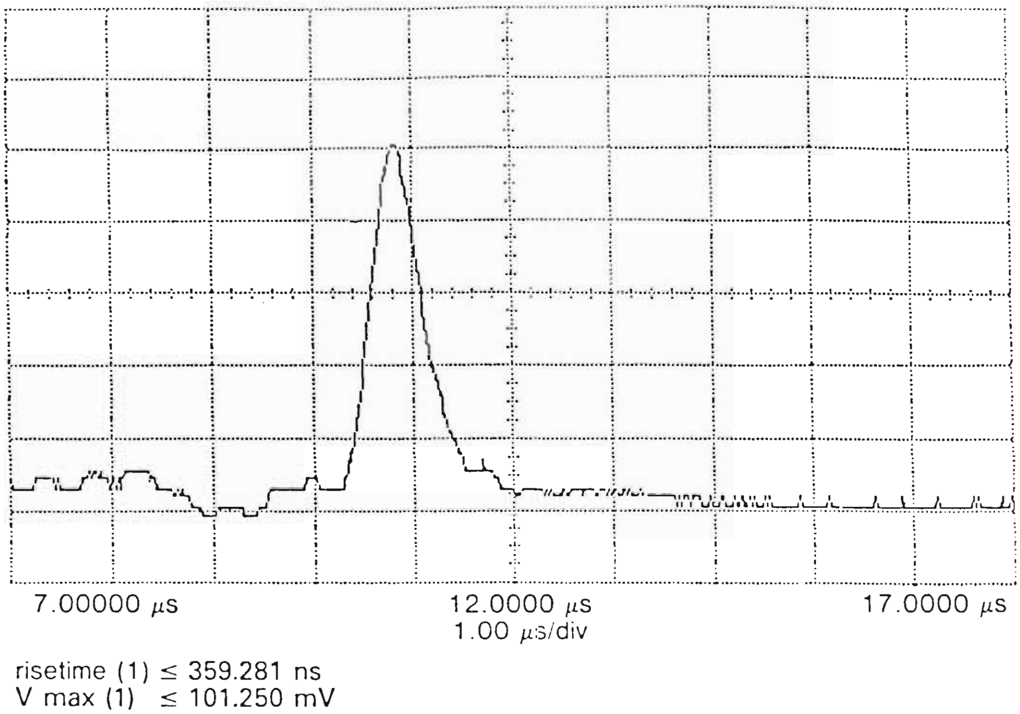

FIGURE 5. Switching curve. $L = 40$ cm, $\Phi = 300$ μm, $C = 5$ nF.

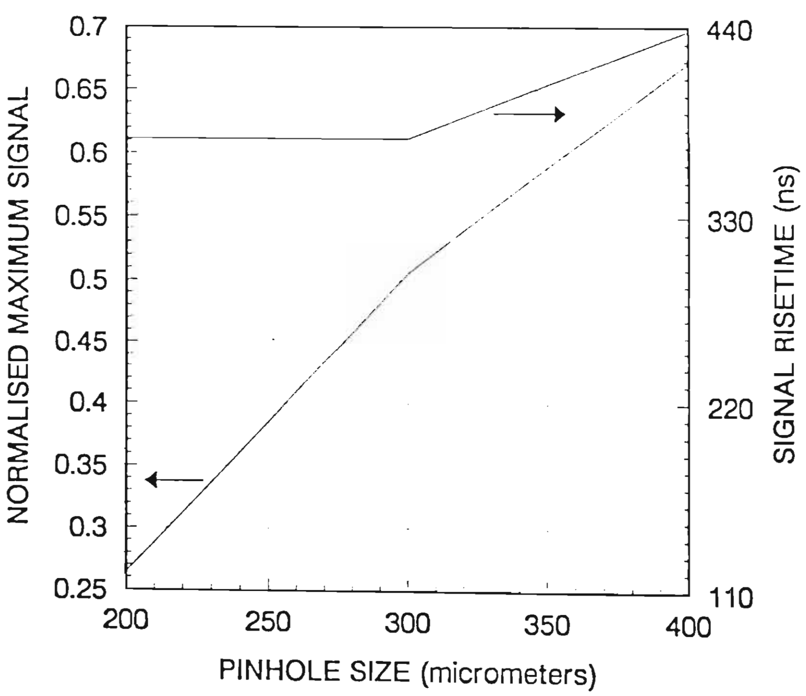

FIGURE 6. Switching rise time and maximum normalized signal versus pinhole size for $L = 40$ cm, $C = 5$ nF.

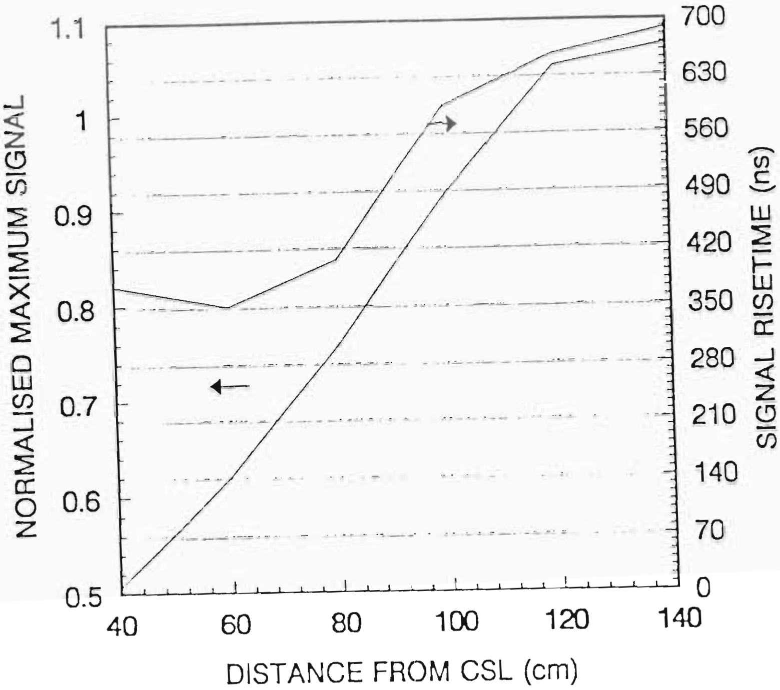

FIGURE 7. Switching rise time and maximum normalized signal versus distance from the CSL for $\Phi = 300\ \mu$m.

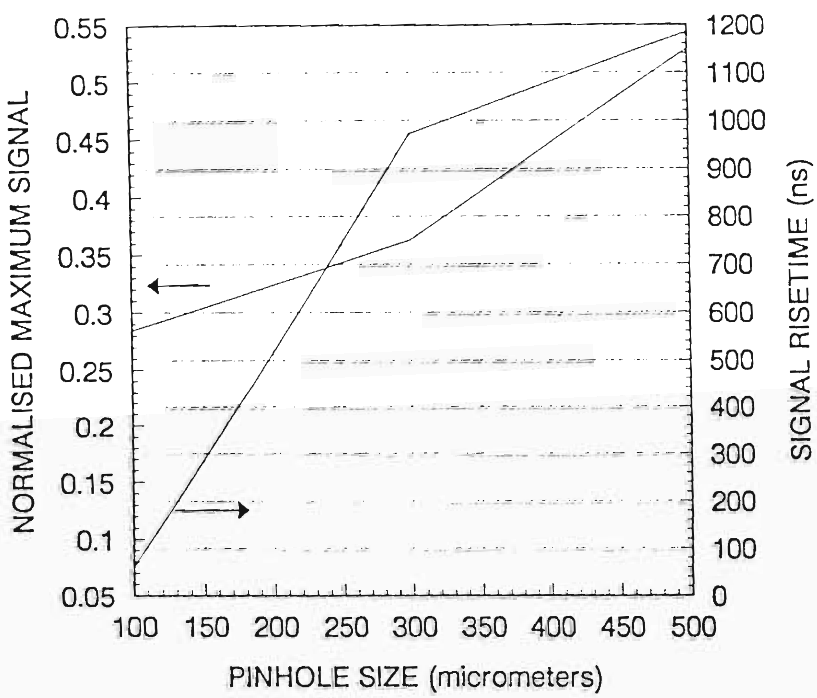

FIGURE 8. Switching rise time and maximum normalized signal versus pinhole size for $L = 40$ cm, $C = 1$ nF.

d. Possibly the worst feature of CSLs is the large electro-optic aspect ratio. The largest aperture obtained so far was only 4 mm. We plan to test a 10-cm electrical diameter lens in the hope of obtaining an 8-mm optical aperture. Another worrying feature of these lenses is that they are lossy. This, we believe, is inherent to their shock wave structure. The rear of the reflected shock refracts some light "in the wrong direction." This is to be expected from refractive fringe studies of shocks (Michaelis *et al.* 1991c). Orientatively we estimate the loss to be about 10%, slightly larger than that due to reflection in conventional lenses.

e. The question of "rep-rating" the lens has only been partially answered experimentally for want of a suitable high-voltage power supply. Operation at 10 Hz confirmed our expectations that the lens could run at moderate frequencies without degradation of the focus. At this repetition rate a typical switching curve such as that in figure 5 remains virtually unaltered. Based on dimension and speed of sound arguments, we would expect the limiting period to be of the order

$$\frac{\text{electrical diameter}}{\text{sound speed}} \approx 1\ \text{ms}.$$

The corresponding "rep-rate" would be 1 kHz, a useful frequency for industrial applications. The final question is that of power consumption. At a rep rate of $f = 1$ kHz, our present eight-pin lens would consume

$$W = f \cdot 1/2 \cdot CV^2 = 1\ \text{kW} \qquad (C = 5\ \text{nF},\ V = 20\ \text{kV}).$$

This is a considerable amount of pulsed power. To reduce this we tested an enclosed CSL that confines the arcs to two rather than three dimensions. An order of magnitude reduction in energy consumption occurs. However, that may be counteracted by the necessity of increasing the electrical diameter.

5. Conclusion

The novel CSL appears to be on the borderline of becoming a promising optical component. The focus is good, but the lens is slightly lossy. The lens focuses quickly, but not quite quickly enough for efficient Q-switching. The aperture is disappointingly small but might be scaleable. The lens may be rep-rated but consumes appreciable electrical power and could be incredibly noisy.

Acknowledgments

This work was supported in part by the Plasma Physics Research Institute (P.P.R.I.) and the Laser Applications Research Institute (L.A.R.I.S.A.).

REFERENCES

Barnard, J.J. 1989 *Appl. Opt.* **28**, 438.
Bacon, M. *et al.* 1989 *J. Appl. Phys.* **66(3)**, 1075.
Buccellato, R. *et al.* 1993a *Opt. Laser Technol.* **25**, 247.
Buccellato, R. *et al.* 1993b *Opt. Commun.* **101**, 350.
Michaelis, M.M. *et al.* 1991a *Laser Part. Beams* **9**, 641.
Michaelis, M.M. *et al.* 1991b *Nature* **353**, 547.
Michaelis, M.M. *et al.* 1991c *Opt. Laser Technol.* **23**, 283.
Notcutt, M. *et al.* 1988 *Opt. Laser Technol.* **20(5)**, 243.
Siegman, A.E. 1986 *Lasers* (University Science Books, Mill Valley, California).
Waltham, J.A. *et al.* 1990 *Laser Particle Beams* **8(1)**, 361.

Scaling up the colliding shock lens

M. Kuppen, M. M. Michaelis, R. Buccellato, and N. Lisi
Plasma Physics Research Institute, University of Natal, Durban, South Africa

(Received 16 March 1995; accepted for publication 14 June 1995)

In this paper we characterize the behavior of a new pulsed gas lens, the colliding shock lens. We show how input energy, electrical diameter, number of discharge electrodes, and enclosing the discharges, affect its optical aperture and focal length. Experimental results are presented for three different lenses and for a 1 cm aperture lens with a focal length of 1.5 m. We derive a simple colliding shock lens scaling law. © *1995 American Institute of Physics.*

I. INTRODUCTION

With the ever-increasing power of pulsed lasers, breakdown-induced damage to solid state optics is becoming a growing concern. The use of gas rather than solid lenses extends the breakdown threshold by three orders of magnitude. For 20 ns pulses of visible light for example, the threshold intensity for uncoated glass optics lies in the 1 GW/cm^2 range, an intensity easily reached at the output window of table top systems. Breakdown in air at STP, for the same pulse length occurs at just below the terawatt/cm^2 level.

Recently, our group developed a novel pulsed gas lens, the colliding shock lens or CSL, (1) Fig. 1(a). This is a spin off from our study of the refractive fringe diagnostic of shocks in air reported in this journal (2) and of the plasma lens/isolator invented by Rumsby and Michaelis. (3) In the latter device four converging laser-produced plasmas were used either to focus or to interrupt a laser beam. The first CSL was very similar. Four electric arcs are stuck in air on the circumference of a circle to generate four converging shock waves. These shocks create a cigar-shaped region of high density air at the center of the circle which acts as a graded index or GRIN lens. By adjusting the time delay between convergence and the arrival of the pulsed laser beam, the aperture and focal length of the lens can be varied. Typical parameters for the first lens are an optical aperture of 1 mm for a focal length of 50 cm. The focus [Fig. 1(b)] is near-diffraction limited and the diameter of the circle of arcs is 1 cm. In this form it is unlikely to be a useful device.

Converging shocks have been extensively studied from the early 1940s primarily because of their ability to produce extremely high pressures and temperatures on convergence. This property also made them very attractive for use in laser fusion schemes. The theoretical treatment by Guderley[4] of a converging strong cylindrical or spherical shock wave has served as the basis for much of this work.

The method of converging shock creation ranged from the experiment of Perry and Kantrowitz[5] which involved the use of a tear-drop-shaped body placed in the center of a shock tube to force a planar incident shock wave to implode; to cylindrically imploding shocks created by detonating cylindrical explosive shells (Matsuo and Fujiwara).[6] Some experimenters[7] used multiple detonations to create what was initially a polygonal-shaped converging structure. This polygon was found to produce a circular (or cylindrical) converging shock wave prior to implosion.

Other methods involved the rupturing of two glass spheres each containing gases at different pressures, to study the behavior of the collision of two shock waves[8].

Experimental evidence has shown that for moderately strong shocks ($M \leq 2.4$), converging cylindrical shock waves are stable. Knystautas, Lee, and Lee[7] showed that when a number of planar detonation waves converge towards a center, Mach reflections result in a smooth cylindrical converging shock wave provided the obtuse included angle between the intersecting wave fronts is of the order of 100° or greater.

Since most of the work involving converging shocks was directed towards understanding the creation of the high temperature and pressure region at the point of convergence, much attention was given to the implosion stage of the process. Very little attention was paid experimentally to the expanding stage.

Also, although much work was done on shocks generated by electric arcs in air,[9,10] to the best of the authors' knowledge, they have not been used before for the production of converging shock waves. Our first refractograms[1] of the converging shocks indicated that a Mach addition of more than four shocks, would make the lens more effective. The first prototype was improved by providing it with eight pairs of opposing electrodes. The optical aperture increased to 2 mm for the same 50 cm focal length.

II. THE CSL AND THE SCALING QUESTION

As mentioned above, the first CSL had too small an aperture to be useful, although its optical quality seemed promising. But it did serve to pose the following question: could the CSL be scaled up? Two contradictory arguments were put forward.

According to the pessimist's view, refraction towards the focus is caused only by the narrow shock front gradient. This view is supported by our own refractive fringe study of shocks[2,10] and is illustrated by Fig. 1(c) in which the weak shocks have passed through each other, virtually undisturbed. According to this view, the lens would only work so long as the separating shock fronts are not too far apart, which explains why the first lens has a millimetric aperture. The aperture of the CSL would not scale up beyond a small geometric factor times the shock front thickness.

The optimistic counterargument runs as follows. The

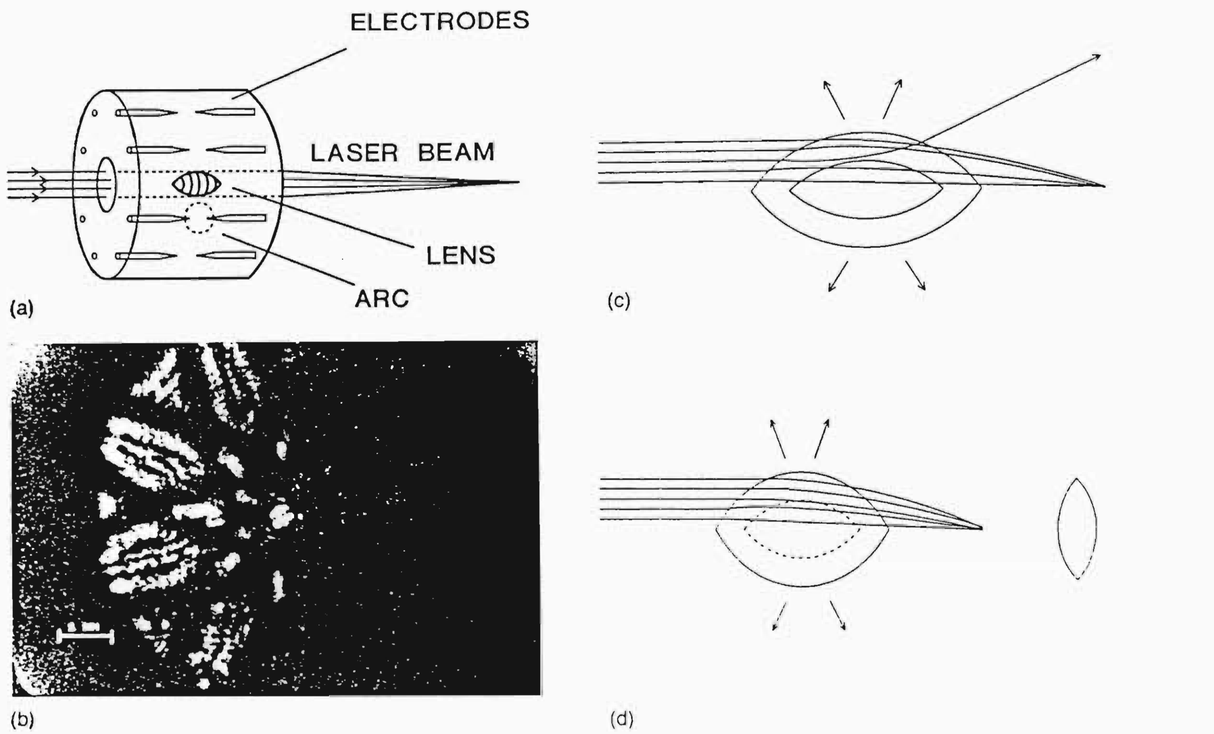

FIG. 1. (a) Schematic representation of the CSL. (b) Focus obtained with the first CSL at a focal length of 50 cm. (c) Schematic showing the lensing properties of weak shocks after collision. (d) Schematic showing the lensing properties of strong shocks after collision.

central collision of converging shocks produces a region of high density in which all "memory" of the early shocks is erased by nonlinear effects. This view is supported by the post-collision frames of Ref. 1 which show a circular rather than polygonal expansion front. This front may have a weaker gradient than the initial shocks and is therefore broader. The angular deflection of a ray being low, it is permissible to integrate the density along the ray, assuming that the ray's radial position does not change inside the lens. Integration of the hollow cigar gives the familiar lenticular shape: Figs. 1(d) and 3(b). Although it is true that only the front refracts light "inwards," the gradient of the shock rear is not strong enough to cancel the effect of the front. Gas inside the cigar plays a compensatory role which cannot be forgotten as in the first argument.

A millimetric gas lens is useless. A centimetric CSL would have many industrial applications. A decimetric pulsed gas lens could serve as the final focusing element for a laser fusion reactor.[11] Not being able to resolve the above discussion computationally, we decided it experimentally. In this paper we report how various factors (input electrical energy, electrical diameter, lens geometry) affect the optical aperture and focal length. With the successful operation of a 1.5 cm aperture CSL, we now believe the more complex second scenario.

III. EXPERIMENTAL APPARATUS

The experimental apparatus used for the following set of experiments was the same as that used by Buccellato *et al.*[1] Figure 2 is a schematic representation of the circuit in which C refers to the charging capacitor which is discharged through the electrodes of the CSL.

The CSL consists of two 5-mm-thick plexiglass plates which support eight or sixteen pairs of opposing electrodes: Fig. 1. (The plates can be either square as in Fig. 2, or circular as in Fig. 1). The separation between the plates can be adjusted from 1 to 4 cm.

The electrodes used in this experiment are constructed from 0.5-, 1-, 2-mm-diam stainless steel pins depending on the maximum energy to be stored in the capacitor. The electrode separation was always set at 0.5 mm. The electrodes are connected in series to ensure that the gaps break down simultaneously. A circular window is cut out of each of the

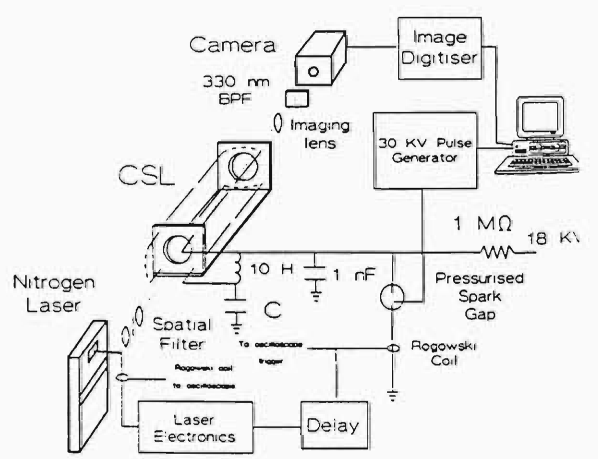

FIG. 2. Schematic representation of the CSL experimental setup. C refers to the charging capacitor.

plexiglass plates to allow a nitrogen laser beam (337 nm) to be shone through. It is with this beam that the properties of the CSL are studied.

The charging capacitor (C) is initially charged to 18 kV through a 10 H inductor by means of a high voltage dc power supply. A 5 V computer signal triggers the pulse generator resulting in a 30 kV pulse of 1 μs duration being sent to the extra electrode of the pressurized spark gap. This causes the spark gap to break down, pulling one side of the CSL to ground. The 1 nF capacitor provides the initial energy to break down the spark gap. The potential difference across the CSL produces the ring of simultaneous arc discharges. Each of these arcs generates an expanding spherical shock wave. The expanding shock waves collide at the center of the CSL and a high pressure, temperature, and density region is created. We call this the "implosion stage." A short time (of the order of microseconds) after collision, the expansion of this high density region results in the axisymmetric "cigar"-shaped density distribution which forms the graded index lens.

The detection circuit for this experiment is capable of detecting either the shock structure at various times or the focal spot for different focal lengths. This is accomplished in the following way: a Rogowsky coil in the CSL discharge circuit sends a signal to a delay box when the CSL "fires." This signal is then delayed and used to trigger the spatially filtered and expanded nitrogen laser beam. The beam then passes through the windows of the CSL before falling on the face plate of a charge-coupled device camera and is digitized by means of an Oculus 200 frame grabber. A 330 nm interference filter with a bandwidth of 10 nm is placed in front of the camera to select out the nitrogen beam from the light generated by the arcs. To study the behavior of the shock waves, a convex lens is used to image in the shock plane (Fig. 2). By varying the delay of the nitrogen laser one obtains a sequence of shadowgrams for the shock waves, from convergence to collision and finally divergence. This enables us to calculate the size of the lensing region formed by the cigar.

By removing the imaging lens and allowing the laser beam to fall directly on the face plate of the camera, the quality and size of the focal spot can be evaluated for different focal lengths. To avoid confusion in the terminology, we henceforth refer to the maximum diameter of the cigar-shaped lensing region as the "optical aperture" of the lens, to the plexiglass structure incorporating the electrodes as the CSL, and to the diameter of the circle of electrodes as the "electrical diameter."

IV. CHOICE OF VARIOUS CSL DESIGNS

To characterize the CSL one must determine the extent to which the various parameters (energy, electrical diameter, number of electrodes, wall geometry) affect the optical aperture, the focal length, and the quality of the focus. To this end the following parameters were varied.

A. Shock strength

The first question that needs to be answered is how the shock strength affects the lensing region. In our experiments, the shock strength is varied by changing the capacitance of the charging capacitor while keeping the voltage constant.

B. Electrical diameter

The electrical diameter is increased by using different CSLs. Some half-dozen CSLs were constructed to gain experience with these devices.

C. Number of electrodes

By increasing (or decreasing) the number of pairs of electrodes on the CSL, we can change the shape of the imploding shock structure and hence the shape of the lensing region.

D. Enclosure

We experiment with enclosed and unenclosed CSLs to determine whether confinement of the shocks affects the quality of the lensing. The CSL is enclosed by encasing it in a Plexiglass tube and reducing the separation of the vertical walls.

We now present a summary of the physical characteristics of the four CSLs constructed to test these concepts. The CSLs will be labeled CSL 1–4.

CSL1 : This is the original CSL (see Buccellato *et al.*).[1] It has eight pairs of electrodes arranged on a circle of diameter 11 mm. The diameter of the windows is 7.5 mm. CSL1 is unenclosed.

CSL2 : This CSL has an electrical diameter of 33.5 mm and a window diameter of 11 mm. This second unenclosed CSL has eight pairs of electrodes.

CSL3 : To see how enclosing the CSL would affect its lensing properties, we constructed a CSL with the same electrical diameter and windows as the preceding one but enclosed it in a plexiglass cylinder of diameter of 40 mm. This CSL like the preceding two is also fitted with eight pairs of electrodes. The wall separation was reduced from 40 to 10 mm.

CSL4 : The final CSL has an electrical diameter of 80 mm and a window diameter of 50 mm. The distance between the end plates is 21.5 mm and the diameter of the plexiglass tube is 120 mm. This lens can be fitted either with eight or sixteen pairs of electrodes.

V. RESULTS AND DISCUSSION

In order to better understand the scaling results we first briefly reexamine the process of GRIN lens formation.

When the pressurized spark gap in the CSL power supply breaks down, the electrical discharges between opposing pairs of electrodes in the CSL act as point sources for spherically expanding shock waves. As mentioned before, these shock waves collide at the center of the CSL. On collision of two or more shock waves, a high density, pressure, and temperature region forms. In our experiments where $M \approx 1.5$, we do not expect the region to become turbulent, except for higher energies, as explained below. This region then expands to form the cigar-shaped region already described. Figure 3(a) is a computed density profile that results during

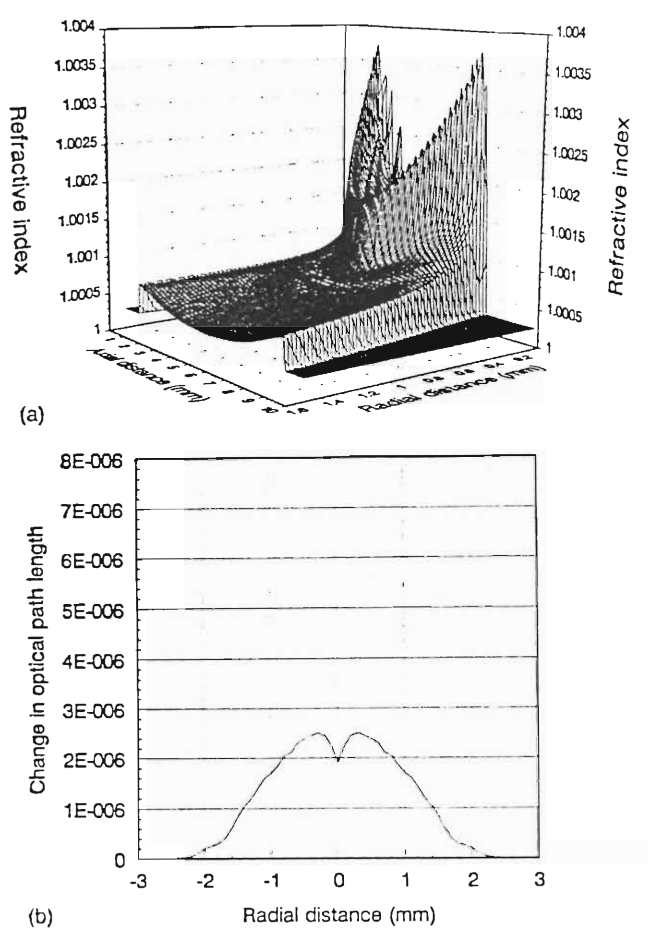

FIG. 3. Computed refractive index field of the CSL 1 μs after initial shock wave reflection. Inset below: integrated optical path length difference.

the expansion phase.[12] Only half the lensing region or "cigar" is shown. The refractive index increases sharply near the edges of the cigar and a depression is visible in the center.

Although this profile looks extraordinarily complicated, its computation allows one to verify the following statement, which simplifies the ray optics. There are virtually no radial deviations within the lens. This is because the refractive index differs from unity by less than one percent and the refractive index gradients and the angular deflections are small. (Less than 5 degrees).

To calculate the latter it suffices to integrate the density along the path of each fixed radius paraxial ray. The complicated profile then reduces to the familiar lenticular shape: Fig. 3(b) (The central "hole" may be computational).

We now compare the performance of various lenses. Typical parameters reported for the first eight arc colliding shock lens[1] were an optical aperture of 2 mm for a focal length of 52 cm and an input energy of 0.8 J. (C=5 nF). The focal spot size was near-diffraction limited.

A. Increasing the electrical aperture (unenclosed CSL)

By using CSL2 and keeping the same charging capacitor, we are able to determine the effect an increase in electrical diameter has on the focal length and optical aperture for the unenclosed CSLs. We would expect that since the energy falls off with shock radius R, the larger CSL (CSL2) should produce a weaker converging shock wave, since the shocks travel a greater distance before colliding. Hence, CSL1 should have a shorter focal length than CSL2 for the same optical aperture (or conversely a larger optical aperture for the same focal length).

Figure 4(a) shows a plot of optical aperture versus time after collision for CSL2. This is obtained by imaging in the shock plane of the CSL. We can see that the optical aperture increases with time. The focal length also shows the same trend [Fig. 4(b)]. Combining these two results, we obtain a plot of focal length versus optical aperture [Fig. 4(c)]. To compare CSL2 with CSL1, we read off the optical aperture for a known focal length, i.e., 52 cm. The lens diameter for this length is 0.5 mm (2 mm for CSL1). It is clear that the strength of the shocks on implosion is greater for CSL1 than for CSL2. For the same optical aperture, CSL1 has a shorter focal length than CSL2.

We can conclude that for the unenclosed case, increasing the electrical aperture must be accompanied by a corresponding increase in input energy to maintain and in fact improve the performance of the CSL.

B. Enclosing the CSL

Intuitively it would seem that by enclosing a CSL, reducing the loss of energy, and confining the shock waves to two dimensions rather than three, we should be able to produce stronger shock waves and hence better focusing (i.e., shorter focal lengths and larger optical apertures than with the unenclosed lens). We therefore constructed CSL3 which is an enclosed version of CSL2.

Figure 5(a) shows the focal length versus optical aperture for CSL2 and CSL3. The capacitor used was the same for both (5 nF), hence the input energy was the same as well (0.81 J). We also plot f number versus focal length for CSL2 and CSL3 [Fig. 5(b)].

The difference in the behavior of the two CSLs is striking. CSL3 has an optical aperture of 2.2 mm at 0.9 m focal length while CSL2 has an aperture of 0.7 mm for the same focal length. The f number of CSL3 is better than that of CSL2 by a factor of ≈ 3.

A quantitative assessment of how different types of enclosure strengthen the shocks, will require further investigation. But clearly, this is a promising feature of colliding shock lenses.

C. Varying the energy

Having established that the enclosed lens works well, we now adopt it for the energy dependence studies.

Three different capacitor sizes are used with CSL3. They are 5, 21, and 100 nF. These corresponded to energies of 0.8, 3, and 16 J, respectively. The energy increases by up to a factor of 20.

Figure 6(a)shows the focal length versus optical aperture for CSL3 at the different energies. We achieve an optical aperture of 4 mm at a focal length of 1.3 m for 100 nF.

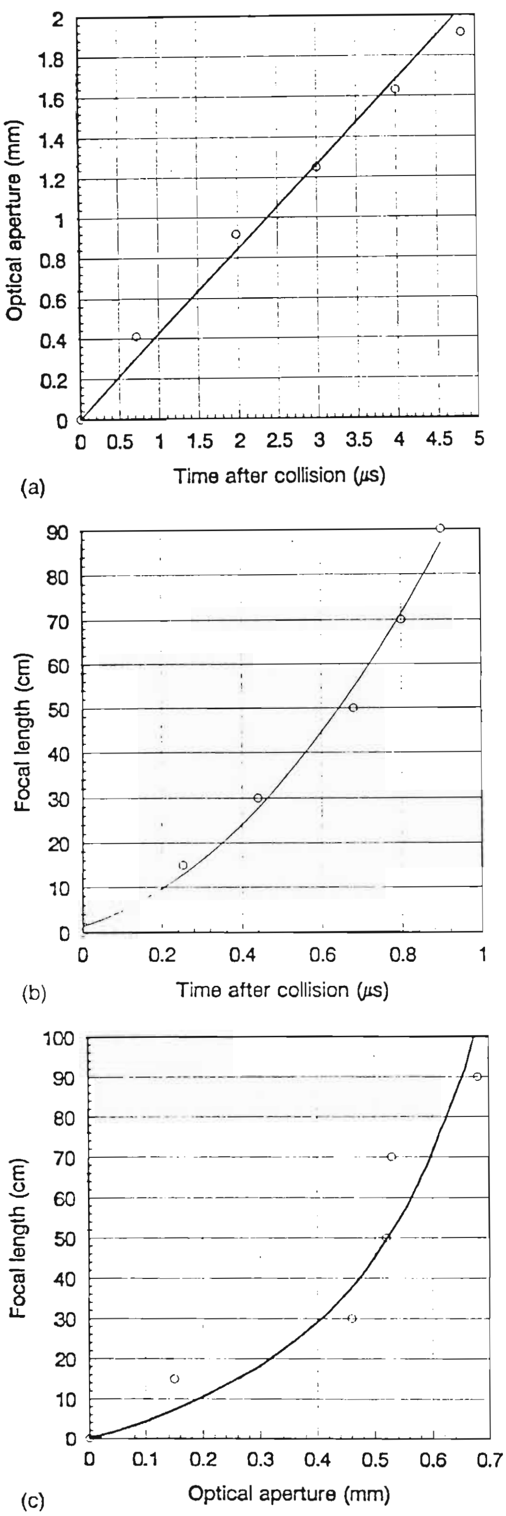

FIG. 4. (a) Plot of optical aperture vs time after collision for CSL2 using a 5 nF charging capacitor. (b) Focal length vs time after collision for the CSL2 - 5nF charging capacitor. (c) Optical aperture vs focal length for the CSL2 - 5nF charging capacitor.

Plotting the f number versus focal length [Fig. 6(b)] we see an improvement in the f number for 100 nF as compared to the 5 and 21 nF.

An attempt to use a 250 nF capacitor to increase the input energy by a factor of 2.5, was not successful. Although a cigar-shaped core did form, the quality of the focus was very poor indeed. We attribute this to the onset of turbulence, known to occur when strong shocks collide.

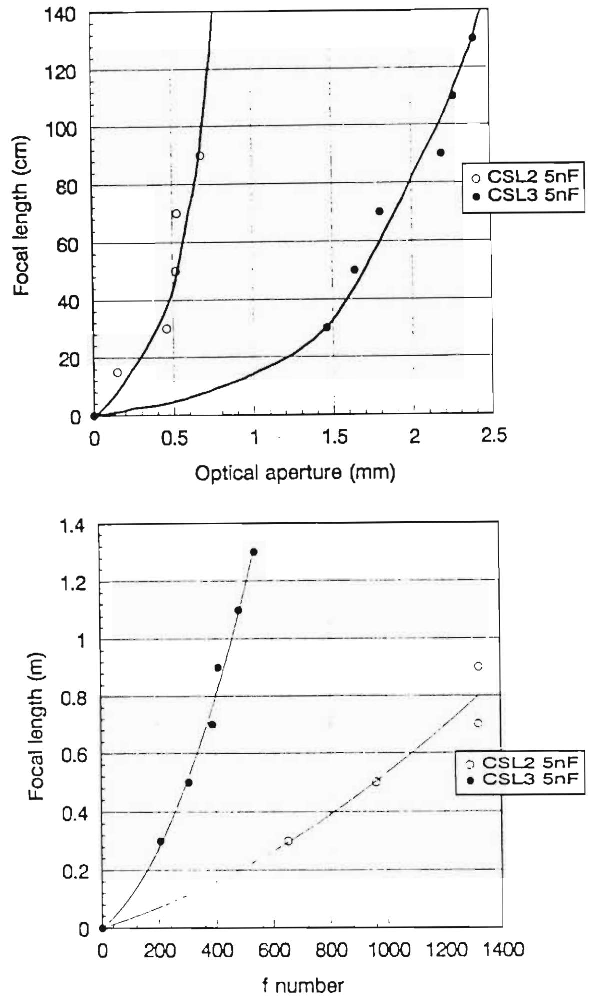

FIG. 5. (a) Comparative focal length vs optical aperture for the CSL2- and CSL3 - 5nF charging capacitor. (b) f number vs focal length for CSL2- and CSL3-5nF charging capacitor.

D. Increasing the electrical diameter (enclosed CSL)

Increasing the electrical diameter alone will not result in a larger optical aperture for similar focal lengths. This increase must also be accompanied by an increase in the input energy. There are two reasons for this. The first is that Mach addition requires large included angles. The second is that addition only occurs for strong shocks.

A larger electrical diameter results in weaker shock waves colliding near the center. Circular symmetry may then not be attained. We tried CSL4 with an eight electrode pair configuration. As expected this does not form a good lens since circular symmetry of the cigar is not achieved. Figure 7(a) shows the polygonal shock structure created by the collisions in this configuration. Circular symmetry has not been obtained.

E. Changing the number of electrodes

To regain circular symmetry in CSL4, eight more pairs of electrodes were inserted converting it into a sixteen pair

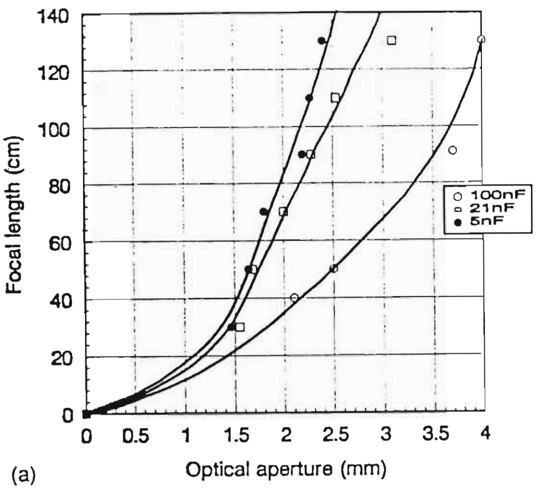

(a)

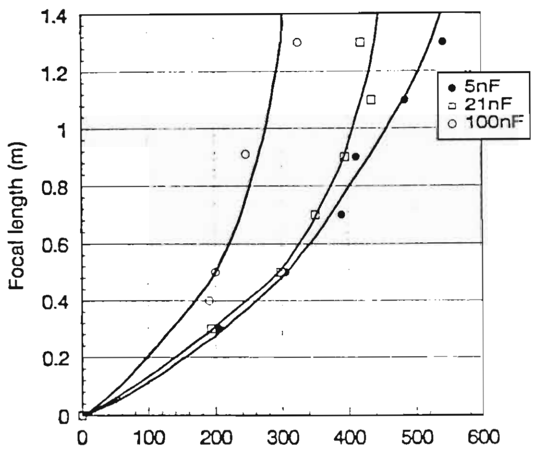

(b)

FIG. 6. (a) Focal length vs optical aperture for CSL3 using 5, 21, and 100 nF charging capacitors. (b) f number vs focal length for CSL3 using 5, 21, and 100 nF charging capacitors.

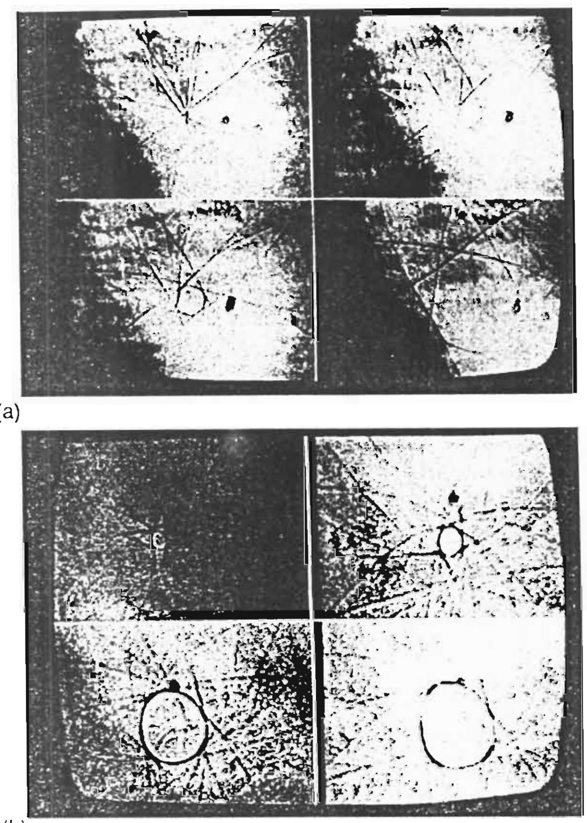

(a)

(b)

FIG. 7. (a) Sequence of colliding shock images [(a) implosion; (b) 6.2 μs; (c) 7.4 μs, and (d) 14 μs after implosion] taken using CSL4 having an eight pair electrode pair configuration and a charging capacitor of 100 nF. Magnification=0.33. (b) Sequence of colliding shock images [(a) 0.3 μs; (b) 1.5 μs; (c) 3.9 μs, and (d) 4.3 μs after implosion] taken using CSL4 with a sixteen electrode pair configuration and a charging capacitor of 100 nF. Magnification=0.5.

electrode CSL. The imploding shock waves achieve symmetry early. This can be seen from the sequence of four pictures showing the shocks after collision [Fig. 7(b)]. The circularly symmetric nature of the shock structure is evident. So adding more shocks was necessary for this large diameter CSL to symmetrize and to form a lens.

Figure 8 shows the focal length versus optical aperture for three different capacitor sizes viz. 21, 100, and 250 nF. Since we now have larger radii shock waves forming an axisymmetric cigar, we can expect a larger optical aperture. But since the density gradients for the same input energy may be weaker, we would expect to see an increase in the focal length (see Fig. 9).

It is interesting to note that CSL3 becomes turbulent at 250 nF. If we could increase the input energy into this CSL, it would perform better than CSL4. However every CSL has an upper limit for input energy. CSL4 with sixteen pairs of electrodes was very stable for the 250 nF capacitor. From Fig. 8 we see that CSL4 at 250 nF has an optical aperture of 8.2 mm for a focal length of 1.3m. The focal spot at this distance is shown in Fig. 10. It has a full width at half-maximum of 200 μm. By gas lens standards, this is close to diffraction limited.

VI. CSL SCALING THEORY

An approximate scaling theory for CSLs can be derived with the help of the following assumptions.

(i) All the electrical energy stored in the charging capacitor is transferred to the shock waves by the arcs.

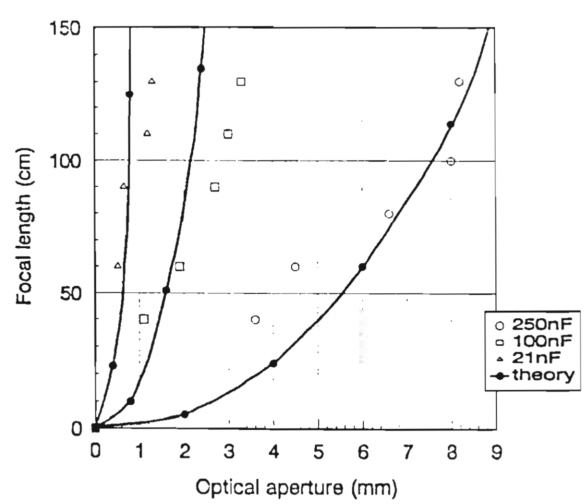

FIG. 8. Focal length vs optical aperture for CSL4 (sixteen electrode pairs) using 21, 100, and 250 nF charging capacitors.

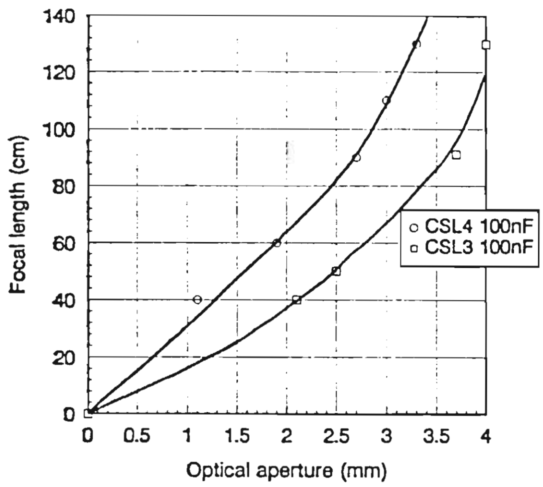

FIG. 9. Focal length vs optical aperture for CSL3 and CSL4 using a 100 nF capacitor.

(ii) A certain fraction of this energy is contained in the gas forming the lens. This fraction is represented by the product of a "geometric energy factor" G and a "shock weakness factor" G'.

(iii) For the purpose of calculating refraction, the actual density profile, however complex, can be approximated by a cigar-shaped, high density region with a constant refractive index gradient.

(iv) A simple order of magnitude focal length calculation is acceptable.

Clearly, all these assumptions can be examined and refined in great depth. But at this stage of development, we find the following simple calculation useful.

Only a fraction $W = G\,G'(1/2CV^2)$ of the total energy in the shocks is contained in the compressed gas of the lensing region, where

$$G^2 = \frac{1.}{20}\left(\frac{r}{R}\right)^3$$

and G' is a fitted parameter. G is the areal cross section that the lens offers up to the spherically expanding shock front. It is obtained by assimilating the cigar to two cones, each of height l and base radius r. Simple trignometry shows that the half-length of the cigar is

$$l = \sqrt{2rR},$$

where R is the radius of two intersecting shocks.

G' represents the fraction of shock wave energy contained in the supersonic front as opposed to that which has been dissipated in forming the long shock rear and the shock tail. No figures are available for this factor, but simple visual examination of typical density and temperature curves,[13,14] show that it can vary from unity (all the energy is in the strong shock) to a few percent (very little energy is left in the shock itself which now resembles a sound wave). G' is also made to contain the small geometric errors, deliberately made in the rough calculation of G and that following for the focal length f.

In order to calculate the density of the gas in the lens, we now assume that the lens is formed adiabatically, so that

$$W = \frac{1}{\gamma - 1}(p_f V_f - p_o V_o),$$

where the symbols have their usual meaning. The known quantities in this expression are the volume of the lens V_f and the initial pressure: p_o. The volume of the lens is approximated to that of two cones:

$$V_l = \frac{2}{3}\pi r^2 l.$$

Taking $\gamma = 1.4$ and writing

$$p_o V_o^\gamma = p_f V_f^\gamma$$

one obtains

$$\frac{p_f}{p_o} - \left(\frac{p_f}{p_o}\right)^{1/\gamma} = \frac{0.4W}{p_o V_f}.$$

The right-hand side is known and p_f/p_o may be obtained graphically.

Knowing the average density $\rho_f = (V_o/V_f)\rho_o$ in the lens, the refractive index gradient may be calculated very approximately as follows.

The refractive index of air is roughly $n = 1 + 3\times10^{-4}\rho$. The uniform refractive index gradient is therefore $(n - n_o)/r$ and a median ray traversing the lens $r/2$ mm away from the axis, is refracted by an angle

$$\theta = l(n - n_o)/r$$

and comes to a focus a distance $f = (r/2)/\theta$ away. (n_o is the refractive index of undisturbed air).

A little algebra yields the convenient formula

$$f^2 = \frac{1.4r^3}{(\rho - 1)^2 R},$$

where f is in meters and r and R in millimeters.

We now attempt to model our large lens, CSL4. This has an electrical diameter of 8 cm, which yields an 8 mm GRIN lens with a focal length of the order of one meter. If G' is taken as unity, then the calculated focal length is too small.

This example and others, show that predicted focal lengths are a little short for strong shocks and far too short for weak. This was the reason for introducing the G' correction factor. If we take G' as $\frac{1}{2}$ for the strong 250 nF shocks,

FIG. 10. Focal spot at 1.3 m away from CSL4 (250 nF charging capacitor).

$\frac{1}{30}$ for the weaker 100 nF, and $\frac{1}{100}$ for the very weak 21 nF, we obtain rough agreement. (See the calculated curves for Fig. 8). This simple theory and the scaling experiments described in earlier sections lead us to construct a final enclosed CSL with an electrical diameter of 26 cm powered by a half μF capacitor charged to 17 kV. Our first experiments with this lens showed it to be capable of generating a 1.5 cm aperture lens with a focal length of 1.5 m.

In this attempt to determine whether the aperture of the CSL can be scaled up, we find the following.

(1) Enclosing the lens improves its performance.
(2) Increasing the input energy also increases the aperture and decreases the focal length. However there is an upper limit to the amount of energy one can put into the shocks. The small lens (CSL3) with eight pairs of electrodes becomes unstable with the 250 nF capacitor whereas with more electrodes and a larger electrical aperture, CSL4 (sixteen electrode pairs) is very stable.
(3) Simply scaling up the electrical diameter does not necessarily increase the lens aperture. There has to be an accompanying increase in energy and perhaps more important, enough shocks for circular symmetry to be attained before implosion. The smaller CSLs (2 and 3) worked with eight sets of electrodes whereas the large CSL (CSL4) needs more electrodes to achieve symmetry.

In conclusion, we have shown that the colliding shock lens can be scaled up to useful apertures and how to do so. We have derived a simple CSL scaling law.

ACKNOWLEDGMENTS

The authors wish to thank the workshop staff of the Physics Dept. of the University of Natal. This work was partly supported by the Foundation for Research and Development.

[1] R. Buccellato, N. Lisi, and M. M. Michaelis, Opt. Commun. **101**, 350 (1993).
[2] M. Bacon, R. N. Campbell, P. F. Cunningham, and M. M. Michaelis, J. Appl. Phys. **66**, 1075 (1989).
[3] P. T. Rumsby and M. M. Michaelis, Opt. Commun. **21**, 337 (1977).
[4] G. Guderley, Luftfahrt-forsch **19**, 302 (1942).
[5] R. W. Perry and A. Kantrowitz, J. Appl. Phys. **22** 878 (1951).
[6] H. Matsuo and K. Fujiwara, Phys. Fluids A **2**, 266 (1992).
[7] R. Knystautas, B. H. Lee, and J. H. S. Lee, Shock Tube Symposium, Phys. Fluids Suppl. I, 1969 (unpublished).
[8] I. I. Glass and L. E. Heuckroth, Phys. Fluids **2**, 542 (1959).
[9] K. Muraoka, M. Hamamato, and M. Akazaki, Jpn. J. Appl. Phys. **19**, 293 (1980); M. Hamamoto, K. Muraoka, and M. Akazaki, *ibid*. **20**, 443 (1981).
[10] M. M. Michaelis, J. A. Waltham, and P. F. Cunningham, Opt. Laser Technol. **23**, 283 (1991).
[11] M. M. Michaelis, P. F. Cunningham, M. Notcutt, and J. A. Waltham, Laser Particle Beams **9**, 641 (1991).
[12] R. Buccellato, University of Natal Doctoral thesis, 1994.
[13] L. I. Sedov, *Methods of Similarity and Dimensional Analysis in Mechanics*, 3rd ed. (Academic, New York, 1959).
[14] Y. B. Zeldovich and Y. P. Raizer, *Physics of Shock Waves and High Temperature Hydrodynamic Phenomena* (Academic, New York, 1966), Vol 1.